UNIVERSITY OF SOUTHAMPTON

Using modelling and data analysis to interpret single-spacecraft observations in the Jovian and Kronian magnetospheres

by

Joseph J. Reed

A thesis submitted in partial fulfilment for the degree of Doctor of Philosophy

in the
Faculty of Physical Sciences and Engineering
Department of Physics & Astronomy

May 2018

UNIVERSITY OF SOUTHAMPTON

Abstract

Faculty of Physical Sciences and Engineering
Department of Physics & Astronomy

Doctor of Philosophy

by Joseph J. Reed

This thesis deals with the interpretation and expansion upon single-spacecraft observations in the Jovian and Kronian magnetospheres. Unlike at Earth where a host of single and constellation in-situ satellites as well as ground based observations give a good global coverage of the magnetosphere, the magnetospheres of Jupiter and Saturn only have a single spacecraft each, Juno (previously Galileo) at Jupiter and previously Cassini at Saturn. With this local data it is then necessary to expand to a global picture. A "viewing region" is a region within the magnetosphere where we would expect to see the signatures of dynamics that occur within the magnetosphere. Unfortunately, the spacecraft are often not in this ideal region and even if they, they are can still 'miss' dynamics that occur. The work in this thesis looks at how modelling and data analysis can overcome the limits of single-spacecraft observations. The first study looks at a simple avalanching 1-D cellular automata sandpile model as an analogue for magnetospheric dynamics of Jupiter. With simple input and threshold rules, the model can reproduce some statistical properties of the Jovian magnetosphere. The work suggests that much of the mass that is lost from the Jovian magnetosphere is lost in small-scale events that may not be seen by in situ spacecraft or selected by automated detection criteria. The second study looks at the use of low frequency extensions, extensions of the Saturn Kilometric Radiation from higher to lower frequencies, as a proxy for magnetospheric dynamics. An automated criteria is developed for the selection of these events during 2006. Two forms of LFE are found: short events (< 20 hours) which are strongly linked with tail-reconnection events, and long events (> 20 hours) which are strongly linked with increased solar wind dynamic pressure. The third study develops a criteria for the selection of narrowband emissions, a low frequency emission which forms part of the Saturn radio spectrum, and analyses these events in relation to the LFE catalogue developed in the second study, and examines some of their statistical properties. The events are found (as in previous studies) to occur in clusters of usually 5 or 6 individual intensifications over a period of several days following periods of increased solar wind dynamic pressure. In this way narrowband emissions are a good proxy for large-scale events in the magnetosphere.

Declarations

The research undertaken during the course of this doctoral programme has led to the submission and publication of the following scientific papers:

J. J. Reed, C. M. Jackman, L. Lamy, W. S. Kurth, D. Whiter. Low Frequency Extensions of the Saturn Kilometric Radiation as a proxy for magnetospheric dynamics. 2018. *Journal of Geophysical Research: Space Physics*. DOI: 10.1002/2017JA024499

J. J. Reed, C. M. Jackman, L. Lamy, P. Louarn. Statistical survey of Saturn's narrowband emissions. 2018. [In Preparation]

"You know, maybe get a ton of cat hair, glue it all over your body, you know, walk around like a cat man in the night through the alleyways, you know. And stop hiding the pigeon."

- Charlie Kelly

Contents

List of Figures

Declaration of Authorship

I, JOE REED, declare that this thesis titled, 'Using modelling and data analysis to interpret single-spacecraft observations in the Jovian and Kronian magnetospheres' and the work presented in it are my own. I confirm that:

- This work was done wholly or mainly while in candidature for a research degree at this University.
- Where any part of this thesis has previously been submitted for a degree or any other qualification at this University or any other institution, this has been clearly stated.
- Where I have consulted the published work of others, this is always clearly attributed.
- Where I have quoted from the work of others, the source is always given. With the exception of such quotations, this thesis is entirely my own work.
- I have acknowledged all main sources of help.
- Where the thesis is based on work done by myself jointly with others, I have made clear exactly what was done by others and what I have contributed myself.

Signed: _____

Date: 18 / 05 / 2018

Acknowledgements

I would like to thank my supervisor, Caitríona Jackman, for helping me throughout this PhD. I will be forever grateful for her effort, guidance, support, understanding and commitment. She has guided (and at times dragged) me through these three years, although I feel her attempts to teach me grammar and how to use, a comma, may ultimately have fallen short.

Thank you to Dan Whiter, my second supervisor, for being a calm voice and for listening and nodding.

I thank the Space Environment Physics Group and the wider Astronomy group for providing a great working environment and for Astro-football which I looked forward to every week.

Andy. There is no way I could have done this PhD without you. You have been the best officemate, housemate and friend I could have asked for. Ly. X.

Frank. For cups of tea, food, Eddie Izzard quotes, chats and everything. Thank you. X.

Jade. Thank you. I'll miss you. High foot. X.

Thanks to the Grosvenor house.

Thanks to my family for being there.

Thanks Mum for being you.

Elisa. Nous avons réussi à le faire. Enfin nous allons pouvoir commencer notre vie ensemble! Je t'aime. X

Chapter 1

Introduction to space plasma physics

1.1 Introduction

This thesis deals with the interpretation and expansion upon single-spacecraft observations in the Jovian and Kronian magnetospheres. Chapter 1 introduces plasma physics, the Sun, the solar wind, the basics of a planetary magnetosphere and a fundamental concept in space physics, magnetic reconnection. Chapter 2 builds on Chapter 1 and discusses some of the properties and physics of Jupiter and Saturn's magnetospheres. Chapter 3 introduces the instrumentation and spacecraft that provided the data used in this thesis. Chapters 4, 5 and 6 cover three projects completed throughout this thesis. Chapter 4 explores the use of an avalanching sandpile model in understanding the dynamics of the Jovian magnetosphere. Chapter 5 is on the development of criteria to select features of Saturn's radio emission, the Saturn Kilometric Radiation, known as low frequency extensions and their use as a proxy for magnetospheric dynamics. Chapter 6 is again on the development of criteria to select another part of Saturn's radio spectrum, the narrowband emissions, and exploring their link with magnetospheric dynamics. Chapter 7 briefly summarises the work done in this thesis and suggests possible future work avenues.

1.2 Plasma physics

A plasma is a quasi-neutral gas of charged particles where particles have thermal energies sufficient to overcome coupling with neighbouring particles. Understanding how plasmas

behave within a magnetic or an electric field is fundamental to being able to understand a lot of the processes that occur in planetary magnetospheres. Plasmas can be generated in two ways. The first is through heating a gas to a point where its average kinetic energy is approximately equal to its ionisation energy, the energy required to remove an electron. This occurs in the solar corona where temperatures greater than 10^6 K readily ionise H to H^+. The second way is through photoionisation, where high energy photon interactions cause atoms or molecules to gain enough energy that they become ionised. This second process occurs in the upper regions of a planet's atmosphere, the ionosphere, usually via the interaction of atmospheric particles with solar ultra-violet radiation.

A plasma must meet three criterion. The first is to do with the length scale of the plasma known as the Debye length:

$$\lambda_D = \sqrt{\epsilon_0 k_B T / e^2 n_e}, \tag{1.1}$$

where ϵ_0 is the permittivity of free-space, k_b is the Boltzmann constant, e is the electron charge and n_e is the density of electrons. In the absence of a confining magnetic field (which would move ions and electrons in ways that will be discussed in the particle motion section 1.2.1) the ions and electrons within a plasma move in all and any direction. However, there will be a slightly higher density of electrons around each ion due to electrostatic attraction. This cloud of electrons shield the E-field of the ion and is known as Debye shielding. The Debye length is the distance at which there is a balance between the thermal particle energy which acts to separate charge and the electrostatic potential energy that tries to restore charge neutrality. The first plasma criterion requires that the physical dimension of the system, L, be much larger than, λ_D, such that the plasma will remain quasi-neutral. The second criterion requires that there are enough electrons within the Debye sphere of radius, λ_D, for the Debye shielding to be effective. This number is called the plasma parameter, Λ, where:

$$\Lambda = n_e \lambda_D^3 >> 1. \tag{1.2}$$

By substituting in the equation for λ_D to the equation for the plasma parameter it describes how the mean potential energy of a particle due to its nearest neighbour (inversely proportional to the mean distance between particles and so proportional to $Ne^{1/3}$) must be much smaller than its mean energy, $k_B T_e$.

The electron plasma frequency is:

$$\omega_{pe} = \sqrt{n_e e^2 / m_e \epsilon_0}, \tag{1.3}$$

where m_e is the mass of an electron. This describes the oscillation of electrons about the ions in a quasi-neutral plasma. A plasma does not need to be fully ionised but if neutrals do exist, the average time between collisions between an electron and a neutral, τ_n, must be greater than the period of the plasma oscillation such that:

$$\omega_{pe}\tau_n >> 1, \tag{1.4}$$

and as such the gas still behaves as a plasma.

An ideal plasma is assumed to be collisionless. This breaks down in the lower regions of the solar and planetary atmospheres where neutral densities are higher (and the third criterion is violated) but it is a good approximation in the solar wind (a stream of plasma from the Sun that will be discussed more below in section 1.3) and the majority of regions in a planetary magnetosphere where the average distance an ion or electron travels without collision is large.

1.2.1 Particle Motion

The behaviour of electric, **E**, and magnetic, **B**, fields is fundamental to plasma physics and are governed by Maxwell's equations:

$$\nabla \cdot \mathbf{E} = \frac{\rho_q}{\epsilon_0}, \tag{1.5}$$

$$\nabla \cdot \mathbf{B} = 0, \tag{1.6}$$

$$\nabla \times \mathbf{E} = -\frac{d\mathbf{B}}{dt}, \tag{1.7}$$

$$\nabla \times \mathbf{B} = \mu_0\Big(\mathbf{j} + \epsilon_0\frac{d\mathbf{E}}{dt}\Big), \tag{1.8}$$

where ρ_q is the charge density, **j** is the current density and μ_0 is the permeability of free space. Equations 1.5 and 1.6 are Gauss' laws of electric and magnetic fields (no magnetic monopoles). Equation 1.7 is Faraday's law and 1.8 is the Ampere-Maxwell law. In equation 1.8, the displacement current term (second term in the brackets) can often be neglected (except in a rapidly changing electric field) reducing to Ampere's law, since $\epsilon_0\mu_0 = 1/c^2$ is small.

1.2.2 Zero Electric Field

The basic equation of motion of a charged particle in an electromagnetic field is given by the Lorentz equation:

$$m\frac{d\mathbf{v}}{dt} = q(\mathbf{E} + \mathbf{v} \times \mathbf{B}), \tag{1.9}$$

where m is the mass of the particle, $\mathbf{v}$ is its velocity, $\mathbf{E}$ is the electric field and $\mathbf{B}$ is the magnetic field. For the case where $\mathbf{E} = 0$, the motion of a charged particle along a magnetic field line can be derived. Solving equation 1.9 for $\mathbf{v}$ for the case where $\mathbf{B} = \mathrm{B}\hat{z}$ gives a general solution that can be integrated to give the variation of position of the particle with time in the x and y axis.

$$x(t) = x_0 + \frac{v_\perp}{\Omega}\, sin(\Omega t + \phi), \tag{1.10}$$

$$y(t) = y_0 + \frac{v_\perp}{\Omega}\, cos(\Omega t + \phi), \tag{1.11}$$

$$z(t) = z_0 + v_\parallel t, \tag{1.12}$$

where ϕ is the phase offset at t = 0, $v_\perp$ the constant velocity perpendicular to the field, $v_\parallel$ the constant velocity parallel to the field, and

$$\Omega = \frac{q\mathbf{B}}{m} \tag{1.13}$$

is the *gyrofrequency* (or cyclotron frequency). Thus particles move in a circle about the magnetic field line with gyrofrequency, Ω, and further, due to the sign of q, ions and electrons rotate in opposite senses (as shown in figure 1.1). The speed along the field line remains constant and so the general shape is that of a helix. Knowing the gyrofrequency, two more variables can be defined: the gyroradius,

$$r_g = \frac{mV_\perp}{qB}, \tag{1.14}$$

the radius of the particles orbit, and the gyroperiod, τ_g,

$$\tau_g = \frac{2\pi}{\Omega} = \frac{2\pi m}{q\mathbf{B}} \tag{1.15}$$

the period of the orbit.

It can be shown that the particle speed remains unchanged in a steady magnetic field for $\mathbf{E} = 0$. From equation 1.9 for $\mathbf{E} = 0$, taking the dot product with $\mathbf{v}$ on both sides gives

$$m\mathbf{v} \cdot \frac{d\mathbf{v}}{dt} = q\mathbf{v} \cdot (\mathbf{v} \times \mathbf{B}). \tag{1.16}$$

Knowing that $\mathbf{v}\cdot(\mathbf{v}\times\mathbf{B}) = 0$, therefore:

$$\frac{d}{dt}(\frac{1}{2}m\mathbf{v}^2) = 0, \tag{1.17}$$

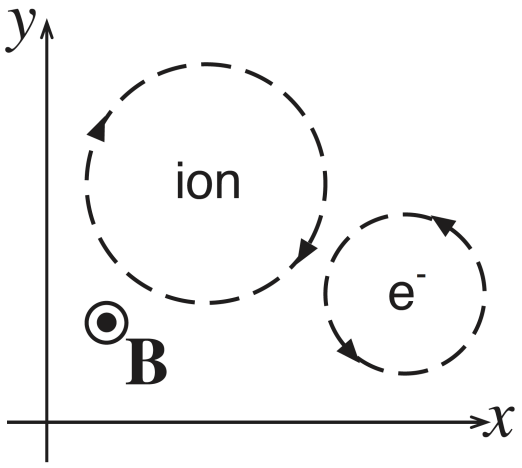

FIGURE 1.1: Schematic showing the relative direction of the circular orbit of an ion and an electron in a non-zero magnetic field. Note that the relative sizes of the orbits are not to scale for particles of the same kinetic energy. [Credit S. Milan, University of Leicester Space Plasma Course notes]

that is, the kinetic energy of the particle does not change with time and $|v|$ is constant. Similarly, the magnetic moment, μ:

$$\mu = \frac{m\mathbf{v}_\perp^2}{2\mathbf{B}} = \frac{\mathbf{W}_\perp}{\mathbf{B}}, \tag{1.18}$$

where $\mathbf{W}_\perp$ is the perpendicular kinetic energy and is also conserved. If the relative change in the magnetic field is much less than the gyrofrequency, the magnetic moment is considered a characteristic constant and is known as the first of three adiabatic invariants.

When considering the perpendicular and parallel components of the velocity, their ratio defines the particle's 'pitch angle', α, where:

$$tan\ \alpha = \mathbf{v}_\perp / \mathbf{v}_\parallel. \tag{1.19}$$

.

If a particle moves along a magnetic field line into a region of increasing magnetic field strength (as in figure 1.2), i.e. where field lines converge, a phenomenon called magnetic mirroring can occur. As B increases, $v_\perp$ also increases in order to conserve the magnetic moment. As can be seen from equation 1.17 this will cause $v_\parallel$ to decrease in order to keep the kinetic energy constant. Eventually, when $\mathbf{v}$ is equal to $v_\perp$ and $v_\parallel = 0$, the particle is mirrored back along the field. A particle with pitch angle α at field strength B_i will mirror at a mirror point with field strength:

$$B_m = \frac{B_i}{sin^2\alpha}. \tag{1.20}$$

Note that the mirror point depends only on α and not on the type or energy of the particle. For a particle travelling from z_0 on a field line, where the field strength is B_0, with initial pitch angle α_0, to a point z, with a field strength B_{max}, the field strength required to cause the particle to reflect increases as α_0 decreases. B_{max} therefore determines the minimum pitch angle, α_0, required for mirroring:

$$sin\ \alpha_0 > \sqrt{B_0/B_{max}}. \tag{1.21}$$

An example of this mirroring is observed on planetary field lines which converge at both ends. The particles become trapped on the dipole field line, 'bouncing' between the two mirror points at either end. As can be seen from equation 1.21, a particle with a lower pitch angle requires a larger magnetic field strength (for a dipole this is closer to the planet) at the mirror point in order to be mirrored. If a particle's mirror point is at a sufficiently low altitude it can collide with an atmospheric particle, producing aurora, in which case it is lost from this trapping region. These particles are said to be within the loss cone.

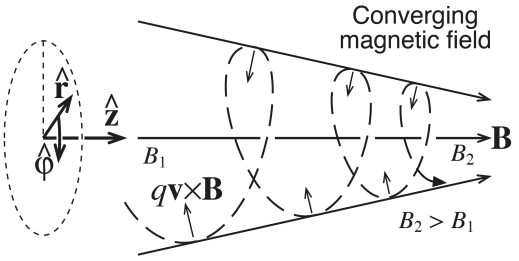

FIGURE 1.2: Schematic showing a particle travelling along its field line into a region of stronger magnetic field. The changing field strength causes a **v** x **B** force acting anti-parallel to the particle causing it to decelerate, come to a stop and "mirror" in the opposite direction. [Credit S. Milan, University of Leicester Space Plasma Course notes]

If a particle is on a field line that converges at both ends (as in a dipole field configuration), it is possible for the particle to oscillate between the two mirror points at a certain mirror frequency, ω. From this a second adiabatic invariant can be defined:

$$J_L = \oint m\mathbf{v}_{\parallel}\mathbf{ds}, \tag{1.22}$$

where $\mathbf{v}_{\parallel}$ is the particle velocity parallel to **B** and **ds** is the element of the path taken by the particle and the integral is taken over a full oscillation between the mirror points. J_L remains constant if there are changes in the field on a timescale that are long compared to the mirror period but the invariance no longer holds during a rapid contraction of a field line such as following a process called magnetic reconnection, a phenomenon that will be discussed in section 1.4.1.

When considering a gradient in the magnetic field strength perpendicular to **B**, as a particle gyrates around a magnetic field line, it moves into a stronger field region and therefore its gyroradius, gets smaller (the curve tightens). As a result ions and electrons drift perpendicular to **B** and $\nabla\mathbf{B}$. This is known as gradient drift and is demonstrated schematically in figure 1.3. The ions and electrons also move in opposite directions to each other which can result in a separation of charge and therefore an electric current.

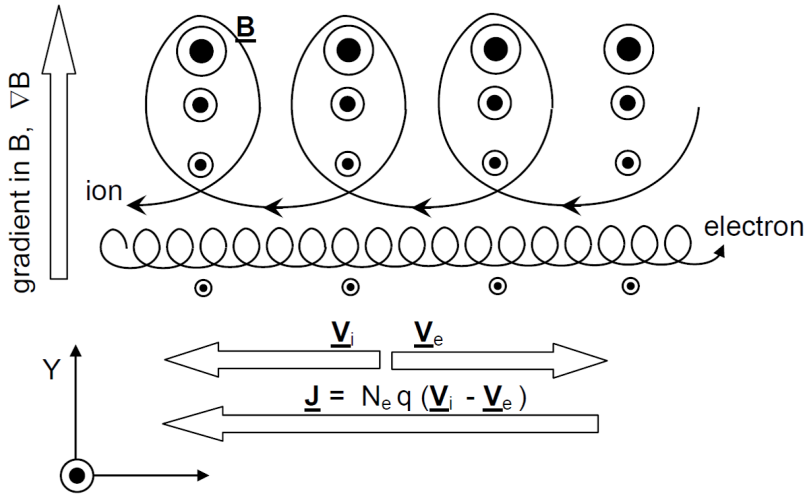

FIGURE 1.3: Schematic showing the drift of electrons and ions relative to each other in the presence of a gradient in a magnetic field up the page. The magnetic field is directed out of the page. The drift causes a separation in charge which causes an electric field from right to left.[Credit S. Milan, University of Leicester Space Plasma Course notes]

If a particle is drifting from a region of weak magnetic field, $\mathbf{B}_1$, to a region of stronger magnetic field, $\mathbf{B}_2$, then:

$$\frac{\mathbf{W}_{\perp 2}}{\mathbf{W}_{\perp 1}} = \frac{\mathbf{B}_2}{\mathbf{B}_1} \tag{1.23}$$

Since the magnetic moment is conserved the particles perpendicular energy increases i.e. $\mathbf{W}_{\perp 2} > \mathbf{W}_{\perp 1}$ in line with equation 1.18. Thus the particle ends up with a gain of energy in the transverse direction. The source of this energy is taken from the drift motion and is known as adiabatic heating, a form of betatron acceleration.

The third adiabatic invariant, Φ, the drift invariant, is concerned with the magnetic flux enclosed by a particle's drift shell and is conserved when changes in the field are slow compared to the particle drift period.

$$\Phi = 2\pi mM/q^2 = constant \tag{1.24}$$

where m is the mass of the particle, M is the magnetic moment of the magnetic field and q is the charge. This invariant has consequences for particles which make up the (inner) Van Allen belt (formed by electrons and ions drifting eastward and westward respectively around Earth's equator). For a slow compression of the magnetosphere by

the solar wind, the belt would move radially inwards (and outwards for a slow decrease in solar wind strength) in order to conserve the flux contained within the particle's orbits.

1.2.3 Non-Zero Electric Field

The effect of an electric field component parallel to the magnetic field can be considered by adding an $\mathbf{E} = \mathrm{E}\hat{z}$ to the $\mathbf{B} = \mathrm{B}\hat{z}$ considered above. The x and y components as derived above would remain, i.e. the circular motion continues with angular frequency, Ω. However, the electric field causes a non-zero acceleration in the $\pm\mathbf{z}$ direction. The ions and electrons are accelerated by the electric field in opposing directions, towards the regions of negative and positive charge respectively. If the electric field was formed by a charge separation within the plasma this motion would eliminate the charge separation and thus the electric field. An external field can also be applied as part of a current system (such as the coupling between the ionosphere and magnetosphere of a planet which will be discussed in section 1.4 of this Chapter and in Chapter 2), in which case the ions and electrons in the plasma continue to be influence by the electric field as described.

Next an electric field component perpendicular to the magnetic field is considered. Assuming $\mathbf{B} = \mathrm{B}\hat{z}$ and $\mathbf{E} = \mathrm{E}\hat{y}$, a proton initially at rest will be accelerated in the positive y-direction by the electric field but will also be accelerated in the positive x-direction orthogonal to both the magnetic and electric field. Eventually $\mathbf{v}_y = 0$, at which point the Lorentz force, $e\mathbf{v} \times \mathbf{B}$, will be in the direction opposite to the electric field force and the particle will move in the negative y-direction being decelerated by the electric field until coming to rest. This pattern repeats and represents the particles moving in a circle with a constant drift in the positive x-direction. The exact trajectory of the particle depends on the ratio of $\mathbf{v}_\perp$ (the perpendicular velocity component of the particle's orbit about the direction of $\mathbf{B}$ in the external rest frame) to $\mathbf{E}/\mathbf{B}$ and several trajectory examples are shown in figure 1.4. A negative particle will be accelerated in the opposite direction by the electric field but will still drift in the same direction as the proton. This drift is known as the 'E x B drift' since it is orthogonal to the electric and magnetic field and can be written in general terms as:

$$\mathbf{V} = \frac{\mathbf{E} \times \mathbf{B}}{B^2}. \tag{1.25}$$

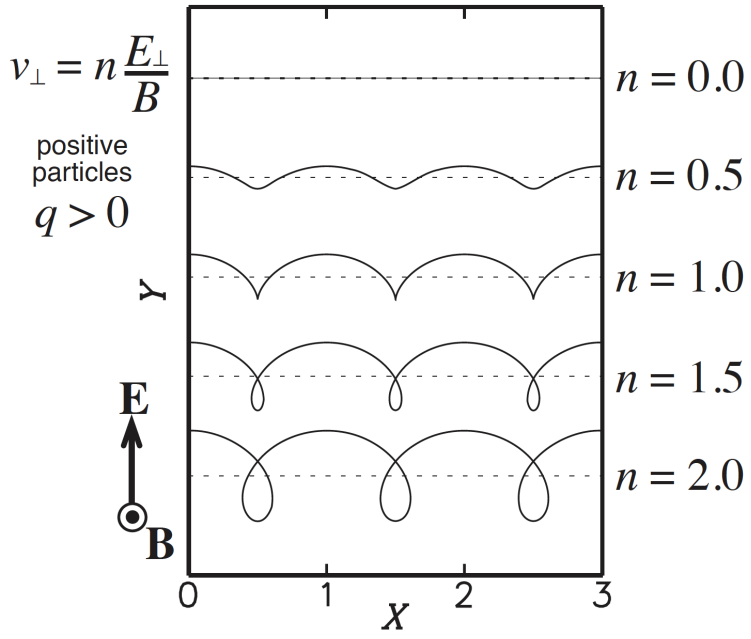

FIGURE 1.4: Demonstrating E x B drift as described in the text for increasing ratio of $\mathbf{v}_\perp$ to $\mathbf{E}/\mathbf{B}$. [Credit S. Milan, University of Leicester Space Plasma Course notes]

1.2.4 The Frozen-In Flow Approximation

Considering the concepts above, if there are two fields **B**(r, t) and **E**(r, t) that vary slowly in space and time (such that the adiabatic invariants remain valid) and given that **E** is perpendicular to **B**, the motion shows a special case known as Alfven's frozen-in theorem. A set of particles centred on one field line at a given time will all remain on the same field line as each other for all times as shown in figure 1.5. This can be thought of in two ways. Either, that the plasma is carrying the magnetic field with it - the *frozen-in* picture, or the field lines are moving and carrying with them the plasma particles. Which way this is thought of depends on the respective energies of the field and the particles.

This interplay between magnetic field lines and plasma can be thought about more quantitatively. Using Ohm's law for a plasma of conductivity, σ,:

$$\mathbf{E} + \mathbf{V} \times \mathbf{B} = \frac{\mathbf{j}}{\sigma}, \tag{1.26}$$

Faraday's law:

$$\frac{d\mathbf{B}}{dt} = -\nabla \times \mathbf{E}, \tag{1.27}$$

Ampere's law (neglecting the displacement current from equation 1.8):

$$\nabla \times \mathbf{B} = \mu_0 \, \mathbf{j}, \tag{1.28}$$

yields the induction equation:

$$\frac{d\mathbf{B}}{dt} = \nabla \times (\mathbf{V} \times \mathbf{B}) \; + \; \frac{1}{\mu_0 \sigma} \nabla^2 \, \mathbf{B}. \tag{1.29}$$

The first term on the right-hand side is the transport term describing the *frozen-in* transport of magnetic flux within the plasma. The second term is known as the magnetic diffusion term. The ratio of these terms is known as the Reynolds number:

$$R_m = \mu_0 \sigma \nu L, \tag{1.30}$$

where ν is the characteristic velocity and L is the characteristic length scale of the plasma. If $R_m >> 1$ the transport term dominates and the plasma and the magnetic field are frozen together. If not, this frozen-in approximation does not hold and the field can diffuse through the plasma. This can lead to a process called magnetic reconnection discussed in section 1.4.1.

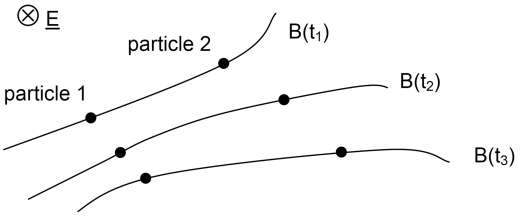

FIGURE 1.5: Schematic of the frozen-in flow phenomenon. As the magnetic field evolves through times, particles 1 and 2 remain associated to the same field line although they can freely move along the line. [Credit D. Whiter Space Plasma Course, University of Southampton]

1.3 The Sun and the Solar Wind

The Sun is a main sequence star with a mass five orders of magnitude greater than that of the Earth's. The visible surface of the Sun at the top of the photosphere, seen on figure 1.6, has a temperature of about 6000 K, but the outer atmosphere, the corona, is hotter than 1 x 10^6 K. The mechanism behind why this region is so hot is a current area of research. The temperature falls radially from the core to the surface where it then rapidly rises to extreme temperatures across the chromosphere outer boundary known as the transition region. Assuming the Sun to be in hydrostatic equilibrium, on application of the equations of mass continuity and momentum, the gas pressure in the corona tends to a value of $\sim 10^{-5}$ Pa. The solar system is travelling through the interstellar medium which has a gas pressure $\sim 10^{-13}$ Pa which is not sufficient to 'contain' the Sun's atmosphere in hydrostatic equilibrium. As a result of this pressure

gradient, the hot coronal plasma is ejected radially outwards at supersonic speeds into interplanetary space to form the solar wind. The composition of the solar wind is ∼84% H^+, 15% He^{++} and 1% other ions.

The presence of a solar wind was first hypothesised by *Biermann and Schlüter* [1951] based on the existence of plasma tails extended beyond the comet and always pointing away from the Sun. The first solutions for the solar wind outflow speeds were estimated by *Parker* [1958] between 500 - 1500 $km\ s^{-1}$ which fits with in situ measurements of the solar wind by spacecraft at the orbit of Earth. The solar wind acceleration takes place within the first few radii of the Sun after which the velocity remains approximately constant with radial distance whilst the density and temperature fall.

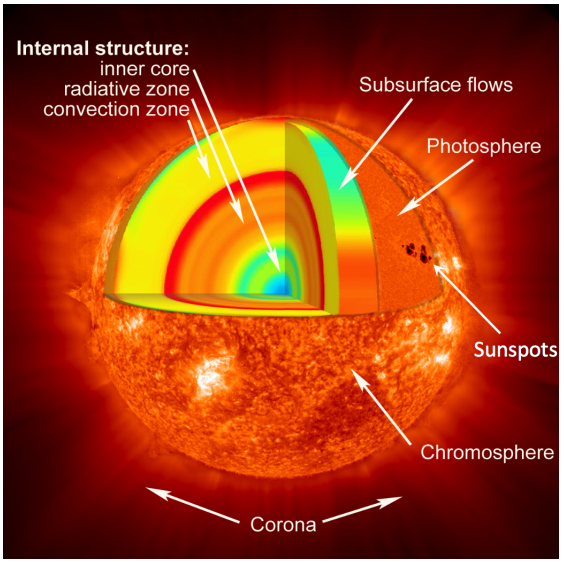

FIGURE 1.6: Schematic of the Sun's interior and atmosphere [Credit to NASA]

The surface magnetic field can be thought of as approximately dipolar and reverses direction every 11 years forming part of a periodic cycle lasting 22 years linked with the complex solar dynamo that produces the Sun's magnetic field. The Sun's activity is linked with this cycle and can be tracked by the number of sunspots, dark spots of strong magnetic field, on the surface. The observed sunspot number as a function of time since 1955 is shown in figure 1.7.

At the start of the cycle the sunspot number is low, the spots are mostly at high latitudes and the suns magnetic field takes the form of a relatively simple dipole. Rising to the peak of the solar cycle, the magnetic field becomes more disordered and the sunspots increase in number, moving to the equatorial region. During this solar maximum, the Sun is much more active. Coronal mass ejections (CMEs - example in figure 1.8), giant magnetic bubbles that hurl billions of tons of plasma into space are much more likely to occur. CMEs disrupt the usual solar wind patterns and can greatly effect planetary

magnetospheres. Following the peak in the solar cycle, the activity dies away and the Sun emerges with a reversed magnetic polarity at the next solar minimum.

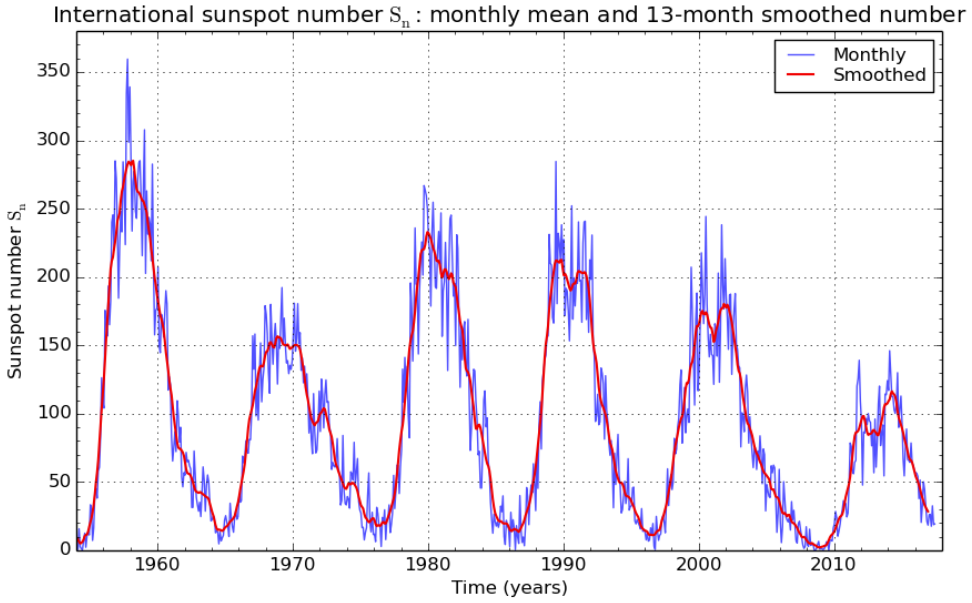

FIGURE 1.7: Plot of monthly (blue line) and 13-month smoothed (red line) sunspot numbers since 1955, obtained from the Solar Influences Data analysis Centre (SIDC), Belgium.

The solar wind carries with it a remnant of the solar magnetic field, called the interplanetary magnetic field (IMF). The solar wind and IMF are an example of the frozen-in effect. The conductivity and length scale ($\sim 10^9$ m) of the solar wind are sufficiently large such that the transport term of equation 1.29 dominates. This case is referred to as the convective limit or ideal MHD. The plasma 'beta', β, is the ratio of thermal to magnetic energy density:

$$\beta = \frac{W_T}{W_B} = \frac{P_T}{P_B} = \frac{2\mu_0 n k_b T}{B^2}, \tag{1.31}$$

where P_T is the thermal pressure, P_B is the magnetic pressure and k_b is the Boltzmann constant. The plasma beta indicates whether it is the plasma that carries the magnetic field ($\beta >> 1$) or the magnetic field is confining the plasma ($\beta << 1$). For typical solar wind values $\beta < 1$, but β does not consider the bulk flow of the plasma which dominates in the case of the solar wind. Therefore, the solar wind is said to carry the IMF with it as opposed to the field carrying the plasma with it.

As the solar wind flows radially away from the Sun carrying with it the IMF the Sun continues to rotate. Two plasma elements released δt apart from a given source point will travel on slightly different radial paths but, in accordance with the frozen-in theorem, will be on the same magnetic field line, the foot of which is frozen into the Sun's surface. This forms an 'Archimedean Spiral' of the magnetic field (as shown in figure 1.9) that

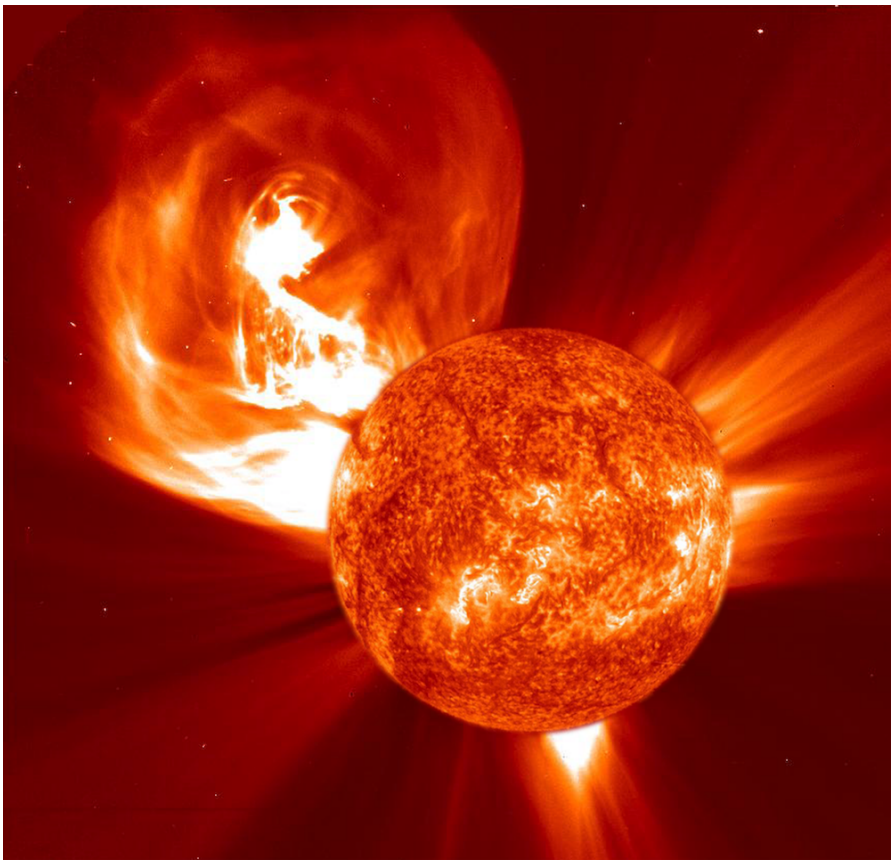

FIGURE 1.8: Coronal mass ejection (CME) erupting form surface of the Sun [Credit to SOHO/NASA].

becomes more tightly wound with radial distance and by the orbit of Saturn, the field lines are at an angle of $\sim 87^{\circ}$ to the radial direction [*Jackman et al.*, 2008], almost completely azimuthal. This configuration is known as the Parker spiral [*Parker*, 1958]. The field lines will carry opposite polarity in the northern and southern hemisphere. This requires, by Ampere's law, the existence of an azimuthal current sheet at the magnetic equator known as the heliospheric current sheet (HCS). Because the Sun's magnetic dipole axis is tilted with respect to its rotation axis the current sheet wobbles up and down across the ecliptic plane (the plane containing Earth's orbit), sweeping 'sectors' of opposite magnetic polarity across the Earth and the other planets as shown in figure 1.10. During solar maximum, this structure is complex and distorted by CMEs but, at solar minimum, the solar field is more dipolar and there is a more clear two-sector structure.

The outward flow speed of the solar wind is highly variable and dependent on the source region as the Sun rotates, and the phase of the solar cycle. This produces periods of fast winds and slow winds. The speed has a bimodal distribution. By comparing the composition of the plasma of the different types of wind it is possible to determine the source of the fast and slow winds (shown in figure 1.11). The slower ($\sim$ 400 km s^{-1}),

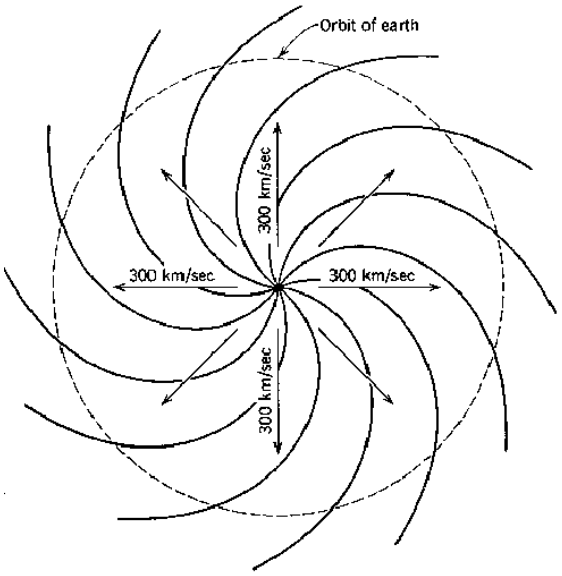

FIGURE 1.9: A sketch of the Parker spiral configuration of the interplanetary magnetic field as viewed from above. The solar wind flows radially away from the Sun dragging with it the frozen-in IMF which get twisted due to the rotation of the sun. The field lines will have opposite polarity above and below the equator. [*Kivelson and Russell* [1995]]

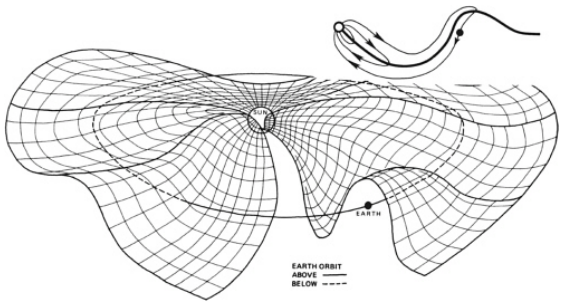

FIGURE 1.10: Current sheet within the heliosphere. Due to the tilt of the magnetic axis relative to the rotation axis the 'ballerina skirt' effect is produced. Inset on top right shows the opposite polarity above and below the current sheet. [*Kivelson and Russell* [1995]]

gusty, denser wind originates from hot regions around the equator, whilst the faster ($>$ 600 km s^{-1}), sparser, steadier wind originates from the interior of coronal holes where the corona is cooler. The tilt of the magnetic dipole to the rotational axis means that regions of both fast and slow wind will be experienced by an observer in a fixed position on the ecliptic plane.

The radial propagations of these speed variations create compression regions where fast regions have caught up with slower regions, and rarefactions where fast regions have pulled away from slower regions. These are known as corotating interaction regions (CIRs) [e.g. *Gosling and Pizzo*, 1999; *Crooker*, 1999]. As each element of the solar wind

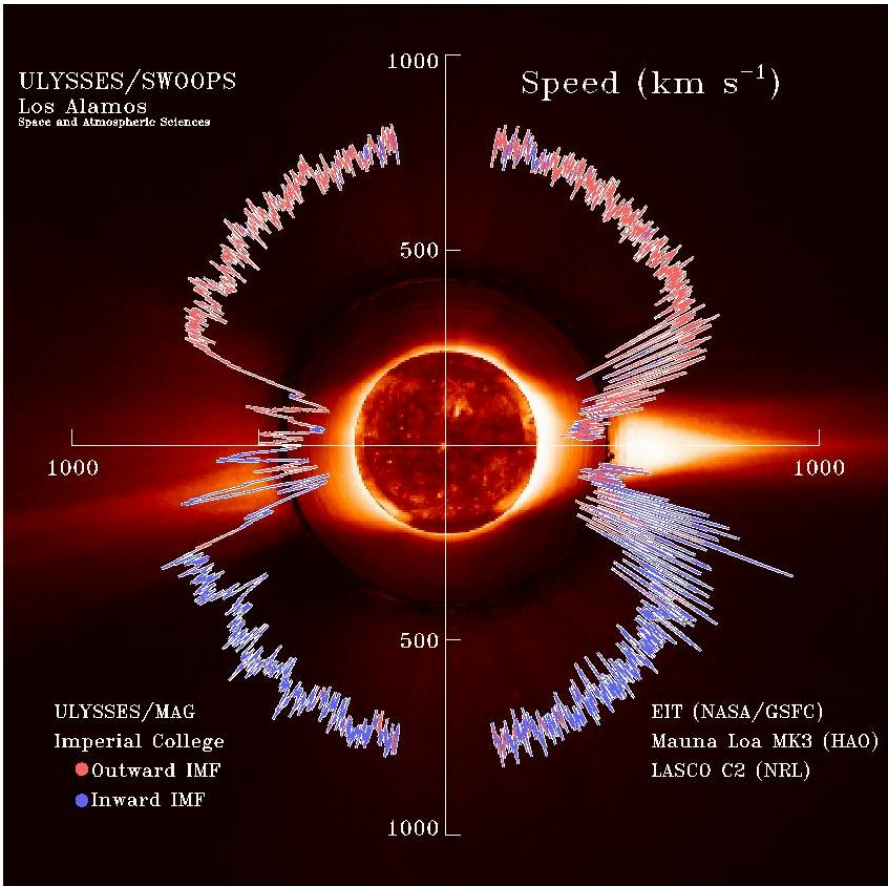

FIGURE 1.11: Schematic of the source of the fast and slow solar wind during solar minimum as measured by Ulysses. The Ulysses spacecraft completed two orbits through the solar system during which it passed over the Sun's south and north poles. [Credit to NASA/*McComas et al.* [2008]]

plasma flows nearly radially outwards from the Sun, the resulting pattern of compressed and rarefied plasma corotates with respect to the rotating Sun as shown in figure 1.12.

Figure 1.13 shows a plot in heliographic latitude and longitude, fixed to the rotating Sun, of the regions of slow (shaded) and fast (unshaded) solar wind outflow, at a distance of (say) a few solar radii, beyond the closed field regions, where the magnetic field is nearly radial. The diagram is specifically for the case of a tilted solar dipole appropriate to the declining phase of the solar cycle. The dashed line shows the boundary between fields that point radially outward from the Sun, and those that point radially inward, thus marking the location of the heliospheric current sheet (HCS). For the present solar cycle, the field points outward south of the line, and inward north of the line. The HCS thus lies centrally within the region of slow plasma outflow. The maximum heliographic latitude reached by the HCS in the north and south indicates the tilt angle of the dipole relative to the Sun's spin axis. The solid lines then mark the northern and southern boundaries of the slow and fast outflows, and thus the slow-fast solar wind stream interfaces (SI), as also indicated in the figure. The forward wave (FW) shock and reverse wave (RW)

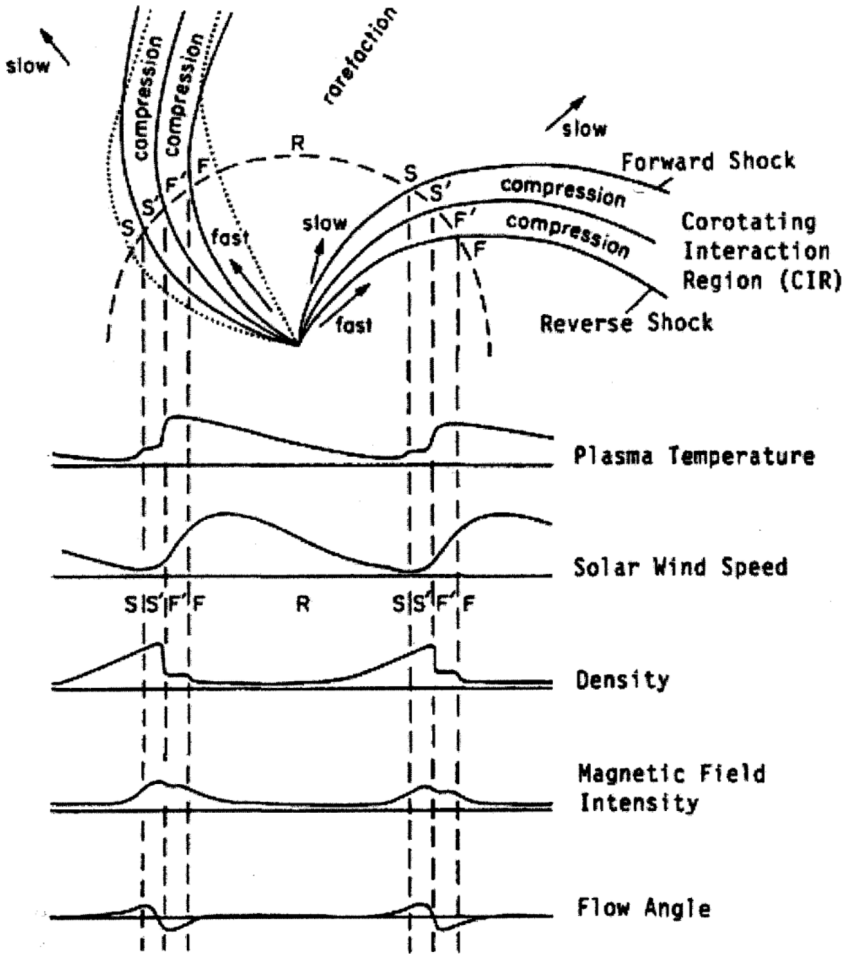

FIGURE 1.12: Schematic diagram of two CIRs corotating with the Sun, along with the associated solar wind and magnetic field signatures at 1 AU. [*Kunow* [2001]]

shock are caused by the fast wind compressing and accelerating the slow wind ahead whilst the fast wind is similarly compressed and slowed as it collides with the slow wind ahead.

Shocks are formed where the local flow speed exceeds the local sound speed. Normally, when something is moving through a medium the disturbance it causes propagates ahead of it at the speed of sound resulting in a gradual change in properties (velocity, density etc). If that something (in this case the fast solar wind) is moving faster than the local speed of sound the disturbances do not have time to be communicated to the rest of the medium resulting in a sharp change in medium properties (velocity, density etc) i.e. the medium can't get out of the way. This is termed a shock.

Shocks can form at several locations in the solar system. As will be discussed in section 1.4, the bow shock is formed upstream of a planetary magnetosphere when the supersonic

solar wind is abruptly slowed. The termination shock is formed at the edge of the solar system where the solar wind encounters the interstellar medium [*Gurnett et al.*, 1993].

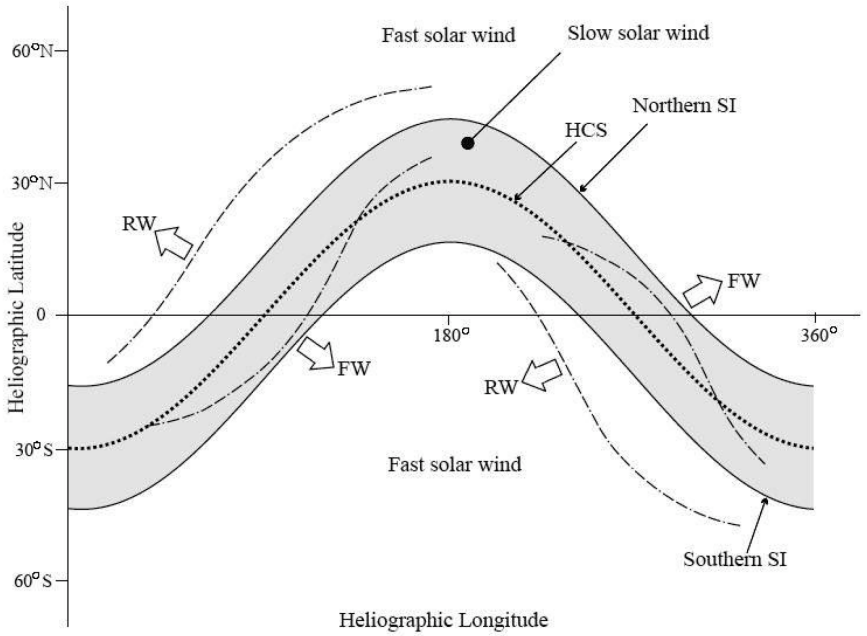

FIGURE 1.13: Sketch of the source regions of slow and fast solar wind flow in heliographic coordinates fixed in the rotating Sun. The dipole solar field is tilted such as it is during the declining phase of the solar cycle. [Adapted from *Gosling* [1996] by *Jackman* [2006]]

Suppose a near-equatorial, near-stationary observer is placed at 180° heliographic longitude as shown on figure 1.13 such that the observer moves from right to left within the diagram with time.

1. They would immediately be in a region of fast solar wind emerging from the southern coronal hole.

2. They would measure a rarefaction region of low solar wind density and field strength and for a given orientation of the solar dipole during a given solar cycle, a radial component of the field directed away from the Sun.

3. As time passes, the solar wind speed falls until the observer passes through the southern SI into slow solar wind plasma before encountering a forward shock propagating away from the northern interface.

4. Solar wind density and field strength will abruptly increase across the shock.

5. This will then be followed by a crossing of the HCS and a sign change of the IMF B_r component.

6. They will then cross the northern SI where the plasma density and field strength will drop.

7. Finally the observer will encounter a reverse shock, moving back into a region of fast wind, where the solar wind density and field strength will drop rapidly again.

The cycle will then repeat with the observer in a region of fast solar wind (a rarefaction region) where the plasma velocity and density slowly drop with time before the compression region associated with the southern SI is encountered. This picture is valid for the declining phase of the solar cycle, where the angle between the rotation axis and magnetic dipole of the Sun is reducing. As such for this period the IMF consists of two sectors per solar rotation, where the sector boundaries marked by the HCS crossings are embedded within two CIR compression regions separated by rarefactions. Typically compressions and rarefactions last around 5 and 7 days respectively [*Jackman et al.*, 2004]. While a pattern of two compressions per solar rotation may be expected at $\sim$1 AU during the declining phase of the solar cycle, it is also possible for these compressions to merge together as the solar wind propagates further into the heliosphere. This can result in structures known as Merged Interaction Regions (MIRs) [*Hanlon et al.*, 2004].

1.4 Magnetosphere

As the solar wind propagates through the heliosphere it eventually encounters an obstacle, a planetary magnetosphere. Inside the magnetosphere it is the magnetic field of the planet that is the dominant field rather than that of the Sun. Without any external influence, a magnetosphere takes the form of a magnetic dipole, with field lines protruding from the magnetic south pole, looping round and returning into the magnetic north pole. The magnetic field of Mercury is oriented in the same way as at Earth (i.e. the magnetic field lines point away from the planets surface in the southern hemisphere, and inward in the north). However, the magnetic dipole is opposite at Jupiter and Saturn, and hence magnetic field lines point from north to south. Jupiter and Saturn have, respectively, the first and second largest magnetospheres in the solar system and their properties and dynamics will be discussed in Chapter 2. The sizes of several magnetospheres of the solar system are shown relative to Jupiter in figure 1.14.

As discussed in section 1.3, the solar wind and IMF are frozen-in together. Equally the planetary field and its plasma environment are frozen together. As the solar wind reaches the planet, the two populations cannot mix, instead forming a thin boundary current sheet, known as the magnetopause, between the two plasmas. The solar wind is supersonic and so as it encounters the magnetosphere a shock wave forms upstream,

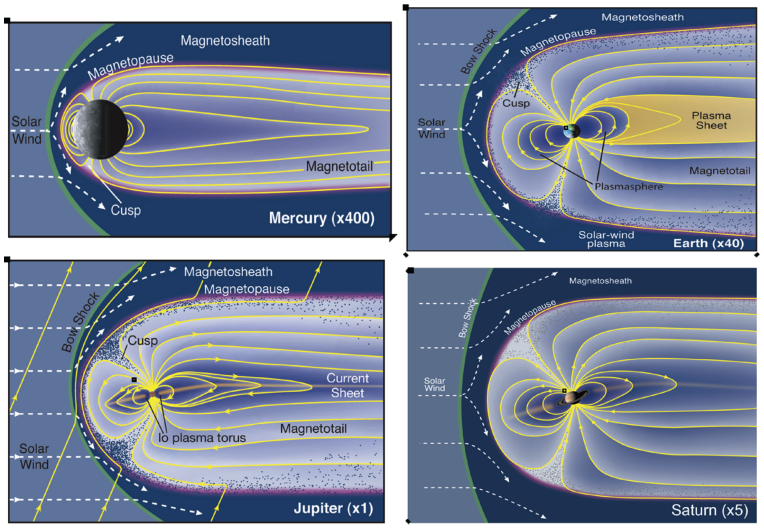

FIGURE 1.14: Schematic comparison of the magnetospheres of Mercury, Earth, Saturn and Jupiter. The Sun is to the left with the solar wind blowing from left to right across the diagrams. Jupiter's and Saturn's nominal magnetopause positions are somewhat larger than this dipole approximation due to substantial internal plasma pressures. [Credit to Fran Bagenal and Steve Bartlett]

known as the bow shock. As it crosses the bow shock, plasma is slowed, compressed and heated. This region is very turbulent and is known as the magnetosheath. Inside the magnetopause is the magnetosphere as shown in figure 1.15.

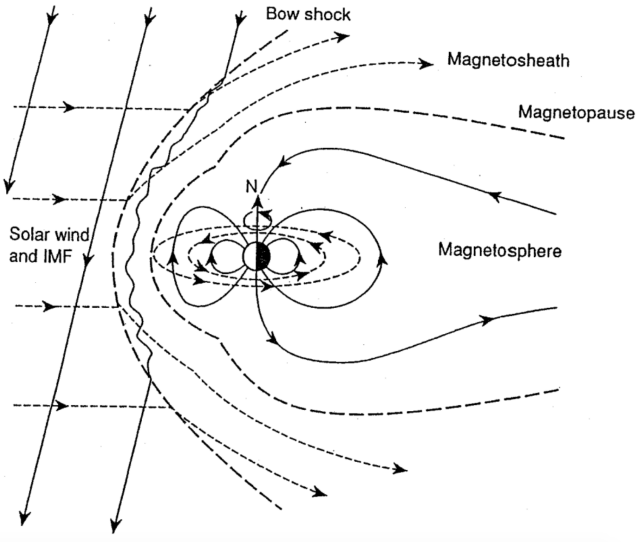

FIGURE 1.15: Sketch of the Chapman-Ferraro closed magnetosphere in the noon-midnight meridian plane, based on the strict application of the frozen-in-flow approximation. The arrowed dashed lines represent plasma streamlines, and the heavy long-dashed lines the bow shock and magnetopause boundaries. [*Cowley* [1991]].

The Chapman-Ferraro Current (CFC) [*Chapman and Ferraro*, 1930] flows on the surface of the magnetopause (and closes in the cross-tail current sheet). The currents are formed due to changes in the the solar wind particle gyroradii as they enter the magnetopause

region. The planetary magnetic field is much stronger than that of the IMF and as particles enter the higher magnetic field regime close to the magnetopause, their gyroradii significantly decrease and the particles are effectively reflected from the boundary (see figure 1.16).

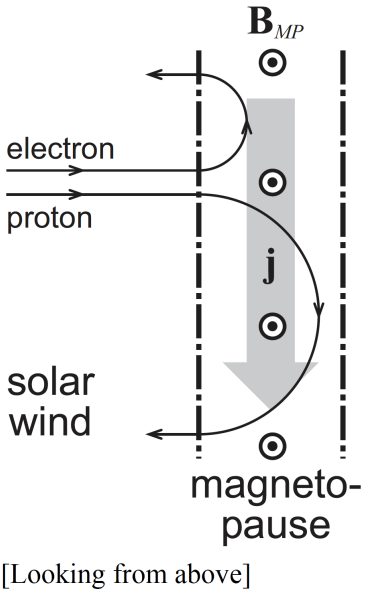

FIGURE 1.16: Schematic showing the change in the gyroradii of electrons and ions as they enter the magnetopause region from the direction of the Sun to the left. They gyrate in the opposite direction leading to a current. In this case the planetary magnetic field is directed into the page causing a current going down the page. [Credit S. Milan, University of Leicester Space Plasma Course notes]

The ions and electrons gyrate in opposite directions resulting in a current. The current itself causes a magnetic field which is parallel to the dipole field inside the magnetosphere and anti-parallel to the solar wind field outside. This increases the field strength just inside the magnetopause relative to an undisturbed dipole field and is known as the compressed field strength. The CFCs are shown by the dashed lines in figure 1.17. In addition to this large scale current system, other current systems exist in the magnetosphere. Field-aligned currents or Birkeland currents can also flow along magnetic field lines in order to couple the magnetosphere to the planet's ionosphere. Pedersen currents flow within the E-region of the ionosphere where the ion motion is affected by collisions with neutrals. In the absence of neutrals, the ions and electrons follow the E x B direction as described above, but at heights below $\sim$ 150 km (at Earth) the ions can collide with neutrals which push them in a direction nearly parallel to E giving rise to Pedersen currents which close in the magnetosphere via the Birkeland field aligned currents. In this way, as will be discussed in section 1.4.2 and Chapter 2, a torque can be applied to magnetospheric plasma causing it to move with the rotation of the planet (corotate).

A magnetotail stretches in the anti-sunward direction from the planet. This is formed due to a streamlining effect by the dynamic pressure of the solar wind. The tail is divided into two northern and southern lobes with oppositely directed radial fields, separated by a cross-tail current sheet across which closes the CFCs. Earth's connected magnetotail (where one end of the field lines are connected to Earth) has been observed at 240 Earth radii (R_E) by *Nishida et al.* [1998] and even sporadically as far as 800 R_E [*Scarf et al.*, 1970].

The size of the magnetosphere is determined by a pressure balance between the solar wind flow and IMF on one side and the magnetospheric field and plasma on the other:

$$P_{SW} + \frac{B_{SW}^2}{2\mu_0} = P_{MS} + \frac{B_{MS}^2}{2\mu_0}, \tag{1.32}$$

where $P_{SW} = 2\ \rho_{SW} V_{SW}^2$ is the solar wind dynamic pressure perpendicular to subsolar magnetopause plane , ρ_{SW} is the solar wind density, V_{SW} is the solar wind velocity, P_{MS} is the plasma pressure, B_{SW} is the IMF strength, and B_{MS} is the planetary field strength. The solar wind flow pressure is much greater than that from the IMF magnetic pressure so for simplicity the IMF pressure is neglected. At Earth the magnetospheric plasma pressure can also be neglected as this is much less than that of the field. Thus the above equation simplifies to:

$$2\rho_{SW} V_{SW}^2 = \frac{B_{MS}^2}{2\mu_0}. \tag{1.33}$$

B_{MS} is the magnetic field strength just inside the magnetopause, given as twice the magnetic dipole field due to the magnetic field generated by the CFCs:

$$B_{MS} \approx 2B_{dipole} = 2B_{eq}\left(\frac{R_P}{R_{MP}}\right)^3, \tag{1.34}$$

where R_P is the radius of the planet and R_{MP} is the magnetopause stand-off distance. Substituting into equation 1.30 and rearranging gives:

$$\frac{R_{MP}}{R_P} = \left(\frac{B_{eq}^2}{\mu_0 \rho V_{SW}^2}\right)^{-1/6}. \tag{1.35}$$

At Jupiter and Saturn the magnetospheric plasma pressure cannot be neglected since Io and Enceladus add ∼1000 and ∼ 250 $kg\ s^{-1}$ of sulphur and water group ions to their respective magnetospheres increasing the plasma pressure. The actual magnetospheric stand-off distance of the planets is twice what would be calculated without the inclusion of the internal plasma pressure. At Saturn P_{MS} is composed of several components: the pressure contribution of suprathermal water group ions [*Sergis et al.*, 2009], the thermal

electron pressure contribution and the cold plasma pressure [*Pilkington et al.*, 2015]. The role of Io and Enceladus in the Jovian and Kronian magnetospheres will be discussed in greater detail in Chapter 2.

The closed magnetosphere was predicted before the discovery of a phenomenon known as magnetic reconnection. The magnetosphere is more complicated than this picture but the closed magnetosphere scenario gives a good picture of the basic components of a planetary magnetosphere.

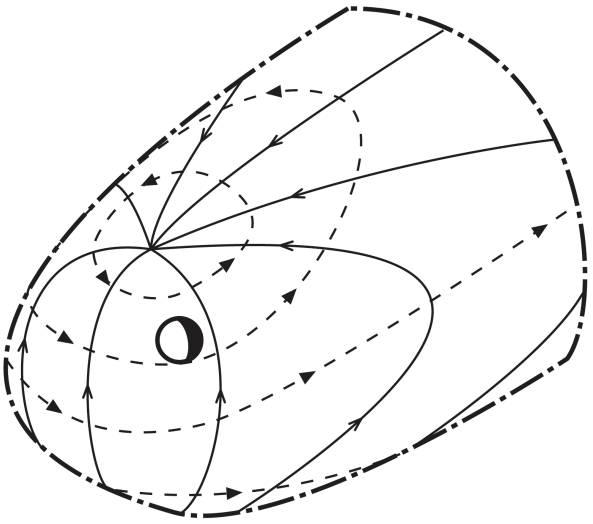

FIGURE 1.17: Chapman-Ferraro currents shown by the dotted lines. The magnetic field lines are given by the solid black lines. This schematic is based on the magnetosphere of Earth. [Credit S. Milan, University of Leicester Space Plasma Course notes]

1.4.1 Magnetic Reconnection

Reconnection is one of the most important processes in space plasma physics and magnetospheres. At a current sheet, the magnetic and particle pressure acting from both sides squeezes the current sheet down to such a small length scale, L, that the Reynolds Number, R_m, approaches unity. To see what this means, consider $R_m << 1$, for which the induction equation becomes

$$\frac{d\mathbf{B}}{dt} = \frac{\nabla^2 \mathbf{B}}{\mu_0 \sigma}. \tag{1.36}$$

Further, by simplifying the current sheet to a thin, infinite plane in the xy plane (figure 1.18), the equation 1.36 reduces to:

$$\frac{d\mathbf{B}}{dt} = \frac{\delta^2 \mathbf{B}_x}{\delta \mathbf{z}^2} \frac{1}{\mu_0 \sigma}, \tag{1.37}$$

where $1/\mu_0\sigma$ is the magnetic diffusivity, η. This equation is a diffusion equation. B diffuses from high to low values within a small diffusion region, towards the centre of a

current sheet where there is minimum B. This condition violates the frozen-in theorem.

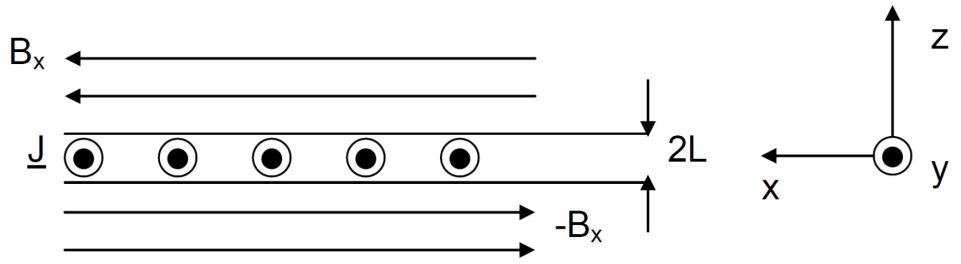

FIGURE 1.18: Infinite planar current sheet in the xy plane. The current is directed out of the page..

With this picture in mind, the magnetopause boundary can be considered. The diffusion of the magnetic field at a localised part of the magnetopause allows the field lines to reconnect as shown in figure 1.19 (this is the start of what is known as the Dungey cycle [*Dungey*, 1961] which will be discussed more in the next section). At the centre of the current sheet where the field lines meet they adopt a new topology where they thread the current sheet in opposite directions on the two sides of the centre. The reconnection site is known as the x-line due to the shape of the field lines. Following reconnection at the magnetopause boundary, there are now field lines that connect the planetary magnetic field to the solar wind and IMF. These field lines are said to be 'open' and solar wind plasma can enter the magnetosphere. Those that have both 'ends' connected to the Planet are said to be 'closed'. The polar caps are regions of open field lines around the northern and southern magnetic pole. The size of the polar cap is a balance between the rate of dayside reconnection which acts to expand the polar cap [*Milan et al.*, 2012, e.g.] and nightside reconnection (where open field lines reconnect and close) which acts to shrink the polar cap [*Lockwood and Cowley*, 1992; *Milan et al.*, 2007]. This is known as the expanding/contracting polar cap paradigm (ECPC) [*Lockwood and Cowley*, 1992; *Cowley and Lockwood*, 1992]

Reconnection is most efficient when the field lines are oppositely directed giving the largest gradient in $\mathbf{B}$. Various studies have attempted to parametrise the dependence of the magnetopause reconnection rate on IMF conditions. One example is *Milan et al.* [2012] who gave a dayside reconnection rate measured as the rate of expansion of the polar cap during periods when the nightside reconnection rate was low. It had the form:

$$\Phi_D = \Lambda v_x^{4/3} B_{yz} sin^{9/2} \frac{1}{2}\theta, \tag{1.38}$$

where Φ_D had units of Volts, Λ is a constant of proportionality, $\mathbf{v}_x$ is the solar wind velocity in the x-direction, $\mathbf{B}_{yz}$ is $\sqrt{\mathbf{B}_y^2 + \mathbf{B}_z^2}$, the transverse component of the IMF

and θ is the angle between the IMF and planetary field known as the clock angle. The Earth's magnetic field is northward, meaning for times when the IMF is perfectly in the southern direction, the reconnection rate is at its maximum. As the clock angle moves away from anti-parallel, reconnection can occur at higher latitudes with already open field lines where magnetic shear is high. Other works have adapted this equation to Jupiter [*Nichols et al.*, 2006] and Saturn [*Jackman et al.*, 2004]. Dayside reconnection at Jupiter and Saturn is discussed in more detail in section 2.6 in Chapter 2. Lobe reconnection does not usually generate open flux, but instead reconfigures it. In this scenario the IMF drapes over the magnetopause such that the orientation of the IMF is anti-parallel to that of the open field lines tailward of the cusp and reconnection occurs.

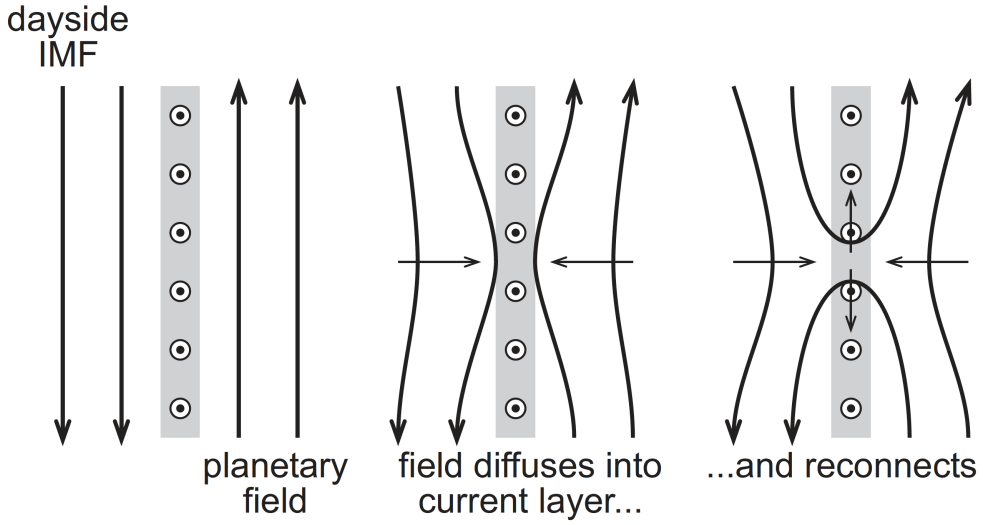

FIGURE 1.19: Schematic showing magnetic field lines diffusing into a current sheet and reconnecting as would be the case at the magnetopause of Earth. At Jupiter and Saturn the direction of the field lines is reversed. [Credit D. Whiter Space Plasma Course, University of Southampton]

1.4.2 Plasma Flow

There are two key plasma circulation cycles which can operate in planetary magnetospheres. The first, is the Dungey cycle [*Dungey*, 1961] which is driven by interaction between the planetary magnetic field and the IMF and is demonstrated schematically in figure 1.20. In this cycle, reconnection at the dayside magnetopause forms open flux tubes which connect from the IMF into the planet's polar caps. These open tubes are pushed anti-sunward due to a streamlining force from the solar wind. They are stretched tailwards and sink towards the tail centre where they reconnect again forming disconnected field lines on the tailward side of the x-line and closed field on the planetward side. The newly closed field lines flow back towards the planet into a more dipolar shape and then on to the dayside of the planet where the cycle can start again. This cycle is

dominant at Earth and Mercury where the interaction of the magnetosphere with the solar wind is the dominant driver of dynamics.

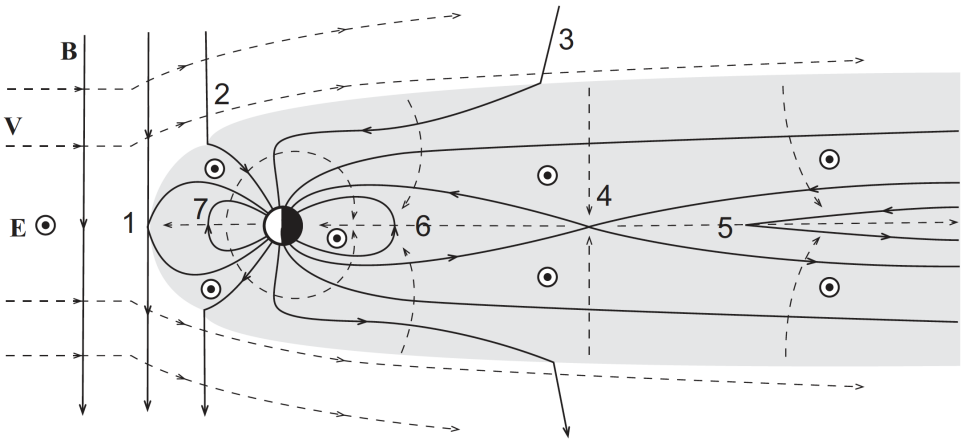

FIGURE 1.20: The Dungey cycle. Dayside reconnection occurs at (1) where IMF and planetary field lines join together. These newly open field lines are dragged over the polar cap (2) (3) before sinking to the centre of the tail and reconnecting (4). The disconnected solar wind field lines move tailwards (5). The newly closed planetary field lines 'dipolarise' towards the planet (6) and return to the dayside of the planet (7). [Credit S. Milan, University of Leicester Space Plasma Course notes]

At Jupiter and Saturn where the dynamics are thought to be driven by the rotation of the planet and the loading of plasma, a second cycle known as the Vasyliunas cycle [*Vasyliünas*, 1983] also occurs. In this cycle, field lines can become loaded with mass as they pass through the inner regions of the magnetosphere. As they rotate around the planet they are constrained by the magnetopause on the dayside but are then free to stretch downtail as they rotate into the dusk sector. They then eventually pinch off to form a tailward plasmoid, and the now empty flux tubes return to the dayside via dawn. The Vasyliunas cycle is sketched schematically in figure 1.21.

At Earth the Dungey cycle causes the magnetospheric plasma to flow towards the Planet (convection). In the equatorial plane, **B** points upwards and the associated **E** points from dawn towards dusk (this is opposite at Jupiter and Saturn where the planetary field is oppositely directed), with magnitude,

$$\mathbf{V}_{conv} = \frac{E_0}{B_{eq}} \left(\frac{r}{R_P} \right)^3 \hat{\mathbf{x}} \tag{1.39}$$

where E_0 has been found experimentally to be between 10 and 20% of the E in the solar wind, B_{eq} is the planetary equatorial field strength, r is the distance from the planet and R_P is the radius of the planet, P.

Inside a magnetosphere, in the absence of other forces, the plasma and field will rotate

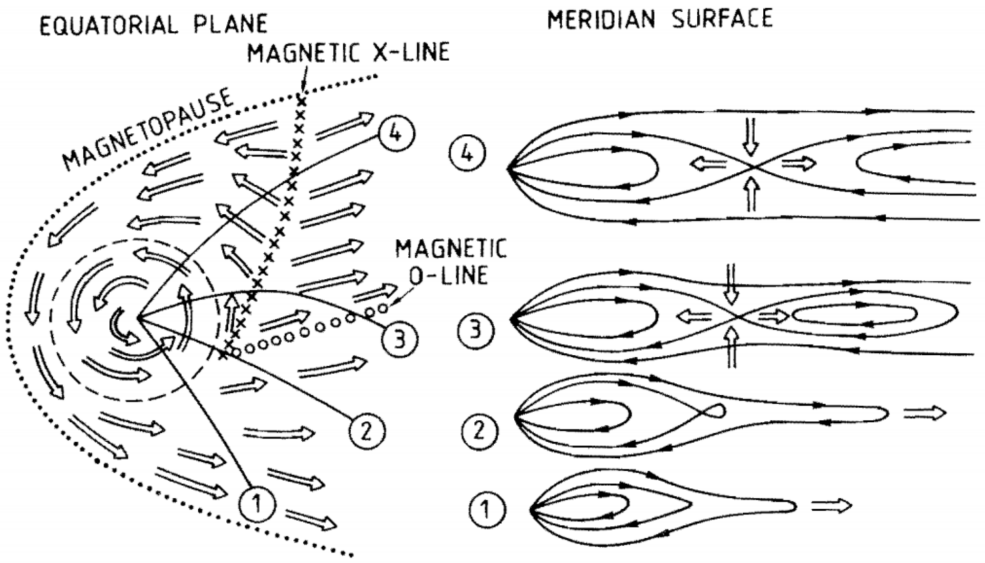

FIGURE 1.21: Qualitative sketch of plasma flow in the equatorial plane (left) and of the associated magnetic field and plasma flow in a sequence of meridian surfaces (right). [*Vasyliünas*, 1983]

around with the planet. This 'corotation' is a result of the transfer of angular momentum from the atmospheric neutral atoms to the plasma ions via collisions in the lower ionosphere. This torque is then communicated to the magnetospheric plasma via field-aligned currents on planetary field lines which are frozen to the ions in the atmosphere (the details of this mechanism at Saturn and Jupiter will be discussed in more detail in Chapter 2). Assuming that everything rotates with the planet (true up to a certain distance from the planet), then the flow due to corotation, in the azimuthal direction can be described by,

$$V_{corot} = r\omega_p \tag{1.40}$$

where ω_p is the angular velocity of the planet. From comparing the two equations for V_{conv} and V_{corot}, it can be seen that corotation dominates for small r and convection at larger r. The stagnation point is the point at which the velocity of the plasma flow is expected to be 0. Based on some average properties of the solar wind at Earth and Earth's magnetic field, this point is expected to be around 4 Earth radii (R_E). Thus at Earth, where the magnetopause distance is $\sim$9 R_E, there is a small corotational core but in general the magnetosphere is convection dominated. Conversely, similar calculations at Jupiter give a stagnation point at $\sim$200 Jovian radii (R_J), outside of the magnetopause boundary of $\sim$ 70 R_J and so the magnetospheric flow of Jupiter is heavily corotation dominated. At Saturn the stagnation point is $\sim$20 Saturn radii (R_S) which is only a few R_S inside the magnetopause.

1.4.3 Plasmoids

Following reconnection, disconnected field lines on the nightside of the planet can form bundles of field and plasma and subsequently move downtail. Such structures are known as plasmoids. The passage of a plasmoid over a spacecraft can be detected in situ by spacecraft observing changes in the topology of the field (via deflections in the north-south B_θ field component [*Russell et al.*, 1998; *Vogt et al.*, 2010]) and by changes in the plasma flow direction [e.g. *Kronberg et al.*, 2008a].

Direct observation of reconnection is rare. At Earth there are some examples of diffusion region detection [e.g. *Øieroset et al.*, 2001; *Eastwood et al.*, 2010; *Burch and Phan*, 2016; *Burch et al.*, 2016]. As briefly mentioned in the magnetic reconnection section above, reconnection involves the diffusion of magnetic field lines towards a central x-line. There are infact two (overlapping) regions of diffusion - the larger ion diffusion region and the smaller electron diffusion region. These diffusion region sizes are determined by the point at which the ions and electrons 'feel' the magnetic gradient. Ions have much larger gyroradii when orbiting the magnetic field and so feel the gradient sooner than the electron. Given the size of the magnetospheres at Jupiter and Saturn and the relatively paucity of spacecraft coverage (compared to targeted spacecraft constellations in Earths tail), it is easy to see why direct encounters with the jovian or kronian x-lines are so rare. At Saturn the only reported example of an encounter with an x-line is that of *Arridge et al.* [2016a]. Despite this, reconnection can be detected indirectly via the products of reconnection such as a plasmoid, a dipolorisation (the recoiling of newly closed field lines) or a travelling compression region (TCR) where the lobe drapes around a plasmoid, can be detected. Figure 1.22 shows how a plasmoid is detected in magnetometer data at Saturn. The left panel in this figure shows the change in the north-south component of the magnetic field, B_θ, for an ideal spacecraft trajectory through the centre of a plasmoid as the plasmoid moves tailwards over the spacecraft (as shown in the right panel). The field is initially small and positive indicating a northward field which corresponds to Saturn's planetary field. As the spacecraft enters the plasmoid, there is an increase in the magnitude of B_θ, showing that the field has become more dipolar. As the plasmoid flows over the spacecraft there is a field reversal from north to south with the field passing through zero at the centre of the plasmoid. Eventually the field returns to its original small and positive value. Various studies have sought to develop automated criteria to search for such events at Earth [*Slavin et al.*, 1989, 1993a, 1995, 2003; *Imber et al.*, 2011], Jupiter [*Vogt et al.*, 2010] and Saturn [*Jackman et al.*, 2014a; *Smith et al.*, 2016], placing constraints on the duration and magnitude of the field signatures.

At Earth there are multiple spacecraft that can detect the products of reconnection including plasmoids. Constellation satellites such as Cluster give simultaneous, spatially

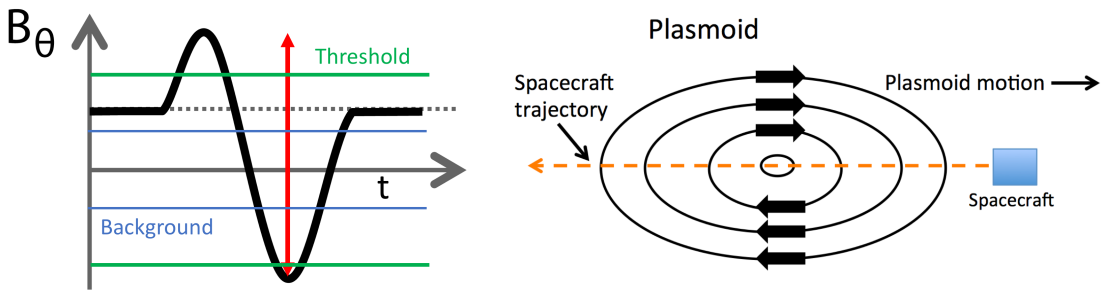

FIGURE 1.22: The left panel shows the B_θ signature as a spacecraft follows an ideal trajectory through a plasmoid as in the right panel. The plasmoid in the right panel is moving to the right with the dotted orange line marking the ideal trajectory of the spacecraft through the centre of the plasmoid. The total deflection in the B_θ signature on the left panel, δB_θ is is marked by the red double-headed arrow. The two horizontal green lines show a possible threshold of detection i.e. a minimum δB_θ for the plasmoid to be detected either by eye or by an event finding algorithm.

separated field measurements allowing constraints to be placed on the dimensions and velocity of plasmoid events. At Jupiter and Saturn a combination of significantly larger magnetospheres and only one spacecraft in orbit at a given time (Galileo and later Juno at Jupiter, and Cassini at Saturn) means that there are limitations on our interpretation of the single spacecraft signatures of reconnection events. As a result, much of the dynamics at Jupiter and Saturn are missed. Chapters 4, 5 and 6 focus on novel methods of modelling and data analysis to resolve some of the issues associated with single spacecraft observations.

1.5 Summary

This Chapter has provided a background discussion of basic plasma physics, the origins and nature of the solar wind and IMF, and the interactions that occur within planetary magnetospheres. Chapter 2 will discuss the magnetospheres of Jupiter and Saturn.

Chapter 2

Magnetospheres of the Giant Planets

2.1 Introduction

In chapter 1 the basics of space plasma physics and magnetospheric physics were discussed. In this chapter the structure and dynamics of the two largest magnetospheres in the solar system, those of Saturn and Jupiter as discussed in more detail.

2.2 Observations

To date there have been two dedicated orbiters at Jupiter. Galileo, launched in 1989, spent 8 years in orbit of Jupiter from 1995 to 2003. In July 2016, Juno arrived at Jupiter, entering into a 53-day polar orbit, for a planned two year mission. There have also been several flybys of Jupiter by the two Pioneer spacecraft, the two Voyager spacecraft, Ulysses, Cassini whilst on its way to Saturn, and New Horizons. Figure 2.1 shows a summary of the trajectories by spacecraft that have visited Jupiter's magnetosphere. There have been four spacecraft visits to Saturn; three flybys and one dedicated orbiter, Cassini. The first spacecraft to arrive at Saturn was Pioneer-11 in 1979 followed shortly by Voyager 1 and 2 in 1980/81 respectively. Cassini arrived at Saturn in July 2004 and has since had its mission lifetime extended several times. On September 15th 2017 Cassini performed its 'deathdive' into Saturn. Figure 2.2 shows all orbits by Cassini during its time at Saturn, known as the "Ball of yarn".

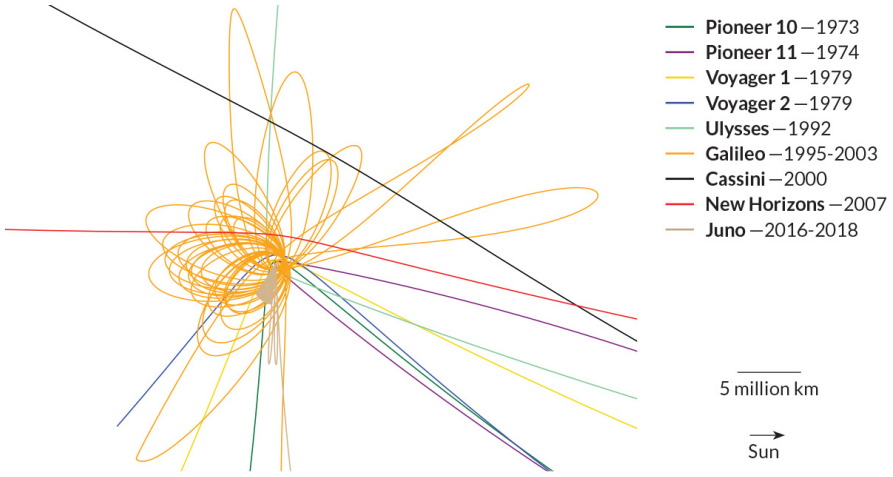

FIGURE 2.1: Schematic of spacecraft orbits at Jupiter [*Crockett and Otwell* [2016]. https://www.sciencenews.org/article/43-year-history-journeys-jupiter-one-graph]

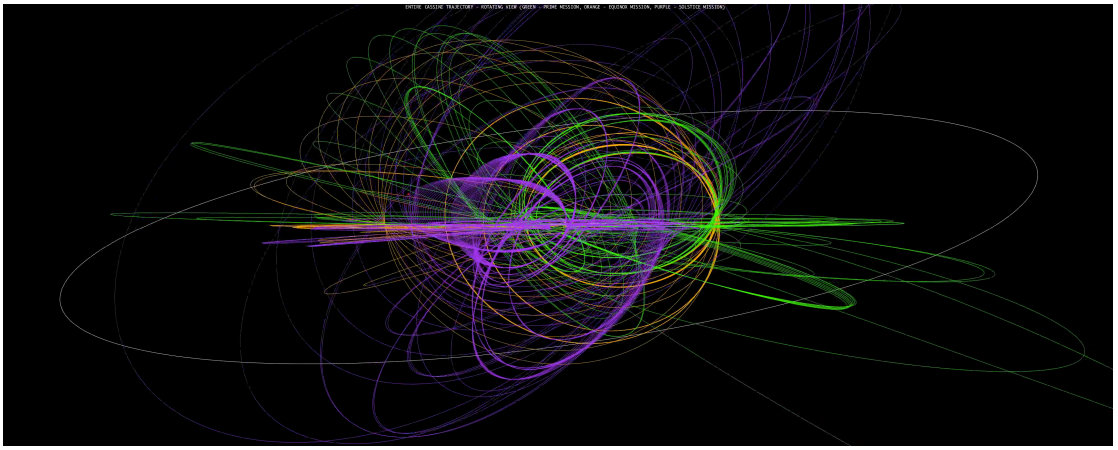

FIGURE 2.2: Referred to as "The ball of yarn". Schematic of Cassini's orbits from insertion on July 1st 2004 to end of mission lifetime September 15th 2017. Green - Prime mission (2004 - 2008). Orange - Equinox mission (2008-2010). Purple - Solstice mission (2010-2017). https://saturn.jpl.nasa.gov/resources/7393/ [Credit to JPL/NASA]

2.3 The Planets: Jupiter and Saturn

Jupiter is the largest planet in the solar system (1 R_J (equatorial) = 71492 km) and all the other planets could fit inside it with room to spare. Fittingly, its magnetosphere, shown schematically in figure 2.3, is the largest structure in the solar system spanning $\sim 10^7$ km across and stretching $\sim 10^9$ km further anti-sunward from its orbit as detected by Pioneer-11 and Voyager-2 spacecraft on their approach to Saturn [*Kurth*, 1981; *Lepping et al.*, 1983; *Goldstein et al.*, 1985]. Jupiter's magnetic field is generated by an internal dynamo driven by a rotating layer of metallic hydrogen. Uncovering more of the exact details of this dynamo and the precise internal composition of Jupiter is one of the missions of Juno. The dipole moment at Jupiter is 1.5 x 10^{27} $A\ m^2$, five orders of magnitude larger than that of Earth. Jupiter is the fifth planet from the Sun at a

distance of 5 Astronomical Units (*AU* - ~93,000,000,000 miles - the distance from the Sun to the Earth) with similar solar wind conditions to that of Saturn [*Jackman and Arridge*, 2011]. The rapid planetary rotation means Jupiter's magnetosphere is almost entirely rotationally dominated. The role of the solar wind in Jupiter's (and Saturn's) magnetospheric dynamics is a topic of debate [e.g. *McComas and Bagenal*, 2008; *Cowley et al.*, 2008] and will be discussed in more detail in section 2.6.

Saturn's magnetosphere, shown in figure 2.4, is traditionally described as the magnetosphere somewhere in between those of Earth and Jupiter. It has various features that make for a unique and fascinating magnetosphere. Saturn is the 6th planet from the Sun, orbiting the Sun at an average distance of 9.5 *AU*. Saturn is a fast rotator, with a rotation period of ~10.7 hours (the exact rotation rate is unknown and will be discussed in more detail in 2.9). This fast rotation and its low density cause the equatorial regions to bulge significantly and the poles to flatten causing the equatorial and polar radius to differ by almost 10%. Throughout this thesis the radius of Saturn, R_S, will be taken as the equatorial radius, 60,268 *km*. A deep metallic hydrogen layer coupled with the planet's rapid rotation leads to a large planetary magnetic field with a dipole moment of 4.6 x 10^{25} $A\ m^2$, three orders of magnitude larger than Earth's. The solar wind dynamic pressure is variable but peaks at ~0.01 *nPa* [*Jackman and Arridge*, 2011], 200 times less than at Earth. Like at Jupiter, the combination of weaker solar wind, stronger planetary magnetic field and fast rotation mean that Saturn's magnetospheric dynamics are generally thought of as rotationally dominated.

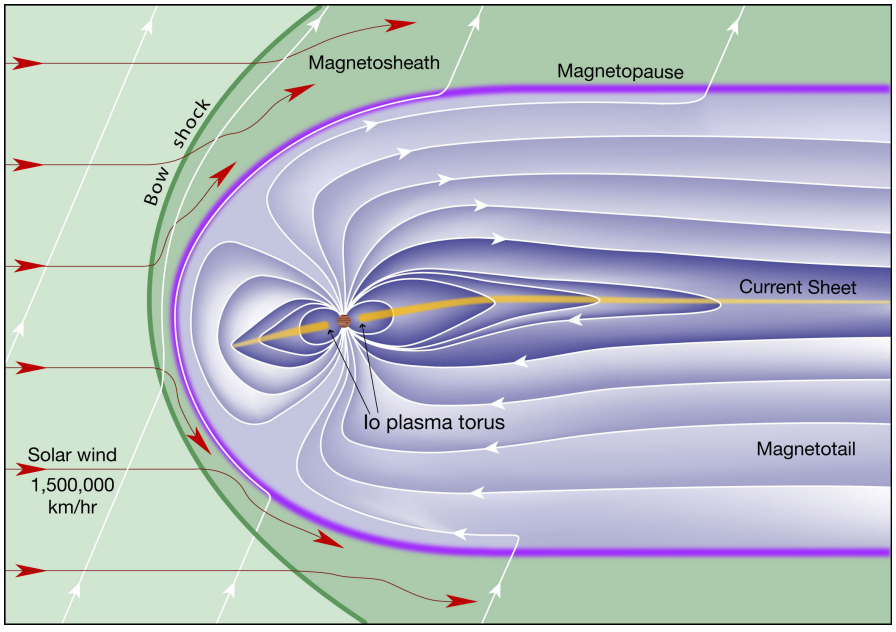

FIGURE 2.3: Schematic of Jupiter's magnetosphere. [Credit to Fran Bagenal and Steve Bartlett]

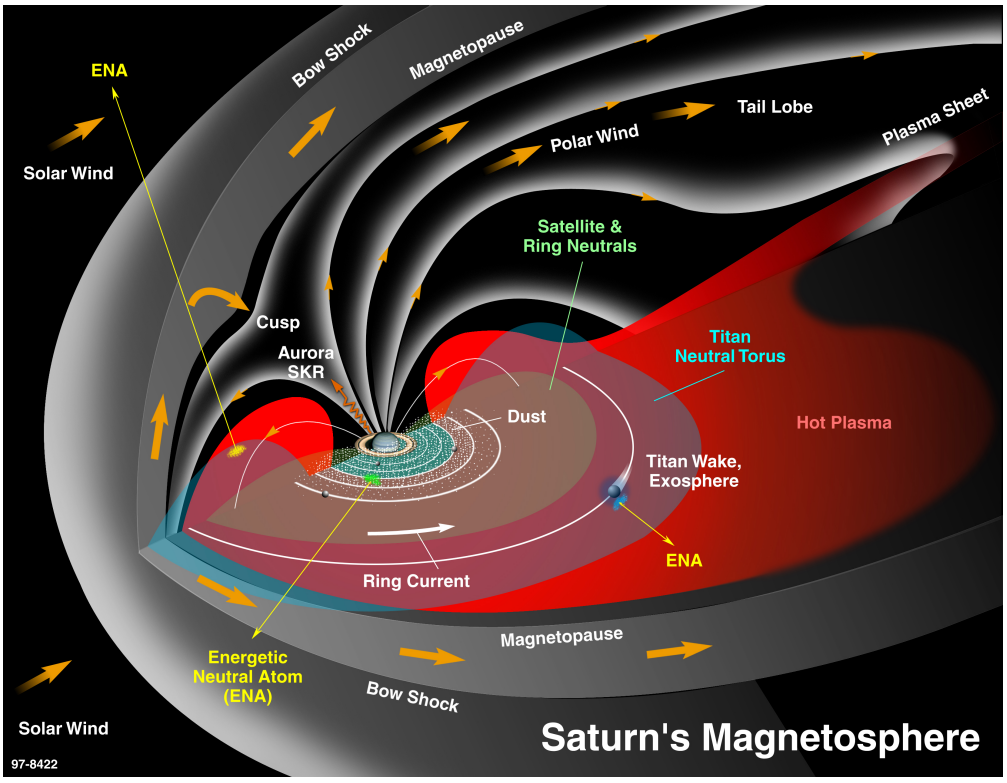

FIGURE 2.4: Schematic of Saturn's magnetosphere. [Credit to NASA]

2.4 Plasma Sources

2.4.1 Io and Enceladus

The main sources of plasma in a magnetosphere are the planet's ionosphere, the solar wind and atmospheres of any moons that orbit within the magnetosphere. Both Jupiter and Saturn contain contributions from all of these sources to varying degrees and in varying proportions. At Saturn, ions are added to the magnetosphere from both the ionosphere and from the solar wind via dayside reconnection or Kelvin Helmholtz (KH) driven reconnection at the flanks of the magnetosphere [*Delamere et al.*, 2013; *Delamere and Bagenal*, 2013]. *Krimigis et al.* [2005] found an abundance of He^{+} ions relative to He^{++} ions in Saturn's plasma sheet, consistent with ionospheric sources. How far and how much of the solar wind penetrates into the magnetosphere is an ongoing debate but light ions of solar origin have been found in the outer regions of the magnetosphere and work by *Masters et al.* [2009] and *Delamere et al.* [2011] show leakage across the magnetopause due to KH vortices. At Jupiter the solar wind has been estimated to provide a mass source on the order of a few tens of $kg\ s^{-1}$ [*Hilbe*, 1983] in the form of electrons and protons. The ionosphere is also a minor source of H_2^+ and H_3^+ ions [*Hamilton et al.*, 1981]. However, these are not the major source of plasma in the Kronian and Jovian magnetospheres. Instead, the main sources are the moons Enceladus and

Io who orbit within the inner magnetospheres of Saturn and Jupiter respectively and have both been observed to play a large role in the dynamics of the Kronian and Jovian systems.

Jupiter and Saturn have over 100 moons between them, the majority of which are small and less than a few kilometres in size. Io is the innermost of the four Galilean moons at Jupiter orbiting well within the inner magnetosphere, 5.9 R_J from the planet [*Belcher et al.*, 1980; *Krimigis and Roelof*, 1983]. It is the most geologically active object in the solar system due to tidal heating from its interaction with Jupiter and two other moons, Europa and Ganymede, with which it is in orbital resonance. Io is slightly larger than Earth's moon and is composed primarily of silicate rock and iron. The tidal bulge on the surface of the moon associated with the gravity of Jupiter, Europa and Ganymede can vary greatly between periapsis and apoapsis, significantly heating the mantle and core of the moon. Due to this tidal heating there are hundreds of volcanoes and lava flows on Io, releasing vast amounts of sulphur, its compounds, and silicate rock into the atmosphere or into space. Figure 2.5 shows Io's volcano Tvashtar, as seen by New Horizons, erupting over 300 km above its surface. This eruption wasn't seen by earlier visiting spacecraft, highlighting the variable nature of Io's volcanism. Canonically, Io ejects $\sim$1000 $kg\ s^{-1}$ of volcanic material into the magnetosphere driving the Vasyliunas cycle and swelling the magnetosphere to twice the size it would otherwise be [*Joy et al.*, 2002]. Various studies have estimated the neutral mass loading rate to be between 500 - 1000 $kg\ s^{-1}$ but can vary from 260 to 1400 $kg\ s^{-1}$ [e.g. *Thomas et al.*, 2004; *Bagenal*, 2007; *Bagenal and Delamere*, 2011, and references therein]. The rate of mass loading of the Jovian magnetosphere by Io and the physical processes behind it are whole topics on their own. Sodium and Oxygen atoms in the atmosphere of Io are heated via inelastic collisions with Io torus ions and escape the moon's gravity to form an extensive neutral cloud encircling around most of Io's orbit. Eventually, one third to one half [*Bagenal and Delamere*, 2011] of the neutrals become ionised via electron impact, forming the Io plasma torus. These ions are then picked up by Jupiter's field lines. This gives an approximate ionic mass loading rate between $\sim$ 100 and 700 kg s^{-1}.

Enceladus is deep inside Saturn's magnetosphere, approximately 4 R_S from the planet. In 2005, Cassini discovered water vapour and ice erupting from vents in the southern hemisphere of Enceladus, likely supplied by a deep subsurface liquid ocean [*Dougherty et al.*, 2005; *Gaidos and Nimmo*, 2000; *Porco et al.*, 2006; *Hansen et al.*, 2006]. The cracks are known as tiger stripes. The internal heating from Enceladus is believed to be due to tidal heating due to its orbital resonance with Dione [*Spencer et al.*, 2009; *Iess et al.*, 2014]. Estimates of the rate at which mass is added to the magnetosphere are in the range 70 - 750 $kg\ s^{-1}$ for neutrals. These neutrals are ionised via a variety of

photolysis reactions [e.g. *Thomas et al.*, 2004; *Fleshman et al.*, 2010] leading to a plasma input of 12 - 250 $kg\ s^{-1}$ [*Bagenal and Delamere*, 2011].

The plasma added to the respective magnetopsheres is 'picked up' by planetary magnetic field lines which drives large-scale dynamics within the magnetosphere. These mechanisms will be discussed in more detail in section 2.6.

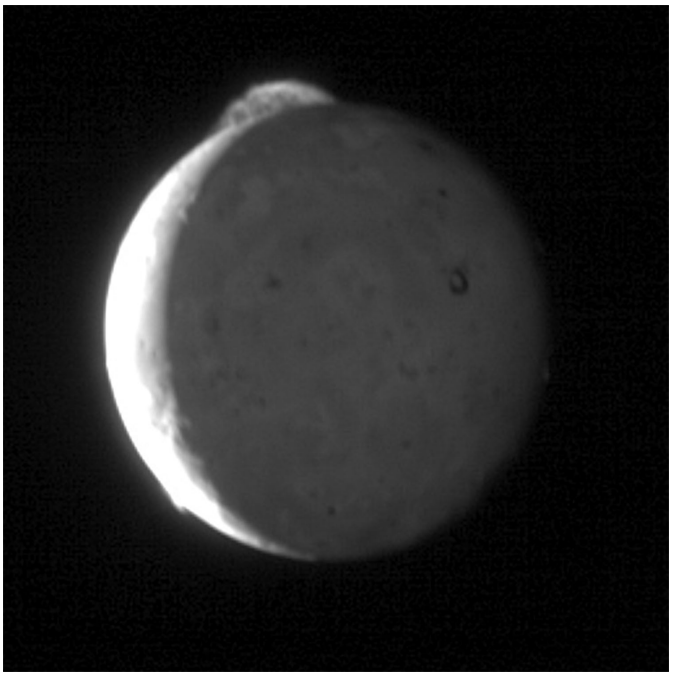

FIGURE 2.5: The volcano Tvashtar erupting on the surface of Jupiter's moon Io illuminated by sunlight as captured by New Horizons. Gif here. [Credit to NASA]

2.4.2 Io Plasma Torus

The orbit of Io is surrounded by a cloud of sulphur and oxygen atoms from the atmosphere of the moon, peaking at a few tens of particles cm^{-3} near Io's orbit and falling off in density either side. The neutral cloud orbits with a velocity $\sim 17\ km\ s^{-1}$ [*Schreier et al.*, 1998], however the plasma in the Io torus roughly corotates. Between one third and one half [*Bagenal and Delamere*, 2011] of the atoms supplied to the neutral cloud are ionised via electron-impact refreshing the plasma torus whilst the rest are lost as high energy neutrals. The plasma torus is variable in mass and brightness on many timescales linked with variability of the volcanic activity [e.g. *Yoshikawa et al.*, 2017] and mass loading from Io. The newly ionised particles from Io are 'picked-up' by the magnetic field lines and accelerated to corotation via momentum transfer from Jupiter's ionosphere via field-aligned currents. The new 'warm' ions are cooled by coulomb collisions with electrons which are in turn cooled by collisional excitation of the lower energy levels of the ions. This leads to the photon emission used to observe the torus.The

plasma torus can be observed remotely via emissions which are mainly in the extreme ultraviolet (EUV) range using Cassini, Hubble or more recently the Hisaki/EXCEED telescope [e.g. *Steffl and Stewart*, 2004; *Yoshioka et al.*, 2012]. A total emitted radiation of 23 *TW* in the whole UV spectral range was measured by Voyager [*Broadfoot et al.*, 1981; *Thomas et al.*, 2004]. *Delamere et al.* [2004a] studied the torus using a physical chemistry model with ion densities obtained by Voyager [*Bagenal*, 1994] and Cassini [*Steffl et al.*, 2004; *Steffl and Stewart*, 2004]. Results show that energy picked up by the ions can only fuel 34 to 74 % of the radiation measured from the torus. One of the feasible physical processes to supply hot electrons to the torus is the centrifugally driven interchange mode, where the returning flux tubes are filled with hot electrons [*Thorne et al.*, 1997]. An alternative scenario is that hot electrons originate from the interaction with Alfven waves that is generated by empty inward flux tubes [*Hess et al.*, 2011]. The Io plasma torus has also been measured in situ by Voyager, Ulysses and Galileo [*Bagenal and Sullivan*, 1981; *Sittler and Strobel*, 1987; *Meyer-Vernet et al.*, 1995; *Frank and Paterson*, 2000; *Bagenal et al.*, 2016]. Their studies (or observations) give plasma density, temperature and magnetospheric conditions within the torus although they are limited to only the regions local to the spacecraft.

2.5 Interaction with the Solar Wind

This section will discuss the magnetospheres of Jupiter and Saturn in context of their interaction with the solar wind. The magnetopause distance is bimodal at Jupiter with a typical standoff distance of $\sim$63 R_J or $\sim$92 R_J as derived statistically by *Joy et al.* [2002]. This bimodality is believed to be due to the compression-rarefaction pattern in the solar wind [*McComas et al.*, 2014]. Work by *Kivelson et al.* [2003] showed evidence of IMF control of the location of the Jovian magnetospheric boundary during the Cassini flyby of Jupiter whilst Galileo was orbiting the planet which gave simultaneous solar wind and magnetosphere data. Statistical analysis of the typical sub-solar magnetopause distance at Saturn gives a bimodal distribution with means at 20.7 and 27.1 R_S with probabilities of 43 and 57% respectively [*Achilleos et al.*, 2008; *Pilkington et al.*, 2015]. As with Jupiter, this bimodalilty derives from the compression-rarefaction pattern in the solar wind as well as the periodic increase and decrease in plasma pressure (that acts to inflate the magnetosphere) with the build up of mass and subsequent reconnection and mass loss.

As mentioned in section 2.3, the role of the solar wind at Jupiter and Saturn is a topic of much debate. One mechanism of interaction is via dayside reconnection. This can occur in two different forms: 1) via oppositely directed field lines at the nose of the

magnetosphere that adds open flux to the system, or 2) at high latitudes which does not add open flux, rather the system is just 'stirred'. Recent work by *Ebert et al.* [2017] found evidence of reconnection along the dawn flank from accelerated flows at Jupiter's magnetopause. The open flux content generated over a solar rotation has been calculated at ∼500 *GWb* [*Nichols et al.*, 2006] based on an estimated magnetopause reconnection rate. Based on the size of the polar cap *Vogt et al.* [2011] calculated the open flux at ∼720 *GWb*. Many studies have shown the solar wind to have an effect on the Jovian auroral emissions following a compression, such as in the radio [e.g. *Barrow*, 1978; *Terasawa et al.*, 1978; *Hess et al.*, 2012], in the infra-red [e.g. *Baron et al.*, 1996], the UV [*Pryor et al.*, 2005; *Nichols et al.*, 2007; *Badman et al.*, 2016; *Nichols et al.*, 2017] and in the X-ray [*Dunn et al.*, 2016].

The dayside reconnection rate and location (i.e. nose vs. flanks) are both a subject of debate at Saturn. The rate of reconnection at the dayside magnetopause may be suppressed by the high Mach number (the ratio of the solar wind velocity to the speed of sound in the solar wind) and high plasma beta (a high ratio of plasma to magnetic pressure) at Saturn [e.g. *Scurry and Russell*, 1991; *Masters et al.*, 2012], although others like *Grocott et al.* [2009] have argued that there is no dependency. Compared to Earth, there is also evidence of more severe diamagnetic drift suppression (where the drift of charged particles within a current sheet can suppress reconnection by disrupting the reconnection outflow jets) at Saturn which limits reconnection onset to higher magnetic shear conditions [*Fuselier et al.*, 2014]. This does not necessarily switch off reconnection, but the reconnection site may move to higher latitudes where the plasma beta is lower (i.e. the magnetic field dominates) [*Desroche et al.*, 2013]. Case studies show evidence of dayside reconnection at Saturn, via in situ observations of accelerated flows and flux transfer events [*McAndrews et al.*, 2008; *Jasinski et al.*, 2016a], and indirect observations of solar wind plasma in the cusp [*Arridge et al.*, 2016b; *Jasinski et al.*, 2016b]. The Kelvin Helmholtz instability is a viscous interaction and can transfer mass, momentum and energy from the solar wind into the magnetosphere. *Delamere and Bagenal* [2013] argued that the KH instability can account for the required plasma mixing at the boundary (the existence of this at Jupiter is uncertain). Reconnection can be triggered by KH activity [*Ma et al.*, 2014] at the magnetopause boundary along the flanks of the magnetosphere. *Delamere and Bagenal* [2010] argue that if the IMF becomes entangled in this boundary mixing then this could potentially be the primary solar wind interaction mechanism at the Saturn's (and Jupiter's) magnetosphere.

In *Cowley et al.* [2003] and *Badman and Cowley* [2007] it is argued that the Dungey cycle and the solar wind can play a significant role at Jupiter (and Saturn). *McComas and Bagenal* [2007] argue against this saying that there is no large-scale Dungey cycle at Jupiter. They reason that considering the timescales between reconnection events at

Jupiter and the solar wind velocity, the reconnection site to close the open field lines in the tail would be more than ∼1500 R_J downtail; further, an approximate return flow speed of 40 $km\ s^{-1}$ means the plasma would take more than 750 hours to return in which time Jupiter would have completed in excess of 100 rotations, twisting the base of the field line. The return flow would also have to compete against the fast radially flowing plasma present at Jupiter. They instead suggest that flux opened on the dayside is closed at the magnetopause before it can travel downtail as demonstrated in figure 2.6. *Cowley et al.* [2008] replied, arguing that this two stage reconnection is unlikely to close all of the flux opened and that their estimates for the Dungey cycle x-line location is an upper limit rather than the actual distance. The role of the solar wind and the Dungey cycle at Jupiter remains a topic of much debate. The Juno spacecraft which arrived at Jupiter in July 2016 will look to resolve this debate.

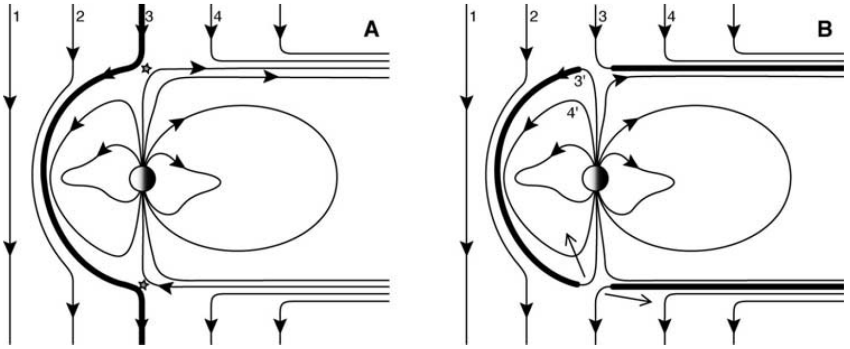

Observations from the magnetotail are used to explore how this open flux is closed.

FIGURE 2.6: Schematic diagram of how open magnetic flux can close at the magnetopause. (a) A southward IMF (1) drapes around the dayside magnetopause (2, 3) until it reconnects with an oppositely-directed planetary field (stars). (b) Flux tube 3 reconnects near the magnetopause near both north and south cusps, creating newly closed (30) and disconnected (3) flux tubes. (Note that Jupiters intrinsic magnetic field is opposite that of the Earth's so erosion near the nose occurs preferentially for northward IMF instead of southward.) After reconnection, the short, newly closed flux tube is free to work its way back toward a more normal closed shape (40), while the long, newly disconnected flux tube (4) is lost down the flanks of the tail. [Credit to *McComas and Bagenal* [2007]]

The main auroral oval at Saturn is thought to be produced by interaction with the solar wind through the shear in the rotational flow across the open-closed field line boundary [*Cowley et al.*, 2003; *Bunce et al.*, 2008a]. The opening and closing of magnetic flux by dayside and nightside reconnection changes the size of the polar cap. *Badman et al.* [2005, 2014] used images taken by the Hubble Space Telescope (HST) to calculate the size of the dark polar cap region in order to calculate the flux content of the open field lines. They found an average of 35 GWb, with a typical range between 10 and 50 GWb. *Jackman et al.* [2004] used an empirical formula (similar to equation 1.38 in chapter

1) to calculate that during few-day solar wind compression periods the dayside reconnection voltage could be ∼100 kV such that ∼30 - 40 GWb of open flux is produced, in line with that observed by *Badman et al.* [2005, 2014]. During few-day rarefaction periods *Jackman et al.* [2004] found that only negligible amount of open flux would be produced and estimated that over one solar rotation, consisting of two compression regions (during the declining phase of the solar cycle), ∼100 GWb of open flux would be produced (later backed up by in situ observations by *McAndrews et al.* [2008]; *Masters et al.* [2014]). Observations from the magnetotail are used to explore how this open flux is closed. In magnetic field observations, following the deflection northward in the field signifying a plasmoid detection, the field can remain deflected for an extended interval. This interval has been interpreted as the Saturn equivalent of the postplasmoid plasma sheet (PPPS) first described at Earth by *Richardson et al.* [1987]. The PPPS represents an interval where previously open flux is being closed by reconnection. Following reconnection, as the newly formed plasmoid moves tailwards, open lobe field lines move into the reconnection region and are subsequently reconnected. The tension in these newly disconnected field lines and fast flowing plasma accelerate the plasmoid downtail [*Richardson et al.*, 1987; *Jackman et al.*, 2011]. Several studies have used estimates of plasmoid duration and loss-rates to calculate how much flux is closed during reconnection. *Jackman et al.* [2011] calculated that a large-scale reconnection event would close ∼3 GWb, in approximate agreement with magnetohydrodynamics (MHD) simulations by *Jia et al.* [2012], thus requiring on average ∼12 large-scale events to cycle all the open flux as measured by *Badman et al.* [2005].

2.6 Structure and Features

Both Saturn and Jupiter have large magnetotails, but that of Jupiter is by far the largest coherent structure in the solar system. Jupiter's is cylindrical in shape with a diameter of up to ∼400 R_J [*Joy et al.*, 2002]. New Horizons travelled down the Jovian tail up to 2500 R_J [*McNutt et al.*, 2007; *McComas et al.*, 2007]. Pioneer and Voyager spacecraft have detected Jupiter's tail as far as 9000 R_J [*Lepping et al.*, 1983] or even further than the orbit of Saturn 5 AU away [*Kurth*, 1981; *Scarf et al.*, 1982; *Goldstein et al.*, 1985]. As with Saturn's tail, it is composed of two lobes with a central, equatorial current sheet which can be detected in situ by changes in the sign of the radial component of the magnetic field

2.6.1 Inner and Middle Magnetosphere

Within the inner magnetosphere, Io and Enceladus load their respective magnetospheres with ∼500 $kg\ s^{-1}$ of sulphur and oxygen ions (in addition to ∼100 $kg\ s^{-1}$ of protons and oxygen ions from Europa) and ∼250 $kg\ s^{-1}$ of water group ions. Outside of ∼1 R_J the dominant force on the plasma is centrifugal (rather than the gravitational attraction of the planet) which confines the plasma to the equatorial plane. *Gledhill* [1967] predicted that this centrifugal force due to the rapidly rotating magnetosphere would lead to a "washer shaped" magnetodisk configuration of Jupiter's magnetosphere at distances between 20 and 50 R_J where the field lines are radially stretched away from a dipole configuration. This was later observed by Pioneers 10 and 11 [*Smith et al.*, 1974, 1975]. This region also exists at Saturn [*Arridge et al.*, 2007, 2008a] extending from a few R_S to within a few R_S of the magnetopause. The magnetodisk configuration at Saturn is shown schematically in figure 2.7. The magnetodisk configuration is supported by a magnetic perturbation due to an eastward flowing azimuthal 'ring current' that radially distends the field lines [*Smith et al.*, 1980; *Connerney et al.*, 1981, 1983]. *Bunce et al.* [2007] concluded that at Saturn the ring current is dominated by the inertial currents associated with the subcorotating Enceladus plasma, rather than hot plasma currents like at Earth. At regions close to the planet, the magnetic perturbations due to the ring current are small compared to the planetary field and so the field remains dipole like. At Saturn the ring current is variable and like many phenomena at Saturn shows modulations on the period of a planetary rotation [*Arridge et al.*, 2007; *Khurana et al.*, 2009; *Provan et al.*, 2009a; *Brandt et al.*, 2010].

Both the Jovian and Kronian magnetodisks respond to increases in solar wind dynamic pressure. During periods of low solar wind dynamic pressure, the field of Saturn has the magnetodisk configuration, but during a solar wind compression, the dayside becomes almost purely dipolar [*Arridge et al.*, 2008b]. This observation was supported by results from *Bunce et al.* [2007] and *Bunce et al.* [2008b] which showed that the ring current strength varies by a factor of three between a compressed and expanded magnetosphere and that during a compression the ring current produced a quasi-dipole field but a more stretched out configuration during an expanded magnetosphere.

Moving radially outwards the ring current associated with the magnetodisk region merges into the tail plasma sheet, a region of higher density hot plasma on closed field lines surrounding the current sheet on the nightside of the planet. This plasma sheet region contains the ionic plasma that is moving radially downtail and will be eventually lost in the form of a plasmoid as will be discussed in the next section.

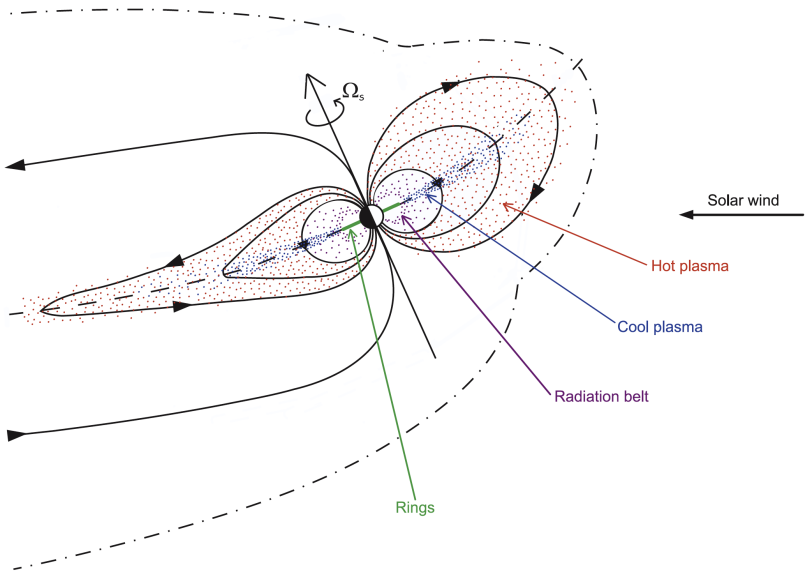

FIGURE 2.7: Sketch of Saturn's magnetosphere in the noon-midnight meridian plane for southern summer conditions with the Sun to the right. The outer black dot-dashed line indicates the magnetopause and the interior solid black lines shown the magnetic field lines. The blue dotted region represents cool water group ions from Enceladus which are transported radially outwards. The plasma is centrifugally confined near the equatorial plane by the plasma rotation with the planet about the tilted spin axis. The red dotted region represents the warm and hot plasma which is transported inwards from the outer regions to an inner boundary at ~7 R_S as shown and is more uniformly distributed along the field lines. The purple dotted region represents the radiation belt of high-energy particles that extends inside this boundary and is limited in the inner region by Saturn's main ring system extending to 3 R_S in the equatorial plane which is represented by the green lines on either side of the planet. The ring current, represented by the distension of the equatorial field lines outward from the planet (the magnetodisk), extends from the inner boundary of the hot plasma region to within a few R_S of the magnetopause on the dayside, while merging into the central tail plasma sheet on the nightside. The diagram also shows the observed displacement of the magnetic equator (where the radial field component switches sign) northward of the spin equator in the outer magnetospheric regions on both the dayside and the nightside of the planet, due to the solar wind flow under southern summer conditions. [*Kellert et al.* [2009]]

Jupiter's magnetosphere contains a giant current sheet approximately 2.5 R_J [*Khurana*, 1992] thick located near its dipole magnetic equator that contains most of the plasma and energetic particles in Jupiter's magnetosphere. Its presence was detected by Pioneers 10 and 11 [e.g. *Smith et al.*, 1974; *Randall*, 1994] and Voyagers 1 and 2 [e.g. *Ness et al.*, 1979a; *Bridge et al.*, 1981] who also found that it contains low energy plasma. It behaves like a rigid structure inside a radial distance of ~50 R_J where the periodic reversals of the B_r component are highly predictable as the current sheet flaps due to the offset between the magnetic and rotational axis of Jupiter.

Saturn's current sheet lies at the centre of the magnetotail. It is a region of high-beta plasma, i.e. high ratio of thermal to magnetic pressure. The current sheet is non-stationary and is observed to 'flap' and 'hinge'. The current sheet hinges out of the

equatorial plane on both the dayside and the nightside forming a bowl shape [*Arridge et al.*, 2008a, 2011]. The direction of the hinging depends on the attack angle of the solar wind. When Cassini first arrived during southern hemisphere summer, the current sheet was hinged upwards approximately 5°. The distance of the hinge point at Saturn, beyond which the current sheet is lifted out of the equatorial plane, was modelled by *Arridge et al.* [2008a] at ∼25 R_S but is highly sensitive to solar wind conditions. The hinging of the current sheet affects the ability of in situ spacecraft to observe tail reconnection as will be discussed in section 2.7.1. The current sheet is also observed to oscillate vertically, termed 'flapping', at a period close to that of the planetary rotation [*Arridge et al.*, 2011; *Provan et al.*, 2012]. The driver behind the flapping is not fully understood due to the almost perfect alignment between the rotation and dipole axis of the planet but is thought to be caused by rotating magnetic perturbations in each hemisphere [*Arridge et al.*, 2008c; *Andrews et al.*, 2010a; *Jia and Kivelson*, 2012]. This flapping motion is also superposed with thickness variations of the current sheet as the perturbations propagate [*Thomsen et al.*, 2017]. There is also an unrelated, shorter timescale flapping over periods of 1 - 30 minutes [*Arridge et al.*, 2007]. Surrounding the current sheet is the plasma sheet, a region of closed magnetic field lines and high plasma beta. Electron distributions in the plasma sheet have been observed by *Arridge et al.* [2009] to have three states: quiet with energies of 0.1 keV; disturbed with energies of approximately 1 keV, and a bimodal state with both previous distributions and an additional cold 0.01 keV component. Ion densities range from 1 cm^{-3} near 20 R_S to 0.1 cm^{-3} near 45 R_S.

2.6.2 Radial Transport

Radial transport of the iogenic plasma from Io and Enceladus occurs through a process of flux tube interchange (a centrifugally driven instability analogous to gravity driven Rayleigh-Taylor driven instability in fluids) whereby magnetic flux tubes (of scale on order 1000 *km* [*Thorne et al.*, 1997] at Jupiter) that are relatively full of cold, iogenic plasma move outwards and relatively empty flux tubes containing hot plasma move inwards [*Krupp et al.*, 2004; *Burch et al.*, 2005; *Hill et al.*, 2005; *Bagenal*, 2007; *Mauk et al.*, 2009; *Dejong et al.*, 2010; *Thomsen et al.*, 2016]. A simulation of the formation of interchange 'fingers' in the RICE model by *Liu et al.* [2010] is shown in figure 2.8. The rate of interchange is proportional to the density gradient. Numerical modelling of the interchange instability at Jupiter reveals that the radial shear in the azimuthal flow due to the drop off from corotation drives the characteristic size of the interchanging flux tubes to finer and finer scales [*Pontius et al.*, 1998; *Wu et al.*, 2007]. The most detectable dynamic features attributable to this instability are sudden, brief incursions of hot plasma into the inner magnetospheric cool plasma [e.g. *Burch et al.*, 2005; *Hill et al.*,

2005]. The hot plasma typically exhibits an energy dispersion, such that more-energetic ions are seen first, followed by lower energy ions, then lower energy electrons, and finally the more energetic electrons. Interchange events also have magnetic field signatures [e.g. *André et al.*, 2005, 2007; *Leisner et al.*, 2005] and distinct plasma wave signatures [e.g. *Menietti et al.*, 2008; *Rymer et al.*, 2009; *Kennelly et al.*, 2013]. *Thomsen et al.* [2016] showed the penetration of suprathermal electrons into the inner magnetosphere of Saturn which supports the case for internal processes such as the interchange process in depositing hot electrons.

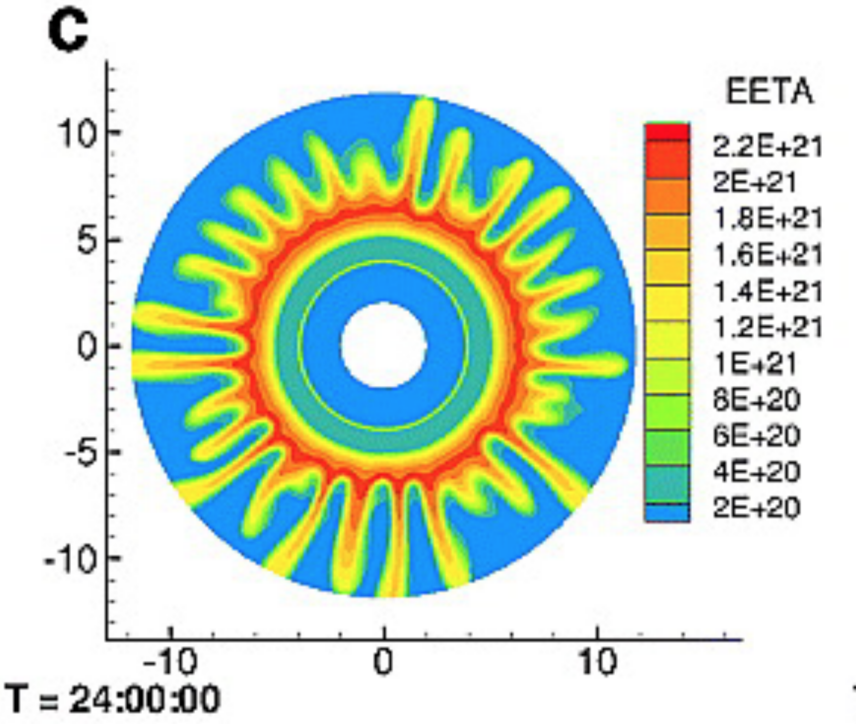

FIGURE 2.8: Simulation results for the evolution of plasma convection in Saturn's inner magnetosphere showing the 'fingers' of flux tube interchange. [*Liu et al.* [2010]]

2.6.3 Corotation Breakdown

Close to the planets, plasma that is frozen to closed magnetic field lines corotates with the planet, but with increasing radial distance the field lines struggle to keep the plasma at corotation and eventually the plasma begins to sub-corotate, 'dragging' the field into a lagging configuration.

Figure 2.9 shows the Jovian current system associated with the magnetosphere attempting to keep the plasma from Io at corotation. As the plasma moves radially outwards, without any torque, conservation of angular momentum indicates that the azimuthal velocity of the plasma would decrease. Since the field lines and the plasma are frozen

together, this creates a differential velocity between the neutrals in the upper atmosphere rotating with the planet and the flux tubes. Collisions between the ions and neutrals form a torque on the flux tubes which spins them back up to corotation. *Hill* [1979] showed that the ionospheric torque is able to maintain corotation for a few tens of R_J but beyond this the angular velocity of the plasma falls away from corotation. The location of Jupiter's main auroral oval maps to the boundary of this breakdown in corotation [*Cowley and Bunce*, 2001]. The location of this "corotation breakdown" is found to be local time dependent from ∼25 $_J$ at dusk to ∼40 R_J in the predawn sector [*McNutt et al.*, 1981].

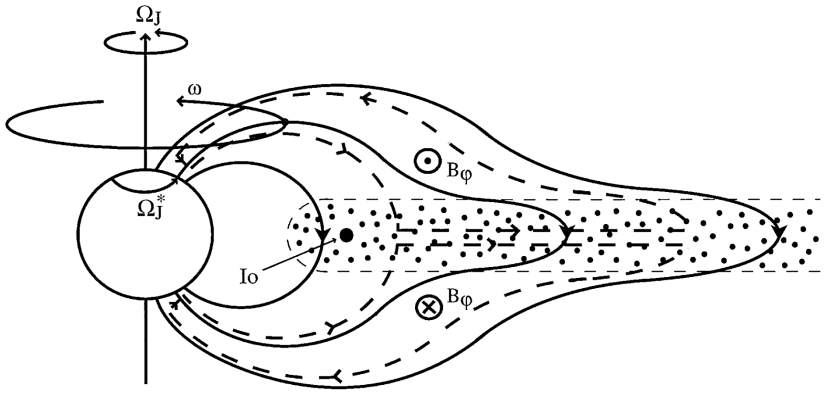

FIGURE 2.9: Sketch of a meridian cross section through the Jovian magnetosphere showing the principal features of the inner and middle magnetosphere regions. The solid line indicate magnetic field lines which are stretched outwards by azimuthal current in the plasma sheet marked by the dotted region. This plasma rotates with the planetary field due to coupling with the ionosphere. Three angular velocities are shown: the planet Ω_j, a shell of field lines, ω and the neutral upper atmosphere where Pedersen currents flow, Ω_j^*. This current system bends the field lines of of meridian planes, associated with azimuthal field components B_Φ. The dashed lines shown the current system associated with the breakdown in corotation of the plasma. [*Cowley and Bunce* [2001]]

At Saturn, as at Jupiter, when the plasma from Enceladus is initially picked up, it is accelerated to corotation by a torque applied on field aligned currents that couple the ionosphere to the magnetosphere. The ionosphere can only apply sufficient torque for plasma that is close to the planet; at a certain radial distance (∼15 R_S) the ionosphere can no longer keep the plasma at corotation and the plasma begins to lag behind corotation [e.g. *Hill*, 1979; *Pontius and Hill*, 2009]. This gives rise to a current system as shown in figure 2.10.

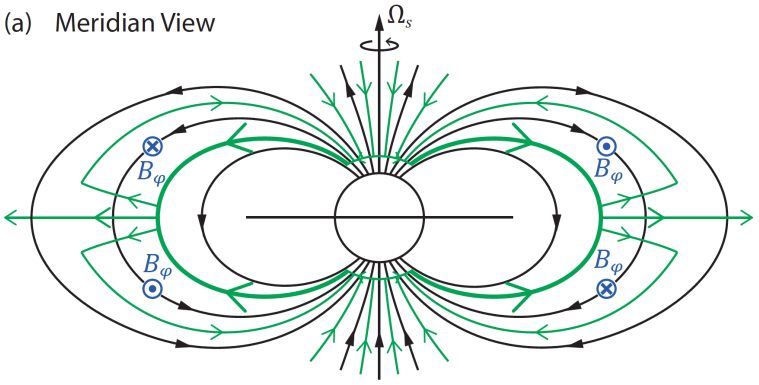

FIGURE 2.10: Sketch showing the field-aligned current system associated with sub-corotation of plasma in Saturn's magnetosphere in a meridian view. The black lines are the planetary field, green lines are the current system and the blue circled dots and crosses the B_ϕ. [Credit to *Hunt* [2016]]

2.6.4 Plasma Flows

The main plasma flows at Jupiter and Saturn are caused by the Vasyliunas cyle (as discussed in chapter 1, where mass is picked up by field lines, rotate around the dayside, stretch tailwards at dusk before reconnecting and returning back to the planet) and the Dungey cycle (driven by the solar wind - although as discussed above the role of the Dungey cycle at Jupiter is highly debated). The time scale for the Dungey cycle refers to the length of time from the opening of the field lines at the dayside to the closing of the field lines on the nightside and is on the order of ∼1 week at Saturn [*Jackman et al.*, 2004] whilst at Jupiter it has been estimated to have a timescale of several weeks at Jupiter [*Badman and Cowley*, 2007]. Work by *Milan et al.* [2005] at Saturn argued that the twisting of open field lines due to the rotation of Saturn gives rise to a twisted lobe region with the formation of concentric cylinders of oldest to newest open flux from the inside out. They suggested that this could also occur at Jupiter. The relative roles of the two plasma flow systems within the two magnetospheres is not yet fully known. The steady state equatorial plasma flows, as envisaged by *Cowley et al.* [2003] and *Cowley et al.* [2004] at Jupiter and Saturn respectively is illustrated schematically in figures 2.11 and 2.12.

2.7 Magnetic Reconnection

Reconnection at Jupiter and Saturn follows the same basic physical process as at Earth, the breaking and reconnection of magnetic field lines, as described in chapter 1, but the drivers and location of reconnection are completely different. This section will outline the current understanding of reconnection in the Jovian and Kronian magnetospheres.

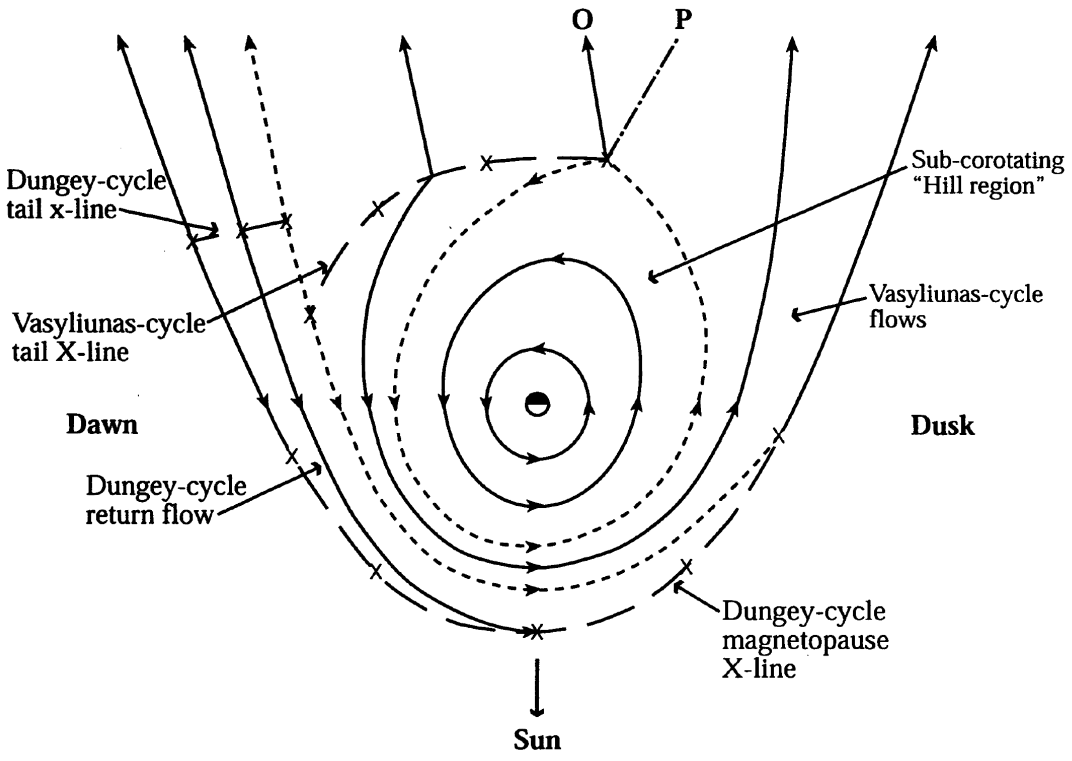

FIGURE 2.11: A sketch of the equatorial plasma flow in Jupiter's magnetosphere. The view is from the north, with the Sun to the bottom. The solid lines are plasma streamlines, and the short-dashed separate different flow regimes. The direction of flow is indicated by the arrows. The long-dashed lines with Xs represent regions of reconnection, associated with the Dungey cycle or Vasyliunas cycle as labelled. The lines labelled O and P indicate the paths of the centres and edges of Vasyliunas cycle plasmoids, respectively. [*Cowley et al.* [2003]]

2.7.1 Detecting Reconnection

The magnetotails of Jupiter and Saturn are extremely large. Unlike at Earth where there are a host of orbiting satellites, Jupiter and Saturn have only had on dedicated orbiter at a time (plus the Hubble and more recently the Hisaki/EXCEED telescopes). This makes detecting reconnection extremely difficult. Reconnection can be detected in situ by observing changes in the topology of the field (via deflections in the north-south B_θ field component [*Russell et al.*, 1998; *Vogt et al.*, 2010]) and by changes in the plasma flow direction [e.g. *Kronberg et al.*, 2008a]. Reconnection in the tail has three main products that can be detected directly by in situ spacecraft: dipolarisations, plasmoids and Travelling Compression Regions (TCRs) (discussed in chapter 1 - caused by the draping of the lobe field lines around either a plasmoid or a dipolarisation and is differentiated by a larger B_r component). Which of these three is detected depends on the relative locations of the spacecraft and the x-line (where reconnection itself took place). On the planetward side of the x-line, following reconnection, previously stretched field

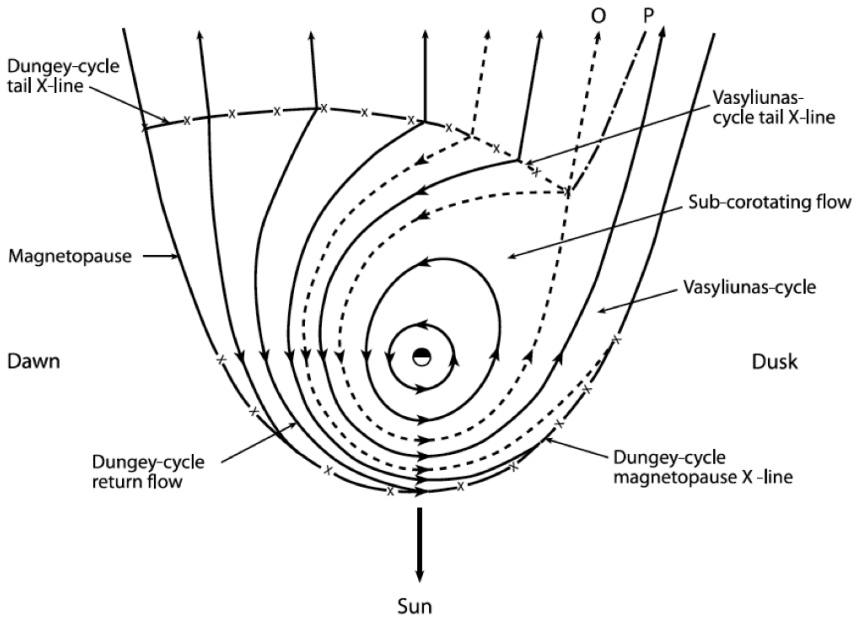

FIGURE 2.12: Schematic of plasma flows in Saturn's magnetosphere. The figure looks down onto the equatorial plane, with dawn to the left, dusk to the right, and Sun to the bottom. The solid lines are plasma flow streamlines. Short dashed lines separate flow regimes. The location of reconnection lines are shown by solid and dashed lines marked with crosses. The curve indicated by the O marks the path of the plasmoid O line in the Vasyliunas cycle (also a streamline, while P marks the outer limit of the plasmoid field lines, which eventually asymptotes to the dusk tail magnetopause). [*Cowley et al.* [2004]]

lines 'dipolarise' to a more dipole-like field structure. Meanwhile, on the tailward side of the x-line, the combination of magnetic field and plasma released down tail is called a plasmoid. The magnetic signature associated with each of these structures is highly dependent on the trajectory of the spacecraft through the structure or, more accurately, the path of the structure over the spacecraft which can be considered stationary in relation. This is demonstrated in figure 2.13 where the B_θ (the north-south component of the field) signature for a plasmoid detected by a spacecraft at three different locations relative to the plasma sheet is shown. Broadly speaking, a plasmoid passing over the spacecraft will register a north-south deflection in the magnetic B_θ, while a dipolarisation will register a south-north deflection. TCRs also give the north-south field deflections that plasmoids and dipolarisations do, but their signatures are modified by the presence of the spacecraft in the lobe. The accompanying B_r (the radial component of the field) signature is greater and there is a quiet background field. The lobe is often identified by the ratio of $|B_r|$ to $|B|$, a measure of how radial the field is. At Jupiter *Vogt et al.* [2010] identified 249 reconnection events using 7 years of Galileo magnetic field data (1996 - 2003), as well as some additional magnetometer data from Pioneer 10, Voyager 1 and Voyager 2. Their criteria required a significant enhancement of the B_θ component of the field over a 1-day running average of $|B_\theta|$ that lasted for at least 60

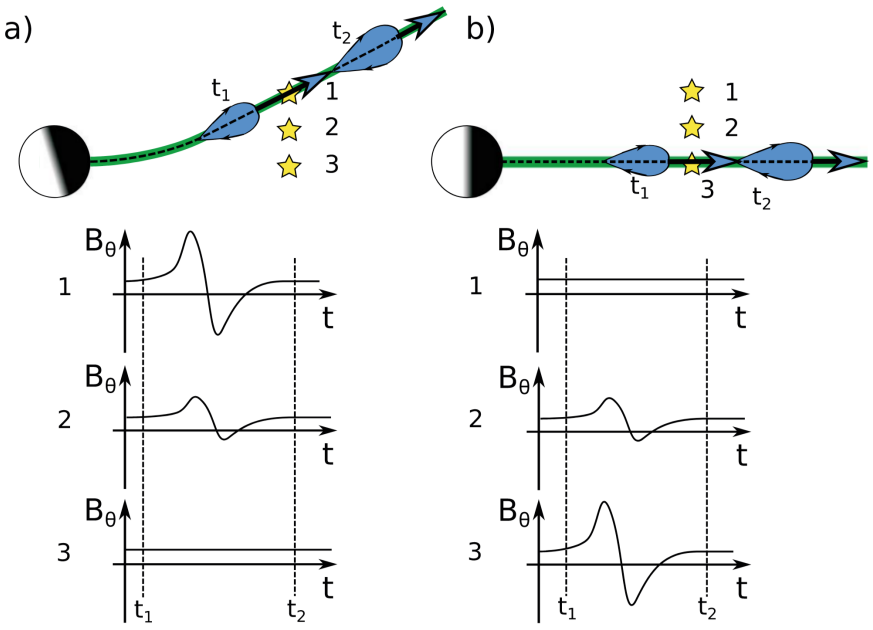

FIGURE 2.13: Schematic showing idealised B_θ magnetometer deflections associated with a plasmoid passing over a spacecraft for three different spacecraft latitude positions (1, 2, 3) and two current sheet hinging scenarios (a and b). The current sheet is indicated by the black dashed line, the green region is the surrounding plasma sheet. A plasmoid is marked in in blue. [*Smith et al.* [2016]]

seconds. They found a statistical separatrix (shown in Figure 2.14) separating inward and outward flow direction using the sign of B_θ as a proxy for the flow direction and found that its radial distance varies with local time. They further examined their events for a periodicity of 2-3 days previous spotted in auroral polar dawn spots [*Radioti et al.*, 2008] and flow bursts [*Krupp et al.*, 1998; *Woch et al.*, 1998] that had been associated with the time scale of the mass loading and release processes via reconnection at Jupiter. They found this periodicity to only exist intermittently.

One particular study at Saturn, *Smith et al.* [2016], identified 2094 plasmoids, dipolarisations and TCRs across three years (2006/09/10) of magnetic field data from Cassini. Their criteria required a significant (relative to field variability) bipolar deflection of the B_θ signature. They found the approximate location of the x-line to be highly variable, unlike at Jupiter, suggesting the x-line dynamics may differ between these two environments. Despite this, a statistical separation between events moving in tailwards or planetwards direction was found between 20 and 30 R_S downtail in the premidnight sector. They also found events across all of the tail, and at a range of radial distances from 15 to over 60 R_S. An earlier study by *Jackman et al.* [2014a] found 69 plasmoids, 17 TCRs and 13 dipolarisations and examined them from a magnetic and plasma perspective. They also found a highly variable x-line location and also found that more events occurred on the dawn than the dusk flank. *Hill et al.* [2008] identified two plasmoids

with sufficient plasma fluxes to determine ion composition. They found the composition was largely by dominated water-group ions, originating from the inner magnetosphere.

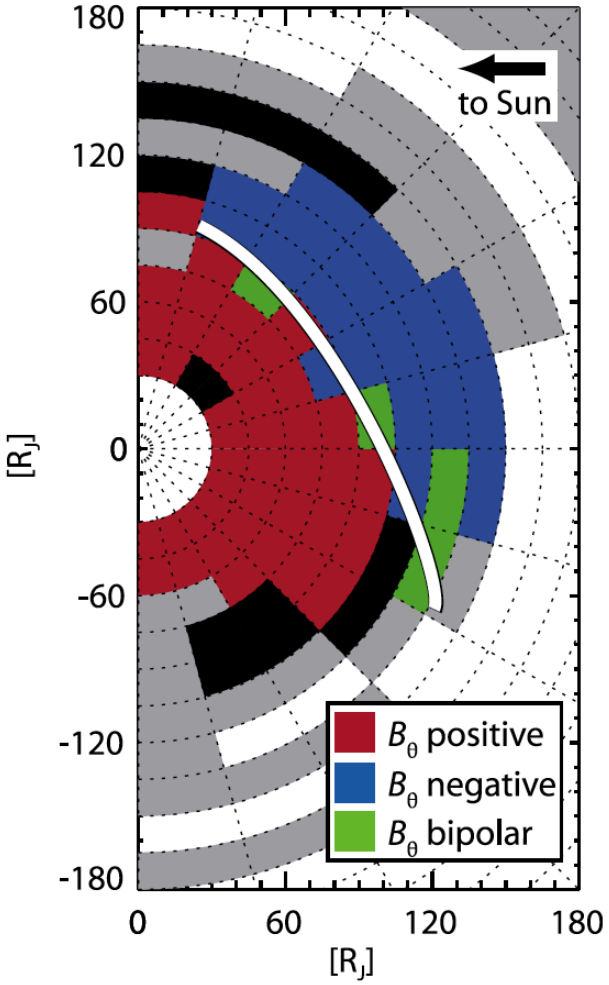

FIGURE 2.14: The distribution of the dominant B_θ signature of reconnection signatures detected by *Vogt et al.* [2010] using Pioneer, Voyager 1 & 2 and 7 years of Galileo data with the criteria described in the text. Red bins are positive most frequently, blue bins are negative most frequently, green bins are 'bipolar' most frequently. The white line represents a statistically derived separatrix, a potential x-line location. [*Vogt et al.* [2010]]

2.7.2 Mass Budget Problem

Over long timescales the mass flow into and out of the magnetosphere should be approximately equal. However, this is not observed to be the case at both Jupiter and Saturn. Various estimates of the mass loss down the Jovian magnetotail from large-scale magnetic reconnection and associated plasmoid ejection based on estimates of plasmoid recurrence rates and estimates of their mass have been made. These studies give a range of mass loss rates between 1 and 120 $kg\ s^{-1}$ [*Bagenal*, 2007; *Kronberg et al.*, 2008b; *Vogt et al.*, 2014] compared to the $\sim$500 $kg\ s^{-1}$ estimated to go in. Similar studies at Saturn

have found mass loss rates of ∼2.59 - 34 $kg\ s^{-1}$ [*Jackman et al.*, 2014b; *Thomsen et al.*, 2014] compared to the ∼ 100 $kg\ s^{-1}$ mean source rate from Enceladus.

Plasmoid volumes used for the above mass budget calculations are based on several assumptions. In the aforementioned works the downtail length was determined by the product of the plasmoid duration (inferred from the B_θ deflection in the magnetometer data) and its downtail velocity (from the plasma flow data). The plasmoid height is assumed to be comparable with the thickness of the plasma sheet. In reality plasmoids form a localised bulge in the plasma sheet and are thus thicker by a perhaps a factor of two. In *Vogt et al.* [2014] the azimuthal width of the plasmoid was assumed to be 2 - 3 hours of local time (45 - 70 R_J) at a mean radial distance of ∼ 90 R_J based on where plasmoids were observed. This width equates to 10 - 30 % of the total tail width of 240 - 340 R_J [*Joy et al.*, 2002], thus in principle the plasmoid widths could be 3 - 10 times larger. However, it is unclear whether plasmoids could be coherent over such distances. Though the length is the best constrained of these dimensions, from single spacecraft data it is difficult to accurately constrain any of these values. In comparison, at Earth, multiple spacecraft allow a high number of and simultaneous measurements to be taken in different locations to constrain the various dimensions. *Slavin et al.* [1993b] found based on measurements of TCRs that the mean plasmoid height (15 R_E) is approximately two times larger than the typical current sheet thickness (7 R_E) while *Kiehas et al.* [2013] found that flux ropes may be spatially confined in the dusk-dawn direction and do not extend across the entire tail.
Some minor uncertainties to plasmoid mass may be introduced by the assumptions that are made regarding the composition of the plasmoids. For example, the spatial variation of density within the plasmoid with respect to the single spacecraft location may lead to an over- or under- estimate of the density depending on the trajectory. As well as this, the particle mass requires an assumption about the composition of the plasma. At Jupiter, *Kronberg et al.* [2008b] assumed that particles had a number density of 0.025 and a particle mass of 16 proton masses (m_p) whilst *Bagenal* [2007] and *Vogt et al.* [2014] used a number density of 0.01 and a particle mass of 20 m_p. The uncertainties introduced by varying assumptions about composition are minor relative to the assumptions made regarding the dimensions of the plasmoids, but nonetheless may contribute to the overall uncertainty.

The frequency of events is also difficult to measure accurately since many events may be missed at Jupiter or Saturn when the spacecraft is not within some 'viewing region'. This can occur when the spacecraft is outside of the magnetopause, the event is too far from the spacecraft to be observed or the event is too small to be detected. For example, *Vogt et al.* [2010], discussed above, defined an event as a deflection in B_θ greater than twice the average background field or three times if the background field was less than 5 nT.

There may be plasmoids which fall below this observational threshold and which could contribute to the overall mass budget, particularly if they occur in sufficient numbers.

At Earth, *Slavin et al.* [1993b] used data from a single spacecraft ISEE 3 and found that a typical plasmoid mass at Earth is ∼280 kg and that the plasmoid rate could be as high as one per hour. This gave a mass loss rate of ∼0.078 $kg\ s^{-1}$. Earlier studies had calculated the mass input from the solar wind between 0.17 and 1.7 $kg\ s^{-1}$. Thus the estimated mass input and output rates could agree within a factor of 2 for the Earth. At first glance this factor does not seem drastically different than the imbalance found at Jupiter or Saturn (factor of $\sim$ 3 or 4) yet it is not seen as a "mass budget problem". There is a key difference to consider though. In the magnetospheres of Jupiter and Saturn, the role that this mass plays is much more significant than at Earth, which is principally driven by the interaction with the solar wind. As discussed in this chapter, the Vasyliunas cycle driven by the mass loading of rapidly rotating field line who stretch down tail and break is the dominant driver of dynamics at Jupiter and Saturn, so understanding how much mass is being added and how this mass is being lost is much more important for the understanding of these magnetospheres. At Earth the mass content and flow is not as important as the solar wind in the dynamics of the magnetosphere.

To account for the observed mass imbalance various other forms of mass loss have been suggested such as mass loss in the far tail, mass loss through planetary wind and a small scale quasi-continuous "drizzle" [*Bagenal*, 2007]. A recent study by *Cowley et al.* [2015] suggested that previous estimates of plasmoid length based on their duration (for example from peak-to-trough of B_θ) was incorrect and only represented a small fraction of the plasmoid structure that the spacecraft observed. Based on timescales between large-scale plasmoid release, ∼15 hours and ∼45 hours at Jupiter and Saturn respectively, mass-loaded flux tubes will have stretched on the order of a few hundred planetary radii downtail and are an order of magnitude larger than previous estimates would suggest. This picture would no longer require the additional hidden small scale mass loss processes. The proposed scenario invokes plasmoid lengths that exceed Cassini and Galileo's downtail exploration distance and thus cannot be fully tested with our available observations.

The topic of mass transport and loss will be discussed in detail in Chapter 4 via the application of a novel sandpile modelling approach to characterise the key elements of the Jovian system.

2.8 Radio Emissions

In this section we will discuss in detail the Saturn Kilometric Radiation (SKR), which is a central focus of chapters 5 and 6, before briefly describing the main radio emissions observed at Jupiter and Saturn.

2.8.1 Electromagnetic Waves

Before discussing the various radio emissions, this subsection will briefly outline the five main types of wave mode that will be discussed in this thesis and later chapters.

- Ordinary (O) mode: A superluminous electromagnetic wave. Its wave vector, **k**, is perpendicular to the magnetic field vector, **B**. It is linearly polarised in that **E** is parallel to **B**. It is ordinary in the sense that its propagation is the same as in an unmagnetised plasma.
- Extraordinary (X) mode: A superluminous electromagnetic wave. Like the O-mode wave, its wave vector, **k**, is perpendicular to the magnetic field vector, **B**. It is a superposition of the O-mode and a wave with **E** perpendicular to **B**.
- R mode: A superluminous electromagnetic wave. Its wave vector, **k**, is parallel to the magnetic field vector, **B**. It is right-hand circularly polarised.
- L mode: A superluminous electromagnetic wave. Its wave vector, **k**, is parallel to the magnetic field vector, **B**. It is left-hand circularly polarised.
- Z mode: A slower than light wave which is a low frequency branch of the X-mode.

Wave modes can be mixtures of the perpendicular and parallel propagating modes described giving oblique propagation. The R-X and the L-O modes are able to escape a magnetosphere because there is no upper-limit to their dispersion curves unlike, for example, the L-X mode which cannot propagate above the plasma frequency without a mode conversion. A mode conversion can occur when a wave reaches some interface at an non-zero angle. For example, when a longitudinal (direction of propagation and displacement of the medium are parallel) wave impacts on a boundary, some of the energy can cause particle movement in the transverse direction, creating a transverse wave. It is via this mechanism that the narrowband emission, discussed in chapter 6, is thought to be created via the mode conversion of Z-mode to L-O-mode emissions at a density gradient.

2.8.2 Saturn Kilometric Radiation

The Saturn Kilometric Radiation is a non-thermal radio emission generated by the cyclotron maser instability in the auroral regions of Saturn originally detected by Voyager 1 [*Kaiser et al.*, 1980]. The typical frequency range is from 3 kHz to 1.2 MHz, peaking between 100 and 400 kHz [*Kaiser and Desch*, 1984; *Lamy et al.*, 2008]. A spectrogram showing 10 days of SKR measured by Radio Plasma Wave Spectrometer (RPWS) aboard Cassini is shown in figure 2.15. This figure also shows an examples of low frequency extensions (LFE) an extension of the main band emission down to lower frequencies. These phenomena will be discussed further in chapter 5.

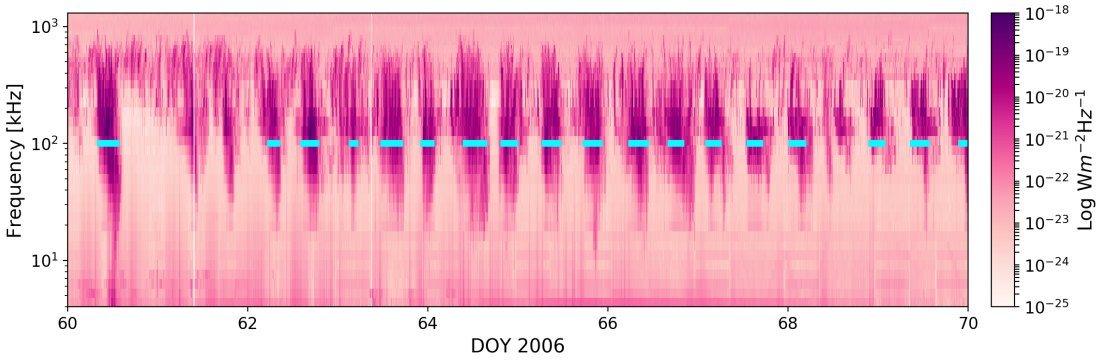

FIGURE 2.15: DOY 60 - 70 2006 of SKR. There are three main features on this spectrum. The CMI generated quasi-continuous 'main band' between 100 and 400 kHz, the 'narrowband', below $\sim$ 40 kHz and low frequency extensions the intense extensions of the main band down to lower frequencies highlighted in cyan.

The SKR is generated via the cyclotron maser instability (CMI) which was first proposed as a mechanism for planetary radio emissions by *Wu and Lee* [1979] and later confirmed to be the generator of the SKR by several other studies [*Lamy et al.*, 2010, 2011; *Mutel et al.*, 2010; *Menietti et al.*, 2011] and is associated with magnetospheric electrons near the auroral regions. When the plasma is sufficiently sparse in the source region, where the local electron plasma frequency, f_{pe}, is less than the electron gyrofrequency, f_{ce}, and unstable electron distributions are present, CMI waves in the extraordinary (X) mode are emitted by electrons that fulfil the resonance equation:

$$f = f_{ce}/\Gamma + k_{\|} v_{\|}, \tag{2.1}$$

where f is the frequency of the emission, **k** is the wave vector, **v** the electron velocity, f_{ce} is the electron gyrofrequency and the subscript $\|$ refers to the projection of the wave vector and electron velocity in the direction parallel to the magnetic field, and $\Gamma = 1/\sqrt{1 - v^2/c^2}$ is the Lorentz factor [*Wu and Lee*, 1979]. The frequency of the emission is close to its low-frequency cutoff frequency $\approx f_{ce}$. *Lamy et al.* [2010] showed the difference between the SKR emission frequency and the local electron cyclotron frequency to be

less than 2%. The waves are emitted in directions quasi-perpendicular to the local magnetic field direction at the source and the emission therefore takes the form of a hollow cone (figure 2.16) the axis of which is aligned with the local magnetic field. This results in strong variations in visibility of the SKR dependent on observer location as shown in figure 2.17. Since the coupling in the CMI is with the electrons, the X-mode emission is right-handed circularly polarised (R-X) with respect to the magnetic field (i.e. the electric field vector rotates in the same sense as the gyro motion of an electron). Specifically, the SKR generated in the northern hemisphere is right-handed whilst the SKR generated in the southern hemisphere is left-handed [*Warwick et al.*, 1982]. SKR can also be produced on the O-mode (a linearly polarize) with purely left-handed (LH) polarization (L-O), although the R-X mode emissions are more intense. The RPWS instrument has the capability to differentiate between LH and RH polarization enabling us to know which hemisphere the emissions are coming from.

The SKR is emitted at close to the cyclotron frequency at the source which is proportional to the strength of the local magnetic field and is therefore inversely proportional to the height of the source. As such, using an internal magnetic field model by *Dougherty et al.* [2005], *Kimura et al.* [2013] showed that the peak emission of the SKR (between 100 and 400 kHz) originates from sources between 0.5 and 1.5 R_S from the planet. The SKR can extend down to 10 kHz or below, which equates to a source region at 5 R_S from the planet or further.

Figure 2.18 shows the spatial distribution of SKR sources found by *Lamy et al.* [2010] using a direction finding method detailed in *Cecconi and Zarka* [2005a]. For each time-frequency measurement of the SKR, the RPWS antenna provides a wave vector, **k**. Assuming a transverse wave and point source, using the Saturn Pioneer Voyager (SPV) magnetic field model [*Davis and Smith*, 1990] and simple current sheet [*Connerney et al.*, 1983] the intersection of each wave vector, **k**, with the iso-surface where f = f_{ce} was found. *Cecconi et al.* [2009] determined the three dimensional source of SKR during one periapsis pass of Saturn by Cassini and found that the SKR sources are located on field lines mapped to the ionosphere between ∼70 - 80° latitude, consistent with the mean location of the main UV and IR auroral oval, and 0400 to 1600 local time range. They also found that the sources are several degrees latitude higher in the southern hemisphere than in the north. The final Cassini orbits close to the planet performed whilst this thesis was being written are looking to probe the SKR source region in more detail.

An important feature of the SKR emission is a strong local time asymmetry in the power of the SKR sources. It has been shown from direction finding methods such as those above [*Farrell et al.*, 2005; *Cecconi et al.*, 2009] that SKR emission sources are

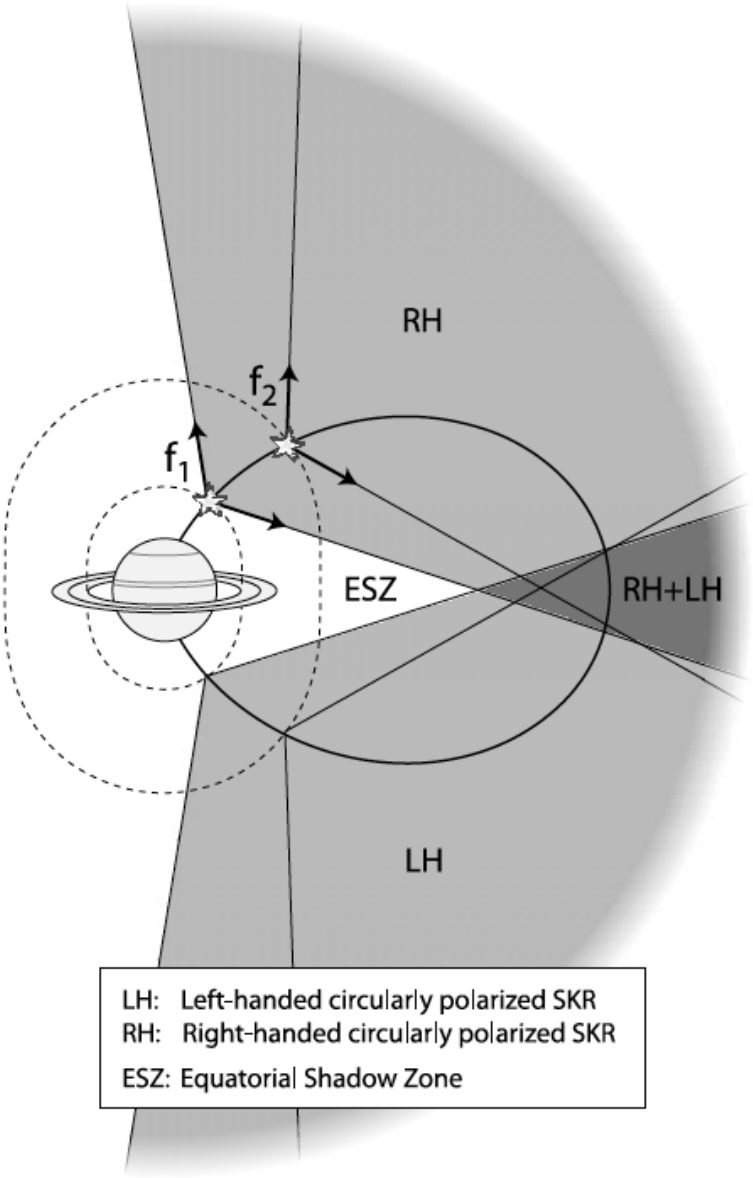

FIGURE 2.16: Sketch of the equatorial shadow zone generated by hollow cone radio beaming. Two stars represent radio sources at two frequencies (f1 and f2) along the same magnetic field line (solid line). The altitude of the sources is fixed by the magnetic field intensity, each source being at the intersection of the magnetic field line and of the iso-contour corresponding to f = f_{ce} (dashed lines), the cyclotron emission frequency. Radio emission is beamed along a hollow cone (black arrows). The shaded regions show the possible 3D distribution of radio sources over a range of longitudes, but radio emission remains excluded from a near-equatorial shadow zone whose shape and extent depend on the detailed source locations and on the beaming angle as a function of frequency. [*Lamy et al.* [2008]]

broadly distributed around a circumpolar oval but the strongest of the SKR emissions are those generated post-dawn between 06 and 11 hours local time [*Lamy et al.*, 2009]. The mechanism behind this will be discussed in the next section.

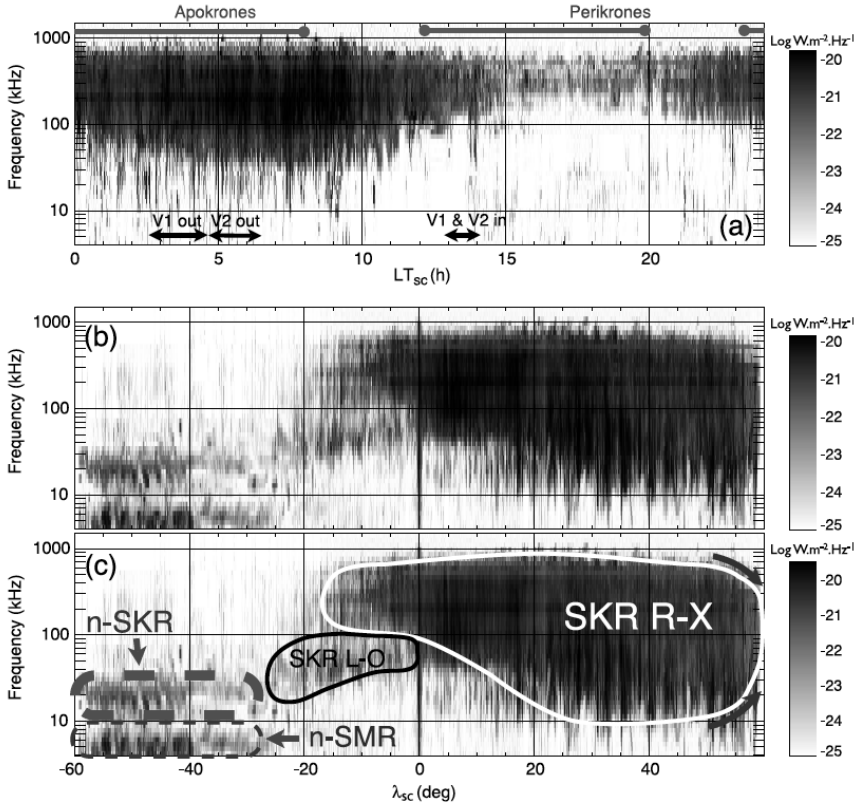

FIGURE 2.17: The SKR visibility is highly variable as a function of both spacecraft latitude and local time. Panel (a) shows the 50% occurrence level of the SKR flux density of highly polarised (V > 0.8) as a function of spacecraft local time and frequency. Panel (b) and (c) again show the 50% occurrence level of SKR, this time as a function of spacecraft latitude and frequency. Panel (c) has the addition of contours emphasising the various components identified on the dynamic spectrum. R-X dominant SKR corresponds to the white contour, n-SMR and n-SKR to the dashed grey contours. The black contour indicates an LF component detected between -25° and 0° of latitude, whose characteristics are compatible with L-O mode emission, and which has a visibility different from R-X mode. [*Lamy et al.* [2008]]

Early work found strong correlation of SKR power with variations of the solar wind. *Desch* [1982] found a strong correlation between solar wind ram pressure and SKR intensity in Voyager 1 and 2 data, whilst later analysis by *Desch and Rucker* [1983, 1985] also found a correlation with solar wind momentum and kinetic energy. *Desch* [1983] found further evidence of this strong solar wind dependence where the SKR was found to 'stop' completely when Saturn was passing through the magnetotail of Jupiter and so was shielded from the solar wind. Work by *Taubenschuss et al.* [2006] found that four solar wind quantities have an influence on the SKR intensity with a similar efficiency ($\sim$ 50 - 60 %) but each with a different lag time. The solar wind bulk velocity has a lag of $\sim$52 hours, $\sim$ 13 hours for the ram pressure, $\sim$30 hours for the y-component of the interplanetary magnetic field and greater than 40 hours for the interplanetary magnetic field strength. *Zarka et al.* [2007] noted a correlation between the solar wind dynamic pressure.

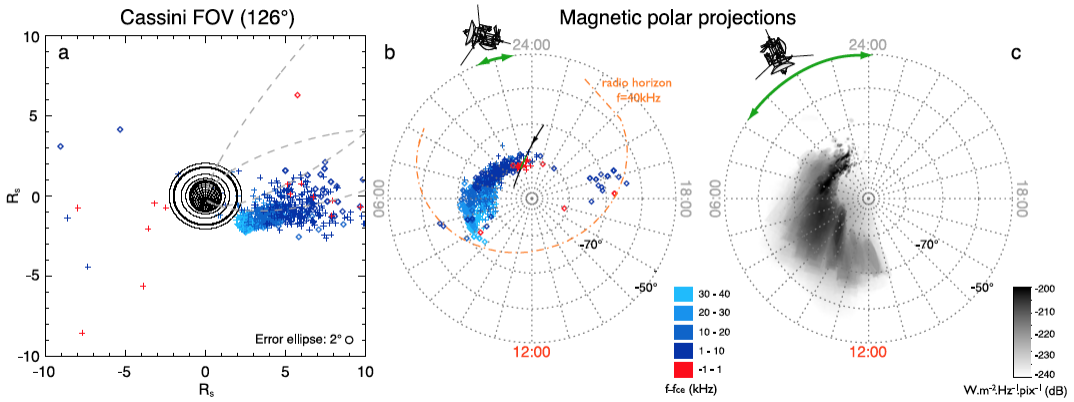

FIGURE 2.18: (a) Location of radio sources in Cassinis field of view (FOV) and (b) magnetically projected down to the planet. (c) Radio map [*Lamy et al.*, 2009] integrated along the extended time interval [0700,1100] UT and frequency range [7,1000 kHz]. [*Lamy et al.* [2010]]

Several works have looked at the response of the SKR to tail reconnection. *Jackman et al.* [2009a] showed a correlation between the occurrence of reconnection in the tail and the extension of the SKR spectrum to lower frequencies, finding that 8 out of 9 by-eye-selected reconnection events had a corresponding extension of the SKR. This study was expanded upon as part of this thesis and will be discussed in chapter 5 which investigates the use of the SKR as a proxy for magnetospheric dynamics.

2.8.3 Radio Emissions at Jupiter

As at Saturn, there are radio emissions from Jupiter's magnetosphere formed via the cyclotron maser instability. The emission band is grouped into several components:

- The narrowband component, nKOM, with frequencies $< \sim 200\ kHz$, originating from the Io plasma torus [*Reiner et al.*, 1993], with a periodicity of ∼10 hours [*Louarn et al.*, 2007].
- The broadband kilometric radiation, bKOM, at frequencies $< 1\ MHz$, originating from high-latitude field lines and showing a rotational modulation [*Ladreiter et al.*, 1994]
- The hectometre component, HOM, between ∼300 kHz - few MHz, originating from high-latitude field lines that pass through the outer edge of the Io plasma torus [*Ladreiter et al.*, 1994; *Zarka et al.*, 2001]
- The decometric components, Io-DAM and non-Io-DAM, with frequencies up to 40 MHz. The non-Io-Dam originates from field lines which thread Io's dense plasma

wake. The exact source of the non-Io-Dam is currently uncertain [*Zarka et al.*, 2001, 2004].

In recent years the radio community has focussed heavily on the wealth of Saturn radio data from Cassini, but there are several notable papers on Jupiter: *Louarn et al.* [2007] who associated energy release events within the tail with enhancements of the flux in the HOM emission and the appearance of nKOM emissions and *Hess et al.* [2014] who looked at the triggering of radio emissions by solar wind shocks. Given that Juno is currently at Jupiter and that Jovian radio emissions can also be detected by ground-based telescopes including the LOFAR and SKA observatories, it is expected that Jovian radio science will flourish in the coming years.

2.9 Saturn's Planetary Period Oscillations

Having discussed the SKR in the previous section, this section will discuss the periodic phenomena that have been observed at Saturn and how the SKR has been used to organise these phenomena.

2.9.1 Periodicities

The gas giant planets Jupiter and Saturn have no fixed visible surface features that allow their rotation periods to be tracked. At Jupiter [*Zarka and Genova*, 1983] the peaks in the auroral radio emission are fixed in period and related to the rotation of the planet. At Saturn this isn't the case, where the periodicity of regularly pulsed SKR (initially believed to be linked to the rotation of the internal field) was found to have changed significantly between the measurements by Voyager [*Desch and Kaiser*, 1981] and those of Ulysses and Cassini 20 years later [*Galopeau and Lecacheux*, 2000; *Gurnett et al.*, 2005] as shown in figure 2.19. This change was too large to be due to a change in the rotation of the deep interior [*Gurnett et al.*, 2007] and as such at the time of writing (January, 2018) the true rotation rate of Saturn is unknown. Unlike at Jupiter, where the misalignment of the rotational and magnetic axis of the planet (usually found in planets with a dynamo generated magnetic field) gives rise to the modulation in the radio emissions, at Saturn the magnetic field is highly symmetrical with a degree of separation of $<<1^\circ$ between the two axes. Therefore, this cannot be the cause of the modulation. The proximal orbits performed by Cassini in the second half of 2017 where the spacecraft's periapsis is within 1 R_S of the planet may allow the detection of higher-order asymmetries that were not previously visible (due to a postulated sub-surface conducting layer that shielded

these terms [*Stevenson*, 1982]) and may help further understand the true rotation rate of the planet.

Despite this (observed) highly symmetrical magnetic field, periodicities on the order of what was believed to be the planetary rotation period have been found in many magnetospheric phenomena at Saturn. As well as in the SKR, periodicities have been observed in the plasma density in the inner [*Gurnett et al.*, 2007] and outer region [*Burch et al.*, 2008, 2009; *Arridge et al.*, 2008c; *Morooka et al.*, 2009; *Jackman et al.*, 2009b] of the magnetosphere, in enhancements of energetic electron and neutral atom fluxes [*Paranicas et al.*, 2005; *Carbary et al.*, 2008, 2009] and in the flapping of the tail current sheet [*Khurana et al.*, 2009; *Arridge et al.*, 2011]. Other work has also observed periodicities in auroral hiss [*Gurnett et al.*, 2009], in ultraviolet auroral emission [e.g. *Provan et al.*, 2009b; *Nichols et al.*, 2010] and in the location of the magnetopause [*Clarke et al.*, 2006, 2010a,b].

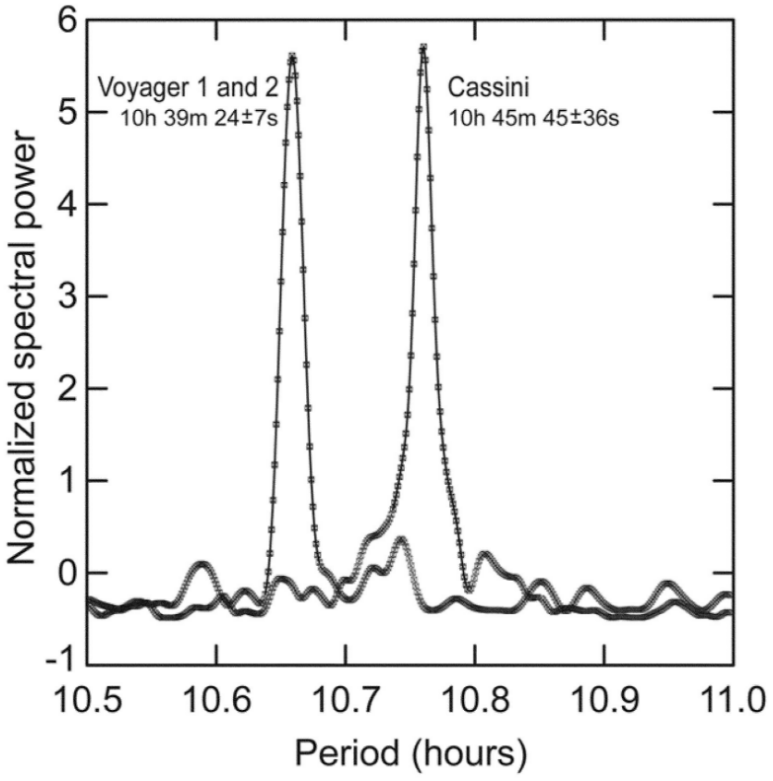

FIGURE 2.19: A comparison of the power spectrum of variations in the SKR intensity as measured by Voyager and Cassini. The Cassini spectrum was accumulated over an interval of a little more than 1 year during the approach to Saturn, from 29 April 2003 to 10 June 2004. The radio modulation period measured by Cassini, 10 hours 45 min 45 36 s, has shifted substantially from the Voyager era in 1980 to 1981. [*Gurnett et al.* [2005]]

In light of this, several works have characterised the SKR periodic variability in order to develop a Saturn Longitude System (SLS) to organise these phenomena. The first SLS was derived using Voyager radio data by first *Kaiser et al.* [1980] and later *Desch*

and Kaiser [1981] before the variability of the periodicity was known. This system had a period of 10.6650 hours, later revised to 10.6567 hours. SLS2 [*Kurth et al.*, 2007] was based on analysis of SKR data from day 1 2004 to day 240 2006 (extended to day 222 2007 for SLS3 [*Kurth et al.*, 2008]) fitting the period as a function of time to a third-order (fifth-order for SLS3) polynomial. The SLS3 analysis revealed a second periodicity of ∼10.8 hours. Further analysis of the SKR led to the realisation that these two periodicities existed at the same time and that the longer period, ∼10.8 hours, was associated with the southern hemisphere, and the shorter period, ∼10.6 hours, was associated with sources in the northern hemisphere [*Gurnett et al.*, 2009]. This eventually led to the development of the SLS4 system which had a northern and southern component [*Gurnett*, 2011]. Later in this thesis (Chapter 5) we use a phase system derived by *Lamy* [2011]. They used Lomb-Scargle analysis, a technique employed to perform spectral analysis of non-continuous data, over a 6-year period from 2004 to 2010 to find the SKR period and related phase systems for each hemisphere. As discussed in the previous section with regards to the SKR power, the SKR period has been shown to change over a wide range of timescales, both short and long. *Zarka et al.* [2007] noted a correlation between the solar wind dynamic pressure and variation of the SKR periodicity of ∼1% over a period of 20 - 30 days. The season of the planet also has a long term effect on the period of the SKR [*Galopeau and Lecacheux*, 2000; *Kurth et al.*, 2008; *Gurnett et al.*, 2009, 2010; *Gurnett*, 2011; *Cowley and Provan*, 2016], for example the shorter northern and longer southern SKR period converged leading up to the 2009 Saturn equinox. The dual periodicities are due to different ionospheric conductivities in the summer versus the winter hemisphere [*Gumett et al.*, 2009].

2.9.2 Perturbation Current Systems

Analysis of magnetic field data revealed periodic perturbations in the various components. The perturbation takes the form of a wave propagating radially outwards from the planet. The magnetic perturbation is associated with two hemispheric rotating current systems (northern and southern (shown in figure 2.20)) that flow into the planet's ionosphere. There is a third 'fixed' current system associated with subcorotation of plasma within Saturn's magnetosphere (such as that described at Jupiter earlier in this section). As the two rotating current systems rotate, they constructively and destructively superpose with the fixed field aligned currents giving rise to the observed magnetic perturbations. As with the SKR, the magnetic perturbations have been organised into a northern and southern magnetic phase system [*Provan et al.*, 2009a; *Andrews et al.*, 2010b]. At 0° the perturbation field points towards the Sun, moving through 360° through dusk, midnight then dawn. *Jackman et al.* [2016] examined the dependence

of plasmoid occurrence on the phase of these magnetic phase systems by comparing a catalogue of 65 plasmoid events detected in 2006 [*Jackman et al.*, 2014a] to the northern and southern magnetic phase systems. They found that the events preferentially occurred for phases associated with the outward displacement of the plasma when the two magnetic systems are in anti-phase [*Burch et al.*, 2009; *Clarke et al.*, 2010a,b; *Hunt et al.*, 2014, 2015], and when the current sheet is thinned, again when the northern and southern magnetic phase systems are in anti-phase [*Provan et al.*, 2012].

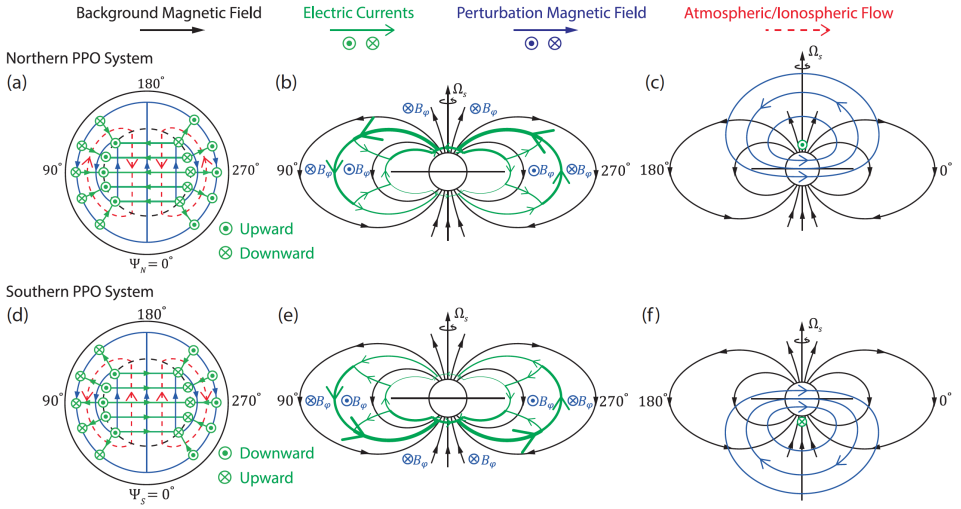

FIGURE 2.20: Sketches showing the northern (top row) and southern (bottom row) PPO current systems and field perturbations. Line format is give at the top of the figure. (a) and (d) show the northern and southern ionosphere, both viewed from the north, the currents, field perturbations and atmospheric flows to drive such a current system are shown. (b) and (e) show the current systems in the $\Psi_{N,S}$ = 90- 270° meridian plane (where Ψ is the respective magnetic phase), together with the direction of the field perturbations. (c and f) illustrate in the $\Psi_{N,S}$ = 0- 180° meridian plane the northern and southern perturbation fields associated with the current systems.[*Hunt* [2016]]

The modulation of the SKR is driven by these rotating current systems. As the current systems sweep around the planet, they pass through the SKR source regions located on the auroral ovals causing the emission at that location to periodically intensity. The strongest SKR sources are found in the postdawn to prenoon sector [e.g. *Lamy et al.*, 2008, 2009]. In *Southwood and Kivelson* [2009], they describe a region of increased field aligned currents due to magnetic shear from a viscous interaction between the solar wind and magnetosphere. Thus it may be that the observed modulation of the SKR comes from the rotation of upward field aligned currents associated with each hemisphere current system through this region. This led to the prediction that SKR modulations should be strobe-like in a wide local time sector from post-midnight to noon via dawn dominated by the post-dawn sources. This was later confirmed by *Lamy et al.* [2011, 2013] which describes an active region (> 90° wide) passing through the dawn

sector. During the pre-equinox interval various work [e.g. *Andrews et al.*, 2008, 2010a; *Provan et al.*, 2009a, 2011] found excellent agreement with SKR and magnetic period and phasing such that SKR maxima in each hemisphere occurred when the upward field-aligned current of the corresponding rotating current system is located in the dawn sector near where the most intense SKR sources lie, consistent with the above discussion. During equinox and post-equinox this picture has become less clear and is a current area of debate [e.g. *Andrews et al.*, 2011; *Fischer et al.*, 2015; *Cowley and Provan*, 2016].

Chapter 3

Instrumentation

3.1 Introduction

The work in this thesis uses a variety of data and data products. Chapter 4 refers to a catalogue of reconnection events detected in Jupiter's magnetosphere using magnetometer data from Voyager 1 and 2, Pioneer 10 and Galileo. Chapter 5 uses radio emissions detected at Saturn by Cassini, a catalogue of reconnection events found in Cassini magnetometer data and the output of a solar wind propagation model where solar wind conditions at the orbit of Earth are propagated out to the orbit of Saturn. This chapter will first give a brief overview of the various spacecraft missions before discussing the different types of instrumentation used and how they operate.

3.2 Spacecraft Missions

Figure 3.1 shows sunspot number versus time from 1970 - 2010 with the various spacecraft that have visited Jupiter and Saturn marked. This section will first briefly discuss the earlier fly-by missions of Voyager 1 and 2 and Pioneer 10, followed by the more recent dedicated orbiters of Galileo and Cassini in more detail.

3.2.1 Pioneer 10 and 11

The Pioneer missions were intended as trailblazers to the subsequent Voyager missions. Prior to the Pioneer missions, no spacecraft had ventured further than the asteroid belt between Mars and Jupiter. Pioneer 10 and 11 were launched in spring 1972/73 respectively and flew past Jupiter in November and December 1972/73 respectively.

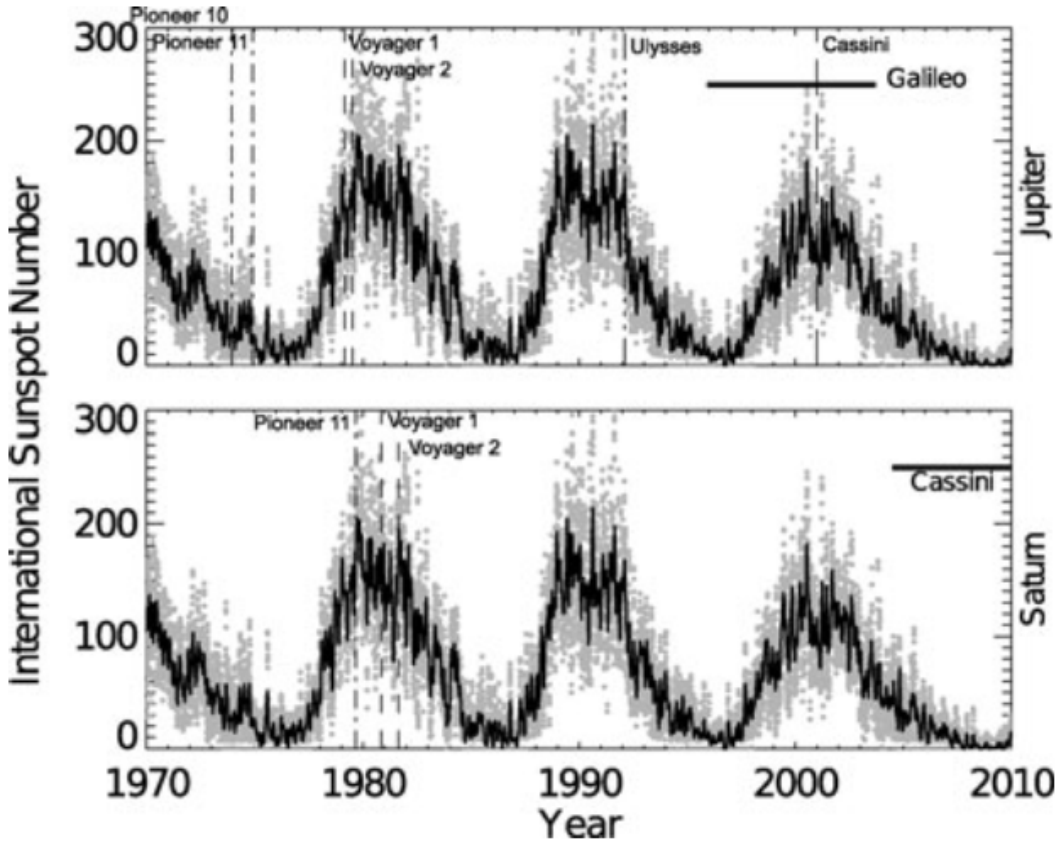

FIGURE 3.1: Sunspot number from 1970 2010. The top and bottom panel shows the timings of the closest approach to Jupiter and Saturn respectively of several fly-by spacecraft. The time spent by the two dedicated orbiters, Galileo and Cassini are also shown by the solid horizontal black lines. The grey dots show the daily sunspot numbers (from SIDC), while the black traces show the solar-rotation smoothed values. [*Jackman and Arridge* [2011]]

Contact was lost with Pioneer 11 in the mid-nineties. Pioneer 10 continued until January 2003 when contact was lost due to loss of power to its radio transmitter. It was 80 AU from Earth at the time.

3.2.2 Voyager 1 and 2

In *Pale Blue Dot*, Carl Sagan wrote that "Voyager 1 and 2 are the ships that opened the Solar System for the human species, trailblazing a path for future generations" and as of August 2017, Voyagers 1 and 2 are the furthest man-made objects from Earth and will remain so for some time. The two identical Voyager spacecraft each weighing 2 tons (over half of which was fuel) were launched in summer 1977. Their trajectories through the solar system, known as "The Grand Tour", were calculated as part of a summer project by Gary Flandro at Caltech in 1965 when he realised that the planets would be arranged in such a way in the 1980s to provide an opportunity to fly past all of the

planets with a single spacecraft. Voyagers 1 and 2 arrived at Jupiter in March and July, respectively, 1979.

3.2.3 Galileo

Named after the astronomer Galileo Galilei, the Galileo spacecraft consisted of an orbiter and entry probe. Work on the spacecraft began at Jet Propulsion Laboratory in 1977, while the Voyager 1 and 2 missions were still being prepared for launch and 12 years later, the 2.7 ton spacecraft was launched on the Space Shuttle Atlantis in October 1989. After three gravity assists, one from Venus and two from Earth, it reached Jupiter in December 1995. Over the next 8 years Galileo completed 34 orbits of Jupiter before plunging into Jupiter's atmosphere. Galileo's prime mission was a two-year study of the Jovian system. A variety of orbits, each of which lasted about two months, allowed Galileo to sample different parts of the planet's extensive magnetosphere. The orbits were designed for close-up flybys of Jupiter's largest moons. Once the prime mission concluded, an extended mission started on December 7, 1997; the spacecraft made a number of flybys of Europa and Io.

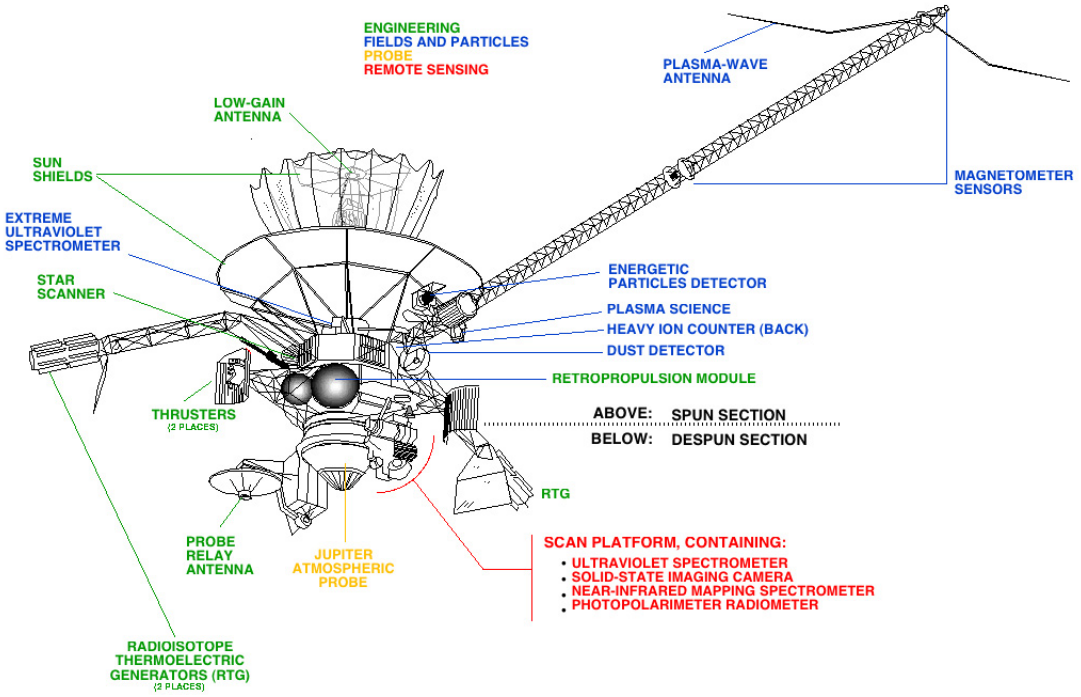

FIGURE 3.2: A Galileo spacecraft schematic and its onboard instruments. [Credit to Nasa]

The Galileo spacecraft is shown in figure 3.2. One section of the spacecraft (above the dotted line on figure 3.2) rotated at three rpm, keeping Galileo stable and holding

six instruments that gathered data from many different directions, including the fields and particles instruments. The other section of the spacecraft was an antenna, and data were periodically transmitted to it. The propulsion subsystem consisted of a 400 N main engine and twelve thrusters. The thrusters were mounted in groups of six on two 2-meter booms. The fuel for the system was 925 kg of monomethylhydrazine and nitrogen tetroxide. Two separate tanks held another 7 kg of helium pressurant. The propulsion subsystem was developed and built in West Germany, the major international partner in Project Galileo.

The science objectives of the Galileo Orbiter were numerous but can be summarised to the following:

- investigate the circulation and dynamics of the Jovian atmosphere;
- investigate the upper Jovian atmosphere and ionosphere;
- characterize the morphology, geology, and physical state of the Galilean satellites;
- investigate the composition and distribution of surface minerals on the Galilean satellites;
- determine the gravitational and magnetic fields and dynamic properties of the Galilean satellites;
- study the atmospheres, ionospheres, and extended gas clouds of the Galilean satellites;
- study the interaction of the Jovian magnetosphere with the Galilean satellites; and,
- characterize the vector magnetic field and the energy spectra, composition, and angular distribution of energetic particles and plasma to a distance of 150 R_J.

3.2.4 Cassini-Huygens

The Cassini-Huygens mission to Saturn consists of a two-part spacecraft. Its formal beginning was in June 1982, the project being a joint undertaking by the National Aeronautics and Space Administration (NASA) in the United States who supplied the Saturn orbiter, the European Space Agency (ESA) who supplied the Titan probe and the Italian Space Agency (ASI) who supplied the high gain antenna as well as other instruments for both the orbiter and the probe. The orbiter is named after the French/Italian astronomer Giovanni Domenico Cassini, who discovered several Kronian satellites and ring features

(including the famous Cassini division) in the period 1671-1685. The probe is named after the Dutch astronomer Christiaan Huygens who discovered Titan in 1655. The overall mission is managed by the Jet Propulsion Laboratory (JPL), Pasadena, California. Huygens operations were carried out by ESA from its European Space Operations Centre (ESOC) in Darmstadt, Germany.

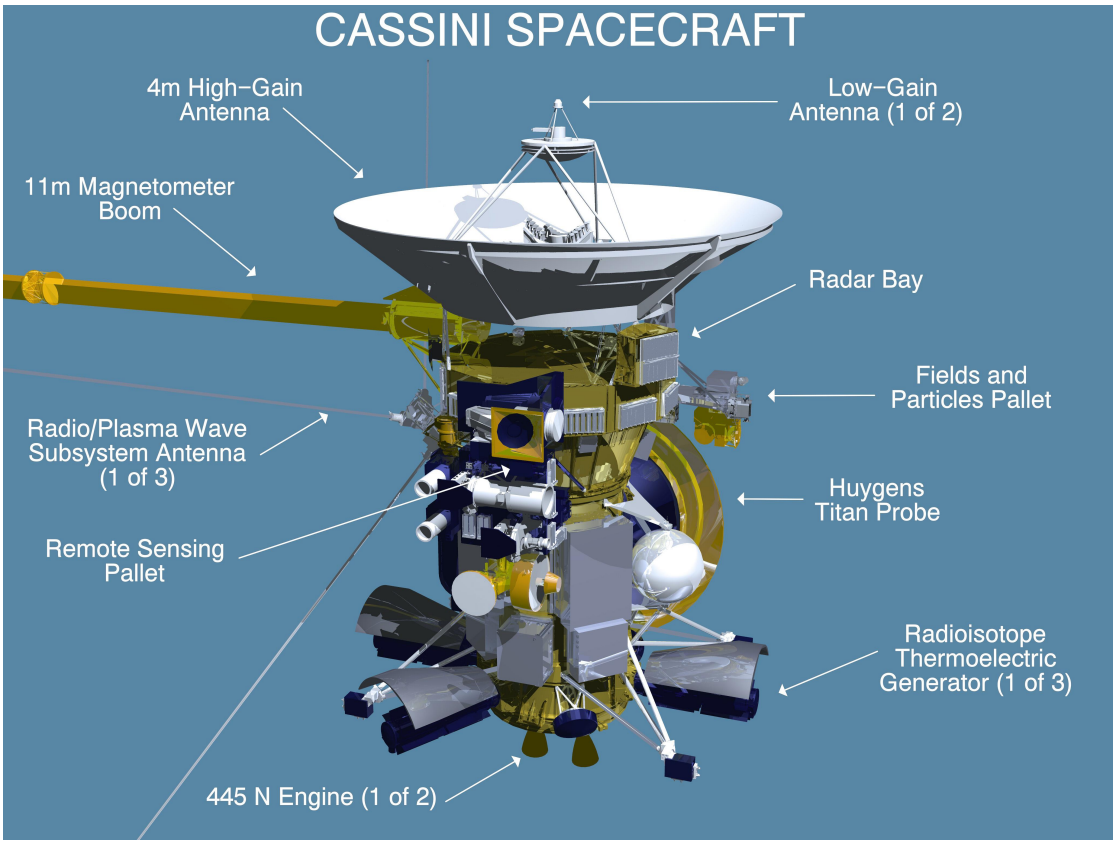

FIGURE 3.3: Diagram of the Cassini spacecraft showing the main components and several of the onboard instruments. [Credit to Nasa]

Cassini-Huygens was launched on 15 October 1997 from Cape Canaveral on its 7-year journey to Saturn arriving in June 2004. The vast distances involved and its large mass, meant the spacecraft could not be directly flown to Saturn. Consequently, two Venus swingbys, plus Earth and Jupiter gravity assists were necessary to accelerate the spacecraft toward Saturn, ∼1.3 billion km from Earth.

As shown in Figure 3.3, Cassini consists of several sections, all stacked vertically on top of each other. Most of the orbiter's scientific instruments are installed on one of two body-fixed platforms. These are called the remote-sensing pallet, and the particles and fields pallet. An 11-metre long boom supports sensors for the Dual-Technique Magnetometer (where two types of magnetometers are used, which will be discussed in section 3.3.1). At the top of the stack is the large, 4-metre-diameter high-gain antenna. Centred and

at the very top of this antenna is a relatively small low-gain antenna. Another low-gain antenna is located near the bottom of the spacecraft. These antennae are used for two-way communication through the Deep Space Network (DSN) via an X-band radio link. Electrical power for the Cassini spacecraft and instruments is provided by three Radioisotope Thermoelectric Generators (RTGs). RTGs provide power through the natural radioactive decay of plutonium (Pu-238). The heat generated by this process is then changed into electricity by solid-state thermoelectric converters. Cassini is a three-axis stabilized spacecraft (in contrast to for example Juno which is spinning). Either reaction wheels or the set of 0.5 N (Newton) thrusters can change the attitude of the spacecraft. Since the instruments are body-fixed, frequent attitude changes must be done in order to point them. Consequently, most of the spacecraft activities are made without a real-time communication link to Earth. All data are recorded on two solid-state recorders, each of which has a storage capacity of about two gigabits.

Cassini-Huygens has eighteen specially designed instruments, twelve on the orbiter and six on the Huygens probe. The list of science objectives for the mission is large, but can be categorised under five main headings: the planet itself, the rings, Titan, the icy satellites and the magnetosphere. The Saturn chapters of this thesis (5 and 6) focus primarily on the dynamics of Saturn's magnetosphere and the properties of Saturn Kilometric Radiation and as such some of the science objectives directly related to the magnetosphere and the SKR are listed below (the magnetometer objectives are also shown schematically in figure 3.4):

- Determine the configuration of the nearly axially symmetric magnetic field and its relation to the modulation of Saturn Kilometric Radiation (SKR).
- Investigate wave-particle interactions and dynamics of the dayside magnetosphere and the magnetotail of Saturn and their interactions with the solar wind, the satellites, and the rings.
- Improve our knowledge of the rotational modulation of Saturn's radio sources, and hence of Saturn's rotation rate.
- Determine the location of the SKR source as a function of frequency, and investigate the mechanisms involved in generating the radiation.
- Obtain a quantitative evaluation of the anomalies in Saturn's magnetic field by performing direction-finding measurements of the SKR source.
- Establish the nature of the solar wind-magnetosphere interaction by using SKR as a remote indicator of magnetospheric processes.

- Study the fine structure in the SKR spectrum, and compare with the fine structure of terrestrial and Jovian radio emissions in order to understand the origin of this fine structure.

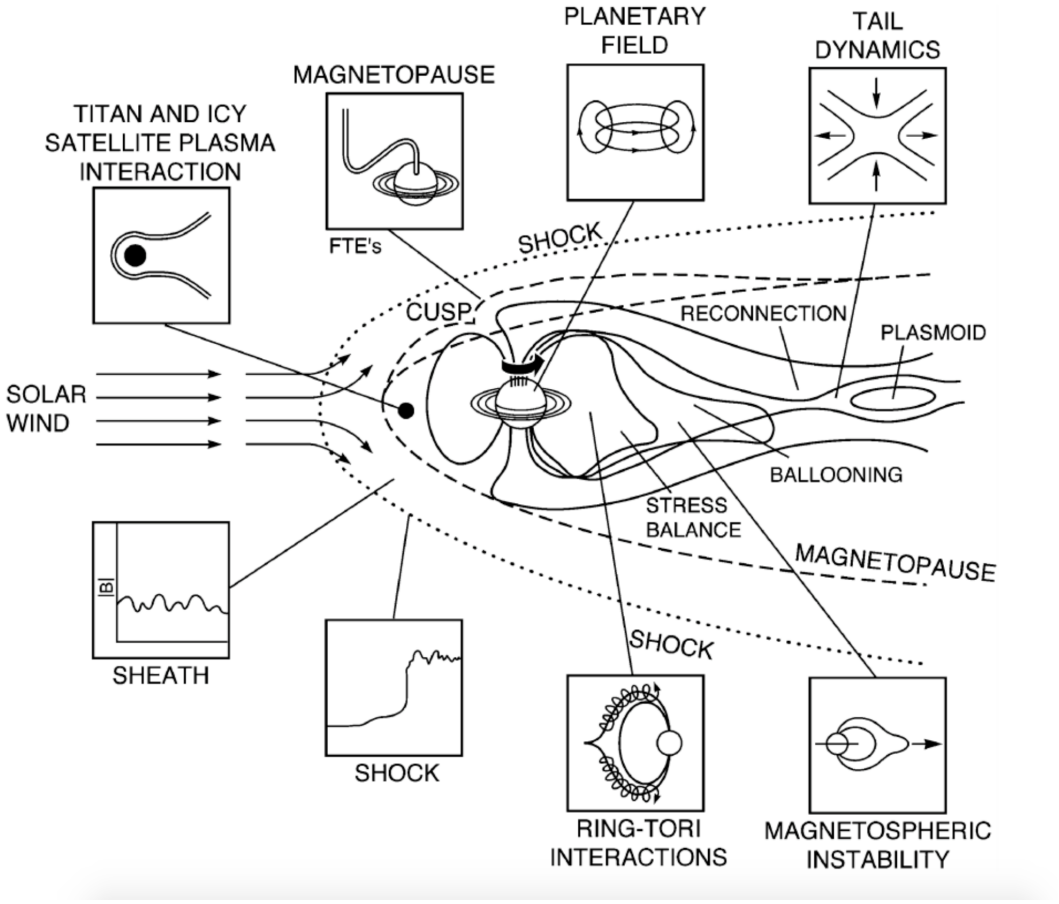

FIGURE 3.4: Schematic of Saturn's magnetosphere and magnetometer science objectives [*Dougherty et al.* [2004]]

3.3 Instrumentation and Data

This section will discuss the magnetometers found on the spacecraft used in this thesis, the instrument used for detecting the radio emission at Saturn and the mSWiM model that gives predicted solar wind conditions at the orbit of objects in the solar system.

3.3.1 Magnetometers

This section will outline the workings of several magnetometer types and which spacecraft they can be found on. The location of the magnetometer instruments on Cassini is shown in figure 3.5.

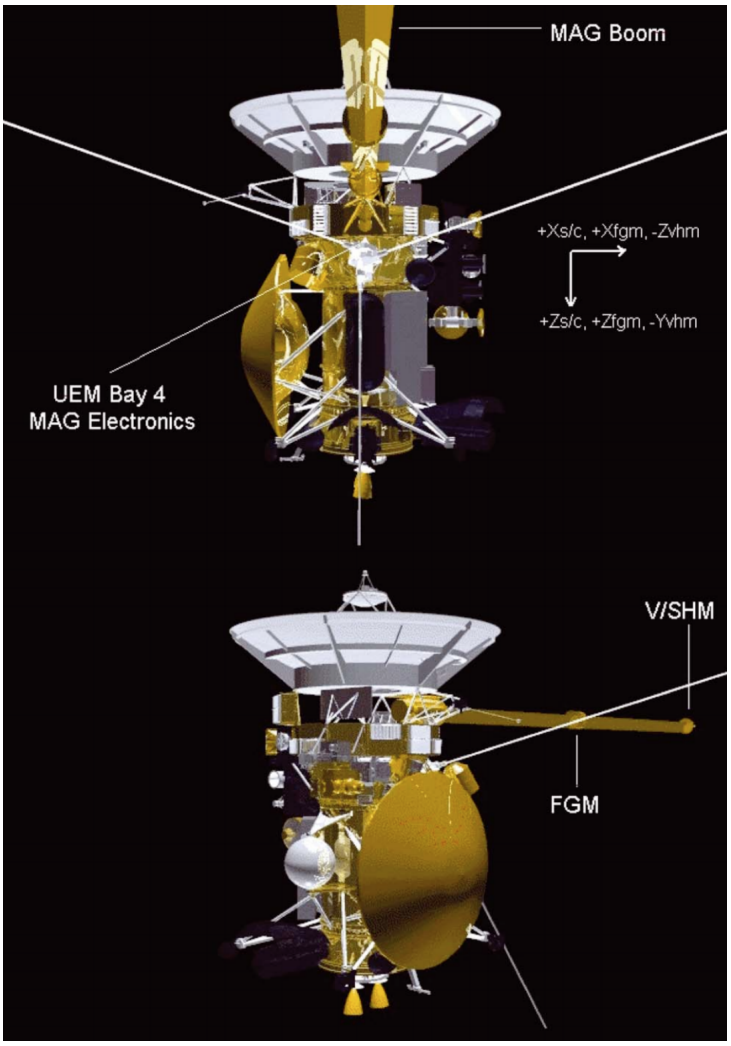

FIGURE 3.5: The placement of magnetometer hardware on the spacecraft is shown as well as the axes of the sensors [*Dougherty et al.* [2004]]

3.3.1.1 The FluxGate Magnetometer

The fluxgate magnetometer (FGM), mounted halfway along a spacecraft boom in order to reduce spacecraft contamination, is best for measurements at high frequency and it operates over an extremely wide dynamic range from very low fields ranging up to measurements in Saturn's high field. This type of magnetometer can be found on Cassini, Galileo and both Voyager missions [*Dougherty et al.*, 2004; *Kivelson et al.*, 1992; *Behannon et al.*, 1977; *Ness et al.*, 1971]. The FGM type magnetometers are chosen often due to their low power, robustness and success on previous missions.

A photograph of the FGM from Cassini with its case removed showing the location of the single-axis sensors on the sensor block, together with its associated electronics, is shown in Figure 3.6. The FGM is based on three single-axis core flux-gate sensors mounted on a machinable glass ceramic block. In each sensor, a drive coil is wound around an

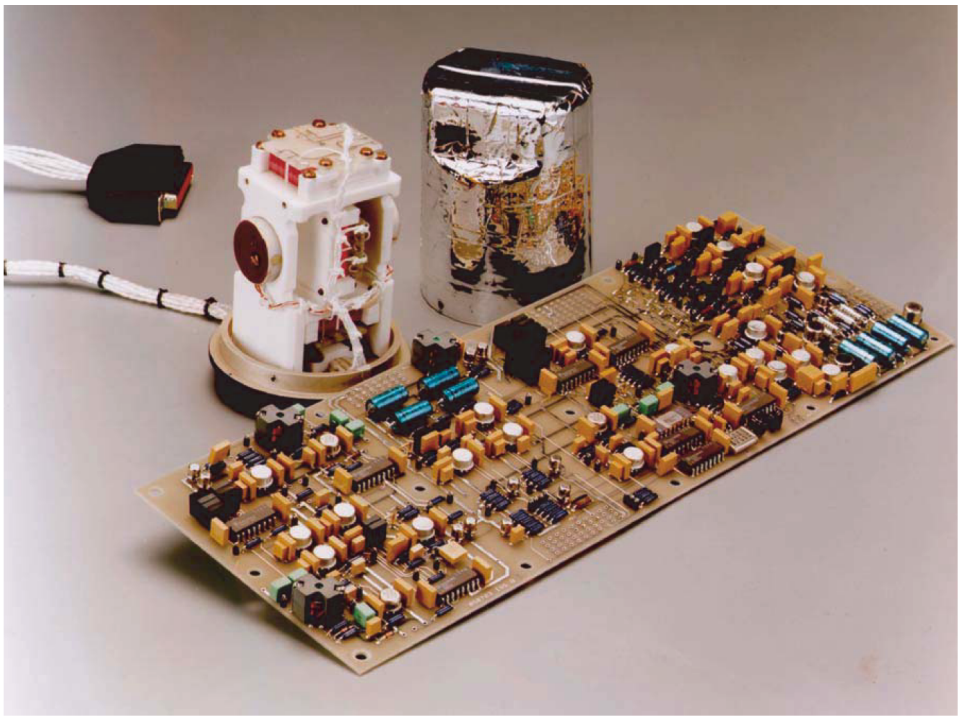

FIGURE 3.6: Ultra Electronics photograph of the FGM (with cover off) and electronics board. [*Dougherty et al.* [2004]]

enclosed high permeability ring core. The drive coil is driven by a crystal-controlled square wave which is used to generate a magnetic field driving the core to saturation twice per cycle. The presence of an ambient magnetic field component parallel to the axis of the sense coil causes the saturation of the core to become asymmetrical. This induces a second harmonic of the drive frequency in the sense coil which is proportional to the magnitude of the magnetic field component along that axis. This signal is processed through a narrow band amplifier tuned to the second harmonic of the drive frequency, which attenuates harmonics other than the second. The result is then integrated and converted to a current which is fed back to the sensor coil to cancel out the ambient field. The integrated output voltage, amplified and corrected for scale factor and alignment errors, is proportional to the ambient field. The three analogue vector components are passed to the data processing unit for analogue to digital conversion and data processing. On Cassini, changing the electronics feedback path and the output amplification allows the sensor to be operated in one of four different full scale magnetic field ranges (40 nT; 400 nT; 10,000 nT; 40,000 nT), whilst on Galileo the outboard sensors have dynamic ranges of +32 nT and +512 nT and the inboard sensors have dynamic ranges of +512 nT and +16,384 nT. Switching between ranges in normal operations is automatic, controlled by the data processing unit, but all parameters are also modifiable by command.

3.3.1.2 Vector Helium Magnetometer

The Vector Helium Magnetometer (VHM) experiment found aboard Cassini (as part of its Dual-technique magnetometer) and Pioneer 10 and 11 [*Hall*, 1975] is a sensitive magnetometer at the tip of a boom to reduce the effects of the residual spacecraft magnetic field, and to assist the balance of this spin stabilized spacecraft. The operation of the vector helium magnetometer is based on field dependent light absorption (the Zeeman effect) and optical pumping to sense the magnetic field. Helium in an absorption cell is excited by a radio frequency (RF) discharge to maintain a population of metastable long-lived atoms. Infrared radiation at 1083 nm from a helium lamp, also generated by RF excitation, passes through a circular polariser and the cell to an infrared detector. The absorption (pumping efficiency) of the helium in the cell is dependent on the ambient magnetic field direction. The optical pumping efficiency is proportional to $\cos(2\theta)$ where θ is the angle between the optical axis and the direction of the magnetic field. This directional dependence is utilized in the vector mode by applying low frequency sweep fields rotating about the cell, which allow the extraction of the three orthogonal ambient field components. These fields are fed back using a set of triaxial Helmholtz coils mounted on the sensor housing around the cell. The sensor for the magnetometer consisted of a cell filled with helium that is excited by electrical discharge at radio frequencies and infrared optical pumping. Changes in helium absorption caused by magnetic fields passing through the magnetometer are measured by an infrared optical detector. This signal is then transformed into a magnetic field signature.

A year after Saturn orbit insertion in July 2004, the VHM stopped operating. This meant that the calibration procedure became much more complicated. As a result, calibration now required regular rolls of the entire spacecraft in a quiet background magnetic field about two distinct axes in order to enable calibration of the data from the still operational FGM.

Magnetometer data is used in chapters 4 and 5 of this thesis. In chapter 4, which discusses work relating to the drivers and dynamics of the Jovian magnetosphere, a catalogue of reconnection signatures detected in situ in Jovian magnetic field data by *Vogt et al.* [2010] is used. Chapter 5 discusses the use of the Saturn Kilometric Radiation as a proxy for magnetospheric dynamics. In this chapter, two catalogues of reconnection events detected in Kronian magnetic field data by *Jackman et al.* [2014b] and *Smith et al.* [2016] are discussed.

3.3.2 The Cassini Radio and Plasma Wave Investigation

An overview of the current knowledge of Saturn's radio emissions is presented in chapter 2 and data from the Cassini Radio and Plasma Wave Spectrometer (RPWS) [*Gurnett et al.*, 2004] is used in chapter 5 and 6 as a remote proxy of Saturn's magnetospheric dynamics. The RPWS investigation was designed to study radio emissions, plasma waves, thermal plasma, and dust in the vicinity of Saturn. Compared to Voyager 1 and 2, which were the only spacecraft to have made radio and plasma wave measurements in the vicinity of Saturn, the Cassini RPWS instrument (shown on Cassini in figure 3.7) had several new capabilities. These include (1) greatly improved sensitivity and dynamic range, (2) the ability to perform direction-finding measurements of remotely generated radio emissions and wave normal measurements of plasma waves, (3) both active and passive measurements of plasma resonances in order to give precise measurements of the local electron density, and (4) Langmuir probe measurements of the local electron density and temperature. With these new capabilities it has been possible to perform a broad range of studies of radio emissions, wave-particle interactions, thermal plasmas and dust in the vicinity of Saturn.

The RPWS instrumentation consists of three electric antennas, three magnetic antennas, a Langmuir probe and its associated electronics, and five specialized receivers. A simplified block diagram of the RPWS instruments is shown in figure 3.8. Three monopole electric field antennas, labelled Eu, Ev, and Ew, are used to provide electric field signals to the various receivers. The orientations of these three antennas relative to the x, y, and z axes of the spacecraft are shown in figure 3.7. By electronically taking the difference between the voltages on the Eu and Ev monopoles, these two antennas can be used as a dipole, Ex, aligned along the x-axis of the spacecraft. The Eu and Ev antennas also can be used to sound the local plasma by transmitting short pulses. In an alternate mode of operation, they can be biased and used as Langmuir probes to measure the phase velocity of density structures in the plasma. The tri-axial search coil magnetic antennas, labelled Bx, By, and Bz in figure 3.8, are used to detect three orthogonal magnetic components of electromagnetic waves. The search coil axes are aligned along the x, y, and z axes of the spacecraft. The spherical Langmuir probe, shown at the bottom of the block diagram, is used for electron density and temperature measurements. Both the electric antennas and the Langmuir probe can be used to detect dust impacts.

Signals from the electric and magnetic antennas are processed by five receiver systems shown in the middle column of the block diagram: a high frequency receiver that covers the range from 3.5 kHz to 16 MHz for high frequency spectral, polarization, and direction-finding measurements, and which provides simultaneous auto- and cross-correlation measurements from two selected antennas; a medium frequency receiver that

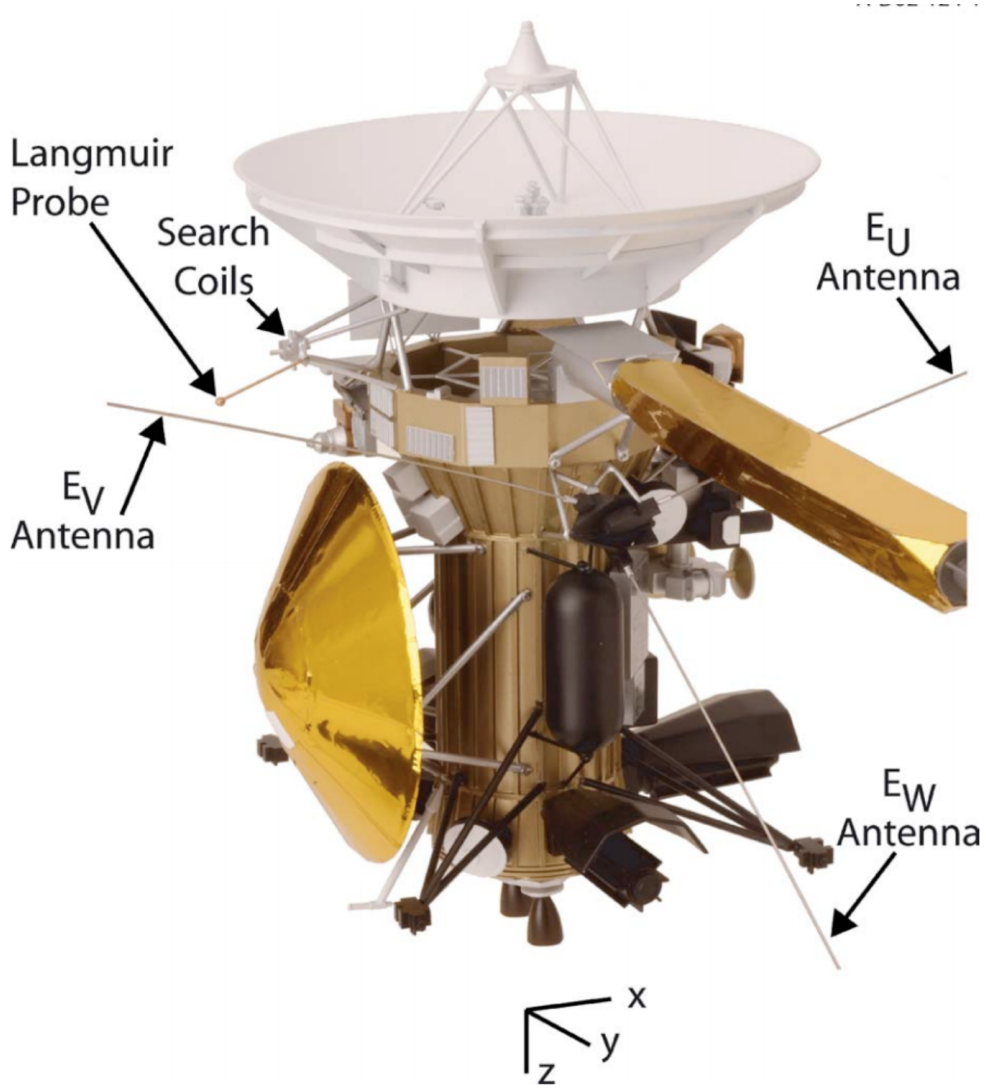

FIGURE 3.7: The Cassini spacecraft showing the locations of the RPWS sensors and their relationship with other structures on the spacecraft. [*Gurnett et al.* [2004]]

covers the range from 24 Hz to 12 kHz for medium frequency spectral measurements; a low frequency receiver that covers the range from 1 Hz to 26 Hz for low-frequency spectral measurements; a five-channel waveform receiver that covers the range from 1 Hz to 2.5 kHz in two bands, 1 Hz to 26 Hz and 3 Hz to 2.5 kHz, to perform wave normal and fine-scale plasma structure measurements; and a wideband receiver that has two frequency bands, 60 Hz to 10.5 kHz and 800 Hz to 75 kHz to provide high-resolution frequency-time spectrograms. In addition, a sounder transmitter can be used to stimulate plasma resonances over a frequency range from 3.6 kHz to 115.2 kHz. Each receiver determines the power per Hertz in that frequency band (i.e. the total power in that filter divided by the filter width in Hz), and that is what is plotted in the spectrograms.

In chapters 5 and 6 the flux intensity over 48 logarithmically spaced channels and the emission power both as a function of time are used to derive criteria for the selection

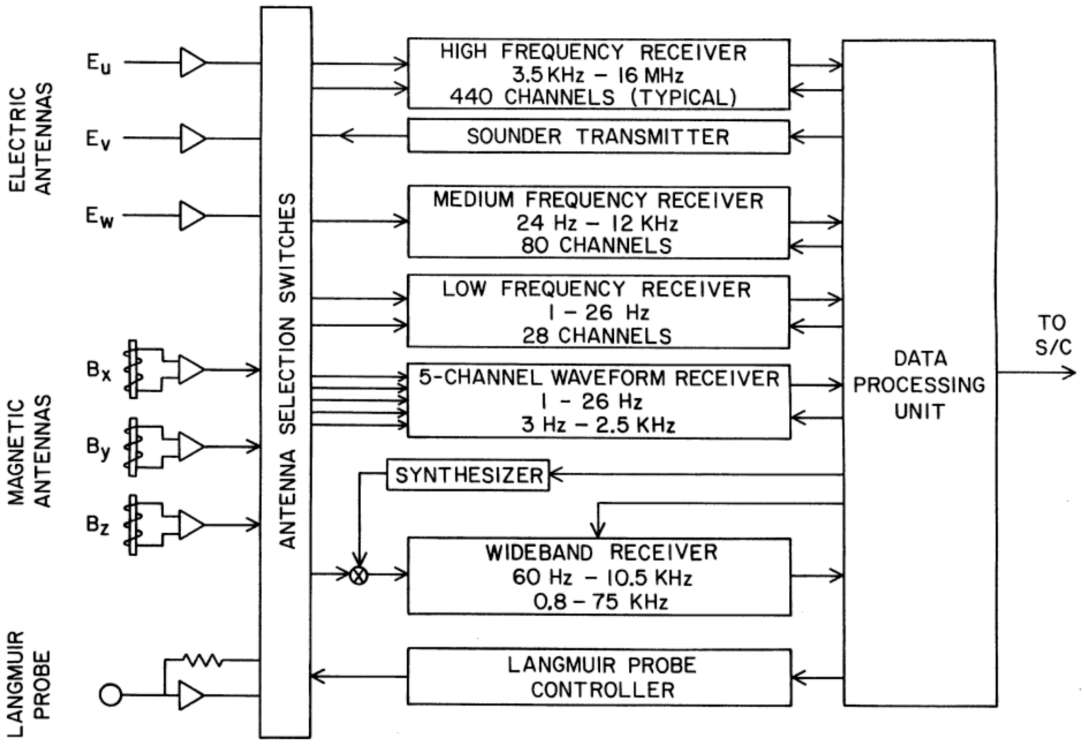

FIGURE 3.8: A functional block diagram of the RPWS instrument. The seven sensors, three electric, three magnetic and the Langmuir probe are shown on the left side. IN the middle, the various receives used to analyse the signals are shown. The data processing and spacecraft interface are on the right. [*Gurnett et al.* [2004]]

of low frequency extensions and narrowband emissions which form part of the Saturn radio emission spectrum. The emission polarisation information is also used to examine narrowband emissions in chapter 6.

3.4 Michigan Solar Wind Model

The Michigan Solar Wind Model (mSWiM) was developed in order to provide solar wind conditions at a range of solar system objects beyond Earth's orbit. Using measurements of solar wind conditions near Earth orbit as input, the 1.5-D Magnetohydrodynamics (MHD) model [*Zieger and Hansen*, 2008] propagates these conditions radially outwards. It is implemented with the Versatile Advection code (VAC) [*Tóth*, 1996], a software package that solves a system of hyperbolic partial differential equations. The inputs for the model are the magnetic field and plasma parameters of the solar wind at Earth's orbit available from OMNI, a data set compiled from a variety of spacecraft including IMP-8, ACE, Wind, ISEE-3 and Geotail. The primary outputs of the model are the solar wind density, n; the velocity components, v_r, v_t, v_n; temperature, T; and the magnetic field components, B_r, B_t, B_n. The velocity and magnetic field components are given

in the RTN coordinate system where R points radially away from the Sun towards the object, T points toward the cross product of the solar rotation vector and R, and N points toward the cross product of R and T. There are two output cadences available, the "full resolution" output has a variable resolution on the order of minutes, the "hour resolution" output has a resolution of one hour. The prediction efficiency is given as a function of time from the spacecraft's apparent opposition from the target object (i.e. when there is a straight line joining the Sun-Earth-Object) as shown in figure 3.9. The accuracy of the propagation decreases with increasing time from apparent opposition. The solar wind velocity, v, and the solar wind density, ρ are reasonably well predicted, whereas the magnetic field components, particularly B_N (out of the ecliptic plane), are not as well predicted. The model is also more accurate during the late declining phase of the solar cycle associated with recurrent high-speed solar wind streams and a tilted heliospheric current sheet. During solar activity maxima fast dynamic changes on the solar surface and frequency transient events like coronal mass ejections mean the results are less accurate.

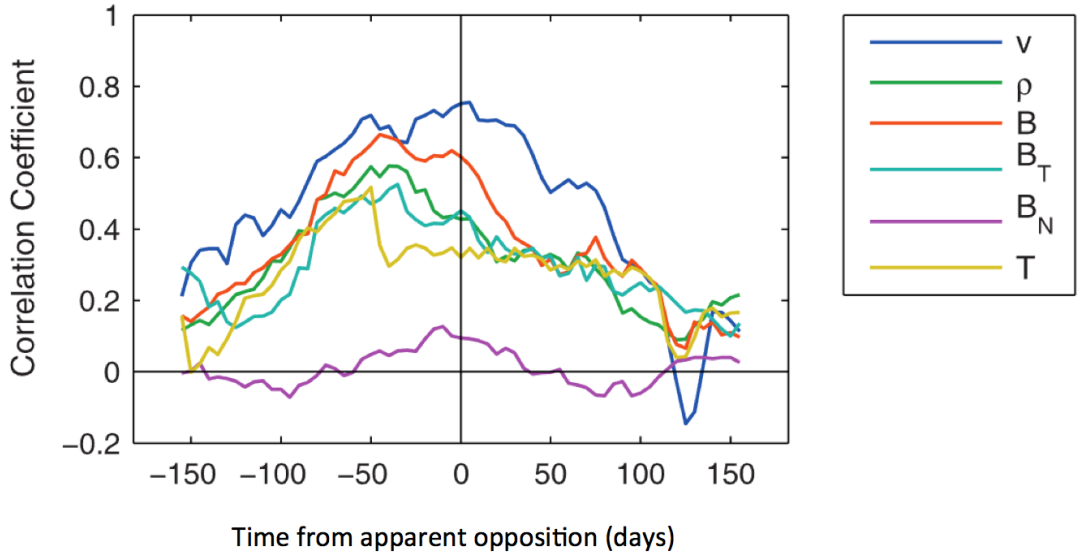

FIGURE 3.9: Average prediction efficiency (linear correlation) of solar wind variables as a function of time from apparent opposition during high recurrence index years (such as 2006). The prediction efficiency is shown for: v, the solar wind velocity, ρ, the solar wind density, T, the solar wind temperature and the three RTN components and total strength of the magnetic field, B. [*Zieger and Hansen* [2008]]

Chapter 4

An avalanching sandpile model as an analogue for Jovian magnetospheric dynamics

4.1 Introduction

The purpose of this chapter is to discuss the use of an avalanching sandpile model as an analogue for Jovian magnetospheric dynamics. As discussed in chapter 2 of this thesis Jupiter is loaded with between $\sim$ 100 and 700 kg s^{-1} of ionic matter from its moon Io. This ionic matter is then picked up by Jupiter's magnetic field lines which then more radially outwards due to centrifugal forces. However, the amount of mass loaded in the magnetosphere by Io is not balanced by the amount of mass observed to leave the system in the form of plasmoids broken off by tail reconnection ($\sim$ 120 $kg\ s^{-1}$). This is referred to as the mass budget problem. In this chapter we explore how a simple 1-dimensional sandpile model can describe some of the properties of Jupiter's magnetosphere and offer a possible explanation to the mass budget problem. We introduce a cellular automaton model that explains the observed plasmoid occurrence frequency and, within this framework, allows us to estimate the "missing" mass from undetected small events. Section 4.2 discusses previous modelling work and describes our sandpile mode with a possible physical analogue. Section 4.3 discusses the outputs of the model such as avalanche sizes and recurrence times. Section 4.4 discusses mass-loss in the system, self-organised criticality, and detection thresholds in a magnetospheric context.

4.2 Modelling

In this section we first discuss previous models and their applications to planetary magnetospheres. We then describe the 1-dimensional cellular automaton sandpile model that we use in this work and how this model is driven.

4.2.1 Previous Model

Magnetospheres are large-scale natural systems that exhibit non-equilibrium phenomena. The properties of these systems are studied using techniques of non-linear dynamics and complexity science [see *Surjalal Sharma*, 1995; *Klimas et al.*, 1996, 2004; *Dendy et al.*, 2007]. Global Magnetohydrodynamics (MHD) models of the Jovian magnetosphere have focused on the dynamics of the magnetotail [e.g. *Fukazawa et al.*, 2005, 2010] while multi-fluid/multi-scale models have been used by [e.g. *Winglee et al.*, 2009] to couple Io's plasma to the Jovian magnetosphere. These models are large and complex, solving multiple equations and tracking various ion species and dynamics throughout the simulation. Cellular automata models, through a few simple rules, are able to recreate a statistical overview of the dynamics such as waiting times between events and event sizes over a range of scales. They can also be used to recreate macro-scale properties of the system such as mass release and energy dissipation. It is then possible to explore a wide range of parameters for various input, thresholds and redistribution rules which allows various aspects of magnetospheres to be investigated. Sandpile models in particular display many of the properties found in the magnetosphere such as the slow build-up and rapid release of energy, and a range of scales across which phenomena occur [*Aschwanden et al.*, 2016].

An example of one model that has had success at Earth with reproducing the statistical properties of substorms (global reconnection events in Earth's magnetotail) is the Minimal Substorm Model (MSM) [*Freeman and Morley*, 2004]. The MSM is a 1-celled cellular automaton and proceeds in the following way. The substorm is driven by proper from the solar wind P which causes energy in the magnetotail, E to accumulates at a rate

$$\frac{dE}{dT} = P. \tag{4.1}$$

F is an energy state that the magnetotail would like to be in. F is determined by the solar wind conditions such that F is a function of P.

$$F = C - DP \tag{4.2}$$

where C is a critical energy threshold and D is a constant related to substorm periodicity. The magnetotail is constrained from adopting state F until it becomes sufficiently stressed with an energy C. At this point, the magnetotail moves to the lower state:

$$E \rightarrow F \quad when \quad E \geq C \tag{4.3}$$

Using an input P from solar wind data (the main driver of Earth's magnetosphere), *Freeman and Morley* [2004] found a remarkably good match between the waiting times (time between two consecutive events) between their events and the waiting times between particle injection events (detected by three geosynchronous spacecraft at 70°E, 135°W and 70°E longitude) in Earth's ionosphere marking substorm onset [*Borovsky et al.*, 1993]. We want to build on the principles outlined in this simple MSM and adapt them to Jupiter's magnetosphere where dynamics (unlike Earth) are thought to be driven less by the solar wind and more by the internal mass loading from Io and the planet's rapid rotation. This single-celled integrate-and-fire (slow build up of energy (loading) and rapid release (unloading)) model could be applied to Jupiter's magnetosphere. The build up and release of energy could represent the stretching and breaking of field lines as at Earth. A multi-celled cellular automaton will allow us to explore not just the timescale of this process but also the various scales and distribution of material throughout the system.

In the companion paper to this chapter, Freeman et al, [in preparation, 2018] analysed the probability distribution of waiting times between 129 (plus 112 additional censored events due to the non-continuous observation) reconnection events at Jupiter identified by *Vogt et al.* [2010]. They found that the distribution is consistent with an Inverse Gaussian (IG) distribution and interpret this as arising from a stochastic integrate-and-fire process. In this system, mass accumulates in the magnetotail until at some threshold the magnetic stress is released in the form of a reconnection event and the cycle repeats. In this paper we use a multi-celled sandpile model to explore the effects of magnetospheric driving and different detection threshold and what this tells us about the Jovian system.

4.2.2 Sandpile Model

Our model is based on the principles from the one dimensional, multi-celled cellular automaton sandpile model used in *Chapman et al.* [1998] to examine Earth's magnetosphere. In this model, sand is added to the first cell until some threshold is reached at which point the sand avalanches down the grid continuing until all cells are below their threshold (an 'internal avalanche') at which point the input begins again. If the sand

reached the end of the grid (a 'systemwide avalanche') the entire pile is emptied and the input begins again. Using this model, *Chapman et al.* [1998] were able to demonstrate a power law relationship in the size of the internal avalanches. They interpreted this as indicating a lack of intrinsic scale in Earth's magnetospheric activity. We build on their model framework here, adapting to represent conditions at Jupiter.

The model proceeds in the following way (see figure 4.1): A grain of sand is added to the first cell ('edge-driven') in the grid at each timestep and the height of sand of that cell is given as h_i. This continues until the local gradient, $z_i = h_i$ - h_{i+1} reaches or exceeds a threshold, a critical gradient fixed in time, z_c. At this point, cell i is unstable and a correction is applied such that any excess is removed and $z_i = z_c$. The sand is then instantaneously and conservatively flattened across the two cells and is referred to as an internal avalanche (IA). If this redistribution causes the local gradient between cells i + 1 and i + 2 to exceed the critical gradient, the avalanche continues to flatten the sand across all three cells. This continues until $z_i < z_c$ for all i. If the avalanche continues to the end of the grid (512 cells), all sand is emptied from the sandpile, and this is referred to as a systemwide avalanche (SWA). These steps are summarised in figure 4.1 which shows an example of the build up of sand in the sandpile to the point of an internal (panel 2 and 3) and then systemwide avalanche (panel 6 and 7).

A correction is applied so that an avalanche is initiated at the exact moment the threshold is reached in order to be more closely analogous to magnetospheric instability/magnetic reconnection triggering. Due to the discrete addition of sand and time iterations (these are just iterations of the model, they are not equivalent to any "real" time), following the addition of some amount of sand, x, between times t and t + 1 the threshold may have been reached without an avalanche i.e. the threshold was reached at t + 0.5 but because we add 'whole' timesteps, the time we would record for the avalanche onset is therefore an overestimate. Further the gradient between the two consecutive cells might exceed the critical threshold i.e. if we are 0.02 grains of sand below the threshold and add 0.05 we now exceed the critical gradient. The correction we apply gets rid of any excess above the threshold and calculates the exact time the threshold was reached. The time of avalanche onset is calculated by the equation:

$$t = t_0 + \frac{z_c - z_0}{x}, \tag{4.4}$$

where z_0 is the height of sand in the cell at t_0 (i.e. at the start of the iteration just before we add any sand), such that the avalanche begins at the exact time of instability and with the 'correct' amount of sand.

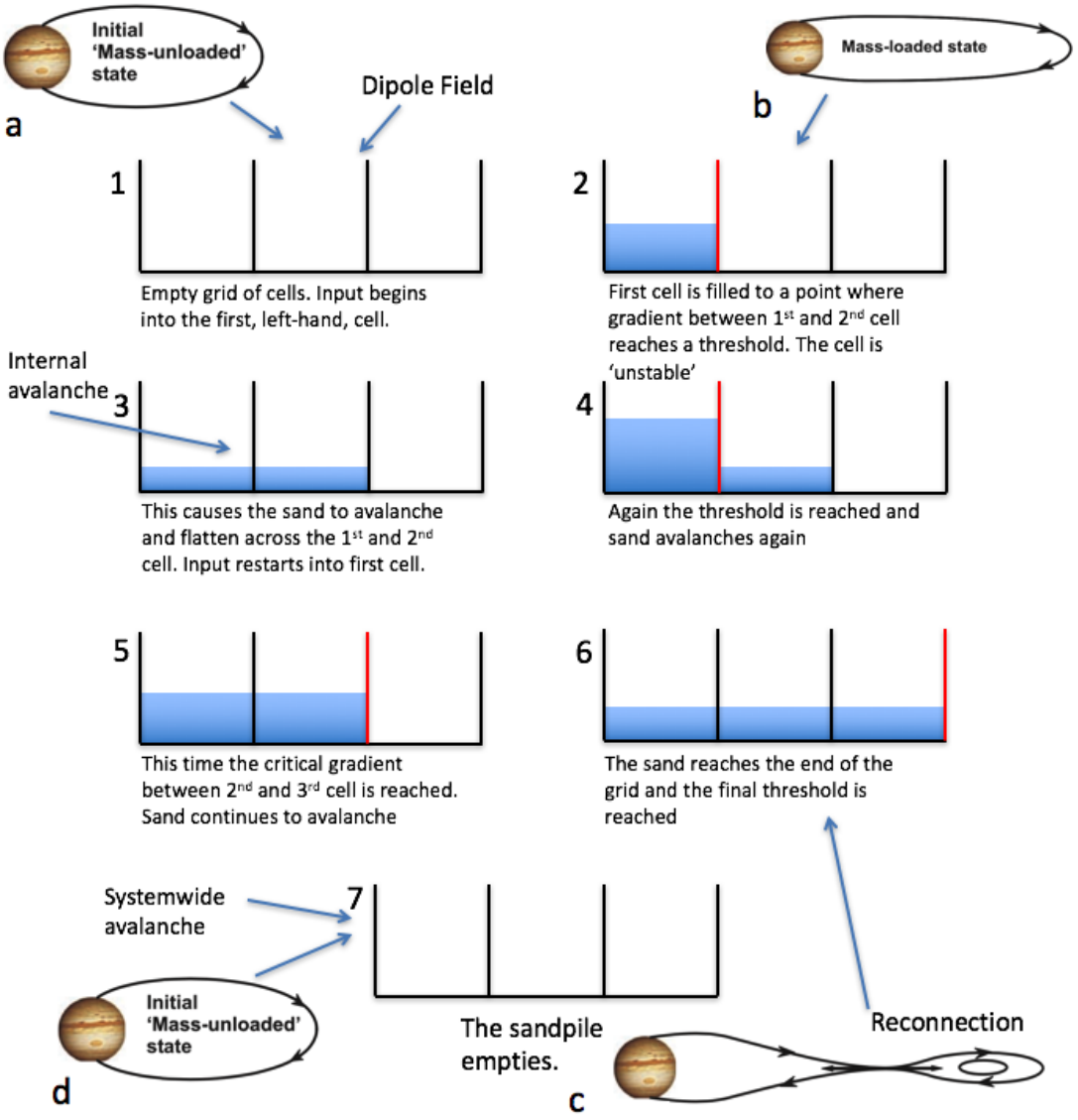

FIGURE 4.1: Showing the build up and avalanching of sand within the sandpile model and the corresponding magnetospheric state. The red line shows the cell edge that is unstable. Panels 1 to 6 show the build up and subsequent internal then systemwide avalanche within the sandpile grid. Panel 1 corresponds to a dipole magnetosphere (inset a) with zero stretching of the field lines. Panel 2 shows cell 1 on the point of avalanching corresponding to a perturbed, stretched magnetosphere (inset b). Panel 6 shows the sandpile on the verge of a systemwide avalanche which corresponds to a global magnetospheric reconnection event (inset c). Panel 7 again shows a purely dipole field following the loss of sand/mass (inset d). Credit to *Kronberg et al.* [2007] for the insets.

4.2.3 Model Driver

Io is the primary driver of the model. Approximately 1000 $kg\ s^{-1}$ of neutral atoms and molecules are lost from Io's atmosphere. These neutrals form the neutral clouds around Io's orbit and between one-third and one-half are subsequently ionised and accelerated

up to corotation speed [*Bagenal and Delamere*, 2011]. These ions are centrifugally confined to the equatorial plane of Jupiter's magnetosphere and are eventually picked up by magnetic field lines. These now heavy field lines move radially outwards. This stretching eventually leads to magnetic reconnection and the loss of mass through plasmoids. The relative role of this Io driver and the solar wind in the dynamics of Jupiter's magnetosphere are hotly debated. In this model we assume that the primary driver of the Jovian magnetosphere is the mass loading from Io in line with multiple previous observational and modelling studies [e.g. *Bagenal and Delamere*, 2011; *Bonfond et al.*, 2012]. The exploration of the influence of the solar wind is outside of the scope of this work.

We collated the mass loading rates available in published literature to better constrain a loading rate and how this varies across time. The results are summarised in Table 4.1 in the appendix section of this chapter. There is a range of mass loading rates, the distribution of which is not inconsistent with a uniform distribution and as such we drive the model with a uniform distribution input (although as long as the input distribution has finite variation and the driving is slow the exact shape does not matter). We assume that the variation for our input distribution accounts for the variation in the Io input and for transient events like large volcanic eruptions. It should be emphasised that the link between volcanic activity and the mass loading rate at Jupiter is not well understood or instantaneous. For example, recent work by *Yoshikawa et al.* [2017] showed that following an eruption by Kurdalagon Patera, a volcano on Io, which erupted in 2015, the EXCEED/Hisaki telescope observed the peak intensity (nearly double to normal) of ionic sulphur emissions approximately two months later.

4.3 Physical Analogue

The physical analogue for the sandpile model is based on the *Kronberg et al.* [2007] model of the build up and loss of mass in the Jovian magnetosphere. This section will first discuss this conceptual model, following much of the argument as laid out in the paper, and what this tells us about the Jovian magnetosphere. Following this, how the sandpile fits to this picture and the magnetosphere will be discussed.

4.3.1 Kronberg 2007 Conceptual Model

Kronberg et al. [2007] present a simple conceptual model that can explain the observed quasi-periodicity of global reconfigurations of the Jovian magnetosphere. From considerations of stress balance [*Vasyliünas*, 1983] in the equatorial (ϕ,r) plane and assuming

(1) ion mass loading from internal plasma sources (i.e. Io) and (2) fast planetary rotation leading to field line stretching due to centrifugal forces, they develop a model based on the build up of mass (and subsequent field line stretching) and subsequent mass loss (and field dipolarisation). The loading and unloading cycle is shown in figure 4.2.

In the corotating system, considering the transverse part of **j** the electric current, the local stress balance following *Vasyliünas* [1983] can be written as:

$$\dot{\rho}(\mathbf{\Omega} \times \mathbf{r}) \times \mathbf{B}_\theta + \rho\mathbf{\Omega} \times (\mathbf{\Omega} \times \mathbf{r}) \times \mathbf{B}_\theta + (\nabla \cdot \mathbf{P}) \times \mathbf{B}_\theta = (\mathbf{j} \times \mathbf{B}_\theta) \times \mathbf{B}_\theta. \tag{4.5}$$

where ρ is the mass density, Ω is the angular velocity of Jupiter, $\mathbf{r}$ is the radial distance, $\mathbf{P}$ is the plasma pressure tensor, and B_θ the north-south magnetic field component. The dot denotes the local derivative with respect to time. They proceed by considering this in the equatorial plane which leads to equation 4.5 being rewritten as:

$$\dot{\rho} r B_\theta \Omega \mathbf{e_r} + \rho\Omega^2 B_\theta r \mathbf{e}_\phi + \frac{\delta P}{r\delta\theta} B_\theta \mathbf{e_r} - \frac{\delta P}{\delta r} B_\theta \mathbf{e}_\phi = -j_r B_\theta^2 \mathbf{e_r} - j_\phi B_\theta^2 \mathbf{e}_\phi. \tag{4.6}$$

i.e. the two components of the electric current density in the equatorial plane. The radial component is proportional to the mass loading rate and supports the corotation of the plasma [e.g. *Hill et al.*, 1983; *Cowley and Bunce*, 2001] and the azimuthal component is dependent on the mass content. To proceed we consider this mass content dependent azimuthal component. Rearranging equation 4.6 for **j** and multiplying by the magnetic permittivity μ_0 gives:

$$\mu_0 \mathbf{j}_\phi = \frac{\mu_0 \delta \mathbf{P}}{B_\theta \delta \mathbf{r}} - \frac{\mu_o \rho \Omega^2 r}{B_\theta} \tag{4.7}$$

Comparisons of Galileo data with model work from *Khurana and Kivelson* [1989] shows that the centrifugal term (second term on right hand side of equation 4.7) and the pressure terms are of the same order [*Kronberg et al.*, 2007] and so on the assumption that the the pressure term changes due to mass loading processes:

$$\frac{\delta \mathbf{P}}{\delta \mathbf{r}} \simeq -\mu_o \rho \Omega^2 r. \tag{4.8}$$

From the differential form of Ampere's equation (equation 1.8 in chapter 1) $\nabla \times \mathbf{B} = \mu_0 j$ and considering the azimuthal component of **j**, we get:

$$\mu_0 \mathbf{j}_\phi = \frac{\delta \mathbf{B}_\theta}{\delta \mathbf{r}} - \frac{1}{r} \frac{\delta \mathbf{B_r}}{\delta \theta} \tag{4.9}$$

i.e. the azimuthal current is determined by the gradients of the magnetic field in the radial and field aligned (θ) direction. From magnetic field data [*Kronberg et al.*, 2007;

Khurana and Kivelson, 1989] the spatial variation of B_θ in r is negligible compared to the meridional variations of B_r, therefore $\delta\mathbf{B}_\theta/\delta\mathbf{r}$ can be neglected and thus:

$$\mu_0\mathbf{j}_\phi \simeq -\frac{1}{r}\frac{\delta\mathbf{B_r}}{\delta\theta} \simeq -\frac{\mu_0^2\rho\Omega^2 r}{B_\theta} - \frac{\mu_o\rho\Omega^2 r}{B_\theta} = -(1+\mu_0)\frac{\mu_o\rho\Omega^2 r}{B_\theta} \tag{4.10}$$

Finally, simplifying, equation 4.10 can therefore be written as:

$$j_\phi = -(1+\mu_0)\frac{\rho\Omega^2 r}{B_\theta} \tag{4.11}$$

Following this argument we can now list several features of the azimuthal current density:

1. The azimuthal current density is proportional to the mass content of the plasma sheet
2. It is also proportional to the angular velocity of Jupiter
3. It is also proportional to the change in the radial magnetic field component in the meridional plane i.e. the radial distension of the field lines.
4. No current density implies no radial stretching of the field lines and no mass.

4.3.2 The Sandpile Model

This subsection will now tie the sandpile model with the conceptual model just described.

As a starting point we say that an empty sandpile is equivalent to an approximately dipole field with no radial stretching and is placed in the equatorial plane with the first cell close to the mass source and the consecutive cells at increasing radial distance. The addition of sand into the sandpile is analogous to the addition of mass to the magnetosphere and the subsequent radial stretching. As sand is added to the first cell (i.e. the field becomes more radially stretched), the gradient between cells 1 and 2 increases. This gradient is representative of some local current density, j_ϕ. In this way, the threshold gradient (i.e. z_c), at which point there is an avalanche of some size, is representative of some critical current density (which will be a function of radial distance) at which point reconnection occurs (i.e. the ion tearing instability). Depending on how much sand is already in the sandpile (i.e how much mass is in the magnetosphere and how radially distended it is), avalanches of different sizes will occur. These different sized avalanches represent a range of reconnection event sizes, from small local dipolarisations with a small amount of mass loss (i.e. avalanche size of a few cells) to large events

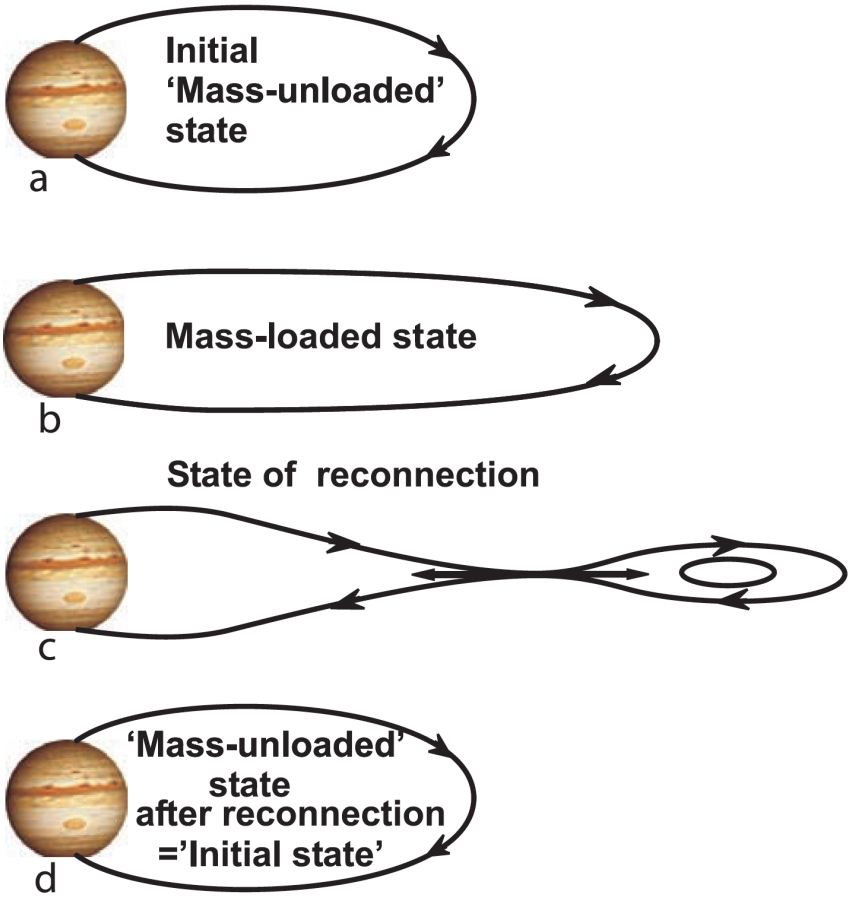

FIGURE 4.2: A sketch demonstrating the periodical nature of the reconfiguration process in the Jovian magnetosphere, showing (a) the initial largely mass-unloaded state prior to excessive mass loading from the internal sources, (b) a stretching of the configuration as a consequence of continuous mass loading and the centrifugal force, (c) a reconnection state which leads to formation of x-line and mass release in a form of plasmoids. This state is reached after sufficient thinning of the plasma sheet allowing for spontaneous reconnection. Also shown is (d) the configuration after reconnection. The Jovian magnetosphere undergoes periodic changes between the first and the third state.

across potentially the whole tail width where a large proportion of the mass is lost (i.e. a systemwide avalanche where all 512 cells become unstable).

As described, the gradient between two cells is representative of the local current density. Rearranging equation 4.11 for $\jmath_\phi$:

$$|j_\phi| = (1+\mu_0)\frac{\rho\Omega^2 r}{B_\theta} = \left|\frac{\delta h}{\delta d}\right| \tag{4.12}$$

where $\frac{\delta h}{\delta d}$ is the gradient between two cells and d is in the direction down the sandpile grid. By summing $\jmath_\phi$ across the entire grid, we get a value that is proportional to how radially stretched the field is since this radial distension is supported by an azimuthal

current.

$$\sum_{i=1}^{512} j_{\phi_i} = \int (1+\mu_0)\frac{\rho\Omega^2 r}{B_\theta}\ \delta\mathbf{r} = h_1, \tag{4.13}$$

where $\delta\mathbf{r}$ is an element in the radial direction and h_1 is the height of sand in the first cell (i.e. the sum of all gradients in the grid). Considering the terms inside the integral, μ_0 is a constant, Ω is the angular velocity of Jupiter and is therefore constant. We can assume that the radial distance from the planet to a point in space, r, is also a constant. Although B_θ changes during magnetic reconnection and plasmoid release (i.e. in terms of a spacecraft moving through the tail or a spacecraft observing a plasmoid moving over it), at any given point in time and space the spacecraft measures one value for this quantity, a snapshot, therefore we can assume B_θ as constant for this case.

Taking the constant terms out of the integral of equation 4.13 gives:

$$\sum_{i=1}^{512} j_{\phi_i} = (1+\mu_0)\frac{\Omega^2 r}{B_\theta}\int \rho\ \delta\mathbf{r} = h_1. \tag{4.14}$$

Integrating the mass density, ρ, in the r-direction (where θ and ϕ are unit-vectors) gives the total mass:

$$M = \int \rho\ \ \delta\mathbf{r} \tag{4.15}$$

Therefore,

$$h_1\ \propto M \tag{4.16}$$

i.e. The height of sand in cell 1, h_1, is proportional to the total mass in the plasma sheet, M.

Therefore, the mass loss from the plasma sheet, ΔM, is proportional to the height change of the first cell in the grid, Δh. Following any avalanche we record the mass loss as the height difference in the first cell to immediately before the avalanche. Further to this, since during a systemwide avalanche all sand leaves the grid, the mass loss from the first cell during a systemwide avalanche is the maximum mass that can be held by the plasma sheet. This allows us to refer to all internal avalanches relative to the largest mass loss. Following this analogue, 'avalanche size' will be used to describe the mass lost from the plasma sheet as described in the physical analogue and 'avalanche length' will refer to the number of unstable cells. With this physical analogue we also avoid any assumptions of the plasmoid dimensions (width, length or height). Our calculation of its 'mass' is based on the change in azimuthal current in the system.

Key Points of the Physical Analogue:

1. The model represents the radial stretching and subsequent dipolarisation of the magnetosphere driven by mass loading (from Io) and mass loss (via plasmoid release).

2. The 1-D sandpile is 'located' in the equatorial plane with the first cell at an inward radial distance with consecutive cells further out in radial distance.

3. The input of sand represents the field becoming more radially stretched and the build up of mass in the magnetosphere.

4. Avalanches (Internal and Systemwide) represent local and global scale dipolarisation, and mass loss.

5. A systemwide avalanche represents the largest magnetospheric disturbance across the entire tail.

4.4 Results

We performed a variety of runs on the model with different critical gradients and inputs in order to explore the effects of a varying driver and how different critical gradients affected the results(For each result and figure, the model parameters will be described. As long as the input remains small compared to the threshold, the results are consistent and differ only by a scale factor between different model parameters). In this section we look at several results from the model; the waiting time distributions between model avalanches and how this is affected by different critical gradients and how we can 'predict' the avalanches in our model and the implication for this in a magnetospheric sense. Firstly we will discuss the appearance of distinct avalanche sizes within our model.

4.4.1 Avalanche Pattern

We find that there are a set of distinct avalanche sizes that occur in a repeatable and predictable pattern as the model progresses. At each iteration sand is put into cell 1 which continues to build until the gradient between cell 1 and cell 2 reaches the threshold, z_c. At this point, cell 1 is unstable and the sand avalanches, flattening across both cells. This is an avalanche of length 1. Following this the sand builds up again to the threshold in cell 1 and avalanches. This may cause cell 2 to become unstable and the sand spreads across the first 3 cells. This is an avalanche of length 2. Following further sand input there is another avalanche of length 1, after that the next avalanche will continue until 4 cells have become unstable i.e. a doubling of length of the previous biggest avalanche,

length 2. This pattern, length 1, 2, 1, will repeat itself until the avalanche length doubles again to 8 cells, after which the entire pattern will repeat until an avalanche of length 16. This repeating pattern followed by a doubling of the avalanche length continues until a systemwide avalanche (512 cells). This pattern occurs for all thresholds and inputs.

The top panel in Figure 4.3 shows a time series of the sand within the plasma sheet as a fraction of its total capacity for an entire sequence of avalanches up to a systemwide avalanche (512 cells or all sand lost). The middle panel shows an enlargement of the orange box from the top panel demonstrating the fractal nature of the sandpile and the repetition of a sequence of smaller events before the occurrence of a larger event. The bottom panel shows the avalanche length i.e. the number of cells that became unstable at each time, t, from t_o up to a size 128 avalanche, over the same enlarged interval as shown in the middle panel. In this panel the different sized avalanches and repetitive pattern can be seen, as well as the intervals of no avalanches where sand is accumulating in the grid. We call these intervals 'waiting times', where the waiting time

$$\Delta T = t_{x+1} - t_x \tag{4.17}$$

where t_x is the instantaneous time that event x occurs. This pattern is also observed within the magnetosphere. There are intervals of magnetic reconnection interspersed with intervals where the tail is sub-critical and magnetotail energy and flux may be building up prior to intervals of loss.

4.4.2 Event Waiting Times

Within the model the waiting time is a function of the critical gradient threshold and the input rate. The companion paper to this chapter, Freeman et al, [in preparation 2018] shows that the waiting time between observed magnetic reconnection events at Jupiter (following a statistical censoring of events from *Vogt et al.* [2010]) can be represented by an Inverse Gaussian (IG) distribution. Our model reproduces this result for all model runs that have a constant threshold and an input that is drawn from a random distribution with finite variance (i.e. Gaussian, random) (see Table 4.2 in appendix). This suggests that Jupiter's magnetosphere can be thought of as a system, like our model, that is being driven at a variable rate to some fixed threshold at which point magnetic reconnection occurs. In this simple model, the variable driving of the model by the addition of sand represents the variability of the rate that mass is added to the magnetosphere from Io.

Figure 4.4 shows the waiting time distributions between some of the distinct internal avalanches of different sizes. Each distribution is plotted with an IG distribution created

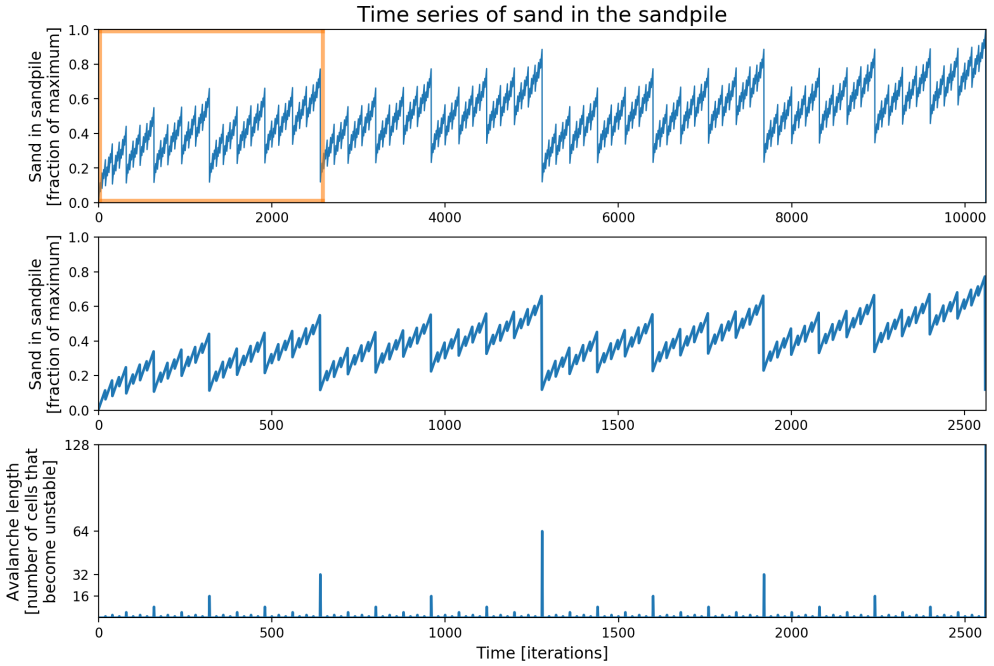

FIGURE 4.3: Time series of the sand in the plasma sheet as a fraction of the total sand capacity. This is for a model run for a constant threshold of 0.2, a constant input of 0.01 per iteration and ran until there has been one systemwide avalanche (the pattern of avalanches and mass loss is the same for all model runs). The figure demonstrates SOC with the series of smaller avalanches that build to a larger one when the smaller ones can no longer take the system below a critical point. The top panel is for a whole series of avalanches up to a systemwide avalanche. The middle panel is an enlargement of the orange box on the top graph showing the time series of sand between t_0 and a size 128 avalanche. The bottom panel shows the avalanche length i.e the number of cells that became unstable during that avalanche. between t_0 and a size 128 avalanche and is an enlargement of the region in the orange box on the top panel.

from the mean and standard deviation of that waiting time distribution. Our model demonstrates that the waiting times between avalanches of a particular size is IG. For the waiting time distributions between each avalanche size we perform a Kolmogorov-Smirnov (KS) test comparing the distributions to an IG. The KS test measures how likely it is that two samples are not from the same overriding distribution by quantifying the distance between the two cumulative distribution functions. The test gives KS statistics of 0.08, 0.03, 0.02 respectively. The KS-test also gives a p-value, the probability that the KS statistic would be that high on the assumption that the two distributions are from the same distribution. They were all under the benchmark 5%. This means we cannot reject the null hypothesis that these distributions are from the same overarching distribution, in other words, the waiting time distribution between the avalanches is statistically indistinguishable from an IG distribution. We also note that the fit with the IG distribution improves with avalanche size.

The waiting time between an avalanche of a given size is approximately the same each cycle, but the variation increases with avalanche size (i.e. larger avalanches having more

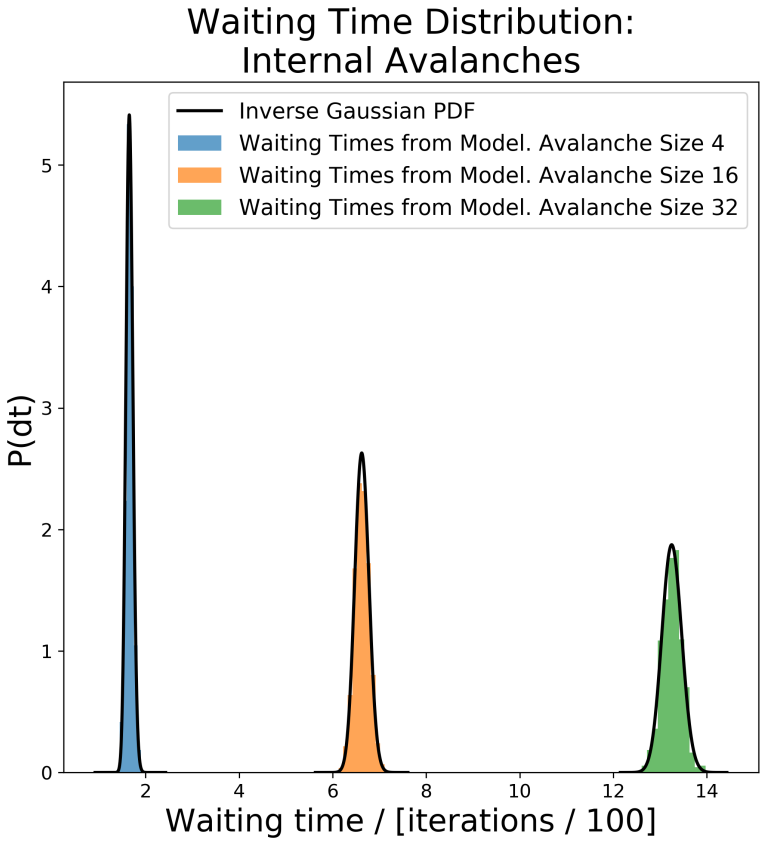

FIGURE 4.4: Waiting time distributions between internal avalanches of three different sizes: 4 (blue), 16 (orange) and 32 (green). The blue is the smallest size and most frequent, the green is the largest and least common. The black line is an Inverse Gaussian distribution created from the mean and standard deviation of the waiting time distributions. This model run was a for a constant threshold value of 0.2, a uniformly distributed input in range [0, 0.02], and a gridsize of 512 cells. The waiting times in terms of iterations will change depending on the relative input rate and threshold but the frequency of an avalanche always decreases with increasing avalanche size and can be predicted by an inverse gaussian distribution.

variation in their waiting times). As well as avalanche size, there is also an increase in the variation and mean of the waiting time distribution with threshold. These dependencies on avalanche size and the cell threshold are intuitive in our model since both factors will increase the number of iterations before an avalanche of that size occurs and so the random walk to that level can vary more. As can be seen in Figures 4.3 and 4.4, smaller avalanches occur much more frequently than larger avalanches. The smaller avalanches redistribute a small amount of sand in an effort to keep the sandpile 'subcritical' as discussed at the end of this section.

An IG distribution is 'inverse' in that a Gaussian distribution describes the distance reached by a random walk at a fixed time, whilst an IG describes the time taken for a random walk to reach a fixed positive level. The time for a random walk to reach a

fixed level, α, n times is

$$IG(n\mu, n^2\lambda), \tag{4.18}$$

where μ is the mean time to reach the fixed level, α, and is given by $\frac{\alpha}{\nu}$ (where ν is the average step size of the random walk), and λ is the shape parameter of the IG distribution and is given by $\frac{\alpha^2}{\sigma^2}$ (where σ is the standard deviation of the random walk step size). In our physical model, ν can be thought of as an average mass loading of the magnetosphere from Io with some variance to that loading rate, σ^2. The time to reach a fixed level, $\alpha > 0$ (a critical threshold in the magnetosphere at which point a reconnection event of some size occurs), is distributed by an IG distribution. Given the pattern of avalanches within the sandpile model, we can use the IG equations to predict the mean waiting time between avalanches of a particular size, and the variation in that waiting time. Since we know the pattern of avalanches that precedes an avalanche of any given size, we know how many times the fixed level, $\alpha > 0$, has to be reached. For an avalanche of length 8, we know that there first must be avalanches of length 1, 2, 1, 4, 1, 2, and 1. Therefore, length 8 is the eighth avalanche and the fixed level α must be reached eight times. The mean waiting time to reach α n times is

$$\mu = n\left(\frac{\alpha}{\nu}\right). \tag{4.19}$$

So for an avalanche of length 8 for a fixed level, α (threshold), of 0.2, and a uniformly distributed input in the range [0, 0.02] with mean 0.01, the mean waiting time is 160 (= 8 * 0.2 / 0.01) iterations which matches the output from our model. The shape parameter of the IG distribution is:

$$\lambda = n^2\left(\frac{\alpha^2}{\sigma^2_{input}}\right) \tag{4.20}$$

where σ_{input} is the standard deviation of the input distribution. For an IG distribution the variation is:

$$\left(\frac{\mu^3}{\lambda}\right)^{1/2} \tag{4.21}$$

Substituting equations 4.19 and 4.20 into equation 4.21 gives the variation of the IG distribution as:

$$\frac{\sigma^2_{input} n\alpha}{\nu^3} \tag{4.22}$$

For a standard deviation of the uniformly distributed input, σ_{input}, of 0.00577, this gives a waiting time variation of 53.3 iterations which also matches our model (as summarised in Table 4.2 in the appendix). This statistical predictability will be discussed further in a magnetospheric context in section 4.5.1

By attempting to keep itself in a sub-critical state with no external input, the sandpile

and the analogous magnetosphere can be thought of as self-organised critical (SOC) systems whereby the system exhibits non-linear energy dissipation (avalanche/plasmoid events) and is slowly and continuously driven towards a critical state (input of sand/stretching of field lines due to mass loading) [*Aschwanden et al.*, 2016]. The bursty nature of magnetospheric phenomena have been interpreted in terms of an open, dissipative non-linear system near a SOC state [e.g. *Lui et al.*, 1988; *Chang*, 1992; *Hoshino et al.*, 1994; *Angelopoulos et al.*, 1996; *Klimas et al.*, 2000; *Chapman and Watkins*, 2001] and power-law shaped probability and size distributions have been measured in various magnetospheric phenomena [e.g. *Takalo et al.*, 1993; *Angelopoulos et al.*, 1999; *Lui et al.*, 2000; *Uritsky et al.*, 2002; *Bristow*, 2008].

As the field lines are stretched, small magnetic reconnection events (i.e. spatially localised events that are narrow azimuthally) keep the magnetosphere from a larger-scale collapse. This occurs until the smaller events can no longer keep the magnetosphere sub-critical and so a larger event occurs (up to a full tail wide event equivalent to a systemwide avalanche in our model). Our model has a 'slow-driving', where the build-up to threshold occurs over a longer timescale than the subsequent collapse. This is a requirement of self-organised criticality and also makes this type of model physically suitable to describe the slow build-up and rapid release of energy that is characteristic of the reconnection process. The driver is needed to push the system back towards a critical state following any avalanche, but the time taken to do this must be much longer than the timescale of the avalanche itself. If the driving is too fast, the system will exhibit 'catastrophic collapse' where the sandpile is never subcritical and most iterations bring a significant sized avalanche. Further justifying the slow driving, this difference in timescales is also found in the magnetosphere where the waiting times between magnetic reconnection events is on the order of hours to days whilst the events occur over timescales of minutes.

4.5 Discussion

Following the results section above we now discuss the larger implications of the model's ability to reproduce the waiting time distribution of reconnection events found at Jupiter. We first outline the physical analogue which links our simple sandpile picture to magnetospheric dynamics.

4.5.1 Mass loss in the model

By looking at the varying sizes of avalanches and how the mass within the model evolves over time, we can draw an analogy with the mass transport and loss cycle in Jupiter's magnetosphere. In our model there are a series of distinct avalanche sizes corresponding to distinct sizes of mass loss from the plasma sheet.

Figure 4.5 shows the relationship between the waiting time (normalised to number of avalanches [so is then consistent across all thresholds and input rates]) and different avalanche sizes (mass loss) (blue line), and the relationship between waiting times and avalanche length (number of unstable cells) (orange line). In order to read figure 4.5, read an avalanche length of e.g. size 128 on the bottom x-axis, follow that to the orange line and see that its waiting time is 128 avalanches on the y-axis, then follow this horizontally to the blue line and read off an avalanche size of 0.66 on the top x-axis. In this way, an avalanche length of 64 unstable cells is 55% of the maximum avalanche size (where the maximum avalanche size equals height change in cell 1 during a systemwide avalanche as discussed in physical analogue), whilst an avalanche with a length of 256 unstable cells (4 x larger) is 77% of the maximum.

Therefore, 'shorter' avalanches have a much higher mass loss per cell than the 'longer' avalanches since an avalanche X times longer than another is less than X times larger in terms of mass loss. If we consider a fixed interval of time from t_0 to the time of a systemwide avalanche, t_{swa}, we can calculate a total mass loss from all avalanche sizes over that period. We can then calculate the fraction of this total mass loss from each avalanche size as shown in Figure 4.6. This figure shows a sharp drop in the contribution of mass loss with increasing avalanche size and the largest events, the systemwide avalanches, are only contributing approximately 2% of the total mass loss. The smallest avalanches, 1 unstable cell, are contributing 25% of the total mass loss, ten times the contribution from the largest events (the 512-celled systemwide avalanches).

Smaller mass loss events are much more frequent than the larger events. These smaller avalanches redistribute sand to keep the sandpile from passing a critical point until a point is reached where they can no longer sustain this sub-critical state and a larger avalanche is needed to redistribute sand. This pattern of small, internal avalanches building up prior to a large, systemwide avalanche is illustrated in Figure 4.3. This can be understood in a magnetospheric context as many, frequent 'adjustments' of the magnetosphere before a larger, more critical instability is reached at which point there is a larger event/avalanche. The greater variance in the waiting times between larger events can be attributed to the variance in the mass loading since it is a longer 'random walk'. Although we cannot predict when an event of a particular size will happen in the

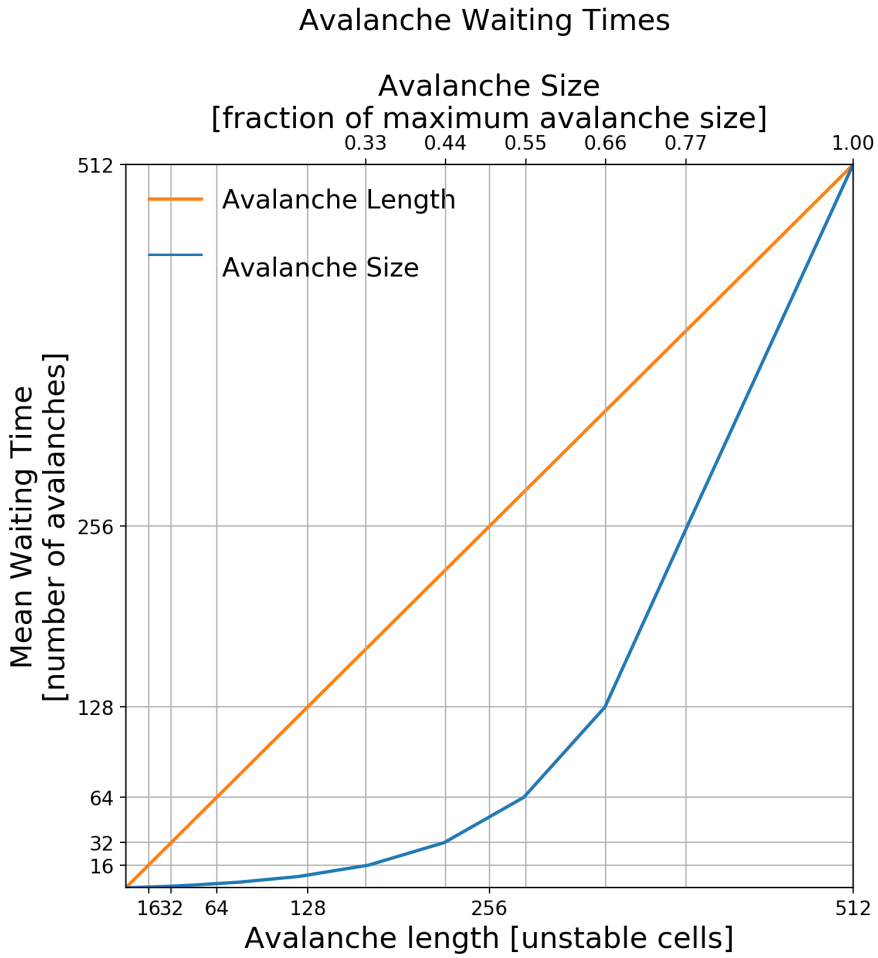

FIGURE 4.5: The blue line shows the relationship between the avalanche size (as a fraction of maximum size) and waiting times between events of that size. The orange line shows the relationship between the avalanche length (number of unstable cells) and waiting times between events of that size. The waiting times have been normalised to number of avalanches. In order to read the graph, read an avalanche length of e.g. size 128, follow that to the orange line and see that its waiting time is 128 avalanches, then follow this horizontal line to the blue line and read off an avalanche size of 0.66. There is a non-linear increase in the waiting times between avalanche sizes showing that although the largest events have the longest waiting times, events of significant sizes are still happening frequently. There is also a non-linear relationship between the avalanche length and avalanche size, with an avalanche X times longer, not being X times larger in terms of mass loss. This model run was for a constant input of 0.01 grains of sand per iteration, a threshold of 0.2 and a 512-celled grid.This results is the same for all input rate and thresholds.

Jovian magnetosphere, following this analysis we can make several comments on their occurrence. Small events will happen most often, with larger events much more rarely. The smaller events will occur much more regularly spaced in time, whilst the larger events will have much more variation in their spacing.

This leads us onto section 4.5.2 where we put this into the context of plasmoid size.

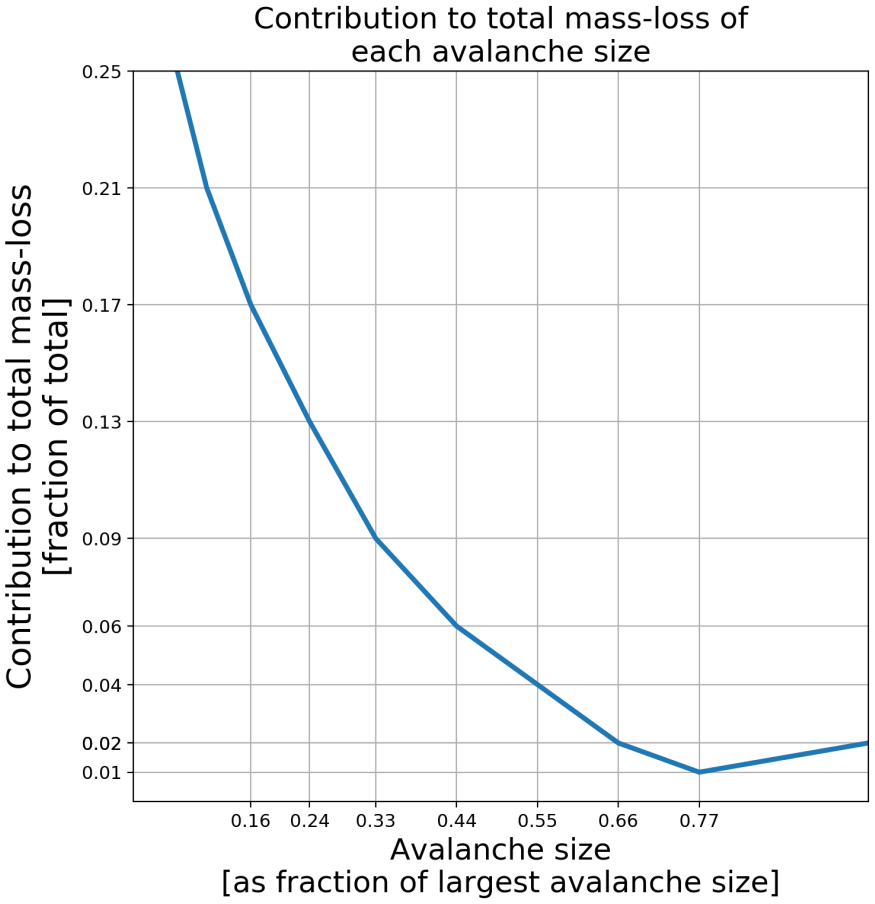

FIGURE 4.6: The contribution of total mass loss from each avalanche size as calculated from all avalanches up to the first systemwide avalanche. Before a systemwide avalanche there is a fixed number of each avalanche of a smaller size, therefore the total mass loss from each of these avalanches within a fixed interval i.e. between two systemwide avalanches, can be calculated and from that their contribution to the total mass loss in this period. This model run was for a constant input of 0.01 grains of sand per iterations, a threshold of 0.2 and a 512-celled grid. It was ran until one systemwide avalanche occurred. This results is the same for al input rate and thresholds.

4.5.2 Detection thresholds

The IG distribution of Freeman et al. [in preparation, 2018] is based on the waiting times between 129 (+112 censored) reconnection events from *Vogt et al.* [2010]. These correspond to plasmoid detections, manifested as bipolar changes in the field. An example of the physical picture which leads to this field change is shown in Figure 4.7. The left panel in this figure shows the change in the north-south component of the magnetic field, B_θ, for an ideal spacecraft trajectory through the centre of a plasmoid as the plasmoid moves tailwards over the spacecraft (as shown in the right panel). The field is initially small and positive indicating a southward field which corresponds to Jupiter's planetary field. As the spacecraft enters the plasmoid, there is an increase in the magnitude of B_θ, showing that the field has become more dipolar. As the plasmoid flows over the

spacecraft there is a field reversal from north to south with the field passing through zero at the centre of the plasmoid. Eventually the field returns to its original small and positive value. Various studies have sought to develop automated criteria to search for such events, placing constraints on the duration and magnitude of the field signatures. In the *Vogt et al.* [2010] paper, the algorithm for finding events required that B_θ must be enhanced by three times the background level (running average over 1-day period), exceed 3 nT or -2 nT and must remain enhanced for longer than 60s.

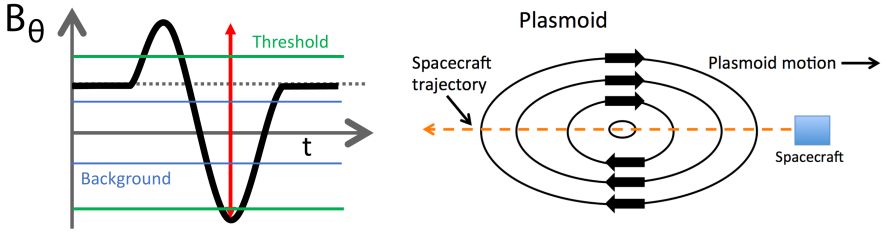

FIGURE 4.7: The left panel shows the B_θ signature as a spacecraft follows an ideal trajectory through a plasmoid as in the right panel. The plasmoid in the right panel is moving to the right with the dotted orange line marking the ideal trajectory of the spacecraft through the centre of the plasmoid. The total deflection in the B_θ signature on the left panel, δB_θ is is marked by the red double-headed arrow. The two horizontal green lines show a possible threshold of detection i.e. a minimum δB_θ for the plasmoid to be detected either by eye or by an event finding algorithm.

There are two conditions that affect the observed B_θ signature. The first is the size of the plasmoid, and the second is the trajectory taken through the structure itself. For a given trajectory along the centre of the current sheet where plasmoids are formed, we might expect a larger field deflection for a larger plasmoid. Likewise a smaller deflection would be measured for a smaller event. For a plasmoid of a given size, the trajectory of the spacecraft relative to the structure will also affect the size of the B_θ deflection. The further the spacecraft passes from the centre of the current sheet, the smaller the measured deflection will be. In this model we assume that we have a 'global' view of the magnetosphere, and follow an ideal trajectory through the centre of the plasmoid.

With these considerations we can link the different sized avalanches in the model to different sized events in the magnetosphere (the smallest avalanches being analogous to the smallest of magnetic reconnection events, and vice versa). For an ideal trajectory, the smaller events will give a smaller B_θ deflection and it is possible that this event will not meet the criteria used by the detection algorithms and will be 'missed'. Here we make an analogue to the avalanches in the model. If we assume that we can only observe avalanches above a certain percent of the maximum size, we will miss all smaller avalanches. If we take the avalanche times for our simulation and remove those events smaller than or equal to 33% (an arbitrary value) of the maximum size, the waiting time distribution between all these events remains an IG as shown in figure 4.8.

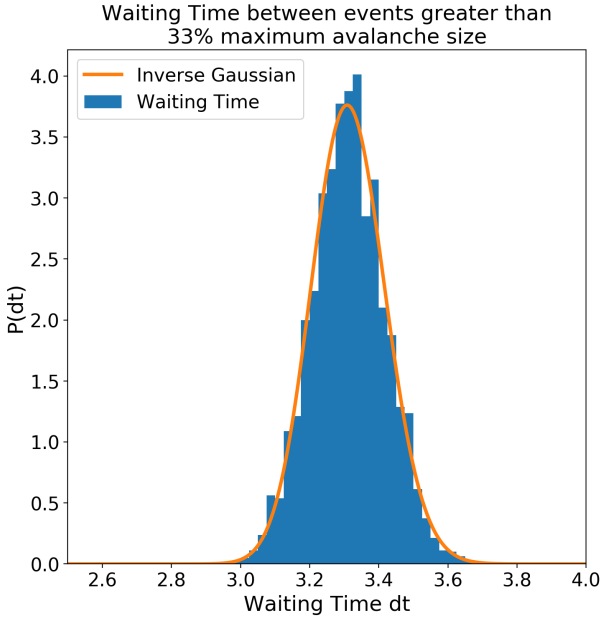

FIGURE 4.8: Waiting times between events larger than 33% of the maximum size. The blue shows the waiting time distribution from the model between. The orange line shows an IG distribution. This is valid for all input rates and thresholds in terms of being able to be predicted by an IG distribution.

This leads onto Figure 4.9, that shows the fraction of total mass loss that we would see if we miss avalanches smaller than this size. The orange line shows the fraction of the total mass loss that would be seen if avalanches smaller than 33% of the maximum size were not observed. Only 15% of the mass loss comes from avalanches larger than this size. Although the small avalanches are significantly smaller than the larger and systemwide avalanches, they are much more common and so over a given interval, contribute much more to the total mass loss.

This model demonstrates that a significant fraction of the mass loss within the magnetosphere could come from small but frequent magnetic reconnection events (noting that this model is assuming that the magnetosphere is driven purely by the mass loading from Io, there may be further mass loss processes associated with solar wind interaction). These events then may not be detected by in situ spacecraft due to the spacecraft not being in a region that it would be able to observe this event. Further, if the spacecraft detects an event (as in sees some sort of magnetic perturbation) it may then be that by-eye or automatic detection (dependent on some threshold) does not select that event. As such this can help towards resolving the mass budget problem as described in chapter 2.

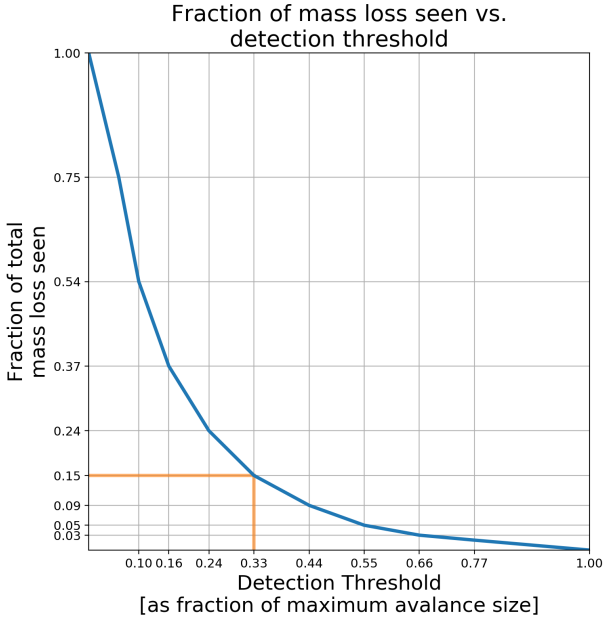

FIGURE 4.9: Mass loss seen with different detection thresholds. The detection thresholds are equivalent to the different avalanche sizes within the model as fractions of the largest size. The plot shows the fraction of the mass loss that would be missed if only events greater than X could be observed. The orange line shows an example, if only events larger than 33% of the maximum size could be observed, only 33% of the total mass loss would be seen. This figure is valid and the same for all threshold and input rates for a 512-celled grid.

4.5.3 Varying the detection threshold

Building on this point, we looked at how the number and distribution of events found by the *Vogt et al.* [2010] criteria changes as the threshold varies. Part of their criteria is that the field must increase a certain factor above a background field averaged over a 24 hour period. In their paper, for an average field strength of < 5 nT, a factor of 3 increase over the background field is required (if the background is greater than 5 nT, the required increase is only a factor of 2). In order to explore how changing this threshold effects the events that are selected we looked at where new events appeared and disappeared when varying this threshold between a factor of 1.5 (the least strict) and 5 (the strictest) in increments of 0.25. The results are shown in figure 4.10.

It is clear that as the threshold becomes less strict, many more events are found. Panel G (on figure 4.10 and subsequent figures of a similar format) shows the distribution of events for the threshold used in *Vogt et al.* [2010] of a factor of 3 which led to 249 events. As the threshold becomes less strict, from 3 to 1.5, the number of events found nearly doubles from 249 to 578. These new events appear mostly in the dusk sector. As the threshold becomes more strict, from requiring a factor of 3 increase over the background field to requiring a factor of 5, the number of events more than halves from 249 to 120

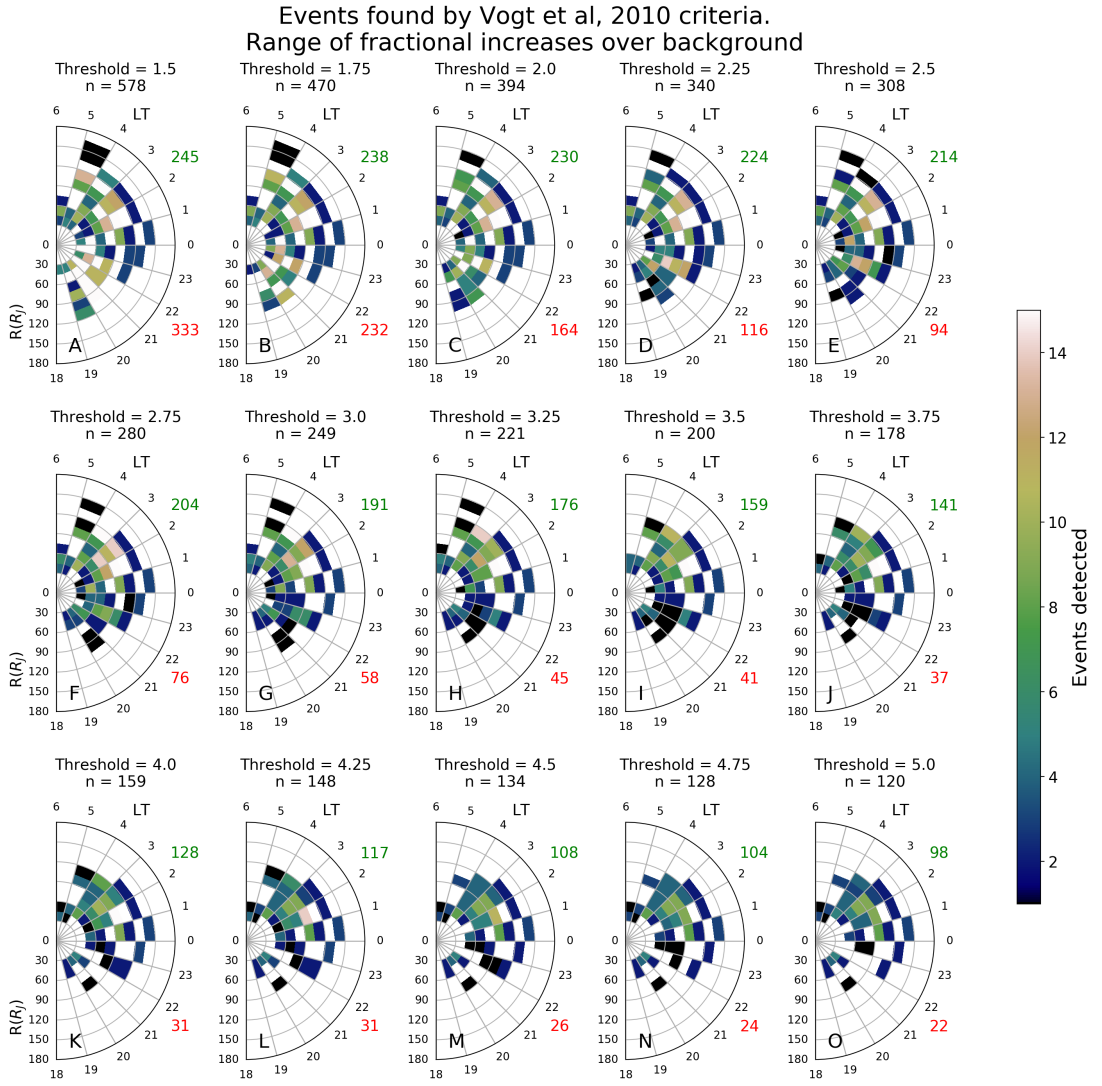

FIGURE 4.10: 15 panels showing the distribution of events as the criterion for fraction increase over the background field changes from 1.5 to 5 in increments of 0.25. The data are binned into local time bins of 1 hour and radial distance bins of 15 R_j. The colour scale represents the number of events detected in that bin. The number of events found at dusk and dawn are marked in red and green respectively.

with nearly all the events in the dusk sector disappearing. On the right of each panel the number of events in the dawn (in green) and dusk (in red) sector is listed. There is a 60% reduction in the number of events found in the dawn sector between the least and most strict thresholds whilst there is a 94% reduction in the number of events in the dusk sector. The events that remain for the stricter thresholds represent a subset of the *Vogt et al.* [2010] catalogue, and thus may be considered to be the largest, most unambiguous reconnection events in Jupiter's tail.

The smaller number of events that are found when the threshold is stricter almost certainly represent real events, but many of the additional events found with a less strict threshold are highly likely to represent other types of behaviour such as the motion of the

current sheet across the spacecraft. Therefore, whilst we include the less strict threshold panels (A to F) on this and subsequent figures, only the change in events from panels G to O will be considered. Considering just panels G to O (stricter threshold) on figure 4.10, there is an approximate 50% decrease in the number of events detected at dusk and at dawn. However, there are considerably more events observed at dawn than dusk, with at least four times as many events being observed at dawn than dusk. The raw number of events observed in different sectors of the tail may be misleading, however, since one section could have been observed much more frequently than another. In order to account for this we now consider the time spent by the spacecraft in different regions, and normalise by this quantity.

Figure 4.11 shows the number of hours of available data used by *Vogt et al.* [2010] (gathered from Voyager 1 & 2, Pioneer and Galileo). At small radial distances, the data are reasonably spread across the equatorial plane, but with increasing radial distance there is a strong dawn-dusk asymmetry with more coverage at dawn than dusk. The spacecraft spent the majority of its time between 60 to 150 R_J and between 2200 and 0300 LT. There is approximately 5000 hours of data in the dawn sector and 3000 hours in the dusk sector. We can now use the observation data to more rigorously assess the recurrence of our events.

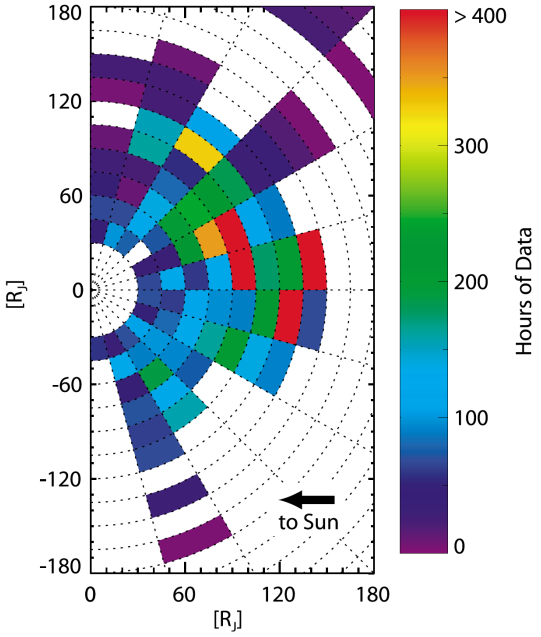

FIGURE 4.11: The number of hours of available data plotted in bins of 15 R_J in radial distance by 1 h in local time. This is an equatorial plane view, and the Sun is to the left. White represents bins with no available data. [From *Vogt et al.* [2010]]

Figures 4.12 shows the number of events detected per hour of spacecraft observation time as a function of radial distance and local time. Again considering just panels G to O (where we can be reasonably sure that the events are actual events), the rate of

event detection is considerably higher at dawn than at dusk, with dawn rates peaking between 0100 and 0300 LT. Having said that, as seen on the distribution of spacecraft observation time shown in figure 4.11, there is very little observing time outside of 90 R_J at dusk which may play a role in this lower rate i.e. the spacecraft may not have sampled far enough downtail to see all the dusk events.

As the threshold becomes stricter from panel G to O the rate of events detected at dusk rapidly drops off; until at the strictest threshold the rate of detection is ∼0.01 event per hour. Compared to the dawn side where there are peaks in event detection rates 6 times greater, it is clear that an event is much more likely to be observed at dawn. This disparity holds even if we compare just the radial distances within 90 R_J, outside of which there is very little data at dusk. The rate of event detection remains relatively high even up to the strictest threshold in the region within 120 R_J between 0100 and 0400 LT.

Figure 4.13 shows the distribution of events found as a function of radial distance and latitude in R_J. The number and rate per hour of events found north (in green) and south (in red) of the equatorial plane is also marked. As the threshold increases the number of events and rate of events drop. The rate of events found per hour decreases by a factor of ∼2 in the north and by a factor of ∼2.3 in the south between panels G and O. There is an 50% decrease in events found in the north and south between the same two panels.

Based on figure 4.13 it seems there is a slight asymmetry in the rate of event detection north or south of the current sheet. Reconnection events are expected to form in the current sheet and so the further from the current sheet the spacecraft is, the less likely it is to register a magnetic signature or if it does this signature will be smaller and may not be selected by eye or by event detection algorithms. The spacecraft latitude may also influence the background field level as the spacecraft moves between the plasma sheet and lobes. However, the majority of the data in this study were taken from Galileo at equatorial latitudes and previous work such as *Bagenal* [2007]; *Kronberg et al.* [2008b]; *Vogt et al.* [2014] have assumed a plasmoid height of 2 - 12 R_J, so the plasmoid is likely to always be seen (not considering the azimuthal or radial dimensions).

Censoring, or survival analysis is a way of accounting for the spacecraft leaving the viewing region (or not re-entering it) before an event (i.e. observing a plasmoid) can occur. Ignoring the times outside of the viewing region would likely mean underestimating the frequency of long waiting times because they would be more likely to be interrupted by a gap. Waiting times are thus grouped in to two types; uncensored (where the interval between two consecutive events does not contain a data gap) and censored (where the waiting time is the interval from the end of one event until the time the spacecraft leaves

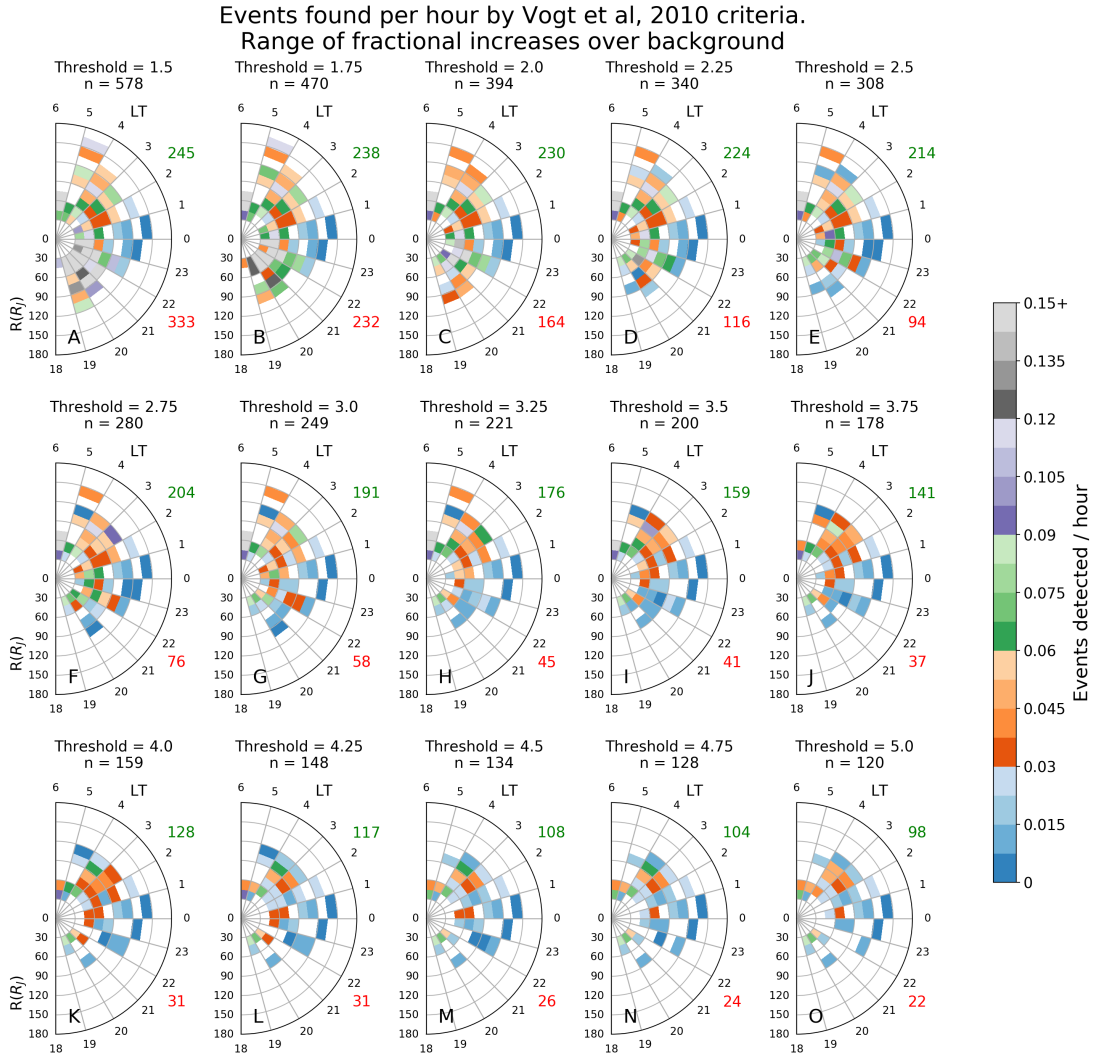

FIGURE 4.12: 15 panels showing the distribution of events as the criterion for fraction increase over the background field changes from 1.5 to 5 in increments of 0.25. The data are binned into local time bins of 1 hour and radial bins of 15 R_j. The color scale represents the number of events detected in that bin per hour of spacecraft observation time.

the viewing region). In the latter case, the actual waiting time is not known but it is known to be longer than the recorded time. Using the Kaplan-Meier estimator which is a maximum likelihood estimator [*Cox and Oakes*, 1984] that the waiting time exceeds a time, t_w a set of censored events can be derived and a waiting time distribution function can be estimated. In the censoring done by Freeman et al, [in preparation 2018], there is an underlying assumption that the probability of observing an event throughout the entire viewing region is equal. Based on the analysis presented in this section, this assumption may need to be revisited as there is a higher rate of event detection at dawn than dusk for a range of event detection thresholds. However, this is with the caveat that the observation time by the spacecraft is asymmetric, with very little observation time outside of 90 R_J at dusk.

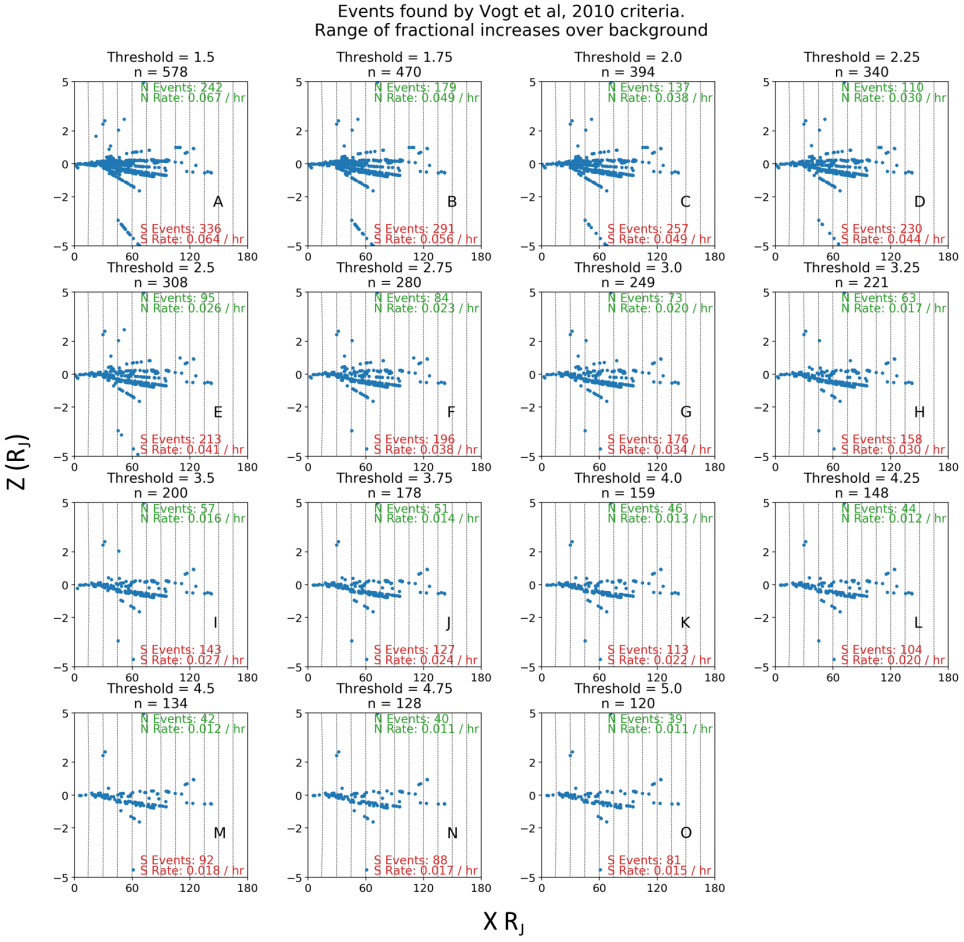

FIGURE 4.13: 15 panels showing the distribution of events as a function of latitude and radial distance as the criterion for fraction increase over the background field changes from 1.5 to 5 in increments of 0.25.

4.6 Summary

We present a cellular automaton sandpile model as an analogue for the Jovian magnetosphere in attempts to understand the role of the variable mass loading from Io in Jupiter's magnetospheric dynamics. We summarise our findings as follows:

1. With a constant threshold at which a cell becomes unstable and a finite-variance input distribution, our model recreates an Inverse Gaussian waiting time distribution between avalanche events, consistent with that found in observational data.

2. There are a range of distinct avalanche sizes within our model with frequency decreasing with increasing size.

3. Over a fixed time period, mass loss from frequent, smaller avalanches is much larger than the mass loss from the rarer, larger avalanches.

4. If we do not 'observe' these smaller events we miss a significant proportion of the total mass loss in our model. e.g. If we do not observe events smaller than 33% of the maximum sized avalanche, we only observe 15% of the total mass loss

5. Small, frequent mass loss events may be significant in the mass budget of Jupiter.

4.7 Appendix

4.7.1 Mass loading from Io

This table summarises work into calculating the mass loading of the Jovian magnetotail from Io.

Author	Measurements used	Neutral or plasma source	Mean Loading Rate ($kg\ s^{-1}$)	Range ($kg\ s^{-1}$)
Sandel et al. [1979]	Extreme Ultra-violet (EUV)	Plasma	1000	—
Hill [1979]	Plasma flow	Plasma	1000	—
Barbosa et al. [1983]	EUV	Plasma	850	—
Smyth [1992]	Optical emission lines	Plasma	225	—
Bagenal [1997]	Plasma fluxes	Plasma	—	180 - 580
Wilson et al. [2002]	Sodium emission lines	Neutral	—	130 - 970
Delamere et al. [2004a]	Plasma conditions	Neutral	—	363, 392, 1180
Saur et al. [2003]	Plasma fluxes and UV	Plasma	200	—
Smyth and Marconi [2005a]	3D calculations	Plasma	275	—
Smyth and Marconi [2005b]	Neutral cloud model	Plasma	—	800 - 1200
Delamere et al. [2004b]	Cassini UVIS	Neutral	—	1500 - 600
Steffl, A., priv. comm., [2015]	Cassini UVIS	Neutral	—	500 - 700

TABLE 4.1: The mass loading rates collated from literature are summarised here in chronological order. For each loading rate the measurements used and whether it is a neutral source or plasma source is stated. Some works quoted single values while others quoted ranges and this is reflected in the final two columns of the table. UVIS is the Cassini Ultra-Violet Imaging Spectrograph

4.7.2 Model Output

Tables 4.2 and 4.3 below contain the results from model runs discussed in the text and illustrated in figures 4.3, 4.4, 4.5, 4.6, 4.8 and 4.9. The table also displays our predicted values using the methods detailed in the paper. The model was run for a variety of thresholds and input rates.

Threshold	Input. (detail in caption)	SWA Waiting Time (SWAwt) Mean (model)	SWAwt Mean (predicted)	SWAwt Variance (model)	SWAwt Variance (predicted)
0.1	U[0, 0.02]	51.17	51.20	16.83	17.07
0.1	U[0, 0.002]	511.97	512.00	172.02	171.67
0.2	U[0, 0.02]	102.41	102.40	34.37	34.13
0.2	U[0, 0.002]	1024.01	1024.00	341.76	341.33
0.3	U[0, 0.02]	153.62	153.60	50.84	51.20
0.3	U[0, 0.002]	1535.96	1536.00	512.44	512.00
0.4	U[0, 0.02]	204.80	204.80	68.45	68.27
0.4	U[0, 0.002]	2048.03	2048.00	682.94	682.67
0.5	U[0, 0.02]	256.03	256.00	84.6	85.33
0.5	U[0, 0.002]	2559.9	2560.00	854.01	853.33
0.6	U[0, 0.02]	307.26	307.20	102.54	102.40
0.6	U[0, 0.002]	3070.9	3072.00	1023.12	1024.00

TABLE 4.2: Table summarising model runs and results. Column 1 gives the threshold i.e. the maximum gradient between two adjacent cells. Column 2 gives the distribution of the input followed by the range or the mean and standard deviation. Column 3 gives the mean waiting time for a systemwide avalanche from the model and column 4 gives the predicted mean waiting time for a systemwide avalanche. Column 5 gives the waiting time variance for a systemwide avalanche from the model and column 6 gives the predicted waiting time variance. There is no variation on waiting times for the constant input cases. The input follows the following forms. "U[0,0.02]" is a uniform distribution in the range 0 to 0.02 (and similar for U[0, 0.002]). "Constant (0.01)" means a constant input of 0.01 per iteration.

Threshold	Input. (detail in caption)	SWA Waiting Time (SWAwt) Mean (model)	SWAwt Mean (predicted)	SWAwt Variance (model)	SWAwt Variance (predicted)
0.7	U[0, 0.02]	358.44	358.40	119.69	119.47
0.7	U[0, 0.002]	4584.06	3584.00	1194.01	1194.67
0.8	U[0, 0.02]	409.61	409.60	136.99	136.53
0.8	U[0, 0.002]	4095.5	4096.00	1364.86	1365.33
0.9	U[0, 0.02]	460.82	460.80	153.87	153.60
0.9	U[0, 0.002]	4607.94	4608.00	1535.45	1536.00
1.0	U[0, 0.02]	512.03	512.00	171.05	170.67
1.0	U[0, 0.002]	5119.96.	5120.00	1706.32	1706.67
0.1	Constant (0.01)	51.2	51.2	—	—
0.2	Constant (0.01)	102.4	102.4	—	—
0.3	Constant (0.01)	153.6	153.6	—	—
0.4	Constant (0.01)	204.8	204.8	—	—
0.5	Constant (0.01)	256.0	256.0	—	—
0.6	Constant (0.01)	307.2	307.2	—	—
0.7	Constant (0.01)	358.4	358.4	—	—
0.8	Constant (0.01)	409.6	409.6	—	—
0.9	Constant (0.01)	460.8	460.8	—	—
1.0	Constant (0.01)	512.0	512.0	—	—

TABLE 4.3: Table summarising model runs and results. Column 1 gives the threshold i.e. the maximum gradient between two adjacent cells. Column 2 gives the distribution of the input followed by the range or the mean and standard deviation. Column 3 gives the mean waiting time for a systemwide avalanche from the model and column 4 gives the predicted mean waiting time for a systemwide avalanche. Column 5 gives the waiting time variance for a systemwide avalanche from the model and column 6 gives the predicted waiting time variance. There is no variation on waiting times for the constant input cases. The input follows the following forms. "U[0,0.02]" is a uniform distribution in the range 0 to 0.02 (and similar for U[0, 0.002]). "Constant (0.01)" means a constant input of 0.01 per iteration.

Chapter 5

Low Frequency Extension of the Saturn Kilometric Radiation as a proxy for magnetospheric dynamics

5.1 Introduction

The purpose of this chapter is to assess the use of the Saturn Kilometric Radiation (SKR) as a proxy for magnetospheric dynamics and solar wind activity at Saturn. The SKR was discussed in detail in chapter 2 therefore here we discuss just the main features and mechanism of the SKR and a specific feature of the SKR; a low frequency extension. The Saturn Kilometric Radiation (SKR) was originally detected by Voyager 1 [*Kaiser et al.*, 1980]. The typical frequency range is from 3 kHz to 1.2 MHz, peaking between 100 and 400 kHz [*Kaiser and Desch*, 1984; *Lamy et al.*, 2008]. The SKR is quasi-continuous and is generated via the cyclotron maser instability (CMI) [*Wu and Lee*, 1979; *Lamy et al.*, 2010, 2011; *Mutel et al.*, 2010; *Menietti et al.*, 2011] on field lines near the auroral regions. The CMI process involves the beaming of a radio emission excited by energetic (1 - 20 keV [*Cowley et al.*, 2004]) auroral electrons via cyclotron resonance at frequencies close to the local electron cyclotron frequency, $f_c = qB/(2\pi m)$, where q is the electron charge, B is the local magnetic field strength and m is the electron mass. The frequency of the emission is proportional to the strength of the local magnetic field of the source and is therefore inversely proportional to the height of the source cubed ($1/\mathrm{R}^3$). *Lamy et al.* [2010] showed the difference between the SKR emission frequency and the local electron cyclotron frequency to be less than 2% and so, using an internal magnetic field

model by *Dougherty et al.* [2005], *Kimura et al.* [2013] showed that the peak emission of the SKR (between 100 and 400 kHz) originates from sources between 0.5 and 1.5 R_S from the planet (1 R_S = 60268 km). The SKR can extend down to 10 kHz or below, which equates to a source region at 5 R_S or further.

The features that we will be focusing on in this study are SKR Low Frequency Extensions, an expansion of the entire kilometric spectrum and in particular of the main band from high to low frequencies. An LFE is a signature of a global intensification of the SKR spectrum and, like the quasi-continuous higher frequency SKR, is produced via the CMI mechanism. LFEs were studied in particular detail by *Jackman et al.* [2009a] who correlated them with episodes of magnetotail reconnection at Saturn and associated them with an extension of the radio source to higher altitudes along the field lines. They suggested that following reconnection, field-aligned currents are set up whose electron density exceeds that which can be carried by the plasma without more acceleration. This leads to a taller acceleration region where the 'top' is farther up the field line and may coincide with an SKR source region at correspondingly large distances. Here, the magnetic field strength will be lower, hence the cyclotron maser will produce radio emissions at lower frequencies. At Earth the acceleration region and the CMI source region coincide as the former is required to produce a plasma cavity devoid of cold plasma and thus the conditions for CMI to operate [e.g. *Delory et al.*, 1998; *Louarn and Le Quéau*, 1996; *Pritchett et al.*, 2002]. At Saturn the plasma may already be low enough density to allow the CMI to operate without the acceleration region, but the exact link between the acceleration region and the source region is not well understood.

Through examining long intervals of SKR data the aims of this study are to automate the search for LFEs so that a large statistical base can be built up and to examine their properties and their use as a proxy for magnetospheric dynamics. We focus our statistical search on Cassini data from 2006 due to the deep tail orbits and good spacecraft local time and low latitude coverage. These factors have also made 2006 of interest to those looking at magnetotail dynamics and as such there is a large catalogue of tail reconnection events [*Smith et al.*, 2016] (hereafter S16) that we can compare to. Previous work such as *Jackman et al.* [2009a] has defined LFEs based on intensification and the change in frequency of the emission somewhat arbitrarily. For this work we make this identification process more robust, by statistically examining the SKR spectrum for significant departures from 'average' behaviour. In section 5.2 we discuss the dataset used, while section 5.3 outlines the criteria for detecting LFEs. Sections 5.4 to 5.6 discuss the properties of LFEs such as their latitudinal and local time visibility (section 5.4), the properties of a subset of the LFEs associated with solar wind dynamics (section 5.5), and the non-solar wind associated LFEs (section 5.6). Section 5.7 examines the relationship of the LFEs with known reconnection events.

5.2 Data

For this chapter we combine various datasets from the Cassini spacecraft at Saturn in 2006. Cassini's orbit in 2006 gave good tail coverage in terms of local time and latitude (see Figure 5.1) as well as containing the deepest tail-orbits of the Cassini mission (out to 68 R_S). Processed RPWS data [*Gurnett et al.*, 2004] is used to develop criteria for selecting LFEs. We then use Cassini Magnetometer [*Dougherty et al.*, 2004] data, a catalogue of reconnection events [*Smith et al.*, 2016], the northern and southern SKR phase systems [*Lamy*, 2011] and modelled solar wind data from Michigan Solar Wind Model (mSWiM) [*Zieger and Hansen*, 2008], to examine multiple aspects of magnetospheric dynamics.

We use a high-resolution (90 second) power time series integrated over the 40 - 100 kHz and 100 - 600 kHz spectral bands during 2006 in order to develop our criteria for selecting LFEs. The power is given in W sr^{-1}. We also use a high resolution (90 second) dataset consisting of the intensity of the observed radio waves as a function of time and frequency for comparison with our power dataset to ensure we are selecting events that represent low frequency extensions. This flux intensity is given in units of W m^{-2} Hz^{-1} and normalised to one astronomical unit (AU) from the source region. These datasets are similar to those derived by *Lamy et al.* [2008] using RPWS data which is based on previous work by *Zarka et al.* [2004] and *Cecconi and Zarka* [2005b]. Our dataset differs slightly from the dataset used by *Lamy et al.* [2008] in that whereas they restricted data to those with a circular polarisation ($|V|$ >0.8) and a signal to noise ratio (>10 dB), we have no criterion placed on the circular polarization. The 100 - 600 kHz range is selected to include the main band region of the SKR (100 - 400 kHz). The 40 - 100 kHz range is selected to include the region below the main band where a low frequency extension would extend in to, the lower limit of 40 kHz being selected to limit the pollution from narrowband emissions.

In order to assess the use of LFEs as a proxy for magnetospheric dynamics, we use the S16 catalogue of 2094 dipolarisation, plasmoids and travelling compression regions (TCRs) detected during 2006. Many of these events occur in chains, with multiple reconnection signatures observed within 3 hours of each other. These chain events were deemed in S16 to represent multiple signatures of magnetic field reconfiguration likely linked to the same episode of reconnection. We thus suggest that chain events may be linked to a single response of the SKR and hence we only consider the first event out of each chain. This left a total of 234 plasmoids, TCRs and dipolarisation detected between day of year (DOY) 1 and 282 of 2006 as the in situ viewing conditions for reconnection events changed significantly toward the end of the year. Using the mSWiM model which propagates measurements of various solar wind parameters taken near Earth to the orbit

of Saturn we are also able to compare our LFE catalogue with simultaneous solar wind behaviour.

To investigate the relationship between the occurrence of LFEs and the SKR phase, we use the phase dataset developed by *Lamy* [2011] that organises SKR maxima. They used Lomb-Scargle analysis, a technique employed to perform spectral analysis of non-continuous data, over a 6-year period from 2004 to 2010 to find the SKR period and related phase systems for each hemisphere. The northern and southern emissions were separated by their circular polarisations (left-handed for southern, right-handed for northern) allowing individual periods to be found and phase systems defined. Each hemispheric phase system has a phase of $0/360°$ when the respective SKR emission reaches its peak.

5.2.1 Visibility of SKR

The visibility of the SKR varies with spacecraft local time, latitude and radial distance. Due to the coned beaming of the emission from the high-latitude northern and southern source regions, there exists an equatorial radio shadow zone with the furthest extent at 6 - 7 R_S for frequency range 80 - 900 kHz [*Lamy et al.*, 2008]. Figure 7 of *Lamy et al.* [2008] is a 2-D schematic of the equatorial shadow zone. Additionally, figure 11 from *Lamy et al.* [2008] shows SKR spectra as a function of spacecraft local time and latitude based on 2.75 years of RPWS observations. Whilst the SKR is observed from all local times, the maximum intensity and bandwidth are recorded on the morning side between 02h and 08 h with weakest emissions between 16h and 20h. Most of the SKR is observed between latitudes of $-20°$ to $+60°$ [*Lamy et al.*, 2008; *Kimura et al.*, 2013] whilst at latitudes greater than $\pm$ 20 $°$ the visibility of the lower frequencies increases. Due to this variability with the location of the observer, our criteria for selecting LFEs are dependent on spacecraft location.

5.3 Automated Detection of Low Frequency Extensions

5.3.1 Criteria

We now discuss our criteria for automatically selecting low frequency extension features from the SKR. We examined the behaviour of the SKR throughout 2006, including the statistical variations in power and emission frequency and used this to identify a training set of LFEs by visual inspection. We then developed criteria that best picked out these types of events. When trying to identify a LFE we were looking for three

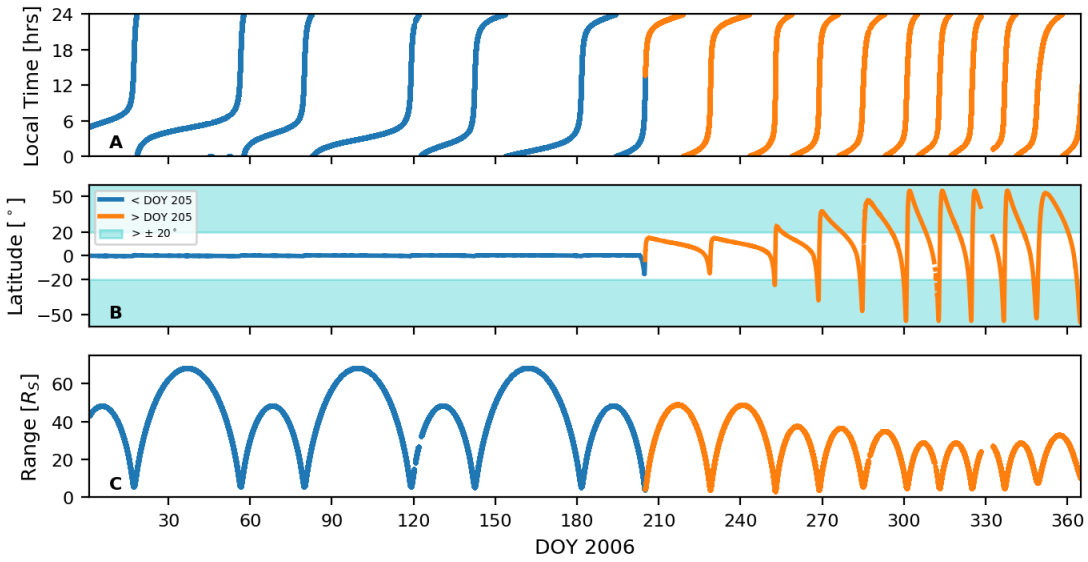

FIGURE 5.1: Local time (Panel A), latitude (Panel B) and radial distance of Cassini from Saturn in R_S (Panel C). The location traces are split between pre (blue) and post (orange) DOY 205 when Cassini changed to a higher latitude trajectory. We separated our data into regions where the spacecraft latitude was less than | 20°| and where the latitude is greater than |20°|. The latter region is marked by the cyan shaded regions on panel B.

features that needed to be quantified: (1) An intensification in the higher frequency region; (2) A significant extension of the emission down to lower frequencies and (3) An intensification at these lower frequencies (the second and third feature being closely linked). In developing these criteria we account for the significant variation of SKR visibility with both spacecraft local time and latitude as has been shown by several previous studies including *Lamy et al.* [2008]; *Kimura et al.* [2013] and discussed above.

As discussed in section 5.2, during 2006 Cassini explored a range of latitudes (-56° to +55°) and due to the differing SKR visibility we split our analysis into equatorial and higher latitudes to illustrate the different behaviour. Figure 5.2 shows the variation of SKR power with local time over two spectral ranges from our dataset, 40 - 100 kHz and 100 - 600 kHz as a function of spacecraft local time during 2006 for (A) Latitudes between -20° and +20° and, (B) latitudes greater than +20° or less than - 20°, for the 80 and 70th percentile respectively. For each frequency range the received power is initially binned into local time bins four hours wide. These bins are then interpolated to 0.1 hour bin sizes and smoothed over a four hour window to give a smooth curve (coloured lines in Figure 5.2). This gives a power threshold for each local time section 0.1 hours wide that the power must exceed. Results from comparison with a training set matched with a desire for statistical significance gave the final thresholds as the 80th percentile for the 40 - 100 kHz spectral range and the 70th percentile for the 100 - 600 kHz spectral range.

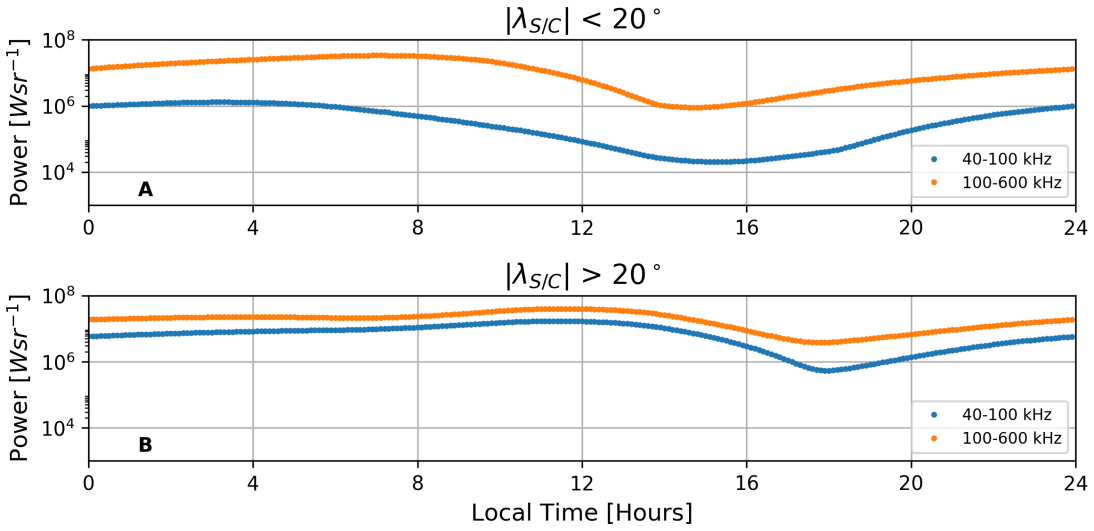

FIGURE 5.2: The integrated SKR power across two spectral ranges, 40 - 100 kHz (blue) and 100 - 600 kHz (orange) as a function of spacecraft local time. The 80th percentile of the 40 - 100 kHz spectral range and the 70th percentile of the 100 - 600 kHz spectral range is shown. Panel A shows low latitudes regions between -20° and 20°, Panel B shows latitudes greater than ±20°. The data were initially binned into 4 hour local time bins and then interpolated to bins 0.1 hours wide and then smoothed across 4 hours.

A key benefit of this approach is to achieve a smooth development of the automated criteria to avoid large sharp threshold jumps as the spacecraft moves between adjacent local time sectors. Due to the trajectory of the spacecraft there is no time spent by the spacecraft at local times 2 - 3 h and 14 - 15h for latitudes greater than ±20° despite a threshold being shown at these local times. The threshold shown at these local times has been interpolated across the data gaps but will not be applied to any data.

To summarise, our criteria for selecting LFEs are as follows:

1. The integrated power in the 100 - 600 kHz frequency band must be greater than the local time dependent 70th percentile for each latitude range.

2. The integrated power in the 40 - 100 kHz frequency band must be greater than the local time dependent 80th percentile for each latitude range.

5.3.2 Clustering

The LFE algorithm returns each time step in the RPWS dataset that matches the criteria as defined above. This gave 37077 points across 2006 that satisfied the criteria. In practice, the SKR displays intensifications and LFEs on much longer timescales than the 90 second cadence of the dataset, and thus we applied a simple clustering algorithm

to gather the points which fulfil the LFE criteria into local groups which represent distinct LFEs as shown in Figure 5.3. The "maximum gap size", defined below as 200 minutes, was again empirically tuned to give the best agreement with our by-eye training set. The clustering works as follows:

1. First point, i_1, is put into cluster 1
2. If at second point, i_2, i_2 - i_1 <= X, where X is the maximum gap size = 200 minutes, i_2 is put into cluster 1.
3. Else if i_2 - i_1 > X, a new cluster is started and, i_2 is put into that.
4. Continue for all points

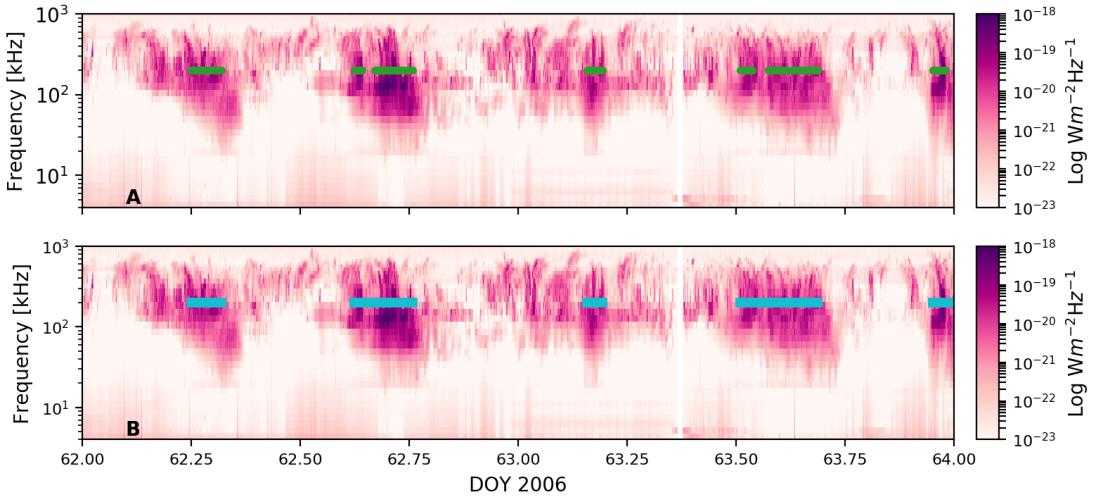

FIGURE 5.3: Example of LFE point clustering on an two day period between DOY 62 and 64 2006. Panel A shows 258 points (green circles) that satisfy the LFE criteria. Panel B shows those points clustered into 5 distinct LFEs (cyan rectangles) following the removal of the clustered events shorter than 30 minutes. The maximum distance allowed between two points to be part of the same cluster is 200 minutes.

Following the clustering of the points that meet the LFE criteria we inspected the catalogue and removed those shorter than 30 minutes to ensure we were selecting sustained LFE events. On further examination of the entire catalogue, it became apparent that our LFE detection criteria selects intense short events (such as those shown in Figure 5.3) well, but does not select longer duration events that, whilst intense, are not continuously *extended*, as successfully. These longer duration events are variable in intensity throughout and therefore can be split into multiple events by our algorithm when they are in fact a single event.

To account for this we "join" shorter events based on the intensity of the power between them. For all events within 2 Saturn rotation periods (1 rotation taken here as 10.7

hours) of the previous event, if more than 50% of the intervening time steps exceed the 60th percentile in the 100 - 600 kHz spectral range, we join these two events into one event. Figure 5.4 shows an example of this joining. The two cyan events in panel A are selected individually by the LFE criteria described above. They are then joined together to form the yellow event shown in panel B due to the SKR remaining significantly enhanced between them. Several further criteria are then applied to ensure we are selecting sustained low frequency extensions. We remove events that start or end with a data gap or those with a large data gap within them. We also remove several events around spacecraft periapsis when the combination of spacecraft velocity and viewing conditions mean we cannot be confident that we are detecting an LFE from the spectrum. Following the application of these criteria we find 282 LFEs for all of 2006.

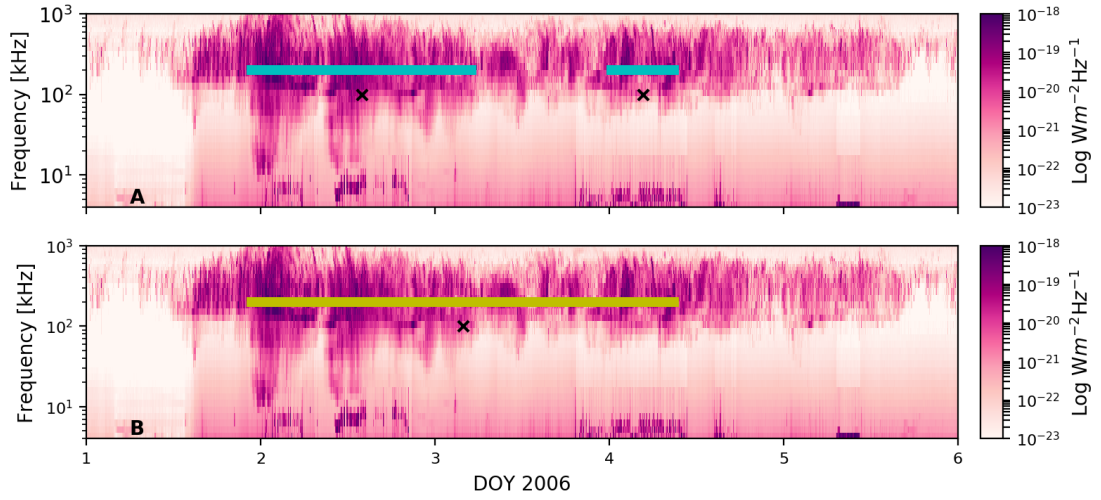

FIGURE 5.4: An example of the application of the 'joining' criteria as discussed in the text. This shows five days of SKR data from DOY 1 - 6. Panel A shows the "LFEs" that were detected by the original criteria and Panel B shows the 'new' LFEs as a result of the joining criteria. By eye it is clear that the SKR remains intense between the original LFEs (particularly when compared to between the events shown in Figure 5.3) and that the whole feature has a different morphology to the events shown in Figure 5.3.

5.4 Properties of LFEs

Now we have a final list of LFEs we begin to investigate their properties. In this section we will look at some of the properties of the LFE catalogue and what this can tell us about their role within the magnetosphere of Saturn. We first consider the distribution of LFEs detected across spacecraft local time and latitude.

5.4.1 LFE Viewing

Figure 5.5 shows the latitude spread of spacecraft trajectory and LFE observations, directly compared (panel A) and normalised to time spent by the spacecraft at that latitude (panel B). Similarly, Panel C and D show the local time spread of spacecraft trajectory and LFE observation, directly compared (panel C) and normalised to time spent by the spacecraft at that local time (panel D). We take the spacecraft latitude and local time for all points throughout each LFE. When normalised to the time spent at the local time (i.e. a fraction of time at a given local time (or latitude) that the LFE criteria was being met), LFEs are observed fairly evenly across most local times with a peak in the early morning sector and a small dip in the pre-dusk sector. This dip comes in the same local time region where the lowest SKR power is seen as shown on figure 5.2. This may suggest that our location dependent criteria do not sufficiently account for the variation in viewing. It should be noted that very little time is spent by the spacecraft at local times between $\sim$ 10 and 19h LT and so the fraction in sectors outside of this region is likely a better representation of LFE viewing. Not many LFEs are observed at equatorial latitudes as a fraction of time spent there and there are almost twice as many observed in the southern hemisphere than the northern hemisphere. As with the local time distribution, the time spent at certain latitudes by the spacecraft is important. It should therefore be noted that 58% of 2006 was spent between ± 1 ° and so the fraction in this region is most likely a better representation of LFE viewing than for example for all latitudes greater than $\pm$ 30 ° which only make up 11% in total of 2006.

For the use of the SKR as a proxy for magnetospheric dynamics, these results are promising. There is good LFE detection at all local times and latitudes. Comparing to in situ algorithms for detecting reconnection events we note that the S16 study only used data when Cassini was on the nightside (18 - 06h) of the planet whereas we observe LFEs whilst the spacecraft is outside this sector, at local times between 6 and 11h. We also observe LFEs whilst Cassini is in the sheath. As such we are potentially observing magnetospheric dynamics that would otherwise be missed. LFEs thus have the advantage over in situ (field and plasma) measurements that they are visible from most spacecraft locations and thus have potential to be used as a remote proxy for magnetospheric dynamics. In order to explore the degree to which they can be used as a remote proxy, we will (in subsequent chapter sections) test their relationships to various tail reconnection and solar wind dynamic pressure. This can then inform the degree of confidence with which we can use LFEs as a proxy for magnetospheric dynamics.

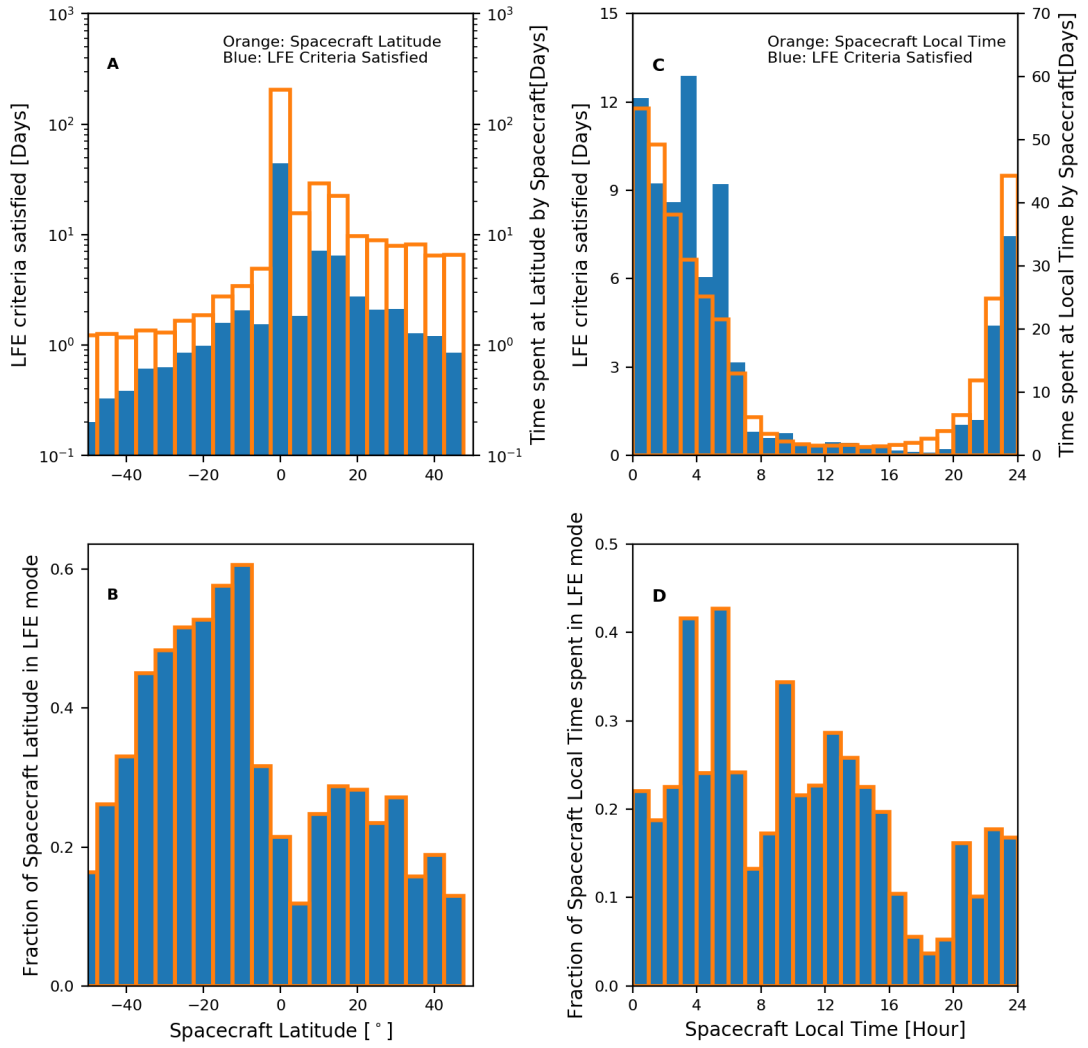

FIGURE 5.5: Distribution of LFEs as a function of spacecraft latitude (Panels A and B) and local time (Panels C and D). Panel A shows the number of days within each spacecraft latitude that satisfied the LFE criteria (blue) and the distribution of spacecraft days at each latitude (orange outline). Panel B shows the fraction of the time the spacecraft spent at each latitude that satisfied the LFE criteria (blue and orange outline). The bin sizes are 5 ° latitude. There is a log scale on Panel A for both y-axes emphasising how many more events are seen at equatorial latitudes and how much more time the spacecraft spent there. Panel C shows the number of days within each spacecraft local time that satisfied the LFE criteria (blue) and the distribution of spacecraft days at each local time (orange outline). Panel D shows the fraction of the time the spacecraft spent at each local time that satisfied the LFE criteria (blue and orange outline). The bin sizes are 1 hour of local time.

5.4.2 LFE Event Classification

We expect to see two types of LFE: 'long' events possibly associated with solar wind dynamics [*Desch and Rucker*, 1983; *Kurth et al.*, 2005; *Bunce et al.*, 2005; *Clarke et al.*, 2009; *Bunce et al.*, 2010; *Kurth et al.*, 2016] and are usually longer than one planetary

rotation, and also 'short' events that have been associated with other phenomena such as tail reconnection [*Jackman et al.*, 2009a; *Lamy et al.*, 2013] and are on the order of a few hours long.

On examining the catalogue of LFEs that we have detected we do see two distinct morphologies of LFE: Longer LFEs that remain intense for multiple planetary rotations (see example in figure 5.4) and shorter LFEs that drop off significantly in intensity between events (see examples in figure 5.3). In order to differentiate between the two we select a threshold split time. Events shorter than this time are classified as 'short', those longer are classified as 'long'. We investigated the average behaviour of the solar wind dynamic pressure during a selection of 'long' and 'short' LFEs for a range of split times. Based on this we selected a threshold time of 20 hours which appears to give the best by-eye (in terms of morphology as discussed) and statistical separation (in terms of relationship with solar wind dynamic pressure) of the different LFE types. The distribution of solar wind dynamic pressure during long LFEs had a mean and a median twice that of the distribution for during short LFEs and a maximum dynamic pressure 50% larger (shown in figure 5.6A). We also performed a Kolmogorov-Smirnov (KS) statistical test which gave a KS statistic of 0.31 and a p-value $< 10^{-70}$ which means we can conclude that the two groups are very likely not sampled from the same overriding distribution i.e. the solar wind behaviour is much different during one set of LFEs to the other. We then further compared the solar wind dynamic pressure average behaviour during long LFEs to the behaviour across the whole year (shown in figure 5.6B). Again, the average dynamic pressure was much stronger on average during the long LFEs than for the year as a whole.

Figure 5.7 shows the longer (blue) and shorter (orange) LFEs plotted against solar wind dynamic pressure as given by the mSWiM propagation model during 2006 for a split time between short and long LFEs of 20 hours. The closest point of apparent opposition, where mSWiM propagation is most accurate, for 2006 is day of year 56. Within 75 days of this period (purple on figure 5.7) we assume an error on mSWiM of $< \pm$ 20 hours, whilst we assume the error is greater than this (up to 50 hours) for periods further than 75 days (cyan on figure 5.7) from apparent opposition. 2006 was also at the minimum of solar cycle 23 and as such there are fewer transient events such as interplanetary coronal mass ejections meaning that mSWiM is particularly accurate. We will now investigate these two classifications further in sections 5.5 and 5.6.

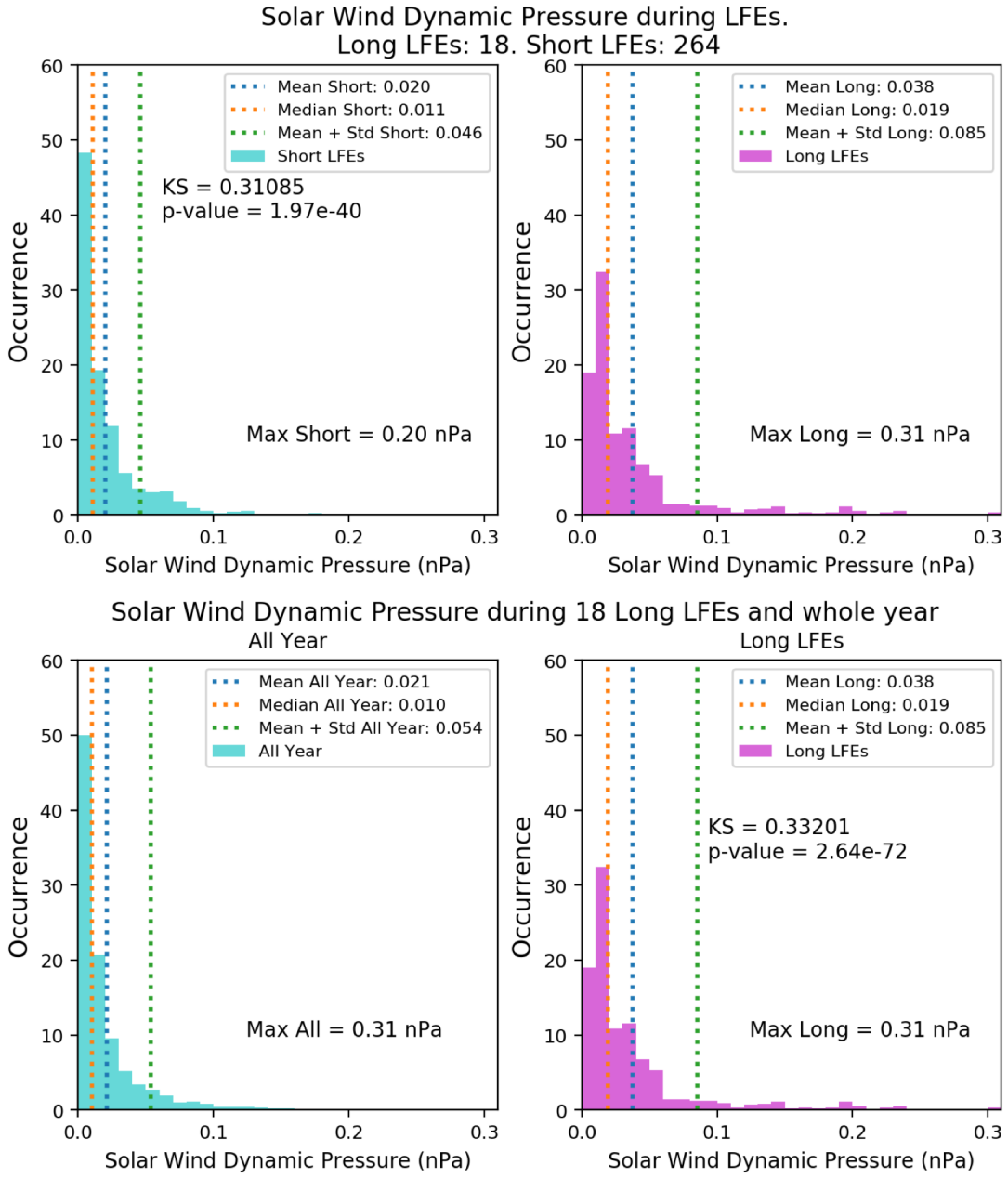

FIGURE 5.6: Comparing the behaviour of the solar wind between short vs. long LFEs (Panels A1 and A2) and behaviour of the solar wind during the whole of 2006 vs. long LFEs (Panels B1 and B2). The solar wind data is taken from the mSWiM model [*Zieger and Hansen*, 2008].

5.5 Long LFEs

In this section we examine further the events that may be associated with solar wind dynamics as per the blue shaded regions in Figure 5.7. We examine their temporal properties and their relationship with phase.

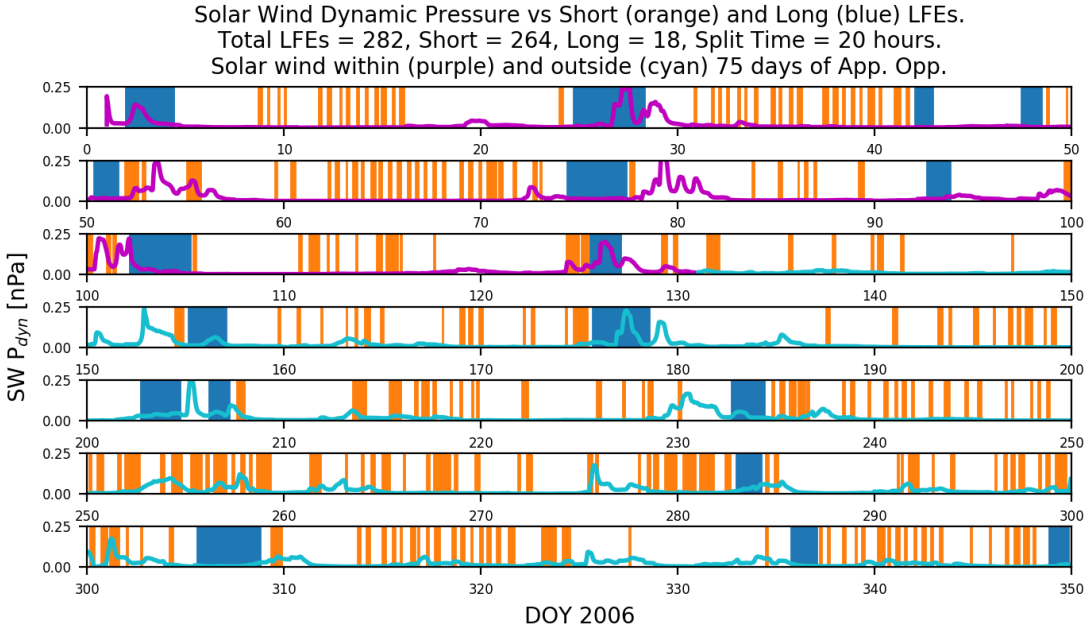

FIGURE 5.7: Comparing solar wind dynamic pressure (purple and cyan) as a function of time with long solar wind driven events (blue) and shorter non- solar wind driven events (orange). There are a total of 282 LFEs, 264 of which are 'short' and 18 that are 'long'. Solar wind dynamic pressure calculated within 75 days of apparent opposition is plotted in purple whilst that calculated further than 75 days is in cyan.

5.5.1 Long LFEs: Temporal Properties

The solar wind movement away from the sun is highly time and space dependent. The rotation of the sun with a period, $P_{Rot} \approx 25$ days as seen by Saturn, results in the interaction of solar wind streams of different speeds. This leads to two types of fronts; compression regions as high-speed solar wind pushes against slower moving plasma ahead, and rarefactions where high-speed streams pull away from slower moving plasma behind [*Parker et al.*, 1964]. These features last longer than a solar rotation and so sweep past the planet at a periodicity of $\sim$ 25 days as co-rotating interaction regions (CIRs). *Jackman et al.* [2004] examined Cassini measurements of the interplanetary magnetic field (IMF) during Saturn approach. They found that the IMF during this period was highly modulated during each solar rotation by CIR-related compressions lasting approximately five days, and longer rarefaction regions typically lasting around seven days. As mentioned, 2006 was at the minimum of solar cycle 23 and so we would expect a well structured two-sector (2 alternating compression region/rarefaction regions) solar wind which would give a period of $\sim$13 days for compression region arrival. *Hanlon et al.* [2004] investigated the evolution of the solar wind between 1 and 5 AU (the orbit of Jupiter) using multiple spacecraft observations and found that two compression regions at the orbit of Earth had merged into one by the time that they reached the orbit of

Jupiter. They examined a transient solar wind stream from Cassini upstream magnetometer data from the period prior to Jupiter closest approach. They found by ballistic projection that it is a merged interaction region (MIR) from two unusually fast solar wind streams that were observed upstream near Earth (they were able to do this due to a planetary alignment at the time). This projection was then confirmed using an MHD propagation model on solar wind data taken at Earth at the time. As such, we might expect either a period of 13 days (if no merging occurs) or a period of ∼25 days which was also seen by *Kurth et al.* [2016]. We now look at the properties of our long LFEs to see if they are consistent with these phenomena.

Figure 5.8 shows the distribution of long LFE durations (Panel A) and waiting times (Panel B). There is a wide range of event lengths with only a slight peak between 20 and 30 hours, highlighting the variable nature of these events which is consistent with the time and spatial variability of the CIRs. The long LFEs can last for many planetary rotations. Four events have a waiting time of less than 10 days, less than either of the periodicities we might expect, although two of these can be accounted for by multiple large LFEs during periods of increased solar wind dynamic pressure. 50% of the LFEs have a periodicity of between 18 and 30 days. This is within the region of time that we might expect if these longer events were associated with the dynamics of the solar wind with one compression per solar rotation. One event had a waiting time of approximately 48 days ($\sim 2\ P_{Rot}$) which suggests we missed an event within a cycle (around DOY 255 on Figure 5.7).

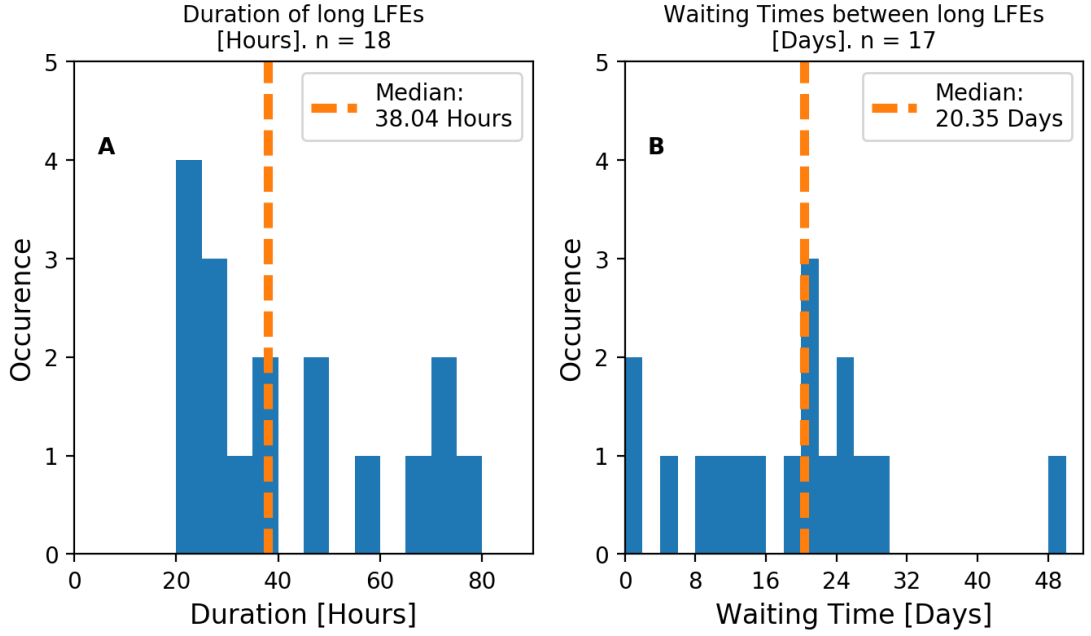

FIGURE 5.8: Solar wind associated LFE durations in hours (Panel A) and waiting time in days (Panel B). The median is marked by the orange line. There are a total of 18 solar wind associated LFEs and 17 waiting times between consecutive events

5.5.2 Long LFEs: SKR Phase

We next look at the relationship of the long LFEs events to SKR phase. If the long LFE events are associated with the solar wind then we would expect no relationship between the timing of these events and the phase of the SKR since the solar wind behaviour is independent of the rotation of Saturn. Figure 5.9 shows the northern and southern system SKR phases at the onset time of the long LFEs. There is no clear clustering of the LFEs at a particular phase, although there are only 18 events and so a relationship may become clearer with more events. It is unclear as to whether we would expect a correlation with long LFEs and the SKR phase: A shock can arrive at any time and so if it this shock that directly drives the long LFE we would expect no relationship with phase. However, this shock arrival may also trigger reconnection, perhaps delayed until some favourable phase when the plasma sheet is thinnest. More events would be required to look further into this with statistical confidence. These events last several planetary rotations and thus the phase of the planet can go through multiple cycles. In light of this we also check the phase relationship for the phase taken at the centre of the event and find that there is still no clear relationship.

We note that we do observe a dependence on phase within some of the long LFEs. During these LFEs that last several planetary rotations, there are multiple intensifications of the SKR and/or multiple extensions down to lower frequencies. These very often coincide with the peak in the SKR phase suggesting there is still some underlying rotational component during these times. An example is shown in figure 5.10

5.6 Short LFEs

We next look at the shorter events from our LFE catalogue. By eye in Figure 5.7 it seems that these events do not typically correlate with increases in solar wind dynamic pressure. We examined this further by comparing the solar wind dynamic pressure behaviour during these short LFEs against the behaviour across all of 2006 (shown in figure 5.11). We found that the mean and median of these distribution are essentially equal and a KS-test comparing the two distributions would suggest that they are very similar. From this we conclude that there is no significant change in solar wind dynamic pressure during short LFEs to non-LFE times and therefore that the short LFEs have no solar wind dependence. In this section and section 5.7 we investigate the drivers behind these events, their association with phase and how well they correlate with tail reconnection events. We first look at their temporal properties.

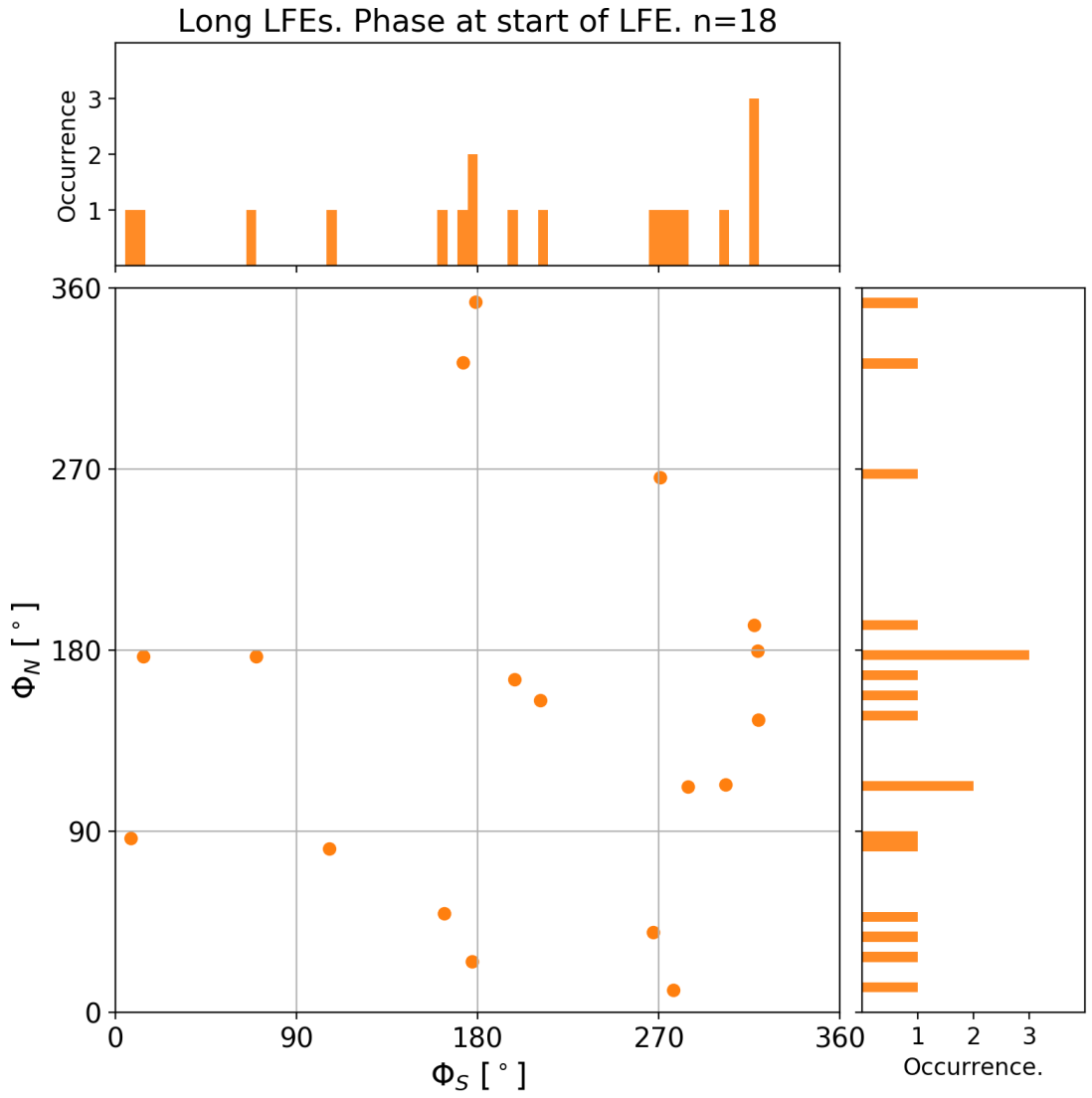

FIGURE 5.9: Scatter plots of long LFEs occurrence with the southern and northern SKR phase. The phase is taken at the start point of the LFE as defined by our criteria. The histograms show the distributions of the scattered points.

5.6.1 Short LFEs: Temporal Properties

Figure 5.12 shows the distribution of LFE duration for the short LFE events (those less than 20 hours) in Panel A and the waiting times between successive short LFE events in Panel B. If these short events were associated with the rotational dynamics of the planet, either through SKR phase and current intensification or tail reconnection we would expect these events to have a duration of less than one planetary rotation and a waiting time on the order of one planetary rotation. We find that 233/264 events are less than 8 hours long with a median for the entire set of 3.1 hours. As expected this is much less than one planetary rotation. We note that these length values are only indicative as their value directly depends on the selection criteria. We also mention our

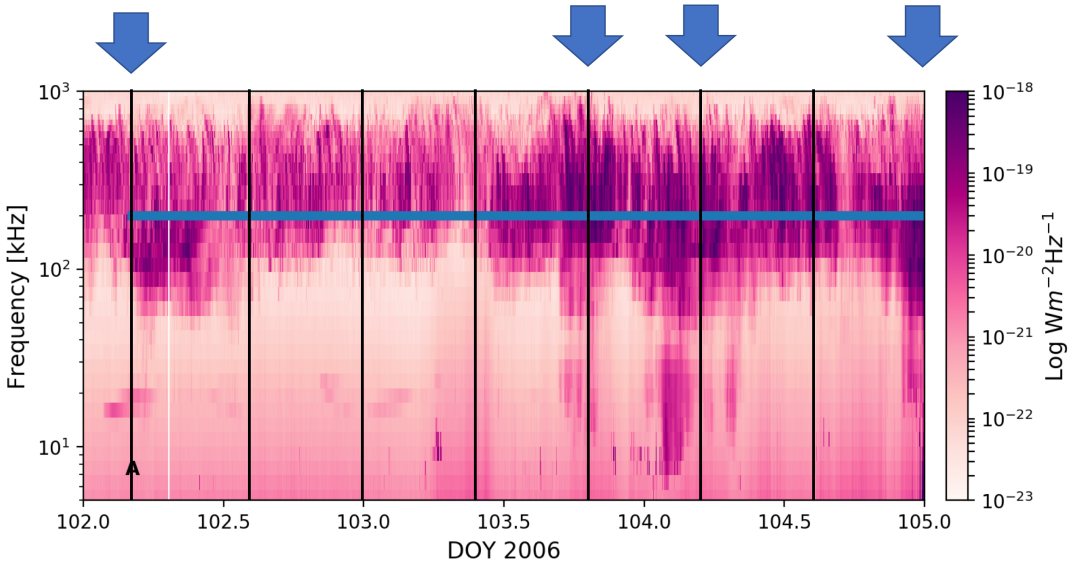

FIGURE 5.10: Example of a long LFE that has a potential underlying rotational component. The LFE lasts from DOY 102 to 105. The black lines mark when the southern SKR phase = 0. The thicker blue arrows above the plot mark times where the long LFE appears by eye to intensify with the planetary rotation when the SKR phase = 0.

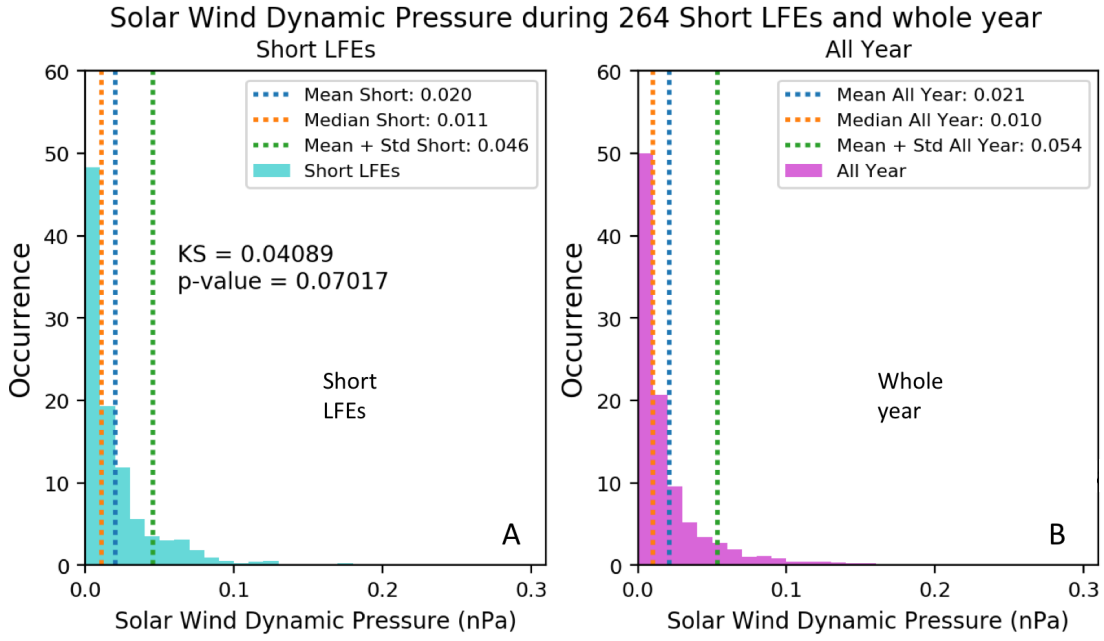

FIGURE 5.11: Showing the solar wind dynamic pressure during short LFEs (Panel A) and during the whole of 2006 (Panel B). The data is taken from the mSWiM propagation model [*Zieger and Hansen*, 2008]. The blue, green and orange dotted lines show the respective mean, mean plus 1 standard deviations and median of the distributions. Both figures are normalised such that the area of the histogram is equal to 1.

minimum length criterion removed all events shorter than 30 minutes and as such the shortest event we observe can be a minimum of 30 minutes.

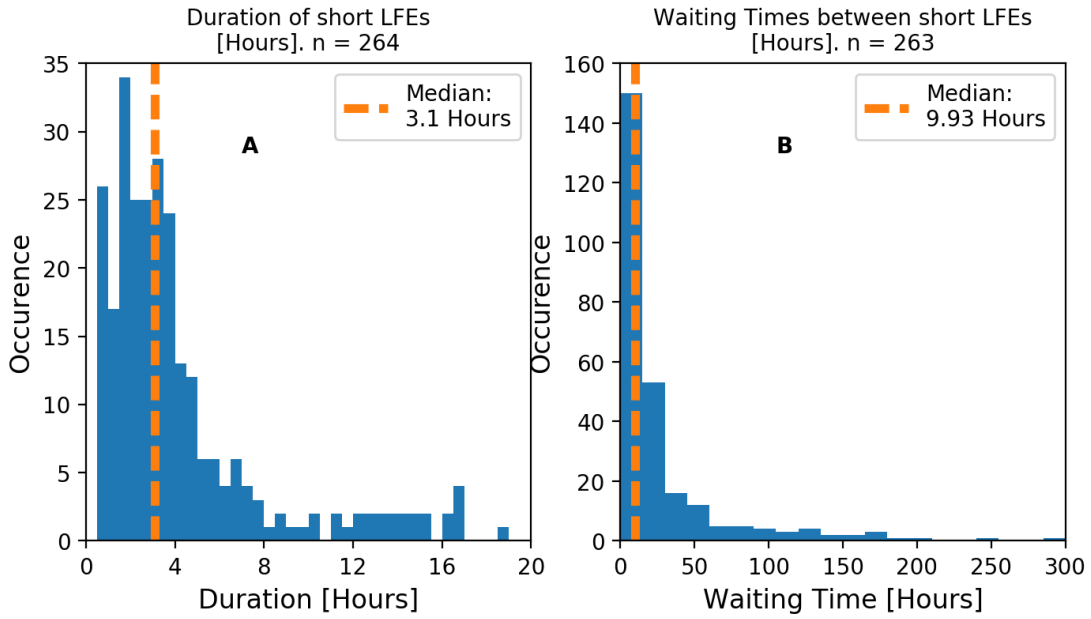

FIGURE 5.12: Short LFE durations in hours (Panel A) and waiting time in days (Panel B). The median is marked by the orange line. There are a total of 264 non-solar wind associated 'short' LFEs and 263 waiting times between consecutive events.

The median waiting time is ∼10 hours and there is a long tail with a few waiting times over a week long. If these LFEs were dependent on just the rotation of the planet, with ideal viewing conditions we might expect a waiting time of order ∼10.7 hours. In this case 63% of our events have a waiting time of less than 11 hours which suggests that this periodicity does exist in some cases. As discussed in section 5.3 on criteria above, there is a large location dependency on the visibility of the SKR and so we are unlikely to be seeing all events which will affect our statistics.

As an additional note, we look at two specific 10-day periods (DOY 30 - 40 and 60 - 70) where the spacecraft has a good consistent viewing as it passes slowly through 4 - 5.1h LT and 2 - 4hr LT respectively on an equatorial orbit. We find 35 LFEs are detected in this period with a median waiting time between 8 and 9 hours and a median length between 2.5 and 3 hours. This gives a median 'cycle' length of 10 to 12 hours. This is consistent with our picture of these events being associated with the rotation of Saturn with period ∼10.7 hours. Histograms of the cycle rates for these two 10-day periods are shown in figure 5.13.

5.6.2 Short LFEs: SKR Phase

We next look at the relationship of these short events with SKR phase. If they are related to the rotation of the planet we would expect to see a relationship between their start time with the SKR phase. 2006 was southern hemisphere summer and so the

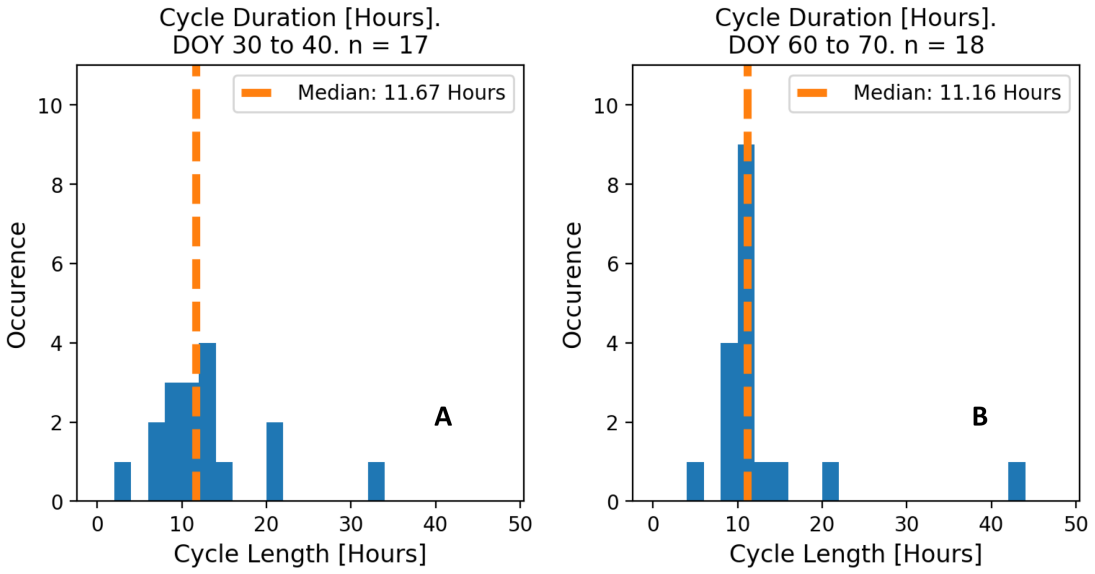

FIGURE 5.13: Histogram showing the short LFE cycle duration (event duration + waiting time to next event) for two intervals: DOY 30 - 40 (panel A) and DOY 60 - 70 (panel B). As discussed, their median duration times are 11.67 and 11.16 hours respectively, which seems consistent with our rotational modulation picture.

current sheet was hinged up out of the equatorial plane. For the first 205 days of 2006, Cassini was in low latitude equatorial orbits, so spent most of the time in the southern hemisphere and therefore had the best viewing conditions for the southern SKR source. Due to this, any phase relationship would be expected to be strongest with the southern SKR phase. Post day of year 205 Cassini moved to higher latitude orbits and so both the northern and southern SKR sources were seen equally.

Figure 5.14 shows the northern and southern system SKR phases at the onset time of the short LFEs. Most of the events (149 out of 264) appear in the rising phase (where the SKR is increasing in power between 180° and the peak 0/360°) of both SKR systems (the upper right quadrant of figure 5.14). The events are mostly grouped into where the northern and southern systems are close to being in phase with each other around 270° southern SKR phase and 270° northern SKR phase. We examined further to explore if the clustering we see in this figure could happen by chance. We randomly selected 264 points in time in 2006 and noted their respective northern and southern phase values and recorded what fraction were in the same upper-right quadrant as our actual data on figure 5.14. We then repeated this 10000 times. The mean percentage of points found in the upper-right quadrant was 24.9% with a standard deviation of 2.7% whereas 56.4% of our events are found in this quadrant. It is therefore highly unlikely that we see this clustering by chance. The results of this analysis are shown in figure 5.15.

If rotationally-driven, nightside events need to rotate towards the dawn sector to match

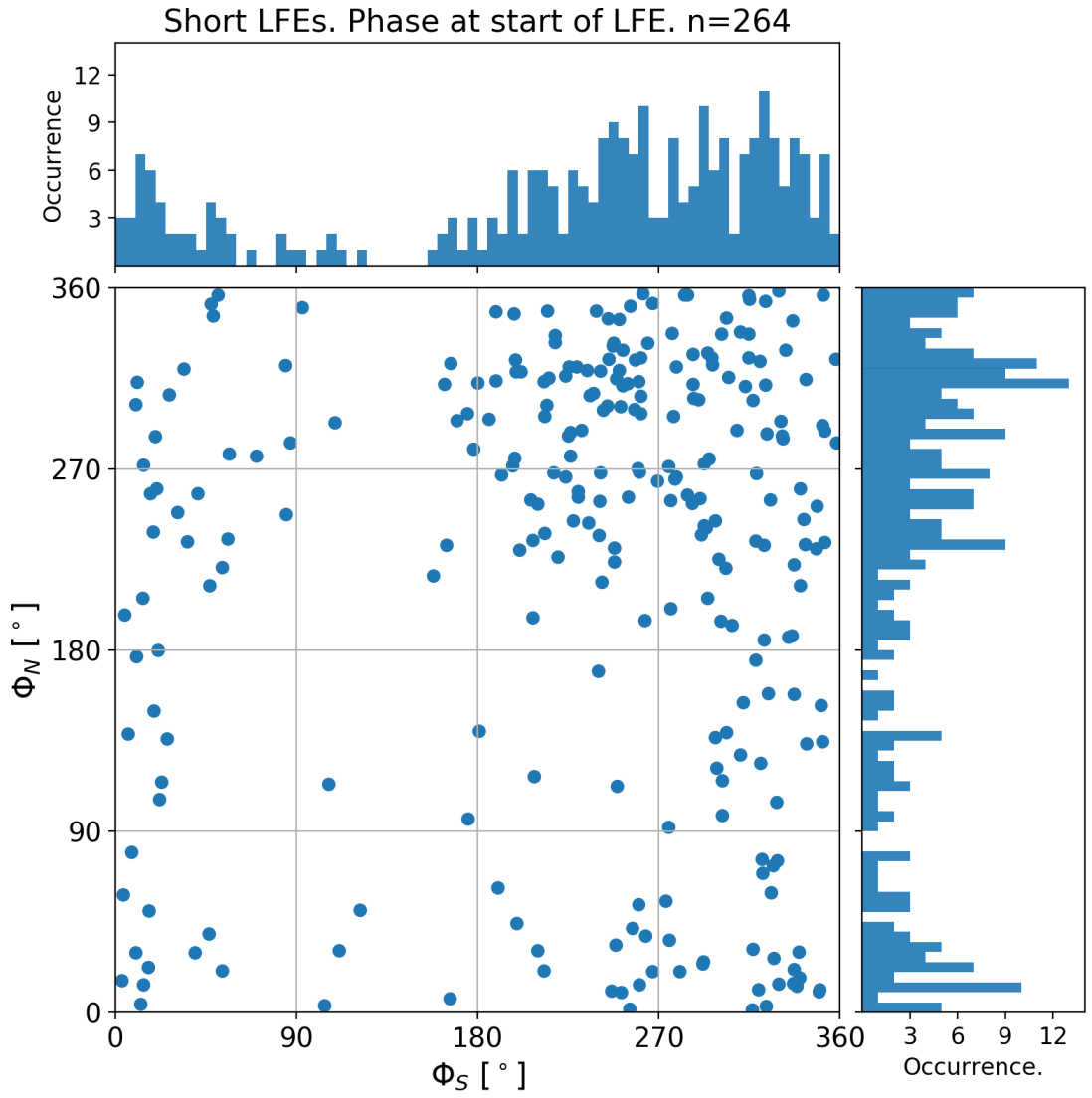

FIGURE 5.14: Scatter plots of non-solar wind associated LFEs occurrence on the southern and northern SKR phase. There are a total of 264 LFEs. The phase is taken at the start point of the LFE as defined by our criteria. The histograms show the distributions of the scattered points. 149 of the 264 events can be found in the upper-right quadrant where the northern and southern SKR phases are greater than 180°.

the expected SKR burst. Hence, considering the phase of the centre point of the LFEs, we would expect the phases to cluster around 0/360°. As shown in Figure 5.16, we do see greater clustering at these points but there are still a few examples of the centre points being completely out of phase with the SKR burst. We found that the clustering around periods where the systems were approximately in phase remained.

From our analysis we can see that there is a good relationship between these short LFEs and the phase of the SKR. *Jackman et al.* [2016] found that there was a dependence of tail reconnection events with the magnetic phase [*Provan et al.*, 2011; *Andrews et al.*, 2011]. The reconnection events used by *Jackman et al.* [2016] are those found by *Jackman et al.*

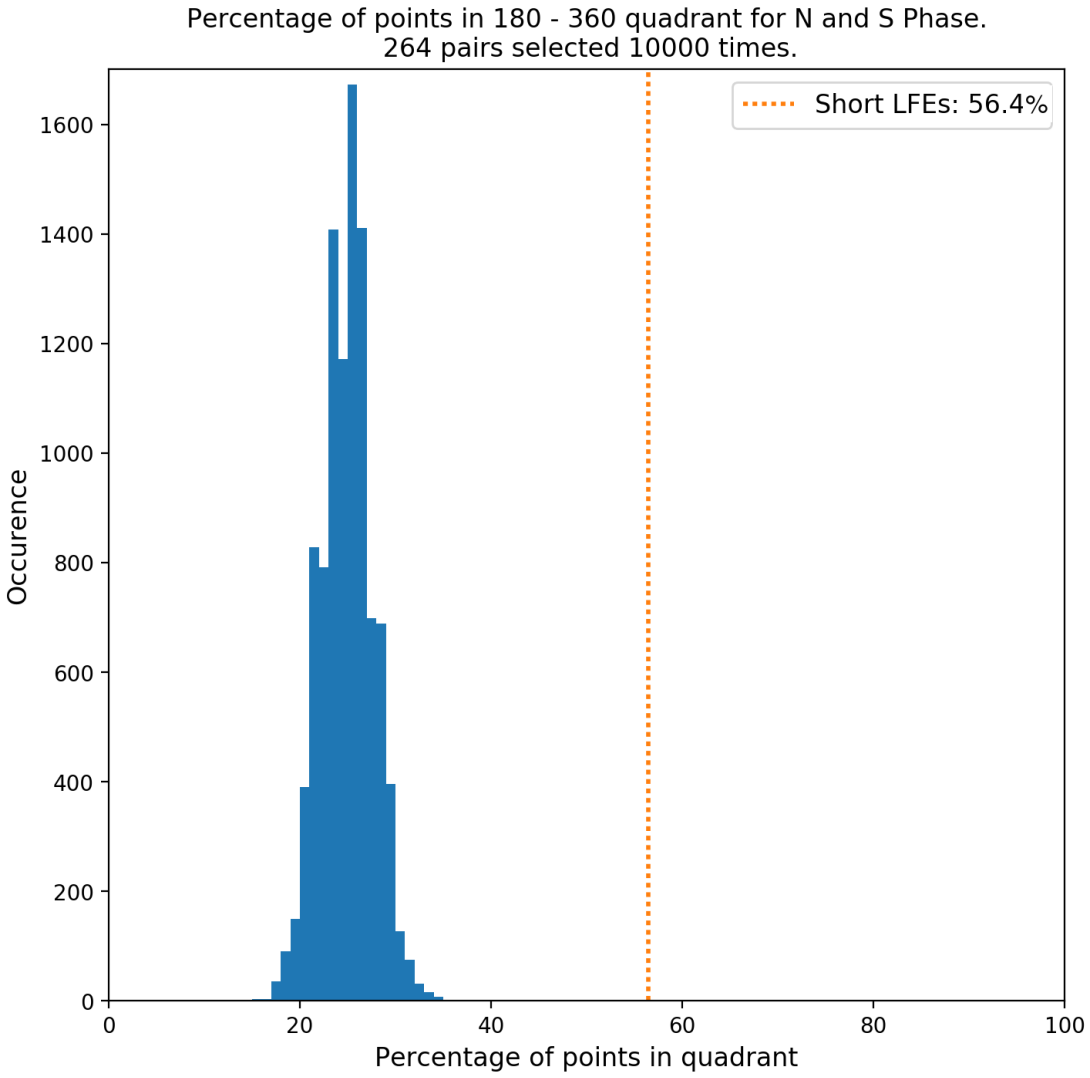

FIGURE 5.15: Significance test for the SKR phase clustering at the start of short LFEs. 264 times were randomly selected 10000 times and the fraction of events that were in the upper-right quadrant (as in figure 5.14) was recorded and is shown in the blue distribution. The orange dotted line shows the fraction of short LFEs that were clustered in this quadrant.

[2014b], a separate study to S16, although we do note that 90% of the events found by *Jackman et al.* [2014b] were also found by the S16 study. By considering the relationship between the SKR and magnetic phase systems we can assess the relationship between our LFE events and the reconnection events found by *Jackman et al.* [2014b]. The reasoning proceeds as follows:

1. *Jackman et al.* [2016] found that their reconnection events were clustered around 90° southern magnetic phase and 270° northern magnetic phase [i.e. $\Delta\Psi_B = 180$] (although the northern SKR phase was used in lieu of the northern magnetic phase [the two being always within ∼1° of each other during 2006]). This relative phase

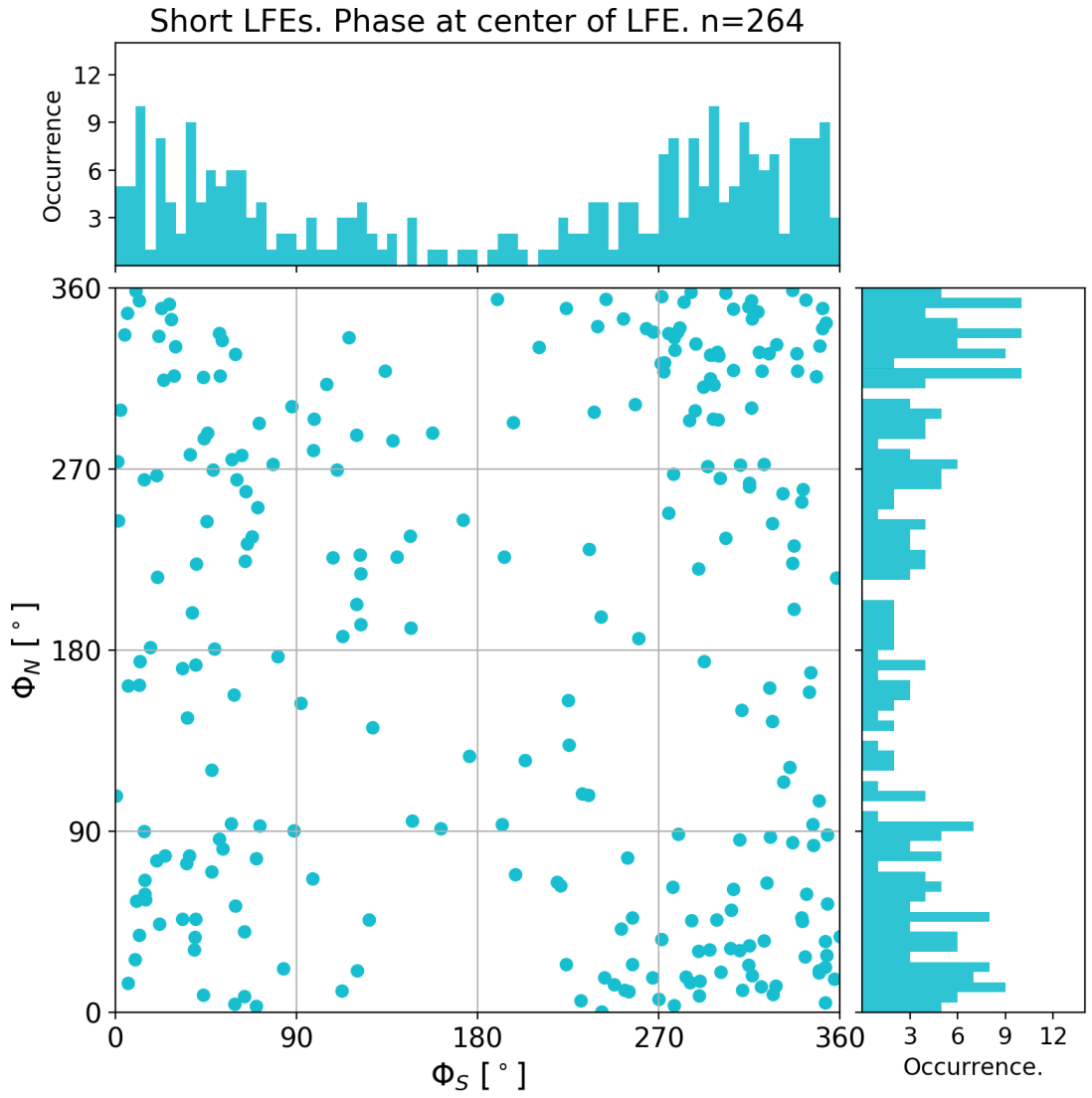

FIGURE 5.16: Scatter plots of non-solar wind associated LFEs occurrence with the southern and northern SKR phase. There are a total of 264 LFEs. The phase is taken at the centre point of the LFE as defined by our criteria. The histograms show the distributions of the scattered points.

is associated with outward movement of plasma and a thin current sheet, ideal conditions for reconnection [*Cowley et al.*, 2016; *Cowley and Provan*, 2017].

2. The difference between the observed SKR and magnetic phase is a function of the spacecraft viewing conditions. During 2006, Cassini's orbit meant that a constant difference of approximately 180° between the southern magnetic and southern SKR phase [*Andrews et al.*, 2011, 2012] was observed. This means a 90° southern magnetic phase coincided with a 270° southern SKR phase.

3. So with this in mind there is good agreement between the phases of the reconnection events and the short LFEs we have detected since the *Jackman et al.* [2016]

events are clustered at 270° in northern and southern SKR phase, just like our short LFEs.

The 'beat phase', $\Delta\Psi_B$, is the difference in phase between the northern and southern magnetic phase systems which drive the SKR modulations [*Andrews et al.*, 2012; *Provan et al.*, 2013]. These two current systems are rotating at slightly different periods and with increasing time these current systems produce beats in the equatorial magnetosphere where the two quasi-uniform perturbation fields co-exist (and single periods over the two polar regions where the individual perturbation fields are uniquely present).

In the next section we will look further at the relationship between the LFEs and a known catalogue of reconnection events to try to establish how useful LFEs are as a proxy for reconnection in the tail.

5.7 LFEs and Magnetospheric Dynamics

In this section we look further at the correlation between our LFE catalogue and tail reconnection events. As discussed in section 5.6, both LFEs and reconnection events occur preferentially at a particular phase of the planet's rotation. In order to assess the use of LFEs as a proxy for tail reconnection we examine the relationship in two ways: firstly checking how many LFEs have an associated reconnection event and secondly how many tail reconnection events have an associated LFE.

5.7.1 Comparison with tail reconnection events

For comparison of LFEs to tail reconnection we need to ensure that we are only using LFEs detected whilst the spacecraft was in a favourable position for detecting reconnection events in situ. The S16 criteria required that the spacecraft was on the nightside of the planet (18 - 06h LT), further than 15 R_S, not in the magnetosheath and finally before DOY 282 in 2006. We removed LFEs that were detected when the spacecraft did not meet these criteria and those that occurred less than 11 hours before leaving this viewing region. This gave 107 LFEs from our initial catalogue of 282 LFEs. For each LFE we checked whether a reconnection event occurred simultaneously or within a given window size before the start or after the end. We then performed the same search for our 234 reconnection events, checking before and after the event for LFEs. For this second analysis we used our complete list of 282 LFEs. For each analysis we split the LFEs into three categories. All, Short ($<$ 20 hours) and Long ($>$ 20 hours). The numbers in each set for each analysis can be found on Figure 5.17.

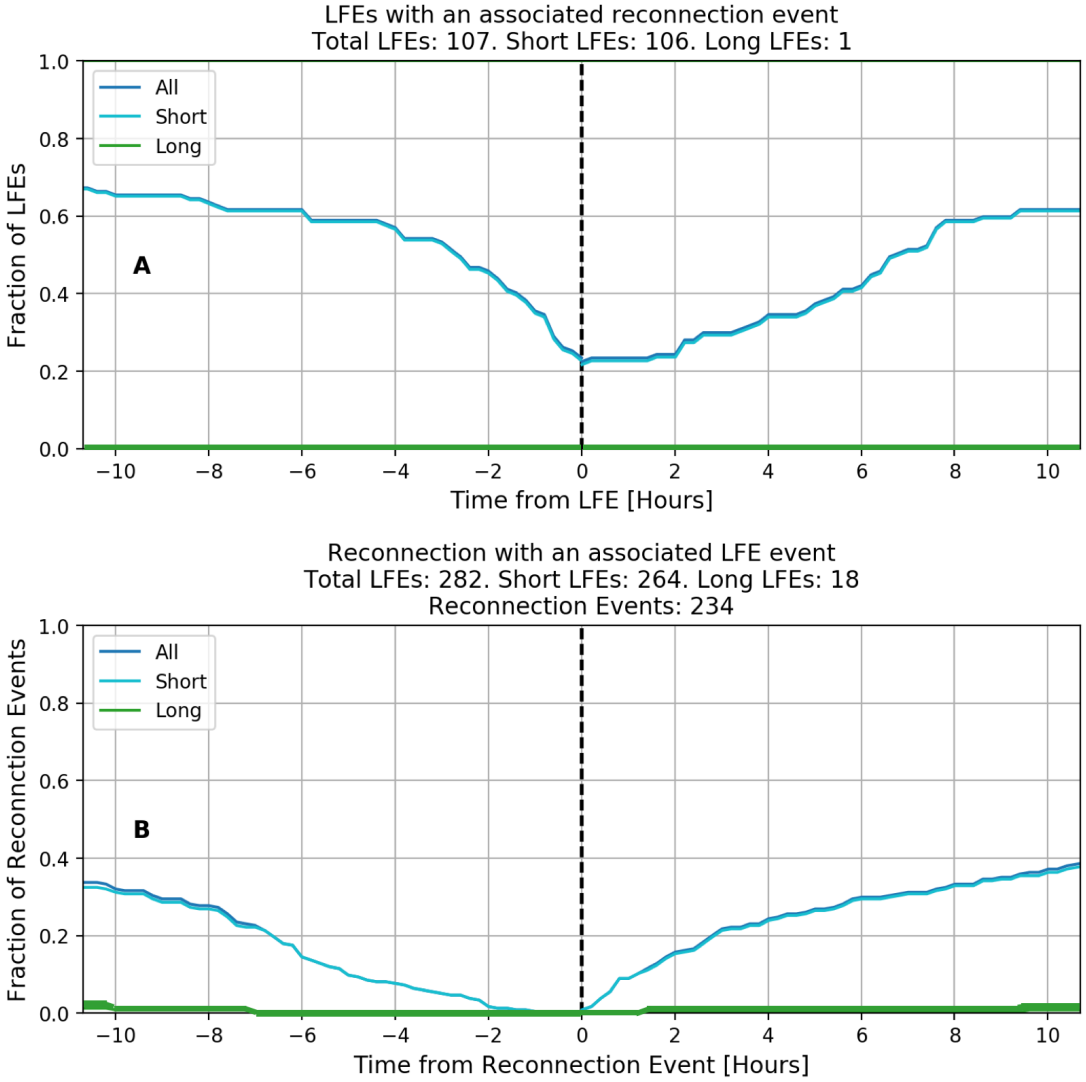

FIGURE 5.17: Panel A shows the fraction of LFEs with an associated reconnection event as function of time before and after the LFE. Only LFEs that are detected whilst the spacecraft is in the reconnection event viewing region as defined by S16 are used. The y-axis shows the fraction of the corresponding set of LFEs (All (blue), Short (cyan) or Long (green - this line has been thickened for visibility)) that have an associated reconnection event either simultaneously or within the window of time. The x-axis gives the window of time in hours either side of the LFE where a reconnection event is looked for. Panel B shows the inverse relationship, the fraction of Reconnection events with an associated LFE as function of time before and after the reconnection event. Here all LFEs and reconnection events are used unlike when searching for reconnection events associated with an LFE. The y-axis shows the fraction or reconnection events that have an LFE (grouped into All (blue), Short (cyan) or Long(green)) within the window of time. The x-axis gives the window of time in hours either side of the reconnection event where a LFE is looked for. On both panels the green line representing the Long LFEs is barely visible since it represents only one LFE on panel A, and a tiny fraction of the total events in panel B (and an even smaller fraction of those).

Figures 5.17 shows the results of these comparisons. Figure 5.17A shows the fraction of LFEs that have an associated reconnection event within a specific window size. Figure 5.17B shows the fraction of reconnection events that have a LFE within a specific window

size. As would be expected, increasing the search window size increases the number of corresponding events found. Approximately 23% of the short LFEs have a simultaneous reconnection event i.e. a window size of zero. 67% of short LFEs have a reconnection event during or within the preceding 10.7 hours of their occurrence, and ∼61% within 6 hours where the graph approximately flattens. Only 40% of reconnection events have any LFE during or within 10.7 hours before or after they occur. We do not perform the analysis for window sizes greater than 10.7 hours as we expect that LFE events found after this length of time are unrelated to the reconnection event due to the periodic nature of the intensifications in the SKR. This correlation between reconnection events and subsequent radio response is perhaps lower than we might have expected given our understanding of the physical mechanism behind LFE driving (as outlined at Earth by *Morioka et al.* [e.g. 2007, 2012] and at Saturn by *Jackman et al.* [2009a]). In order to investigate this further we did a significance check. During intervals that satisfied the viewing region criteria as defined by S16 we placed 106 short LFEs (with a distribution of lengths taken from figure 5.12A) at various randomly selected start times. We then performed the same analysis as described above, seeing what fraction of those events had a reconnection event from the S16 catalogue in the preceding or following 6 hours. We then repeated this 10000 times. The mean number of LFEs with a reconnection event within the preceding 6 hours was 39%. The 61% correlation we have is greater than 4 sigma confidence. The results of this analysis are shown in figure 5.18.

We do not comment on the relationship of the long LFEs to reconnection events since we have only 1 long event within the viewing region which is clearly not enough to be able to comment with any confidence. When finding reconnection events with associated long LFE events, the fraction is extremely low even for window sizes close to 2 planetary rotations. It is perhaps possible that given a shock arrival and compression of the magnetosphere this could trigger reconnection at some particular phase but this is not seen in the current dataset. Overall the fraction of reconnection events with an LFE is much lower than the inverse relationship, suggesting that whilst a LFE is a reasonable proxy that there has been reconnection in the tail, seeing a reconnection event in the tail does not always mean a reaction in the SKR will occur or be observed.

We further investigate the link between reconnection events and LFEs by examining the dependence of this relationship on spacecraft location. We separate the reconnection events into those detected at dusk (n = 80) and those in the dawn sector (n = 154) as seen on Figure 5.19. Due to the better SKR visibility in the dawn sector of the orbit closer to the strongest SKR source region around 8h LT [*Lamy et al.*, 2009], we might have expected a better 'hit' rate for those detected whilst the spacecraft is in the dawn sector. There doesn't seem to be a difference in the fraction of reconnection events with

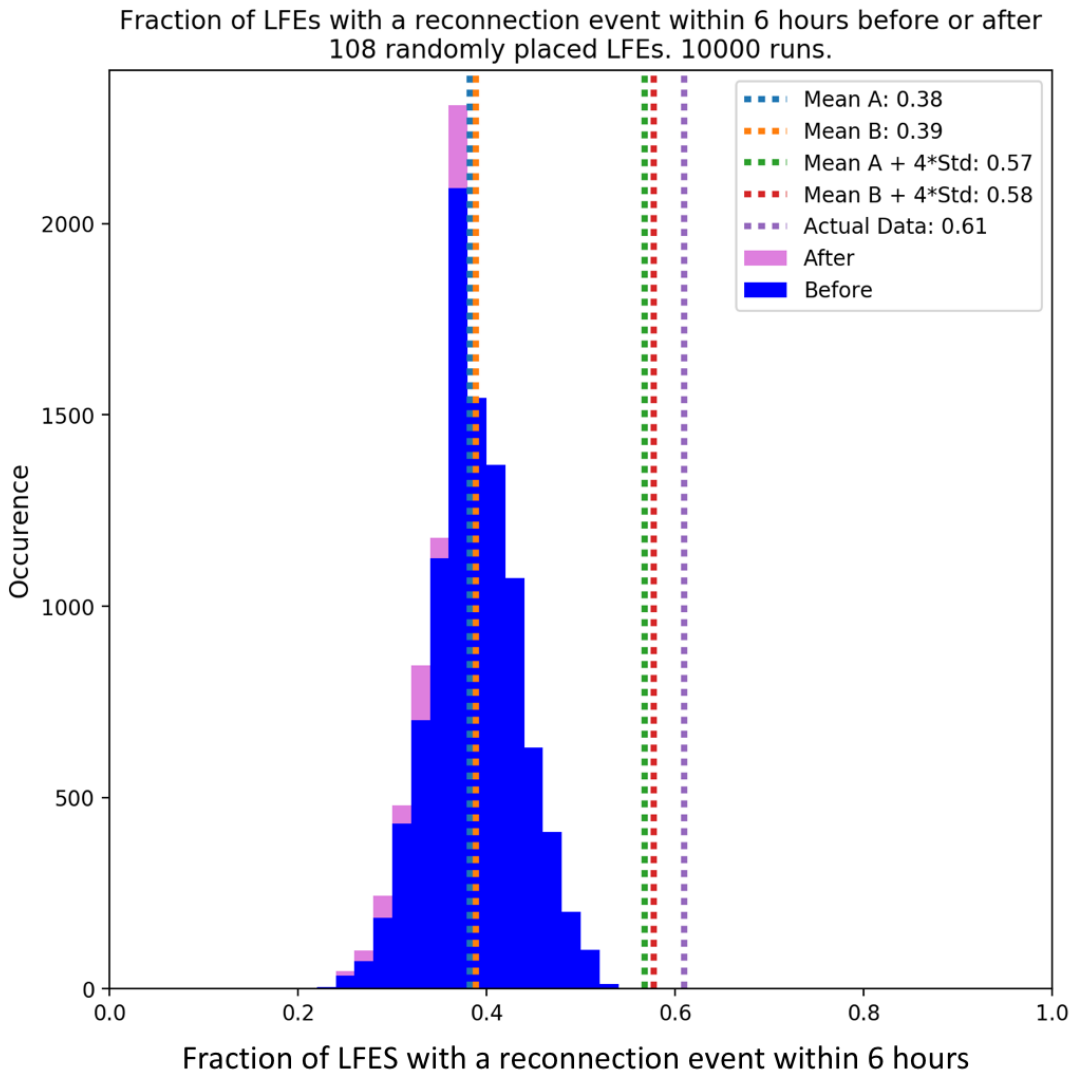

FIGURE 5.18: Significance check of the relationship between LFEs and reconnection events. Shows the fraction of 108 randomly placed LFEs with a reconnection event within the preceding (blue) or following (pink) 6 hours. The analysis was repeated 10000 times. The blue and orange dotted lines shows the mean of the pink and blue distribution respectively. The green and red dotted lines show the mean plus four standard deviations of the pink and blue distributions respectively. The purple dotted line shows the correlation between LFEs and reconnection events found by our analysis.

an associated LFE between dusk and dawn. This suggests that our location dependent criteria has accounted well for the variability in SKR visibility.

5.7.2 LFE Power

As shown and discussed above there is a reasonable correlation between short LFEs and tail reconnection ($\sim 60\%$ of LFEs have a tail reconnection event simultaneously or within the preceding 6 hours) and there is very strong correlation between the short LFEs start

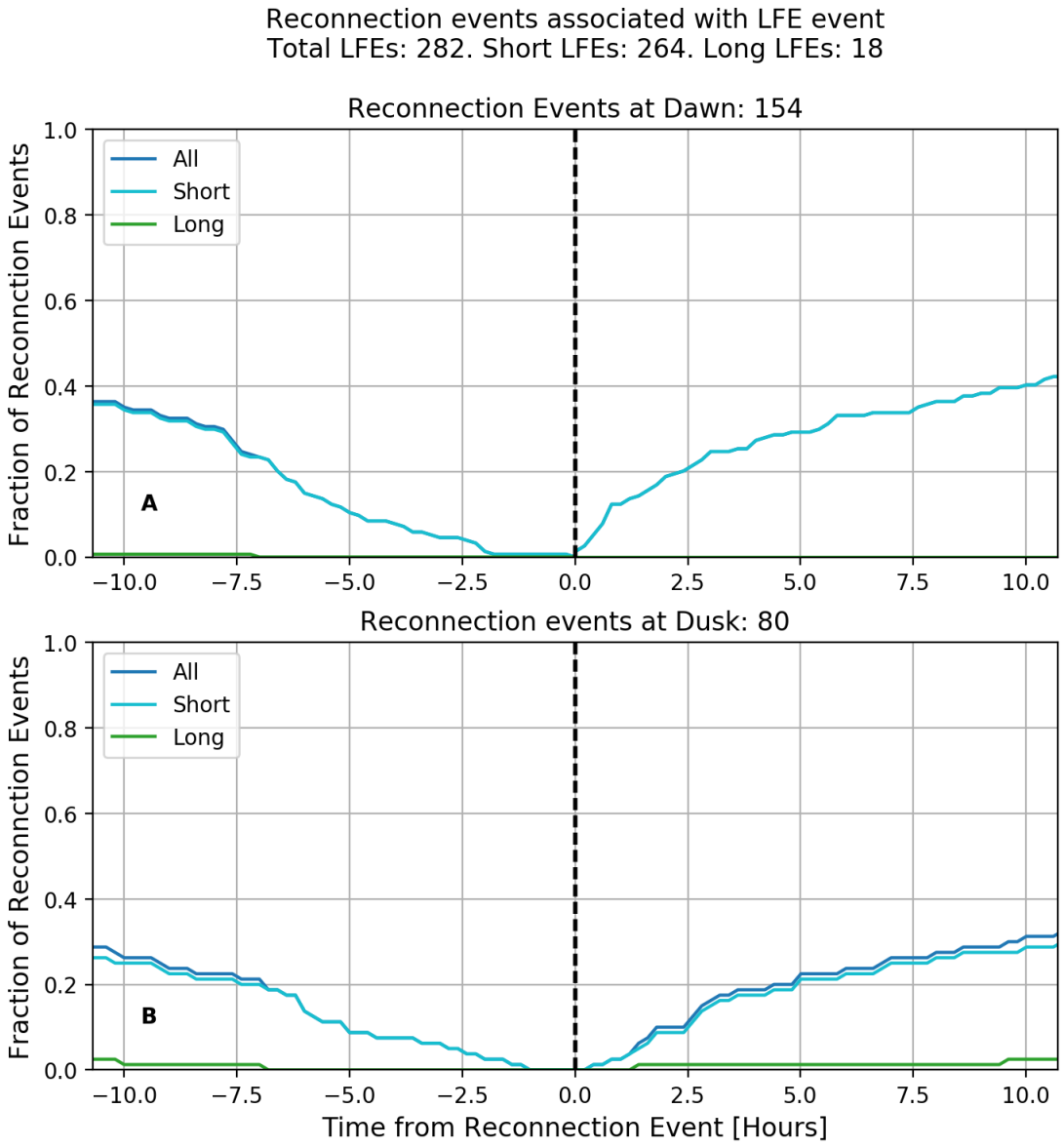

FIGURE 5.19: Panel A: Fraction of reconnection events detected in dawn sector with an associated LFE as a function of window size. Panel B: Fraction of reconnection events detected in the dusk sector with an associated LFE as a function of window size. Here all LFEs and reconnection events are used unlike when searching for reconnection events associated with an LFE. The two panels have a shared x-axis.

time and the northern and southern SKR phase systems. This phase in SKR system (when converted to magnetic phase) is also strongly associated with tail reconnection as shown in *Jackman et al.* [2016]. This suggests a strong relationship between LFEs, tail reconnection and the rotation of the planet. We next explore a potential explanation as to why the correlation between LFEs and tail reconnection is lower than we might expect.

There are two possible scenarios to explain this low correlation between LFEs and tail reconnection. A) Not all LFEs are caused by tail reconnection, or B) The S16 catalogue

that we are using to compare LFEs and reconnection events may be incomplete. During the above analysis, we attempted to limit this latter effect by limiting our LFEs to only those detected when the spacecraft was in a favourable position for detecting reconnection but it is likely that reconnection events (particularly small-scale events) were still missed. Reconnection detection, even within a favourable viewing region, is difficult. The size of the signature is a function of the trajectory of the spacecraft through the plasmoid or region as well as the orbit of the spacecraft considering the hinged current sheet that changes location with season. If (A) (not all LFEs are caused by the increased precipitation of particles along field lines due to tail reconnection) that suggests there are two or more drivers behind these shorter LFEs. To investigate this we next compare the distribution of median emitted powers during short LFEs (<20 hours) that do and do not have an associated reconnection event. A significantly differing distribution of powers between those LFEs driven by reconnection and those not driven by reconnection would allow us to better use LFEs as a proxy for magnetospheric dynamics by parametrising the difference between the two types of short LFEs. If there is no difference in the distributions, this could suggest that in fact all of the LFEs are associated with reconnection and it is just that we have not observed the associated reconnection event in situ in the tail.

Figure 5.20 shows the median emitted power of the short LFEs (n = 106) seen in the S16 viewing region. The LFEs are separated into those with (blue) or without (orange) an associated reconnection event within 6 hours before or after in two integrated frequency ranges: 40 - 100 kHz and 100 - 600 kHz. The Kolmogorov-Smirnov statistic and the p-value comparing the two distributions on each panel is printed. These values show that we are unable to reject the null hypotheses that the two distributions have been drawn from the same distribution, i.e. there is no statistical difference between the distribution of emitted power during LFEs with and without an associated reconnection event. Even varying the window size for searching for associated reconnection events does not improve the KS statistics. This suggests that there is no significant difference in intensity between LFEs caused by reconnection and those not. This could mean that the ∼61% correlation rate between LFEs and reconnection events (within 6 hours) above is due to missed reconnection events rather than a lack thereof. Due to the limitations of a single spacecraft, reconnection events are still being missed despite being in the viewing region.

This is not to say that observing an LFE means there has definitely been reconnection, it is just that it is likely given the strong correlations found between SKR phase (and magnetic phase), LFE occurrence and magnetic reconnection. There are two potential cause and effect mechanisms. 1) The rotational effects associated with the rotating current systems cause tail reconnection (via e.g. current sheet thinning) and *separately*

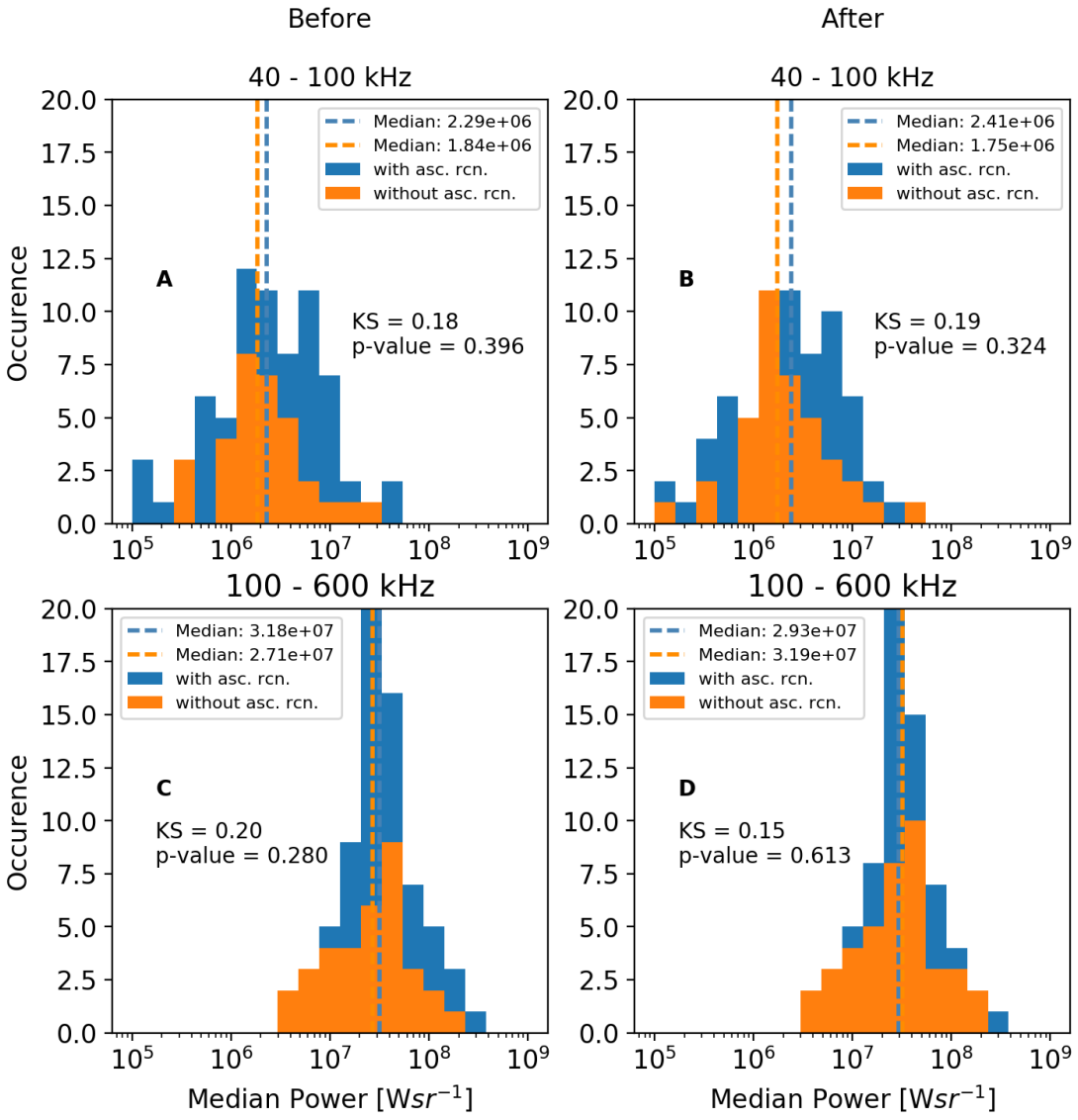

FIGURE 5.20: Histograms showing the distribution of median emitted powers of LFEs with (blue) or without (orange) an associated reconnection event within 6 hours before (Panels A, C) or after (Panels B, D) the LFE in the two integrated power range: 40 - 100 kHz (Panels A, B) and 100 - 600 kHz (Panels C, D). The Kolmogorov-Smirnov statistic and p-value are printed on each panel. Of the 106 short LFEs, there are 72 with an associated reconnection event within 6 hours before and 66 after. There are 34 without an associated reconnection event within 6 hours before and 40 after.

the rotating current systems drive LFEs (i.e. as they reinforce strong field aligned current at a given local time sector). 2) The rotational effects give rise to tail reconnection as described which leads to an LFE via the mechanism discussed in the introduction as particles precipitate into SKR source regions, they move to higher altitudes and the emission frequency lowers i.e. the *Jackman et al.* [2009a] mechanism.

5.7.3 Secondary Data Set

In order to test the reliability of our results above we performed the same analyses with a smaller catalogue derived from a previous, stricter criteria. The criteria for this second LFE catalogue was still based on exceeding a spacecraft-location dependent threshold in the two integrated power bands, but with the additional criterion requiring the flux intensity at a specific low frequency to exceed a threshold. This catalogue contained 188 LFEs, 169 of which are also found in the main criteria described above. The results were consistent with those described above both in the general properties of the short and long LFEs i.e. including duration, recurrence rate and where they were observed; and in their relationship with SKR phase (shown in figure 5.21) and tail reconnection (shown in figure 5.22). The second catalogue showed a better relationship with tail reconnection events (∼75% had a reconnection event simultaneously or within the previous 6 hours compared to 60% for the catalogue described above). We interpret this as the second criteria selecting more significant (greater intensity and/or extended) events which, with the caveat of viewing constraints, may be associated with larger tail reconnection events which are more likely to be observed in the tail.

5.8 Discussion

In this study we have developed criteria for the selection of LFEs of the Saturn Kilometric Radiation from processed RPWS data. 282 LFEs were detected during 2006 based on these criteria. We then investigated the properties of the LFEs such as their duration and recurrence rate. Furthermore we categorised these LFEs into two types 'short' and 'long' and investigated their relationship with SKR phase, solar wind dynamic pressure and a catalogue of tail reconnection events.

On examination of our catalogue of events we found two categories of LFE. Shorter, single extension LFEs and longer, multiple extension LFEs. These two types of LFE were categorised based on their duration (less than or greater than 20 hours) into 'short' and 'long' LFEs. The short LFEs were the most numerous and occurred most frequently. We found 264 of these events with a median recurrence time of ∼10 hours compared to only 18 long events which had a median recurrence time of ∼20 days. The shorter events were assumed to be associated with the rotation of the planet and we would therefore expect a recurrence rate around 10.7 hours (the approximate period of the rotation of the planet). 63% of events have a waiting time of less than 11 hours suggesting this periodicity does exist in many cases. As shown in figure 5.13, for periods of good viewing conditions (DOY 30 - 40 and DOY 60 - 70) the cycle lengths i.e. the event

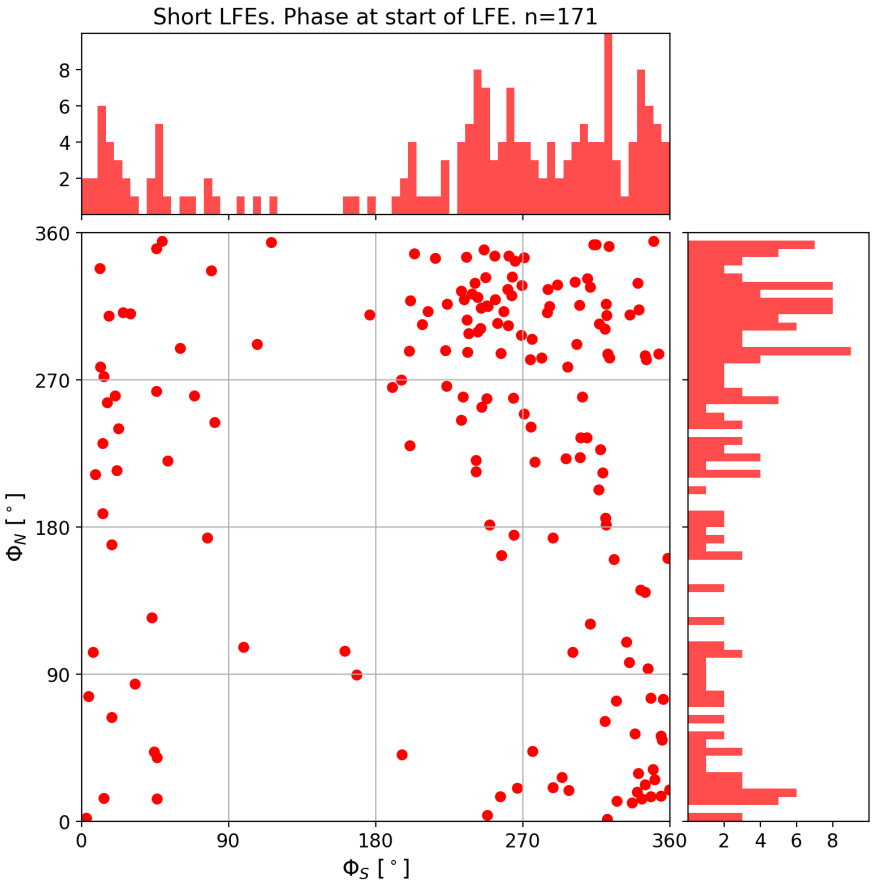

FIGURE 5.21: Scatter plots of non-solar wind associated LFEs occurrence on the southern and northern SKR phase for old LFE dataset. There are a total of 171 LFEs. The phase is taken at the start point of the LFE as defined by our criteria. The histograms show the distributions of the scattered points. 96 of the 171 events can be found in the upper-right quadrant where the northern and southern SKR phases are greater than 180°.

duration plus the waiting time to the next event have medians of 11.67 and 11.16 hours respectively, strongly supporting the rotational modulation picture. The distribution of waiting times for the short LFEs is affected by events that we do not detect or select, reflected by the long tail in Figure 5.12B. Whilst our criteria included a dependency on spacecraft observation location, it is still likely that there are missed emissions due to imperfect location dependent criteria and poor SKR visibility or the beaming of the SKR due to a solar wind compression.

The strong SKR phase dependence of the short LFE events that are detected, where the LFE start times are strongly clustered during the rising ($> 180°$) phase of the southern and northern SKR phase (149 out of 264 LFEs), does further imply a periodicity of the order of a planetary rotation and that the variation in the waiting time distribution is due to missed/non-selected events. The starting SKR phase of the LFE events matched well with the magnetic phase of the reconnection events in *Jackman et al.*

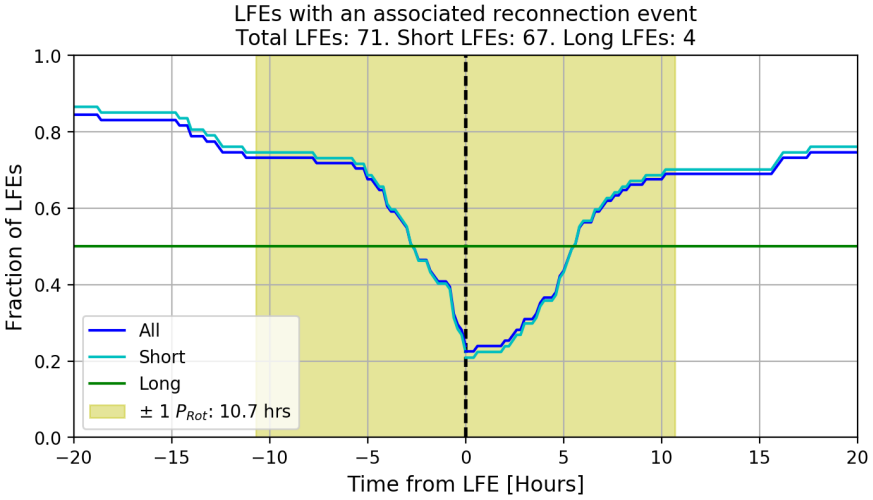

FIGURE 5.22: The fraction of LFEs with an associated reconnection event as function of time before and after the LFE. Only LFEs that are detected whilst the spacecraft is in the reconnection event viewing region as defined by S16 are used. The y-axis shows the fraction of the corresponding set of LFEs (All (blue), Short (cyan) or Long (green)) that have an associated reconnection event either simultaneously or within the window of time. The x-axis gives the window of time in hours either side of the LFE where a reconnection event is looked for.

[2016] when accounting for the 180° phase difference between the southern SKR and southern magnetic phase during 2006. These conditions are favourable for the outward displacement of plasma and a thin current sheet as discussed in section 6.2. This result further strengthens the relationship between the rotation of the planet, reconnection and LFE occurrence.

2006 was near the minimum phase of the last solar cycle where the solar wind is expected to be well structured and regular and so the waiting time of the long events was expected to reflect a pattern of compressions associated with corotating interaction regions in a two-sector solar wind with a recurrence pattern of approximately 25 days as seen by *Kurth et al.* [2016]. We do see a clustering (50% of events) of recurrence times between 19 and 31 days (± 6 days of expected). The median duration of these long events is ∼39 hours, with several lasting more than 2 days (48 hours), and so the 6 day window either side of the expected recurrence time allows for these durations since the recurrence time is calculated from the end of one event to the start of the next event. As discussed in section 5.5 we might also expect a 13 day periodicity to occur. We do see several events with this timescale waiting time, although we do note that some of these are events that occur within a single solar wind compression event. Work on the merging of CIR compression regions with increasing distance from the Sun may make it more likely for a given ∼25-day solar rotation to be dominated by one strong compression, which could lead to the increased importance of a 25-day repetition period over a 13-day one [*Hanlon et al.*, 2004]. *Meredith et al.* [2014] analysed 12 auroral storms, representing significant

brightening and poleward expansion of the auroral oval, detected by the Hubble Space Telescope (HST) at Saturn, and associated with solar wind compression. They found a typical lifetime of $\sim$ 16 hours, significantly shorter than a solar wind associated LFE.

The long LFE catalogue was also examined for correlation with SKR phase. Since most of them last multiple planetary rotations it is not obvious which point of the LFE to assign a phase to and so we checked the correlation between the SKR phase and the long LFE start and centre times. Neither times showed any dependency on the SKR phase as would be expected if these events are dependent on solar wind dynamics rather than internally controlled. It is interesting to note that many of the long LFEs contain multiple intensifications and extensions to lower frequencies which do show a dependency on SKR phase. This illustrates that whilst the solar wind can intensify the SKR above its typical level, the influence of rotational dynamics can also been superposed on this behaviour. Based on their periodicities, the correlation of long LFEs with solar wind dynamic pressure as shown in Figure 5.7 and the morphology of these long LFE events, it would suggest that they are good proxies for solar wind dynamics.

One of the motivations behind this study was to assess how good LFEs are as a proxy for reconnection in the tail. How do LFEs and tail dynamics relate and can this help us overcome some of the issues of single spacecraft observations? In order to do this we compared our catalogue of LFEs to the S16 catalogue of tail reconnection events. We selected LFEs that were detected whilst the spacecraft was in a good location for detecting reconnection events as defined by S16. Of the 107 LFEs detected during this period, 61% of all LFEs had a reconnection event within $\pm$ 6 hours. We then examined the number of reconnection events with an associated LFE. Of the 234 reconnection events, less than 20% had a LFE within $\pm$6 hours. This suggested that whilst an LFE more than likely signified a reconnection event had occurred, a reconnection event does not necessarily lead to a LFE (or one being observed).

We looked for both a reconnection event within a given window before and after a LFE and a LFE within a given window before and after a reconnection event. The mechanism put forward by *Jackman et al.* [2009a] is as follows: Following reconnection, there is an increased precipitation of particles along field lines into the auroral regions. This increases until the electron density is larger than the plasma can carry without acceleration and a potential drop is required. The greater the precipitation, the larger the potential drop, and hence the 'taller' the acceleration region. The top of this acceleration region (which is now radially further from the planet) may coincide with a SKR source region at correspondingly higher altitudes and thus a weaker field strength and so the emission moves to lower frequencies. I.e. As the acceleration region becomes taller the electrons meet the relativistic speeds required for the CMI (along with a plasma density

sparse enough such that the plasma frequency, f_{pe}, is < 0.1 x the electron gyrofrequency, f_{ce}) at a higher altitude which means at a lower magnetic field strength, thus lowering the emission frequency. In this scenario we would expect the causal relationship to be reconnection followed by an LFE. One complication lies in the estimation of the reconnection time. We do not detect reconnection directly, instead we detect its products in the form of a plasmoid, dipolarisation or TCR, and therefore estimates are required on both the reconnection time and location. Following reconnection the energised particles must travel along the field line to the planet, the time taken being dependent on the distance of the reconnection site to the SKR source region. Looking at the LFE/reconnection event relationship further, we find that there are more LFEs with associated reconnection events before than after which can be explained by the *Jackman et al.* [2009a] mechanism timeline (reconnection followed by LFE).

There are several factors that could account for a perhaps lower than expected correlation between LFEs and reconnection events. As discussed above, the visibility of the SKR varies with spacecraft location and so it is possible that an LFE did occur but was not seen despite the location dependency built into the LFE criteria. Another factor is the size of the reconnection event itself. There are a range of reconnection event sizes. As a first approximation to the size of a reconnection event we can look at at the magnitude of the field deflection associated with events, ΔB_θ. Whilst highly dependent on the trajectory of the spacecraft through the structure and this distance of the spacecraft from the magnetospheric current sheet the S16 catalogue observes $|\Delta B_\theta|$ between 0.25 and 4.7 nT, and we would expect there to be a similar variation in SKR response. At Earth, the global impact of tail reconnection might be quantified through examination of flux closure or change in auroral electrojet indices [*Milan et al.*, 2009; *Coxon et al.*, 2014]. However, at Saturn we lack such clear definitive measures of "substorm" size. Future work at Saturn should focus on the examination of the degree to which remote proxies such as radio emissions can serve as proxies for reconnection, not just in terms of timing of events but also in terms of estimating their size/global influence.

$\sim$61% of LFEs seen within the reconnection viewing region as defined by S16 have a reconnection event during or within 6 hours before. This hit rate is reasonable but perhaps not as strong as we would expect if LFEs were indeed a good proxy for reconnection. Despite this a significance test showed that it is highly unlikely that this correlation would appear by chance. Further, if we consider the factors discussed such as the varying strength of the reconnection events, the reconnection events that may have been missed and also consider the very good agreement between the phase of the reconnection events in *Jackman et al.* [2016] and of our LFEs, it would suggest there is in fact a good correlation between reconnection and LFEs at Saturn and that LFEs are indeed a good proxy for tail reconnection within the magnetosphere.

5.9 Summary

In this study we have developed criteria for the selection of low frequency extensions of the Saturn Kilometric Radiation from processed RPWS data. 282 LFEs were detected during 2006 based on these criteria. We then investigated the properties of the LFEs such as their duration and recurrence rate. We also investigated their relationship with solar wind dynamic pressure, a catalogue of tail reconnection events and the northern and southern SKR phase systems.

1. 282 LFEs were detected during 2006
2. 18 of these events were longer than 20 hours and strongly associated with increased solar wind dynamic pressure and showed no SKR phase dependency.
3. Of the 264 events shorter than 20 hours, 107 were detected during periods that satisfied tail reconnection viewing conditions. Of those events ∼61% had a reconnection event within 6 hours or during the LFE. The start of all the short LFEs showed a strong relationship with the rising phase of both the southern and northern SKR phase systems.
4. There was no significant difference in emitted power during LFEs that did and did not have a reconnection event within ±6 hours which would have suggested a different driving mechanism. This suggests the non-perfect correlation may be due to 'missed' reconnection events.

Chapter 6

A Statistical Study of Saturn Narrowband Emissions

6.1 Introduction

Narrowband emissions such as those indicated by the coloured horizontal lines in figure 6.1 (at ∼5 kHz) appear in the lower frequencies of the Saturn Kilometric Radiation (SKR) spectrum which extends from 3 kHz to ∼1500 kHz. They were first detected during the Voyager 1 flyby of Saturn [*Gurnett et al.*, 1983]. The Voyager 1 Plasma Wave Science (PWS) instrument observed a persistent 5 kHz narrowband emission over a 3-day period during which Voyager travelled in from 33.26 R_S below the southern pole of the planet and back out to 58.3 R_S. Since 2004, the Radio and Plasma Wave Science (RPWS) instrument onboard Cassini has revealed more interesting features of Saturn narrowband emissions. With Cassini, a new component of Saturn narrowband emissions was detected at higher frequencies (10 to 70 kHz). These emissions, referred to as 20 kHz narrowband emissions by *Ye et al.* [2009] and as nSKR by *Lamy et al.* [2008], were not observed by Voyager 1 or 2 due to its lower intensity compared to the 5kHz narrowband emission. The 5 kHz emissions (shown on figure 6.1) are detected at all latitudes covered by the spacecraft whereas the 20 kHz emission is only seen from relatively high latitudes [*Wang et al.*, 2010]. A similar emission observed at higher frequencies is found at Jupiter and is called the Jovian narrowband kilometric emission (nKOM) [*Warwick et al.*, 1979; *Kaiser et al.*, 1980; *Reiner et al.*, 1993; *Louarn et al.*, 2007]. At both Saturn and Jupiter, the occurrence of these emissions has been found to be modulated at the approximate rotation period of the planet [*Reiner et al.*, 1993; *Zarka*, 1998; *Louarn et al.*, 2007; *Wang et al.*, 2010]. A similar emission is also observed at Earth where it is known as the terrestrial continuum radiation [*Brown*, 1973; *Gurnett*,

1975; *Kurth*, 1981]. Unlike at Saturn and Jupiter, this emission is not modulated at the planetary rotation period.

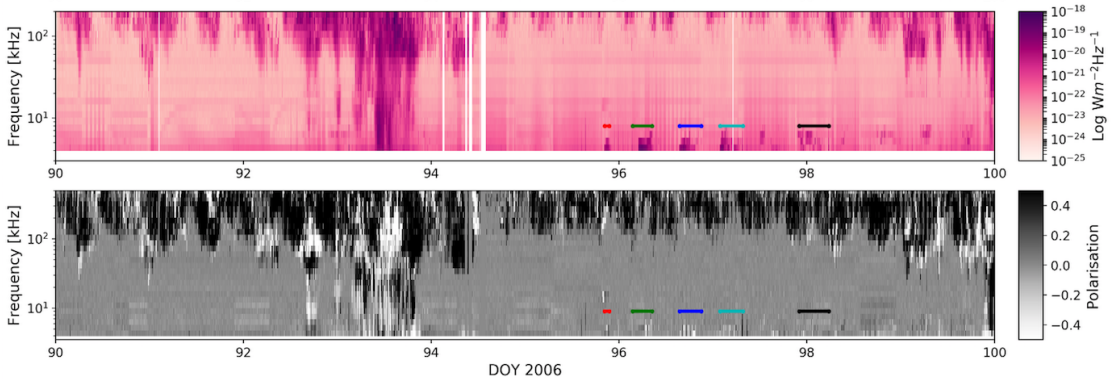

FIGURE 6.1: 10 days of RPWS data showing five 5 kHz narrowband emissions between DOY 90 and 100 in 2006. The top panel shows the SKR intensity as a function of frequency and time. The bottom panel shows the circular polarisation of the emission as a function of frequency and time. Both panels have been cut at the higher frequencies at 500 kHz. The spacecraft is at equatorial latitudes and moves from 1.9h LT to 2.9h LT from 58 to 69 R_S during this 10 day period.

Saturn narrowband emissions are mode converted L-O mode emissions that originate from upper hybrid resonance emissions on the northern and southern boundary of the plasma torus [*Ye et al.*, 2009; *Menietti et al.*, 2009]. The emissions come from different L-shells depending on their frequency: 8 - 10 for the 5 kHz emission and 4 - 7 for the 20 kHz emission [*Ye et al.*, 2009]. They are first generated as Z-mode emissions (a low frequency branch of the extraordinary(X) mode) before the conversion to L-O mode [*Ye et al.*, 2010a]. *Gurnett et al.* [1983] had previously proposed that the emissions are mode converted from electrostatic waves in regions of strong plasma density gradient such as the edge of the plasma disk [*Kurth*, 1981]. *Louarn et al.* [2007] discussed 5 kHz narrowband emissions observed following intensifications of the SKR main band. They linked their observations with evacuations of the plasma disk. For frequencies as low as 4 kHz this implies a density in the source region below 0.3 cm^{-3}. A location they consider for the source is the inner disk around 1 R_S where the density is less than 0.1 cm^{-3} and electromagnetic waves at low frequencies are locally observed [*Wahlund et al.*, 2005]. Evacuation of plasma from the region due to the occurrence of global magnetospheric events would give the densities required for the narrowband generation and give the emission free space to propagate. Based on power measurements of the 5 kHz emission as a function of Cassini radial distance, *Ye et al.* [2010a] found that the power falls off at approximately $1/R^2$ (where R is the radius of the planet) and the most intense emissions are observed around 3 R_S. The most intense emissions are observed inside the plasma torus. More recently *Wang et al.* [2010] associated the 5 kHz narrowband emission with energetic plasma injection indicated by energetic neutral atom brightening events. *Ye et al.* [2009] showed 21 passes of Cassini through the 20 kHz narrowband emission source

region, indicated by a strong electrostatic wave immediately before or after the radio emission. This matched the source location predicted by a model based on an electron density profile [*Persoon et al.*, 2005] and magnetic field model [*Ness et al.*, 1979b]. No convincing source crossings through the 5 kHz source region were found.

Narrowband emissions have been detected at a variety of frequencies between 3 and 70 kHz but the most intense and frequent emissions are those at 5 and 20 kHz. The reason why is still not clear. In mode conversion theories a sharp density gradient is required for the electrostatic z-mode waves to be converted to electromagnetic emissions. *Ye et al.* [2009] suggest that it might be the case that electrostatic waves are generated at all frequencies but sharp density gradients preferentially exist around the source locations of the 5 and 20 kHz emissions. They add that it is possible the 5 and 20 kHz emissions have different source mechanisms due to their different time-frequency structure and lack of 5 kHz source crossings.

Both the narrowband Saturn Myriametric Radiation (nSMR) and the ∼20 kHz emission are oppositely polarised to the SKR with respect to their origin hemisphere (Narrowband emissions: right-handed for southern (positive values in figure scales), left-handed for northern (negative values)) and are emitted in the left-hand ordinary (L-O) mode [*Ye et al.*, 2009]. This opposing polarisation can be seen in figure 6.1 where the main band higher frequency SKR is right-hand polarised (northern source) whilst the highlighted narrowband emissions are left-hand polarised (again a northern source). The 5 kHz emission is only weakly polarised compared to the nSKR and SKR [*Lamy et al.*, 2008]. At the higher frequency end of the nSKR, *Lamy et al.* [2008] noted that the polarisation was the same as that of the SKR, although this may be due to contamination from the SKR source. Polarization measurements confirm that both 5 and 20 kHz narrowband emissions are propagating in the L-O mode, with the exception of some higher frequency narrowband emissions which are R-X mode second harmonic emissions generated by non-linear coupling of two electrostatic upper hybrid waves with opposite wave vectors.

Louarn et al. [2007] observed that the ∼5 kHz emission, the nSMR, appeared after intensification of the SKR. Following comparisons with the Saturn Longitude System (SLS, [*Kaiser et al.*, 1980]) they found the emissions were modulated at slightly less than Saturn's rotation period at ∼10 hours. *Ye et al.* [2010a] found that the 5 kHz emissions have a clock-like source similar to the SKR, intensifying when a particular source region passes through a longitude. *Ye et al.* [2010b] showed that the rotational modulation of the narrowband emissions for the interval between Saturn orbit insertion and equinox (2004 - 2009) showed a dual periodicity similar to that of the SKR as shown in figure 6.2. The narrowband emissions are observed in the opposite hemisphere to their source location much more than the SKR. This is due to the fact that narrowband emissions are

originally generated as Z-mode emission in the plasma torus in a region close to Saturn bounded by the upper hybrid frequency and the Z-mode cutoff frequency contour. These Z-mode emissions can cross the equator before they convert to L-O mode at the edge of the torus and escape.

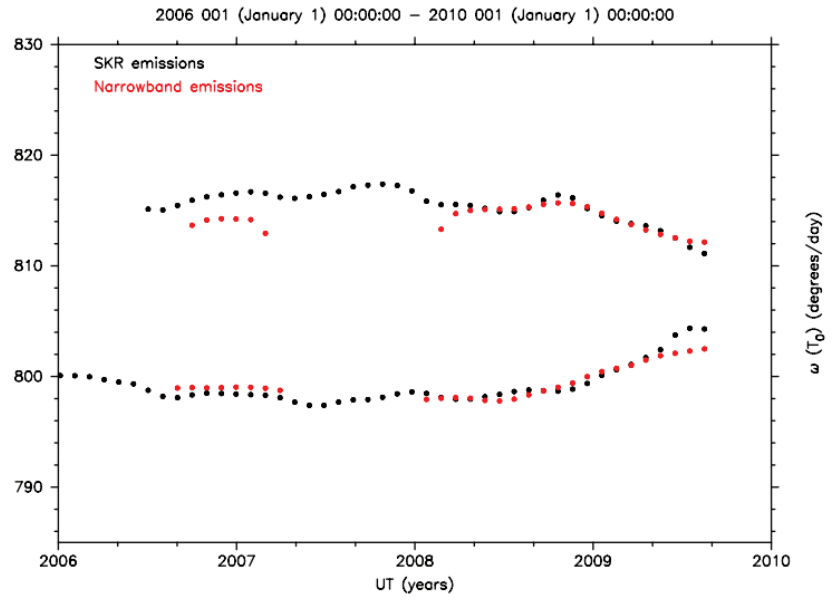

FIGURE 6.2: SKR vs. narrowband modulation periods from 2006 to 2010. The red dots represent the periods of Saturn narrowband emissions. The y-axis label is on the right-hand y-axis and is in degrees per day. The black dots represent the periods of SKR as given by *Gumett et al.* [2009] [*Ye et al.* [2010a]]

Narrowband emissions have also been observed at Jupiter and are known as the n-KOM emission (shown in figure 6.3). They were first reported by *Warwick et al.* [1979]; *Kaiser et al.* [1980]. They are known to be generated from sources that slightly subcorotate in Io's torus [*Reiner et al.*, 1993]. These emissions are observed to follow intensifications in the higher frequency HOM emission, the flux of which is a good proxy for magnetospheric dynamics [*Zarka*, 1998]. The emissions are consistent with O-mode emissions, being left-hand polarised from the northern hemisphere sources, and right-handed from southern sources [*Daigne and Leblanc*, 1986]. *Louarn et al.* [1998] have looked at HOM and nKOM emissions suggesting that intensifications are related to the thinning of the plasma sheet and thus with global Jovian dynamic events. *Reiner et al.* [2000] further reported an intensification of nKOM triggered by IMF sector boundary crossings, showing a solar wind dependence. *Louarn et al.* [2007] showed that whereas the emissions at Saturn are seemingly driven by solar wind interaction, at Jupiter they are linked with internally driven processes with a waiting time between clusters of events between 2 and 10 days.

This chapter builds on the *Louarn et al.* [2007] work mentioned above. In their paper

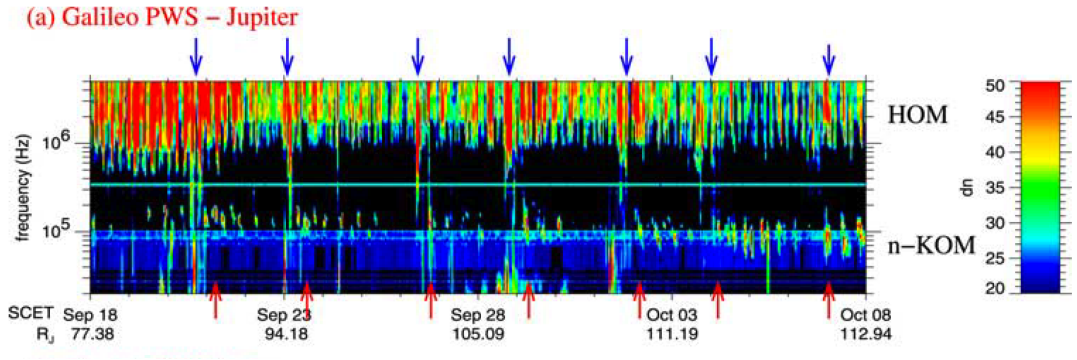

FIGURE 6.3: Galileo observations of Jovian HOM and n-KOM emissions during September to October 1996. The blue arrows mark intensifications of the HOM emissions and the red arrows mark the detection of new n-KOM emissions. [From *Louarn et al.* [2007]]

several narrowband-like emission periods were found at Jupiter and Saturn that correspond to magnetospheric disturbances. As discussed above they found these events to follow intensfications of the main band radio emission (the SKR at Saturn) and are linked with the evacuation of plasma from the plasma sheet region. This chapter expands on this study by automating the detection of the 5 kHz narrowband emissions in Cassini RPWS data from 2006. This is done in order to develop a large catalogue of narrowband emissions that can then be analysed with the aim of assessing their use as a proxy for magnetospheric dynamics. We first discuss the data used in this study, then the criteria used to select narrowband emissions. We then examine statistical properties of these emissions such as their duration and waiting times between the events, before comparing them with a catalogue of LFE events from 2006.

6.2 Data

For the selection of the narrowband emissions, we use a high resolution (90 seconds) dataset consisting of the intensity of the observed radio waves as a function of time and frequency. The flux intensity is given in units of W m^{-2} Hz^{-1} and normalised to one astronomical unit (AU). This dataset is an extension of that derived by *Lamy et al.* [2008] using RPWS data and based on previous work by *Zarka et al.* [2004] and *Cecconi and Zarka* [2005b]. Our dataset differs slightly to that of *Lamy et al.* [2008] in that no criterion was placed on the circular polarization in order to keep highest sensitivity.

In order to assess the link between narrowband emissions and low frequency extension, we use a catalogue of LFEs detected during 2006 using the methods outlined in chapter 5. These events were selected using criteria that required the power to be greater than a location dependent threshold in two integrated power ranges: 40 - 100 kHz and

100 - 600 kHz. To investigate the relationship between the occurrence of narrowband emissions and the SKR phase, we use the phase dataset developed by *Lamy* [2011] that organises SKR maxima. They used Lomb-Scargle analysis, a technique employed to perform spectral analysis of non-continuous data, over a 6-year period from 2004 to 2010 to find the SKR period and related phase systems for each hemisphere. The northern and southern emissions were separated by their circular polarisations (left-handed for southern, right-handed for northern) allowing individual periods to be found and phase systems defined. Each hemispheric phase system has a phase of $0/360^{\circ}$ when the respective SKR emission reaches its peak.

6.3 Automated Detection of Narrowband Emissions

We now discuss the criteria for the detection of the narrowband emissions within the 2006 RPWS data.

6.3.1 Criteria

When trying to identify a narrowband emission we are looking for intensifications of the SKR around 5 kHz which are themselves not a part of a low frequency extension (LFE) (an extension of the SKR main band from higher to lower frequencies). With the thresholds we are trying to select a set of events that have previously been classed as narrowband emissions in *Louarn et al.* [2007]. The final criteria are as follows:

1. The maximum intensity in the kHz frequency range 3.95 to 5.76 kHz must be greater than 5 x 10^{-21} W m^{-2} Hz^{-1}.
2. The maximum intensity in the kHz frequency range 3.95 to 5.76 kHz must be 500 times greater than the maximum intensity in the kHz frequency range 54.98 to 66.36 kHz.

The low frequency range in criterion one was selected as this is the region of the spectrum where we expect to see the narrowband emissions. We required this region to be more intense than the higher frequency region in criterion two so as not to incorrectly select an LFE that had extended from the main band to this lower frequency range.

Before settling on the criteria described, several other criteria formats were tested. Initially, criteria based on the intensity and polarisation at the lower frequencies of the SKR were tried. On inspection of narrowband events selected by eye, the polarisation was

found to be highly variable during an event and as such it was difficult to satisfactorily set a suitable polarisation threshold.

6.3.2 Clustering

The narrowband algorithm returns each time step in the RPWS dataset that matches the criteria as defined above. This gave 11271 (out of 350400) points across 2006 that satisfied the criteria. In practice, the SKR displays intensifications and narrowband emissions on much longer timescales than the 90 second cadence of the dataset, and thus we applied a simple clustering algorithm to gather the points which fulfil the narrowband criteria into local groups which represent distinct narrowband emissions as shown in Figure 6.4. The"maximum gap size", defined below as 150 minutes, was again empirically tuned to give the best agreement with our by-eye training set. The clustering works as follows:

1. First point, i_1, is put into cluster 1
2. If at second point, i_2, i_2 - i_1 <= X, where X is the maximum gap size = 150 minutes, i_2 is put into cluster 1.
3. Else if i_2 - i_1 > X, a new cluster is started and, i_2 is put into that.
4. Continue for all points

Following the clustering of the points that meet the narrowband emission criteria we inspected the catalogue and removed those events shorter than 30 minutes to ensure we were selecting sustained narrowband events. This gave a total of 164 narrowband events for 2006. As a further note, we detect all 5 narrowband emission 'groups' shown by *Louarn et al.* [2007] at Saturn.

6.4 Results: Narrowband Emission Catalogue

Figures 6.5 and 6.6 show 360 days of 2006 SKR data with LFEs detected in chapter 5 (in black) and narrowband emissions detected using the above criteria (various colours). The narrowband emissions show a very strong clustering (shown by the blue boxes) and follow an LFE or period of SKR intensification, most often appearing in groups of at least five. This behaviour matches that observed and discussed by *Louarn et al.* [2007]. There are very few cases where a narrowband emission occurs in isolation. 78 of the 164 (48%) events are seen before DOY 205 (56% of 2006) where Cassini changed from an equatorial

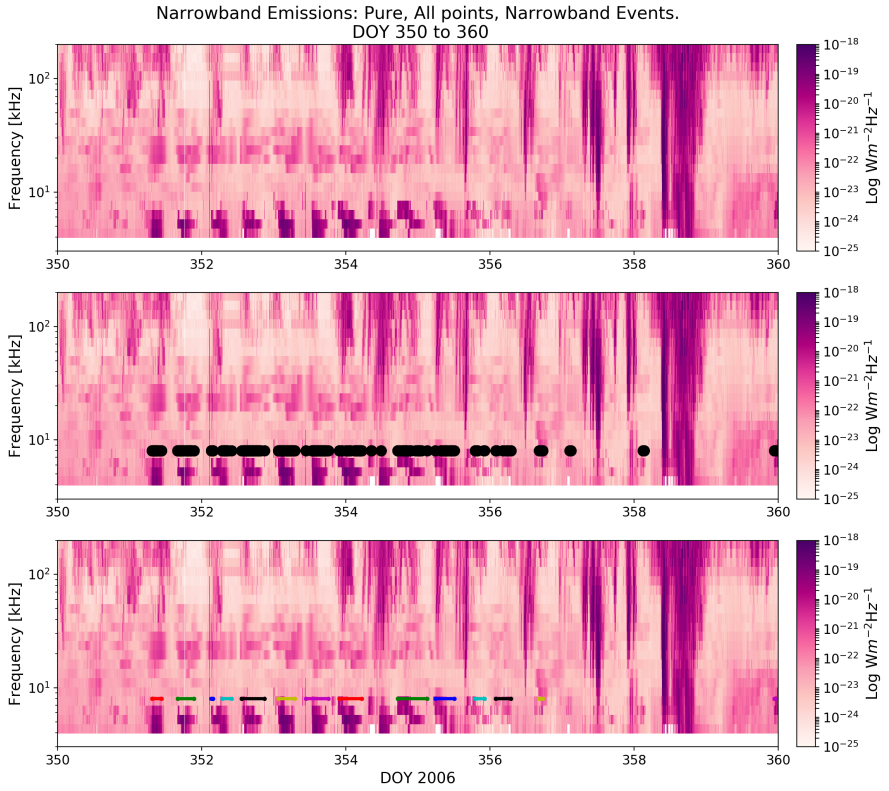

FIGURE 6.4: Example of Narrowband point clustering on a ten day period between DOY 350 and 360 2006. Panel A shows a pure spectrogram of SKR data. Panel B shows 258 points (black circles) that satisfy the narrowband criteria. Panel C shows those points clustered into 13 distinct narrowband 'events' (different coloured rectangles) following the removal of the clustered events shorter than 30 minutes.

to a higher latitude orbit which would seem to suggest a slight latitude dependence on emission visibility. This is in agreement with work by *Louarn et al.* [2007] who noted that the emissions were observed twice as frequently when the spacecraft was at greater than 40° latitude than when it was below 20°. Thus the appearance of narrowband emissions is more frequent than would be deduced from just low latitude observations i.e. the lower rate observed at low latitudes is due to the events not being observed rather than them not occuring. *Louarn et al.* [2007] thus suggested this implies that the narrowband emission visibility is enhanced by a magnetospheric event rather than the event itself triggering an emission.

6.4.1 Narrowband emissions temporal properties

This section looks at two of the temporal properties of the narrowband emissions selected by the criteria. The duration of the narrowband emissions is the time from start to end of the points that meet the criteria following the clustering as described above. The waiting time of the events is the time between the end of one event and the start of the

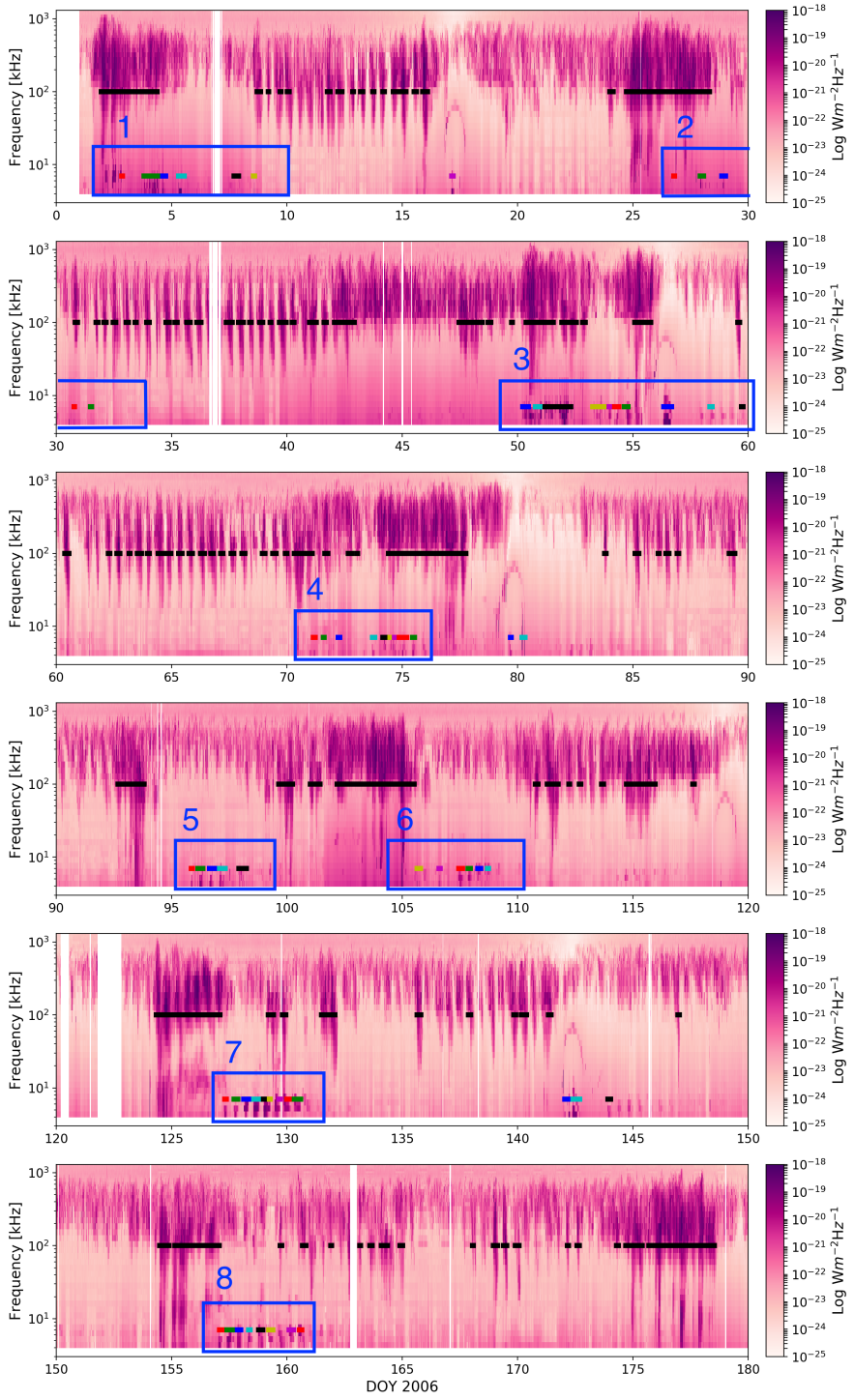

FIGURE 6.5: 30 day long spectrograms with LFEs from the chapter 5 LFE catalogue and narrowband emissions detected in this study from DOY 0 - 180 of 2006. When narrowband emissions are observed there is a very clear clustering together. These clusters have been highlighted by the blue boxes.

following event. Figure 6.7 shows the distribution of narrowband event durations. There are 164 events and a median event duration of 2.86 hours which is of a similar length to the short LFEs found in chapter 5. The events are much shorter than a Saturn rotation

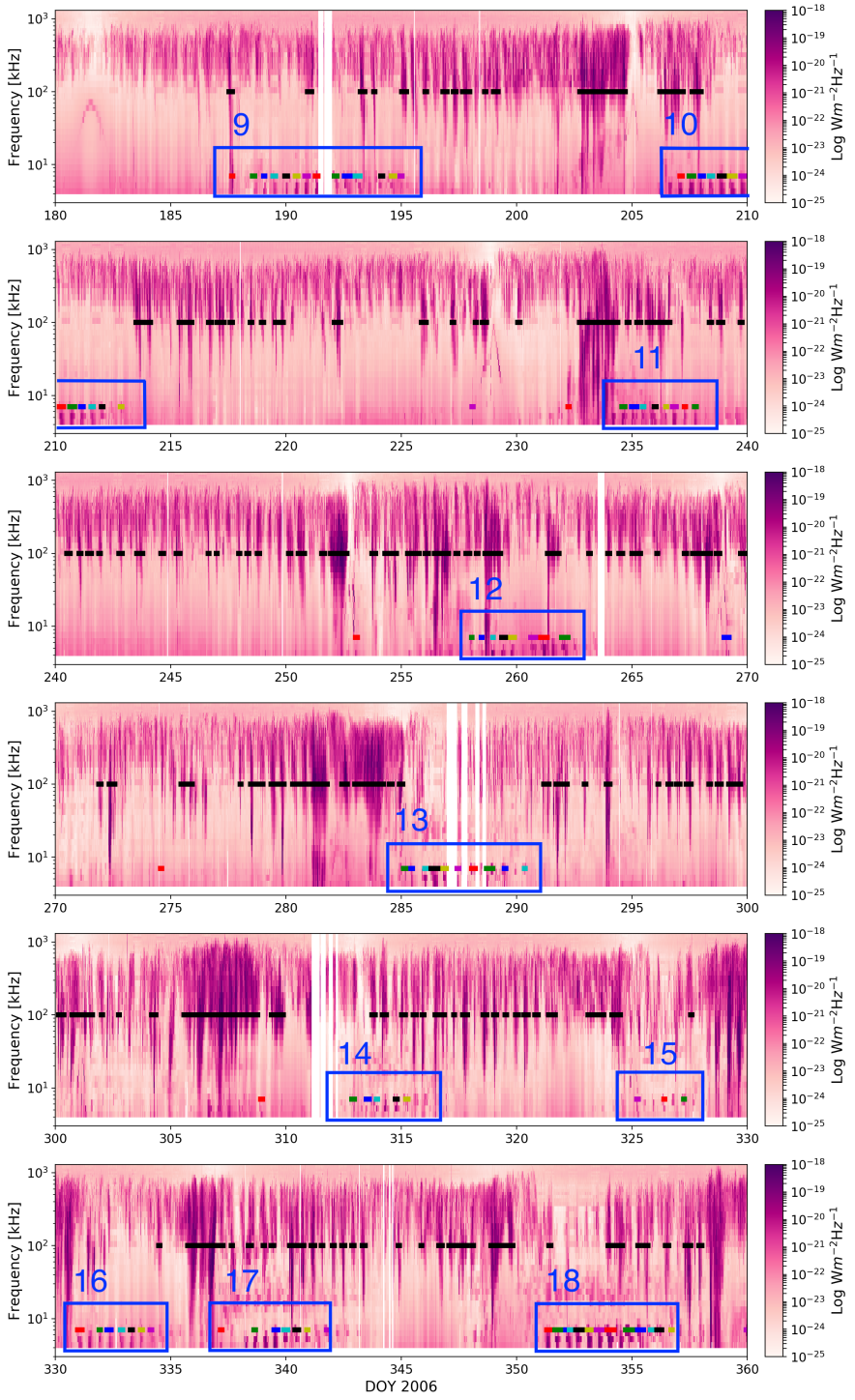

FIGURE 6.6: 30 day long spectrograms with LFEs from the chapter 5 catalogue and narrowband emissions detected in this study from DOY 180 - 360 of 2006. When narrowband emissions are observed there is a very clear clustering together. These clusters have been highlighted by the blue boxes.

period.

We now look further at the 18 clustered events shown across figures 6.5 and 6.6. Figure 6.8 shows the waiting times between the narrowband emissions within each group. The

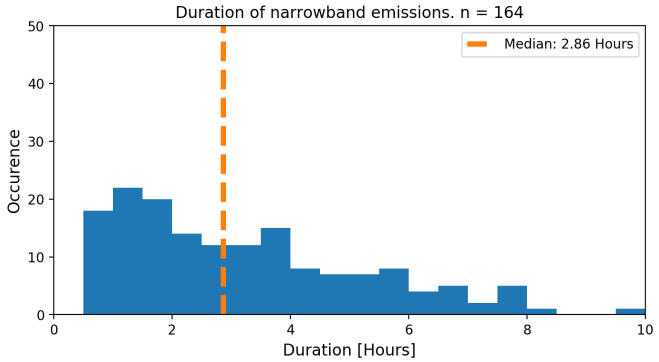

FIGURE 6.7: The distribution (blue) of narrowband emission duration. There are 164 event durations. The orange dotted line shows the median of 2.86 hours.

majority of the events occur within one planetary rotation of another. The long tail can be accounted for by two groups (1 and 3 on figure 6.5) which may suggest our grouping in those cases was not perfect.

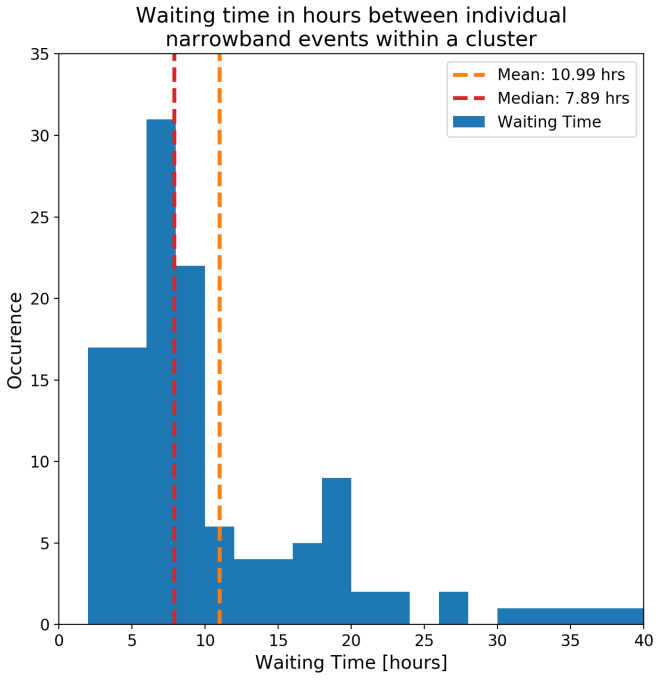

FIGURE 6.8: The distribution (blue) of narrowband emission waiting times within clusters. The orange dotted line shows the median of 7.89 hours. The red dotted line shows the mean of 10.99 hours.

Building on this figure, 6.9 shows the cycle duration within clusters. The cycle duration is the total duration of individual narrowband emissions and waiting times to the next event within a cluster (i.e. duration event i + waiting time between event i and event i + 1). The median is 11.12 hours which is slightly longer than the planetary rotation period. This suggests there is a rotational dependence on the occurrence of these narrowband emissions. This figure and figure 6.8 suggest a strong rotational dependence for the

narrowband emissions once they begin. *Louarn et al.* [2007] observed that the emissions were modulated at slightly less than Saturn's rotation period via comparison with the SLS.

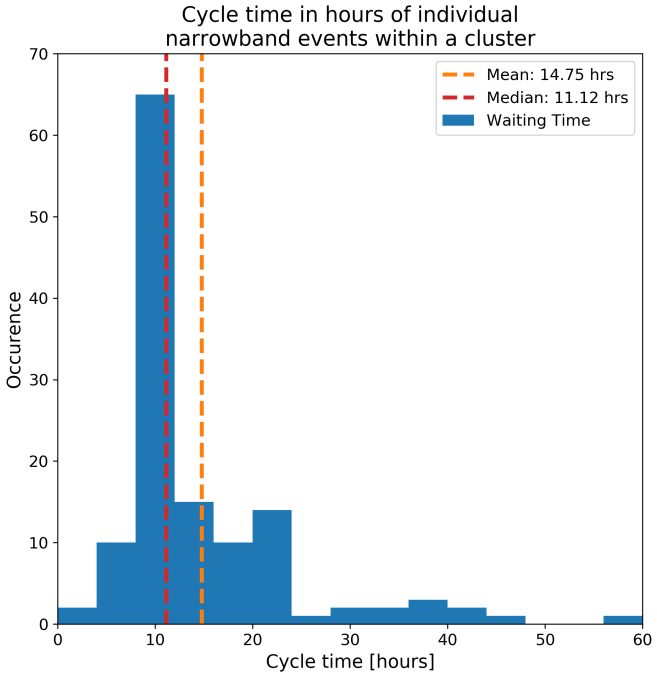

FIGURE 6.9: The distribution (blue) of narrowband emission cycle time within clusters. The cycle time is the total duration and waiting time to the next event of an event within a cluster. The orange dotted line shows the median of 11.12 hours which is on the order of one planetary rotation. The red dotted line shows the mean of 14.75 hours. 30% of all cycle times are between 9 and 11 hours, with a further 21% between 8 and 12.

Figure 6.10 shows the waiting times between the 18 narrowband clusters. 10 of the 18 events occur within a waiting time of 18 - 28 days of another. Figure 6.11 shows the durations of the narrowband clusters; 16 out of 18 of the clusters last between 2 and 6 days with a mean of 4.5 days. With the waiting times between the clusters this gives an cycle time of ∼22 to 32 days which would be in line with the approximate period of the arrival of solar wind compressions of ∼ 25 days as previously observed by *Kurth et al.* [2016]. This approximate period was also observed by *Louarn et al.* [2007].

Since we see a strong rotational dependence on the cycle time for narrowband events within a cluster we next look at their relationship with SKR phase.

6.4.2 Narrowband emissions and SKR phase

This section looks at the occurrence of the narrowband emissions with SKR phase. Figure 6.12 shows the northern and southern SKR phase at the start of the narrowband

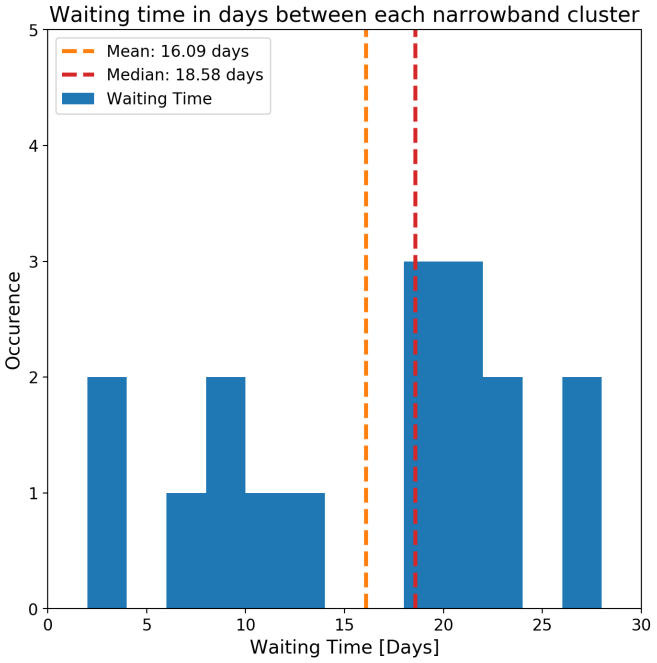

FIGURE 6.10: The distribution (blue) of waiting times between each cluster. There are 17 waiting times between 18 clusters. The orange dotted line shows the median of 18.58 days. The red dotted line shows the mean of 16.09 days.

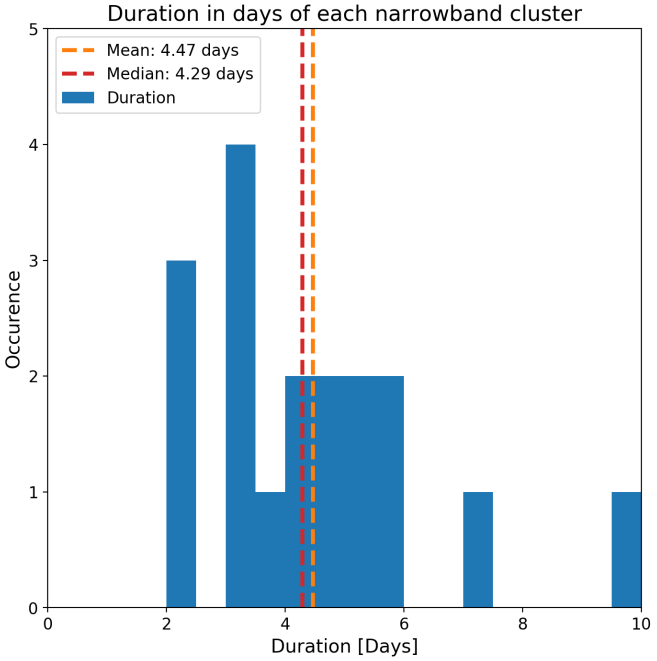

FIGURE 6.11: The distribution (blue) of cluster durations. There are 18 clusters. The orange dotted line shows the median of 4.29 days. The red dotted line shows the mean of 4.47 days.

emissions. The start of the narrowband emissions are strongly correlated to the decreasing phase (0 - 180°) of the southern SKR phase. 127/164 events begin in this section of the phase. The relationship is not as strong with the northern SKR phase where only

89/164 are in the 0 - 180° section of the northern phase. The correlation with the southern SKR further supports the finding of the modulation of the narrowband events with planetary rotation. The clustering around 90° also repeats what was found in *Wang et al.* [2010] and *Ye et al.* [2010a] that the events occur in quadrature with the SKR peak. This relationship is slightly different to that found by *Louarn et al.* [2007] who found that the intensifications occurred at a period slightly less than a planetary rotation. This modulation suggests that the occurrence of large magnetospheric events first provides the conditions that either increase the visibility of the narrowband emissions (as suggested by *Louarn et al.* [2007] and mentioned in context of narrowband emission visibility on spacecraft latitude in section 6.4) or allows them to occur. The modulation with planetary rotation is then superposed 'on top'.

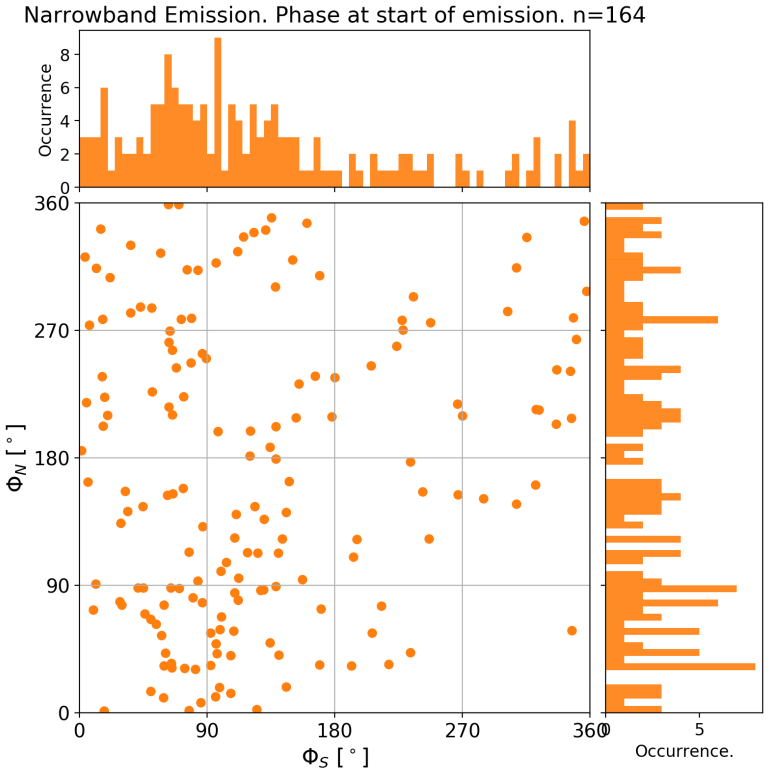

FIGURE 6.12: The northern (y-axis) and southern (x-axis) SKR phase at the start of the narrowband emissions.

There therefore is a strong relationship between the rotation of the planet (in terms of SKR phase and in the cycle time) and the onset of the individual narrowband emissions within clusters. Yet we do not see the emissions all the time instead observing a cycle time (duration plus waiting time) between 22 and 32 days. We next look at the relationship with the solar wind with the narrowband emissions.

6.4.3 Narrowband emissions and the solar wind

This section looks at the narrowband emissions in relation to the solar wind and an example of a long LFE from chapter 5. Figure 6.13 shows the occurrence of all narrowband events (orange) during 2006, the long LFEs as found in chapter 5 (dark blue boxes) and the solar wind dynamic pressure (purple and light blue lines).

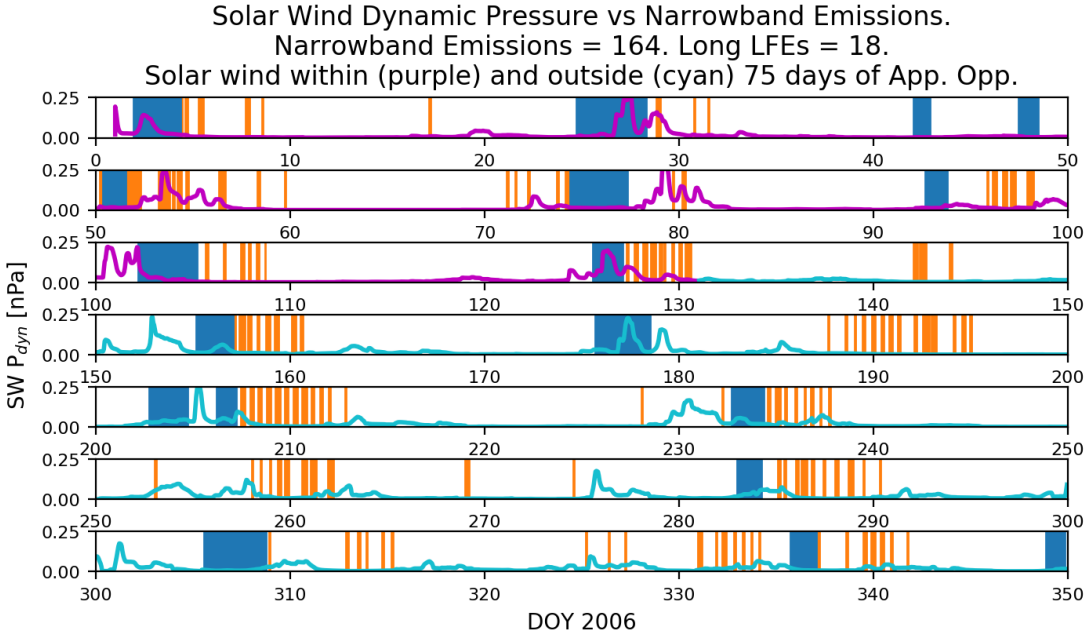

FIGURE 6.13: Comparing solar wind dynamic pressure (purple and cyan) as a function of time with narrowband events (orange) and long LFEs (blue). There are a total of 164 individual narrowband emissions and 18 long LFEs. Solar wind dynamic pressure calculated within 75 days of apparent opposition is plotted in purple whilst that calculated further than 75 days is in cyan.

Figure 6.14 shows the behaviour of the solar wind dynamic pressure for the preceding two days (Panel A1) of the 18 narrowband clusters and for the whole of 2006 (Panel A2), and the SKR power in the 100-600 kHz range for the preceding two days (Panel B1) of the 18 narrowband clusters and for the whole of 2006 (Panel B2). Both the solar wind dynamic pressure and SKR average power is significantly increased during the two days preceding a narrowband cluster. The solar wind in the two days before a narrowband cluster has a mean and median twice that to the year on average. The median SKR power is also twice as strong in the preceding two days to a narrowband cluster compared to the year on average. A Kolmogorov Smirnov (KS) test measures the likelihood two sample distributions are drawn from the same overriding distribution. It returns a KS value based on the distance between the two cumulative distribution functions, and a p-value that gives the probability the KS value would be that high given the assumption that the two distributions are from the same distribution. Comparing the solar wind dynamic pressure in the period just preceding the appearance of narrowband emissions,

and the year overall gives a KS value of 0.23 and a p-value of $<10^{-38}$. Comparing the SKR power in the same two periods gives a KS value of 0.21 and a p-value that $<10^{-36}$. These two results show that the average properties of the solar wind and SKR power are significantly different in the period preceding the narrowband emissions versus the year overall suggesting a relationship between their behaviours and the appearance of narrowband emissions.

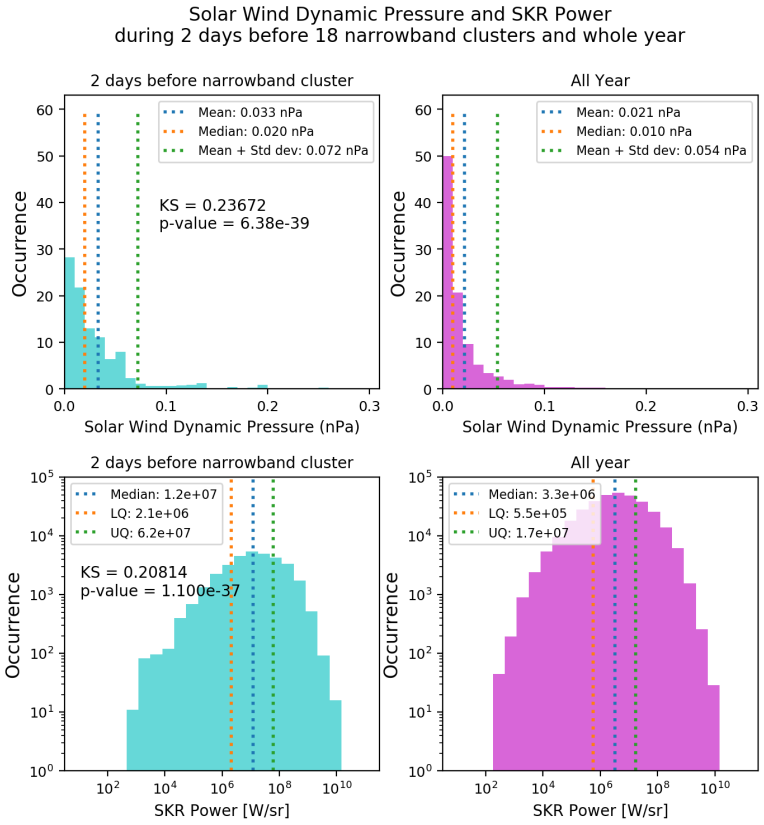

FIGURE 6.14: The distribution of the solar wind dynamic pressure and the SKR power in the two days preceding a narrowband cluster (Panels A1 and B1 respectively) and for the whole of 2006 (Panels A2 and B2).

Unlike long LFEs which have been shown to occur during periods of increased solar wind dynamic pressure in chapter 5, narrowband emissions generally occur following periods of intense solar wind dynamic pressure. During the emissions themselves the solar wind dynamic pressure is not significantly higher than average for the year.

This analysis further supports the link with solar wind (that the narrowband events follow increases in solar wind dynamic pressure) that was suggested in the previous subsection (and in work such as *Louarn et al.* [2007]) following the ~25 day cycle between narrowband emission clusters.

Figure 6.15 shows seven days of SKR data centred on a long LFE beginning DOY 232 and ending DOY 234. Long LFEs are usually associated with periods of increased solar

wind dynamic pressure. Following the long LFE there is a series of smaller periodic LFEs as well as a series of periodic narrowband events that last a period of a few days.

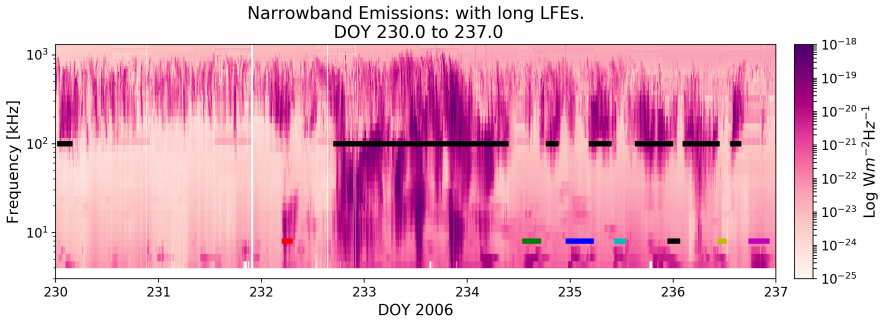

FIGURE 6.15: Example of narrowband emissions following a long LFE (LFE with duration greater than 20 hours). Long LFEs have previously been associated with increases in solar wind dynamic pressure. The long LFE begins around 1800 on DOY 232 and finishes around 0600 DOY 234. The long LFE is followed by several smaller short LFEs as well 6 narrowband emissions.

Narrowband emissions are found to occur during or after 11 out of 18 LFEs classed as long in chapter 5. The clusters of narrowband emissions in figures 6.5 and 6.6 nearly always appear following either a long LFE or a period of quasi-continuous intensification with several short LFEs. As shown in figure 6.14, the solar wind dynamic pressure is also significantly enhanced in the period preceding these narrowband emission clusters.

6.5 Discussion

In this chapter we have developed simple criteria for the selection of 5 kHz narrowband emissions from 2006 RPWS data in order to assess their suitability as a proxy for magnetospheric dynamics. This criteria gave us 164 events which were then clustered into 18 'clusters'.

There are three key results from this study that can now be discussed in context of magnetospheric dynamics:

1. Narrowband emissions appear in clusters lasting a few days with a median cycle time of $\sim$ 11 hours.

2. There is a strong correlation with narrowband emission start time and a specific SKR phase.

3. The narrowband clusters have an approximate cycle time between 22 and 32 days and are strongly correlated with high solar wind dynamic pressure.

The median event duration is approximately 3 hours with a median waiting time of ∼8 hours between events within a cluster. A median cycle duration (duration plus waiting time) was calculated as ∼ 11 hours in line with the approximate rotation period of Saturn (∼10.7 hours). This rotational dependence is further emphasised when comparing the narrowband emission start times with the northern and southern SKR periods which found a strong clustering of emission start times when the southern SKR system was at ∼ 90°. This was also found by *Wang et al.* [2010] and *Ye et al.* [2010a]. As found by this study and by *Louarn et al.* [2007], the rate of events observed is higher at higher latitudes than at lower latitudes. As described in the introduction, this suggests that even though narrowband emissions are not observed throughout the year, it is not because they are not occurring, rather that they cannot be seen. Thus, there is a driver that enhances the narrowband emissions allowing them to be observed; the rotational modulation is then observed 'on top'.

The waiting time distribution between clusters ranges from between a few days and ∼28 days with a median of ∼19 days with most of the clusters lasting between 3 and 6 days. This gives a total 'cycle' period on the order of 25 days or a solar rotation. This is similar to the long LFEs detected in chapter 5, although unlike the long LFEs which occur during times of increased solar wind dynamic pressure, the narrowband emissions tend to occur during and for several days after times of increased dynamic pressure. The narrowband emissions show a high correlation with increased solar wind dynamic pressure in the preceding two days. This high solar wind dynamic pressure can trigger magnetic reconnection in the tail. *Louarn et al.* [2007] suggested that a plasma evacuation of the plasma sheet due to a large-scale reconnection event could lower the density sufficiently for the generation of the Z-mode emissions. Since narrowband emissions usually do not occur following single short LFEs, it seems that an extended period of plasma evacuation associated with large magnetospheric dynamics and also with multiple short LFEs or a large long LFE is required.

Thus the mechanism is as follows: (1) A region of high pressure solar wind arrives at Saturn, (2) There is a large-scale reconnection event within the tail or a prolonged period with many small reconnection events, (3) This causes a significant evacuation of plasma from the plasma sheet leading to an enhancement in the narrowband emissions, (4) The narrowband emissions can then be observed with further rotationally modulated enhancements 'on-top'.

6.6 Summary

In this chapter we have developed simple criteria for the selection of 5 kHz narrowband emissions from 2006 RPWS data. This criteria gave us 164 events across 2006. Based on their strong rotational modulation and appearance following periods of high solar wind dynamic pressure or prolonged magnetospheric activity we conclude that narrowband emissions are a good proxy for the occurrence of large or prolonged magnetospheric dynamics.

Chapter 7

Summary and Future Work

7.1 Introduction

This chapter summarises the three research chapters (4, 5, and 6) within this thesis and then discusses potential future avenues of work that could come from each study.

7.2 Jupiter's mass budget problem

Jupiter's magnetosphere is believed to be primarily driven by a combination of its rapid rotation and an input of plasma originating from one of its moons, Io. However, the amount of mass loaded in the magnetosphere by Io (on the order of $\sim$1000 $kg\ s^{-1}$) is not balanced by the amount of mass observed to leave the system in the form of plasmoids broken off by tail reconnection (up to $\sim$120 $kg\ s^{-1}$). This is referred to as the mass budget problem. Viewing restrictions from single spacecraft are a significant issue in understanding magnetospheric dynamics, meaning that many in situ signatures of mass transport and loss can be missed if they occur at some distance from the spacecraft track through the system. This context led to the study presented in chapter 4.

This study explored the use of a simple 1-D cellular automata sandpile model to reproduce statistical properties of the Jovian magnetosphere. The model acted analogous to a sandpile in that following an accumulation of "sand" in the first cell, upon reaching a threshold gradient between the first and second cell, the sandpile would "avalanche". This behaviour would continue down the length of the sandpile as more sand was added. It was found that with a constant threshold gradient between the cells and a "slow" input of sand, the waiting times (time between consecutive events) between avalanches of different sizes was an inverse gaussian distribution, the same as had been observed

between actual events in the Jovian magnetosphere. A physical analogue relating the moving of sand down the grid with a loss of mass from the Jovian plasma sheet suggested that much of the mass lost from Jupiter's magnetosphere is lost via small-scale mass loss events that may not be observed by spacecraft or selected by event detection algorithms.

This work could be applied to the magnetosphere of Saturn. Like at Jupiter, Saturn has a mass budget problem where there is an order of magnitude difference between mass that is calculated to be added to the magnetosphere (mostly in the form of water ions from its moon Enceladus) and what is observed to leave via plasmoids [e.g. *Jackman et al.*, 2014b]. The simplicity of the model means that a variety of rules (i.e. threshold gradient between cells or redistribution rules following an avalanche) and input (i.e. distribution of sand input) can be explored to try to reproduce some of the statistical properties within Saturn's magnetosphere such as the observed waiting times between tail reconnection events. A comparison with Magnetohydrodynamic (MHD) simulations could also be interesting to see if these models reproduce a similar plasmoid size and occurrence rate as discussed in this work. The mass budget problem could also be studied further with measurements from the Juno spacecraft which arrived at Jupiter in June 2016. Juno's 53 day orbit takes it into the tail of Jupiter where it can observe in situ the magnetosphere and plasma conditions.

7.3 Low Frequency Extensions of the Saturn Kilometric Radiation

The occurrence of magnetospheric phenomena such as tail reconnection within the magnetosphere is difficult to measure accurately since many events may be missed when the spacecraft is not within some 'viewing region'. A viewing region is simply the area of space in which the subject you are trying to observe can be observed. Tail reconnection by definition occurs in the tail region of the magnetosphere but throughout its orbit of Saturn, Cassini passed through various regions where tail reconnection would not be visible such as the dayside of the planet or the magnetosheath. Even if the spacecraft is in the tail it may not be sufficient to observe events. Reconnection products are large, complicated 3D structures, variable in size, but the magnetotail is huge; it is possible a product of reconnection could pass the spacecraft at a distance where it is undetectable. Saturn Kilometric Radiation (SKR) is an auroral radio emission which can be detected quasi-continuously by the Cassini spacecraft. It has been shown to respond to magnetotail reconnection and to changes in solar wind conditions in the form of Low

Frequency Extensions (LFE), and thus offers the potential to be used as a remote proxy for magnetospheric dynamics. This led to the study presented in chapter 5.

In this study 282 LFEs were selected from the 2006 RPWS data. Upon examination of the LFE catalogue, two forms of LFE were found: 264 short ($<$ 20 hours) and 18 long ($>$ 20 hours). The short LFEs were found to be strongly correlated with SKR phase whilst the long events showed no correlation with SKR phase. Of the 264 short events, 156 were detected during periods previously defined as a tail reconnection viewing region by *Smith et al.* [2016]. 61% of these events were shown to have a reconnection event within the previous 6 hours. An analysis of the emitted power found no difference between those LFEs that were found to have an associated reconnection event and those that were not, suggesting that the imperfect correlation could be due to missed reconnection events in the tail rather than a lack thereof. The long LFEs were shown to appear during periods of increased solar wind dynamics pressure and last several planetary rotations. This study concluded that LFEs can be used as a proxy for Saturn's magnetospheric dynamics (i.e. tail reconnection) and solar wind conditions at Saturn.

An interesting extension of the LFE work in chapter 5 would be an analysis of the relationship between the intensity and/or duration of an LFE and the properties of the associated reconnection event. The size of a tail reconnection event is difficult to estimate, particularly with single spacecraft, since the observed signature of an event is highly dependent of the trajectory of the spacecraft through the structure. Future work might be able to model the size of the reconnection events in the *Smith et al.* [2016] catalogue in the context of spacecraft location and trajectory and explore the relationship with the LFEs. The proximal orbits performed by Cassini in 2016 could also reveal more about the SKR source region and how it changes with altitude or the occurrence of magnetospheric dynamics. The high latitude orbits may lead to passes through the SKR source region leading to better understanding of the plasma conditions there. Intensifications of the HOM emission at Jupiter has also been associated with magnetospheric dynamics [*Zarka*, 1998; *Louarn et al.*, 1998, 2000, 2001]; the methods applied in this study could therefore be used at Jupiter to develop a catalogue of HOM intensifications and assess their use as a proxy for magnetospheric dynamics via comparisons with reconnection catalogues such as that of *Vogt et al.* [2010] or against solar wind dynamics using mSWiM [*Zieger and Hansen*, 2008].

7.4 Narrowband Emissions at Saturn

Narrowband emissions have previously been associated with the occurrence of large-scale magnetospheric processes at both Saturn *Louarn et al.* [2007] and Jupiter *Louarn*

et al. [1998]; *Reiner et al.* [2000]. Narrowband emissions at Saturn have been observed to appear and last for several days following the occurrence of an intensification of the SKR, such as a LFE. Several individual emissions are observed over a period of several days, approximately modulated by the planetary rotation period. This study in chapter 6 developed an automated set of criteria for the selection of 5 kHz narrowband emissions from a 2006 SKR dataset. 164 events were found. The narrowband events do not seem to appear after every LFE, they instead seem to appear following large, intense LFEs or prolonged SKR intensifications. They were also found to follow periods of more intense solar wind dynamic pressure. The 164 events of 2006 were grouped into 18 clusters, which had an average cycle time (waiting time plus duration) of ∼25 days. Narrowband emissions are generated as Z-mode emissions in the plasma torus, suggesting that a significant evacuation of the plasma torus leading to the necessary low plasma density conditions is required. In this sense narrowband emissions are a good proxy for the occurrence of large or prolonged magnetospheric dynamics.

As with the LFE work in chapter 5, the proximal orbits of Cassini in 2016 may pass through regions allowing good viewing and measurements of narrowband sources. These measurements would allow a better understanding of the conditions under which narrowband emissions appear, from where they are best seen and what this tells us about their link with magnetospheric dynamics. An extension of this work would be further investigation into the narrowband n-KOM emissions seen at Jupiter and their link with magnetospheric dynamics. This work could also follow the application of the search for low frequency extensions of the HOM at Jupiter.

Bibliography

Achilleos, N., C. S. Arridge, C. Bertucci, C. M. Jackman, M. K. Dougherty, K. K. Khurana, and C. T. Russell (2008), Large-scale dynamics of Saturn's magnetopause: Observations by Cassini, *Journal of Geophysical Research: Space Physics*, *113*(11), doi:10.1029/2008JA013265.

André, N., M. K. Dougherty, C. T. Russell, J. S. Leisner, and K. K. Khurana (2005), Dynamics of the Saturnian inner magnetosphere: First inferences from the Cassini magnetometers about small-scale plasma transport in the magnetosphere, *Geophysical Research Letters*, *32*(14), 1–5, doi:10.1029/2005GL022643.

André, N., A. M. Persoon, J. Goldstein, J. L. Burch, P. Louarn, G. R. Lewis, A. M. Rymer, A. J. Coates, W. S. Kurth, J. C. Sittler, M. F. Thomsen, F. J. Crary, M. K. Dougherty, D. A. Gurnett, and D. T. Young (2007), Magnetic signatures of plasma-depleted flux tubes in the Saturnian inner magnetosphere, *Geophysical Research Letters*, *34*(14), L14,108, doi:10.1029/2007GL030374.

Andrews, D. J., E. J. Bunce, S. W. H. Cowley, M. K. Dougherty, G. Provan, and D. J. Southwood (2008), Planetary period oscillations in Saturn's magnetosphere: Phase relation of equatorial magnetic field oscillations and Saturn kilometric radiation modulation, *Journal of Geophysical Research: Space Physics*, *113*(9), doi:10.1029/2007JA012937.

Andrews, D. J., A. J. Coates, S. W. H. Cowley, M. K. Dougherty, L. Lamy, G. Provan, and P. Zarka (2010a), Magnetospheric period oscillations at Saturn: Comparison of equatorial and high-latitude magnetic field periods with north and south Saturn kilometric radiation periods, *Journal of Geophysical Research: Space Physics*, *115*(12), doi:10.1029/2010JA015666.

Andrews, D. J., S. W. H. Cowley, M. K. Dougherty, and G. Provan (2010b), Magnetic field oscillations near the planetary period in Saturn's equatorial magnetosphere: Variation of amplitude and phase with radial distance and local time, *Journal of Geophysical Research A: Space Physics*, *115*(A4), doi:10.1029/2009JA014729.

Andrews, D. J., B. Cecconi, S. W. H. Cowley, M. K. Dougherty, L. Lamy, G. Provan, and P. Zarka (2011), Planetary period oscillations in Saturn's magnetosphere: Evidence in magnetic field phase data for rotational modulation of Saturn kilometric radiation emissions, *Journal of Geophysical Research: Space Physics*, *116*(9), doi: 10.1029/2011JA016636.

Andrews, D. J., S. W. H. Cowley, M. K. Dougherty, L. Lamy, G. Provan, and D. J. Southwood (2012), Planetary period oscillations in Saturn's magnetosphere: Evolution of magnetic oscillation properties from southern summer to post-equinox, *Journal of Geophysical Research: Space Physics*, *117*(4), doi:10.1029/2011JA017444.

Angelopoulos, V., F. V. Coroniti, C. F. Kennel, M. G. Kivelson, R. J. Walker, C. T. Russell, R. L. McPherron, E. Sanchez, C.-I. Meng, W. Baumjohann, G. D. Reeves, R. D. Belian, N. Sato, E. Friis-Christensen, P. R. Sutcliffe, K. Yumoto, and T. Harris (1996), Multipoint analysis of a bursty bulk flow event on April 11, 1985, *Journal of Geophysical Research: Space Physics*, *101*(A3), 4967–4989, doi:10.1029/95JA02722.

Angelopoulos, V., T. Mukai, and S. Kokubun (1999), Evidence for intermittency in Earth's plasma sheet and implications for self-organized criticality, *Physics of Plasmas*, *6*(11), 4161–4168, doi:10.1063/1.873681.

Arridge, C. S., C. T. Russell, K. K. Khurana, N. Achilleos, N. André, A. M. Rymer, M. K. Dougherty, and A. J. Coates (2007), Mass of Saturn's magnetodisc: Cassini observations, *Geophysical Research Letters*, *34*(9), doi:10.1029/2006GL028921.

Arridge, C. S., K. K. Khurana, C. T. Russell, D. J. Southwood, N. Achilleos, M. K. Dougherty, A. J. Coates, and H. K. Leinweber (2008a), Warping of Saturn's magnetospheric and magnetotail current sheets, *Journal of Geophysical Research: Space Physics*, *113*(8), doi:10.1029/2007JA012963.

Arridge, C. S., C. T. Russell, K. K. Khurana, N. Achilleos, S. W. Cowley, M. K. Dougherty, D. J. Southwood, and E. J. Bunce (2008b), Saturn's magnetodisc current sheet, *Journal of Geophysical Research: Space Physics*, *113*(4), doi:10.1029/2007JA012540.

Arridge, C. S., N. André, N. Achilleos, K. K. Khurana, C. L. Bertucci, L. K. Gilbert, G. R. Lewis, A. J. Coates, and M. K. Dougherty (2008c), Thermal electron periodicities at 20 Saturn Radii in Saturn's magnetosphere, *Geophysical Research Letters*, *35*(15), doi:10.1029/2008GL034132.

Arridge, C. S., H. J. McAndrews, C. M. Jackman, C. Forsyth, A. P. Walsh, E. C. Sittler, L. K. Gilbert, G. R. Lewis, C. T. Russell, A. J. Coates, M. K. Dougherty, G. A. Collinson, A. Wellbrock, and D. T. Young (2009), Plasma electrons in Saturn's

magnetotail: Structure, distribution and energisation, *Planetary and Space Science*, *57*(14-15), 2032–2047, doi:10.1016/j.pss.2009.09.007.

Arridge, C. S., N. André, K. K. Khurana, C. T. Russell, S. W. Cowley, G. Provan, D. J. Andrews, C. M. Jackman, A. J. Coates, E. C. Sittler, M. K. Dougherty, and D. T. Young (2011), Periodic motion of Saturn's nightside plasma sheet, *Journal of Geophysical Research: Space Physics*, *116*(11), doi:10.1029/2011JA016827.

Arridge, C. S., J. P. Eastwood, C. M. Jackman, G. K. Poh, J. A. Slavin, M. F. Thomsen, N. André, X. Jia, A. Kidder, L. Lamy, A. Radioti, D. B. Reisenfeld, N. Sergis, M. Volwerk, A. P. Walsh, P. Zarka, A. J. Coates, and M. K. Dougherty (2016a), Cassini in situ observations of long-duration magnetic reconnection in Saturn's magnetotail, *Nature Physics*, *12*(3), 268–271, doi:10.1038/nphys3565.

Arridge, C. S., J. M. Jasinski, N. Achilleos, Y. V. Bogdanova, E. J. Bunce, S. W. Cowley, A. N. Fazakerley, K. K. Khurana, L. Lamy, J. S. Leisner, E. Roussos, C. T. Russell, P. Zarka, A. J. Coates, M. K. Dougherty, G. H. Jones, S. M. Krimigis, and N. Krupp (2016b), Cassini observations of Saturn's southern polar cusp, *Journal of Geophysical Research A: Space Physics*, *121*(4), 3006–3030, doi:10.1002/2015JA021957.

Aschwanden, M. J., N. B. Crosby, M. Dimitropoulou, M. K. Georgoulis, S. Hergarten, J. McAteer, A. V. Milovanov, S. Mineshige, L. Morales, N. Nishizuka, G. Pruessner, R. Sanchez, A. S. Sharma, A. Strugarek, and V. Uritsky (2016), 25 Years of Self-Organized Criticality: Solar and Astrophysics, *Space Science Reviews*, *198*(1-4), 47–166, doi:10.1007/s11214-014-0054-6.

Badman, S. V., and S. W. Cowley (2007), Significance of Dungey-cycle flows in Jupiter's and Saturn's magnetospheres, and their identification on closed equatorial field lines, *Annales Geophysicae*, *25*(4), 941–951, doi:10.5194/angeo-25-941-2007.

Badman, S. V., E. J. Bunce, J. T. Clarke, S. W. Cowley, J. C. Gérard, D. Grodent, and S. E. Milan (2005), Open flux estimates in Saturn's magnetosphere during the January 2004 Cassini-HST campaign, and implications for reconnection rates, *Journal of Geophysical Research: Space Physics*, *110*(A11), doi:10.1029/2005JA011240.

Badman, S. V., C. M. Jackman, J. D. Nichols, J. T. Clarke, and J. C. Gérard (2014), Open flux in Saturn's magnetosphere, *Icarus*, *231*, 137–145, doi:10.1016/j.icarus.2013.12.004.

Badman, S. V., B. Bonfond, M. Fujimoto, R. L. Gray, Y. Kasaba, S. Kasahara, T. Kimura, H. Melin, J. D. Nichols, A. J. Steffl, C. Tao, F. Tsuchiya, A. Yamazaki,

M. Yoneda, I. Yoshikawa, and K. Yoshioka (2016), Weakening of Jupiter's main auroral emission during January 2014, *Geophysical Research Letters*, *43*(3), 988–997, doi:10.1002/2015GL067366.

Bagenal, F. (1994), Empirical model of the Io plasma torus: Voyager measurements, *Journal of Geophysical Research*, *99*(A6), 11,043, doi:10.1029/93JA02908.

Bagenal, F. (1997), The ionization source near Io from Galileo wake data, *Geophysical Research Letters*, *24*(17), 2111–2114, doi:10.1029/97GL02052.

Bagenal, F. (2007), The magnetosphere of Jupiter: Coupling the equator to the poles, *Journal of Atmospheric and Solar-Terrestrial Physics*, *69*(3), 387–402, doi:10.1016/j.jastp.2006.08.012.

Bagenal, F., and P. A. Delamere (2011), Flow of mass and energy in the magnetospheres of Jupiter and Saturn, *Journal of Geophysical Research: Space Physics*, *116*(5), doi:10.1029/2010JA016294.

Bagenal, F., and J. D. Sullivan (1981), Direct plasma measurements in the Io torus and inner magnetosphere of Jupiter, *Journal of Geophysical Research: Space Physics*, *86*(A10), 8447–8466, doi:10.1029/JA086iA10p08447.

Bagenal, F., R. J. Wilson, S. Siler, W. R. Paterson, and W. S. Kurth (2016), Survey of Galileo plasma observations in Jupiter's plasma sheet, *Journal of Geophysical Research: Planets*, *121*(5), 871–894, doi:10.1002/2016JE005009.

Barbosa, D. D., F. V. Coroniti, and A. Eviatar (1983), Coulomb thermal properties and stability of the Io plasma torus, *The Astrophysical Journal*, *274*, 429, doi:10.1086/161459.

Baron, R. L., T. Owen, J. E. Connerney, T. Satoh, and J. Harrington (1996), Solar wind control of Jupiter's H+3 Auroras, *Icarus*, *120*(2), 437–442, doi:10.1006/icar.1996.0063.

Barrow, C. H. (1978), Jupiter's decametric radio emission and solar activity, *Planetary and Space Science*, *26*(12), 1193–1199, doi:10.1016/0032-0633(78)90059-4.

Behannon, K. W., M. H. Acuna, L. F. Burlaga, R. P. Lepping, N. F. Ness, and F. M. Neubauer (1977), Magnetic field experiment for Voyagers 1 and 2, *Space Science Reviews*, *21*(3), 235–257, doi:10.1007/BF00211541.

Belcher, J. W., C. K. Goertz, and H. S. Bridge (1980), The low energy plasma in the Jovian magnetosphere, *Geophysical Research Letters*, *7*(1), 17–20, doi:10.1029/GL007i001p00017.

Biermann, L., and A. Schlüter (1951), Cosmic radiation and cosmic magnetic fields. II. Origin of cosmic magnetic fields, *Physical Review*, *82*(6), 863–868, doi:10.1103/PhysRev.82.863.

Bonfond, B., D. Grodent, J. C. Gérard, T. Stallard, J. T. Clarke, M. Yoneda, A. Radioti, and J. Gustin (2012), Auroral evidence of Io's control over the magnetosphere of Jupiter, *Geophysical Research Letters*, *39*(1), doi:10.1029/2011GL050253.

Borovsky, J. E., R. J. Nemzek, and R. D. Belian (1993), The occurrence rate of magnetospheric-substorm onsets: Random and periodic substorms, *Journal of Geophysical Research: Space Physics*, *98*(A3), 3807–3813, doi:10.1029/92JA02556.

Brandt, P. C., K. K. Khurana, D. G. Mitchell, N. Sergis, K. Dialynas, J. F. Carbary, E. C. Roelof, C. P. Paranicas, S. M. Krimigis, and B. H. Mauk (2010), Saturn's periodic magnetic field perturbations caused by a rotating partial ring current, *Geophysical Research Letters*, *37*(22), doi:10.1029/2010GL045285.

Bridge, H. S., J. W. Belcher, B. Coppi, A. J. Lazarus, R. L. McNutt, S. Olbert, J. D. Richardson, M. R. Sands, R. S. Selesnick, J. D. Sullivan, R. E. Hartle, K. W. Ogilvie, E. C. Sittler, F. Bagenal, R. S. Wolff, V. M. Vasyliunas, G. L. Siscoe, C. K. Goertz, and A. Eviatar (1981), Plasma Observations near Saturn: Initial Results from Voyager 1, *Science*, *212*(4491), 217–224, doi:10.1126/science.212.4491.217.

Bristow, W. (2008), Statistics of velocity fluctuations observed by SuperDARN under steady interplanetary magnetic field conditions, *Journal of Geophysical Research: Space Physics*, *113*(11), doi:10.1029/2008JA013203.

Broadfoot, A. L., B. R. Sandel, D. E. Shemansky, J. C. McConnell, G. R. Smith, J. B. Holberg, S. K. Atreya, T. M. Donahue, D. F. Strobel, and J. L. Bertaux (1981), Overview of the Voyager ultraviolet spectrometry results through Jupiter encounter, *Journal of Geophysical Research: Space Physics*, *86*(A10), 8259–8284, doi:10.1029/JA086iA10p08259.

Brown, L. W. (1973), The Galactic Radio Spectrum between 130 and 2600 kHz, *The Astrophysical Journal*, *180*, 359–370.

Bunce, E. J., S. W. Cowley, D. M. Wright, A. J. Coates, M. K. Dougherty, N. Krupp, W. S. Kurth, and A. M. Rymer (2005), In situ observations of a solar wind compression-induced hot plasma injection in Saturn's tail, *Geophysical Research Letters*, *32*(20), 1–4, doi:10.1029/2005GL022888.

Bunce, E. J., S. W. Cowley, I. I. Alexeev, C. S. Arridge, M. K. Dougherty, J. D. Nichols, and C. T. Russell (2007), Cassini observations of the variation of Saturn's ring current parameters with system size, *Journal of Geophysical Research: Space Physics*, *112*(10), doi:10.1029/2007JA012275.

Bunce, E. J., C. S. Arridge, J. T. Clarke, A. J. Coates, S. W. Cowley, M. K. Dougherty, J. C. Gérard, D. Grodent, K. C. Hansen, J. D. Nichols, D. J. Southwood, and D. L. Talboys (2008a), Origin of Saturn's aurora: Simultaneous observations by Cassini and the Hubble Space Telescope, *Journal of Geophysical Research: Space Physics*, *113*(9), doi:10.1029/2008JA013257.

Bunce, E. J., C. S. Arridge, S. W. Cowley, and M. K. Dougherty (2008b), Magnetic field structure of Saturn's dayside magnetosphere and its mapping to the ionosphere: Results from ring current modeling, *Journal of Geophysical Research: Space Physics*, *113*(2), doi:10.1029/2007JA012538.

Bunce, E. J., S. W. Cowley, D. L. Talboys, M. K. Dougherty, L. Lamy, W. S. Kurth, P. Schippers, B. Cecconi, P. Zarka, C. S. Arridge, and A. J. Coates (2010), Extraordinary field-aligned current signatures in Saturn's high-latitude magnetosphere: Analysis of Cassini data during Revolution 89, *Journal of Geophysical Research: Space Physics*, *115*(10), doi:10.1029/2010JA015612.

Burch, J. L., and T. D. Phan (2016), Magnetic reconnection at the dayside magnetopause: Advances with MMS, *Geophysical Research Letters*, *43*(16), 8327–8338, doi: 10.1002/2016GL069787.

Burch, J. L., J. Goldstein, T. W. Hill, D. T. Young, F. J. Crary, A. J. Coates, N. André, W. S. Kurth, and E. C. Sittler (2005), Properties of local plasma injections in Saturn's magnetosphere, *Geophysical Research Letters*, *32*(14), 1–4, doi: 10.1029/2005GL022611.

Burch, J. L., J. Goldstein, P. Mokashi, W. S. Lewis, C. Paty, D. T. Young, A. J. Coates, M. K. Dougherty, and N. André (2008), On the cause of Saturn's plasma periodicity, *Geophysical Research Letters*, *35*(14), L14,105, doi:10.1029/2008GL034951.

Burch, J. L., A. D. DeJong, J. Goldstein, and D. T. Young (2009), Periodicity in Saturn's magnetosphere: Plasma cam, *Geophysical Research Letters*, *36*(14), L14,203, doi: 10.1029/2009GL039043.

Burch, J. L., R. B. Torbert, T. D. Phan, L. J. Chen, T. E. Moore, R. E. Ergun, J. P. Eastwood, D. J. Gershman, P. A. Cassak, M. R. Argall, S. Wang, M. Hesse, C. J. Pollock, B. L. Giles, R. Nakamura, B. H. Mauk, S. A. Fuselier, C. T. Russell, R. J.

Strangeway, J. F. Drake, M. A. Shay, Y. V. Khotyaintsev, P. A. Lindqvist, G. Marklund, F. D. Wilder, D. T. Young, K. Torkar, J. Goldstein, J. C. Dorelli, L. A. Avanov, M. Oka, D. N. Baker, A. N. Jaynes, K. A. Goodrich, I. J. Cohen, D. L. Turner, J. F. Fennell, J. B. Blake, J. Clemmons, M. Goldman, D. Newman, S. M. Petrinec, K. J. Trattner, B. Lavraud, P. H. Reiff, W. Baumjohann, W. Magnes, M. Steller, W. Lewis, Y. Saito, V. Coffey, and M. Chandler (2016), Electron-scale measurements of magnetic reconnection in space, *Science*, *352*(6290), aaf2939, doi:10.1126/science.aaf2939.

Carbary, J. F., D. G. Mitchell, P. Brandt, C. Paranicas, and S. M. Krimigis (2008), ENA periodicities at Saturn, *Geophysical Research Letters*, *35*(7), doi:10.1029/2008GL033230.

Carbary, J. F., D. G. Mitchell, S. M. Krimigis, and N. Krupp (2009), Dual periodicities in energetic electrons at Saturn, *Geophysical Research Letters*, *36*(20), L20,103, doi:10.1029/2009GL040517.

Cecconi, B., and P. Zarka (2005a), Direction finding and antenna calibration through analytical inversion of radio measurements performed using a system of two or three electric dipole antennas on a three-axis stabilized spacecraft, *Radio Science*, *40*(3), doi:10.1029/2004RS003070.

Cecconi, B., and P. Zarka (2005b), Model of a variable radio period for Saturn, *Journal of Geophysical Research: Space Physics*, *110*(A12), doi:10.1029/2005JA011085.

Cecconi, B., L. Lamy, P. Zarka, R. Prangé, W. S. Kurth, and P. Louarn (2009), Goniopolarimetric study of the revolution 29 perikrone using the Cassini Radio and Plasma Wave Science instrument high-frequency radio receiver, *Journal of Geophysical Research: Space Physics*, *114*(3), doi:10.1029/2008JA013830.

Chang, T. (1992), Low-Dimensional Behavior and Symmetry Breaking of Stochastic Systems near CriticalityCan These Effects be Observed in Space and in the Laboratory?, *IEEE Transactions on Plasma Science*, *20*(6), 691–694, doi:10.1109/27.199515.

Chapman, S., and N. Watkins (2001), Avalanching and self-organised criticality, a paradigm for geomagnetic activity?, *Space Science Reviews*, *95*(1-2), 293–307, doi:10.1023/A:1005236717469.

Chapman, S. C., and V. C. Ferraro (1930), A New Theory of Magnetic Storms., *Nature*, *126*(3169), 129–130, doi:10.1038/126129a0.

Chapman, S. C., N. W. Watkins, R. O. Dendy, P. Heiander, and G. Rowlands (1998), A simple avalanche model as an analogue for magnetospheric activity, *Geophysical Research Letters*, *25*(13), 2397–2400, doi:10.1029/98GL51700.

Clarke, J. T., J. Nichols, J. C. Gérard, D. Grodent, K. C. Hansen, W. Kurth, G. R. Gladstone, J. Duval, S. Wannawichian, E. Bunce, S. W. Cowley, F. Crary, M. Dougherty, L. Lamy, D. Mitchell, W. Pryor, K. Retherford, T. Stallard, B. Zieger, P. Zarka, and B. Cecconi (2009), Response of Jupiter's and Saturn's auroral activity to the solar wind, *Journal of Geophysical Research: Space Physics*, *114*(5), doi: 10.1029/2008JA013694.

Clarke, K. E., N. André, D. J. Andrews, A. J. Coates, S. W. Cowley, M. K. Dougherty, G. R. Lewis, H. J. McAndrews, J. D. Nichols, T. R. Robinson, and D. M. Wright (2006), Cassini observations of planetary-period oscillations of Saturn's magnetopause, *Geophysical Research Letters*, *33*(23), L23,104, doi:10.1029/2006GL027821.

Clarke, K. E., D. J. Andrews, C. S. Arridge, A. J. Coates, and S. W. H. Cowley (2010a), Magnetopause oscillations near the planetary period at Saturn: Occurrence, phase, and amplitude, *Journal of Geophysical Research: Space Physics*, *115*(8), doi:10.1029/ 2009JA014745.

Clarke, K. E., D. J. Andrews, A. J. Coates, S. W. Cowley, and A. Masters (2010b), Magnetospheric period oscillations of Saturns bow shock, *Journal of Geophysical Research: Space Physics*, *115*(5), doi:10.1029/2009JA015164.

Connerney, J. E. P., M. H. Acuña, and N. F. Ness (1981), Modeling the Jovian current sheet and inner magnetosphere, *Journal of Geophysical Research: Space Physics*, *86*(A10), 8370–8384, doi:10.1029/JA086iA10p08370.

Connerney, J. E. P., M. H. Acuña, and N. F. Ness (1983), Currents in Saturn's magnetosphere, *Journal of Geophysical Research: Space Physics*, *88*(A11), 8779–8789, doi:10.1029/JA088iA11p08779.

Cowley, S., and M. Lockwood (1992), Excitation and decay of solar wind-driven flows in the magnetosphere-ionosphere system, *Annales Geophysicae*, *10*, 103–115.

Cowley, S. W., and G. Provan (2016), Planetary period oscillations in Saturn's magnetosphere: Further comments on the relationship between post-equinox properties deduced from magnetic field and Saturn kilometric radiation measurements, *Icarus*, *272*, 258–276, doi:10.1016/j.icarus.2016.02.051.

Cowley, S. W., and G. Provan (2017), Planetary period modulations of Saturn's magnetotail current sheet during northern spring: Observations and modeling, *Journal of Geophysical Research: Space Physics*, *122*(6), 6049–6077, doi:10.1002/2017JA023993.

Cowley, S. W., E. J. Bunce, and J. M. O'Rourke (2004), A simple quantitative model of plasma flows and currents in Saturn's polar ionosphere, *Journal of Geophysical Research: Space Physics*, *109*(A5), A05,212, doi:10.1029/2003JA010375.

Cowley, S. W., S. V. Badman, S. M. Imber, and S. E. Milan (2008), Comment on "Jupiter: A fundamentally different magnetospheric interaction with the solar wind" by D. J. McComas and F. Bagenal, *Geophysical Research Letters*, *35*(10), doi:10.1029/2007GL032645.

Cowley, S. W., J. D. Nichols, and C. M. Jackman (2015), Down-tail mass loss by plasmoids in Jupiter's and Saturn's magnetospheres, *Journal of Geophysical Research A: Space Physics*, *120*(8), 6347–6356, doi:10.1002/2015JA021500.

Cowley, S. W. H. (1991), The structure and length of tail-associated phenomena in the solar wind downstream from the Earth, *Planetary and Space Science*, *39*(7), 1039–1043, doi:10.1016/0032-0633(91)90110-V.

Cowley, S. W. H., and E. J. Bunce (2001), Origin of the main auroral oval in Jupiter's coupled magnetosphere-ionosphere system, *Planetary and Space Science*, *49*(10-11), 1067–1088, doi:10.1016/S0032-0633(00)00167-7.

Cowley, S. W. H., E. J. Bunce, T. S. Stallard, and S. Miller (2003), Jupiter's polar ionospheric flows: Theoretical interpretation, *Geophysical Research Letters*, *30*(5), doi:10.1029/2002GL016030.

Cowley, S. W. H., G. Provan, G. J. Hunt, and C. M. Jackman (2016), Planetary period modulations of Saturn's magnetotail current sheet: A simple illustrative mathematical model, *Journal of Geophysical Research: Space Physics*, *122*(October), 258–279, doi:10.1002/2016JA023367.

Cox, D. R., and D. Oakes (1984), *Analysis of survival data*, 212 pp., Chapman and Hall, New York.

Coxon, J. C., S. E. Milan, L. B. Clausen, B. J. Anderson, and H. Korth (2014), The magnitudes of the regions 1 and 2 Birkeland currents observed by AMPERE and their role in solar wind-magnetosphere-ionosphere coupling, *Journal of Geophysical Research: Space Physics*, *119*(12), 9804–9815, doi:10.1002/2014JA020138.

Crockett, C., and E. Otwell (2016), The 43-year history of journeys to Jupiter, in one graph, *Science News*, p. 32.

Crooker, N. U. (1999), Heliospheric current sheet structure, *AIP Conference Proceedings*, *93*(1), 93–98, doi:10.1063/1.58738.

Daigne, G., and Y. Leblanc (1986), Narrow-band Jovian kilometric radiation: Occurrence, polarization, and rotation period, *Journal of Geophysical Research*, *91*(A7), 7961, doi:10.1029/JA091iA07p07961.

Davis, L., and E. J. Smith (1990), A model of Saturn's magnetic field based on all available data, *Journal of Geophysical Research*, *95*(A9), 15,257, doi:10.1029/JA095iA09p15257.

Dejong, A. D., J. L. Burch, J. Goldstein, A. J. Coates, and D. T. Young (2010), Low-energy electrons in Saturn's inner magnetosphere and their role in interchange injections, *Journal of Geophysical Research: Space Physics*, *115*(10), doi:10.1029/2010JA015510.

Delamere, P. A., and F. Bagenal (2010), Solar wind interaction with Jupiter's magnetosphere, *Journal of Geophysical Research: Space Physics*, *115*(10), doi:10.1029/2010JA015347.

Delamere, P. A., and F. Bagenal (2013), Magnetotail structure of the giant magnetospheres: Implications of the viscous interaction with the solar wind, *Journal of Geophysical Research: Space Physics*, *118*(11), 7045–7053, doi:10.1002/2013JA019179.

Delamere, P. A., A. Steffl, and F. Bagenal (2004a), Modeling temporal variability of plasma conditions in the Io torus during the Cassini era, *Journal of Geophysical Research: Space Physics*, *109*(A10), doi:10.1029/2003JA010354.

Delamere, P. A., A. Steffl, and F. Bagenal (2004b), Modeling temporal variability of plasma conditions in the Io torus during the Cassini era, *Journal of Geophysical Research: Space Physics*, *109*(A10), 1276, doi:10.1029/2003JA010354.

Delamere, P. A., R. J. Wilson, and A. Masters (2011), Kelvin-Helmholtz instability at Saturn's magnetopause: Hybrid simulations, *Journal of Geophysical Research: Space Physics*, *116*(10), doi:10.1029/2011JA016724.

Delamere, P. A., R. J. Wilson, S. Eriksson, and F. Bagenal (2013), Magnetic signatures of Kelvin-Helmholtz vortices on Saturn's magnetopause: Global survey, *Journal of Geophysical Research: Space Physics*, *118*(1), 393–404, doi:10.1029/2012JA018197.

Delory, G. T., R. E. Ergun, C. W. Carlson, L. Muschietti, C. C. Chaston, W. Peria, J. P. McFadden, and R. Strangeway (1998), FAST observations of electron distributions within AKR source regions, *Geophysical Research Letters*, *25*(12), 2069–2072, doi:10.1029/98GL00705.

Dendy, R. O., S. C. Chapman, and M. Paczuski (2007), Fusion, space and solar plasmas as complex systems, *Plasma Physics and Controlled Fusion*, *49*(5 A), A95–A108, doi:10.1088/0741-3335/49/5A/S08.

Desch, M. D. (1982), Evidence for solar wind control of saturn radio emission, *Journal of Geophysical Research*, *87*(A6), 4549, doi:10.1029/JA087iA06p04549.

Desch, M. D. (1983), Radio emission signature of Saturn immersions in Jupiter's magnetic tail, *Journal of Geophysical Research*, *88*(A9), 6904, doi:10.1029/JA088iA09p06904.

Desch, M. D., and M. L. Kaiser (1981), Voyager measurement of the rotation period of Saturn's magnetic field, *Geophysical Research Letters*, *8*(3), 253–256, doi:10.1029/GL008i003p00253.

Desch, M. D., and H. O. Rucker (1983), The relationship between Saturn kilometric radiation and the solar wind, *Journal of Geophysical Research: Space Physics*, *88*(A11), 8999–9006, doi:10.1029/JA088iA11p08999.

Desch, M. D., and H. O. Rucker (1985), Saturn radio emission and the solar wind: Voyager-2 studies, *Advances in Space Research*, *5*(4), 333–336, doi:10.1016/0273-1177(85)90159-0.

Desroche, M., F. Bagenal, P. A. Delamere, and N. Erkaev (2013), Conditions at the magnetopause of Saturn and implications for the solar wind interaction, *Journal of Geophysical Research: Space Physics*, *118*(6), 3087–3095, doi:10.1002/jgra.50294.

Dougherty, M. K., S. Kellock, D. J. Southwood, A. Balogh, E. J. Smith, B. T. Tsurutani, B. Gerlach, K. H. Glassmeier, F. Gleim, C. T. Russell, G. Erdos, F. M. Neubauer, and S. W. Cowley (2004), The Cassini magnetic field investigation, *Space Science Reviews*, *114*(1-4), 331–383, doi:10.1007/s11214-004-1432-2.

Dougherty, M. K., N. Achilleos, N. Andre, C. S. Arridge, A. Balogh, C. Bertucci, M. E. Burton, S. W. Cowley, G. Erdos, G. Giampieri, K. H. Glassmeier, K. K. Khurana, J. Leisner, F. M. Neubauer, C. T. Russell, E. J. Smith, D. J. Southwood, and B. T. Tsurutani (2005), Cassini magnetometer observations during Saturn orbit insertion, *Science*, *307*(5713), 1266–1270, doi:10.1126/science.1106098.

Dungey, J. W. (1961), Interplanetary magnetic field and the auroral zones, *Physical Review Letters*, *6*(2), 47–48, doi:10.1103/PhysRevLett.6.47.

Dunn, W. R., G. Branduardi-Raymont, R. F. Elsner, M. F. Vogt, L. Lamy, P. G. Ford, A. J. Coates, G. R. Gladstone, C. M. Jackman, J. D. Nichols, I. J. Rae, A. Varsani, T. Kimura, K. C. Hansen, and J. M. Jasinski (2016), The impact of an ICME on the Jovian X-ray aurora, *Journal of Geophysical Research A: Space Physics*, *121*(3), 2274–2307, doi:10.1002/2015JA021888.

Eastwood, J. P., T. D. Phan, M. Øieroset, and M. A. Shay (2010), Average properties of the magnetic reconnection ion diffusion region in the Earth's magnetotail: The 2001-2005 Cluster observations and comparison with simulations, *Journal of Geophysical Research: Space Physics*, *115*(8), doi:10.1029/2009JA014962.

Ebert, R. W., F. Allegrini, F. Bagenal, S. J. Bolton, J. E. Connerney, G. Clark, G. A. DiBraccio, D. J. Gershman, W. S. Kurth, S. Levin, P. Louarn, B. H. Mauk, D. J. McComas, M. Reno, J. R. Szalay, M. F. Thomsen, P. Valek, S. Weidner, and R. J. Wilson (2017), Accelerated flows at Jupiter's magnetopause: Evidence for magnetic reconnection along the dawn flank, *Geophysical Research Letters*, *44*(10), 4401–4409, doi:10.1002/2016GL072187.

Farrell, W. M., W. S. Kurth, M. L. Kaiser, M. D. Desch, D. A. Gurnett, and P. Canu (2005), Narrowband Z-mode emissions interior to Saturn's plasma torus, *Journal of Geophysical Research: Space Physics*, *110*(A10), doi:10.1029/2005JA011102.

Fischer, G., D. A. Gurnett, W. S. Kurth, S. Y. Ye, and J. B. Groene (2015), Saturn kilometric radiation periodicity after equinox, *Icarus*, *254*, 72–91, doi:10.1016/j.icarus.2015.03.014.

Fleshman, B. L., P. A. Delamere, and F. Bagenal (2010), A sensitivity study of the Enceladus torus, *Journal of Geophysical Research*, *115*(E4), E04,007, doi:10.1029/2009JE003372.

Frank, L. A., and W. R. Paterson (2000), Observations of plasmas in the Io torus with the Galileo spacecraft, *Journal of Geophysical Research: Space Physics*, *105*(A7), 16,017–16,034, doi:10.1029/1999JA000250.

Freeman, M. P., and S. K. Morley (2004), A minimal substorm model that explains the observed statistical distribution of times between substorms, *Geophysical Research Letters*, *31*(12), doi:10.1029/2004GL019989.

Fukazawa, K., T. Ogino, and R. J. Walker (2005), Dynamics of the Jovian magnetosphere for northward interplanetary magnetic field (IMF), *Geophysical Research Letters*, *32*(3), 1–5, doi:10.1029/2004GL021392.

Fukazawa, K., T. Ogino, and R. J. Walker (2010), A simulation study of dynamics in the distant Jovian magnetotail, *Journal of Geophysical Research: Space Physics*, *115*(9), 9219, doi:10.1029/2009JA015228.

Fuselier, S. A., R. Frahm, W. S. Lewis, A. Masters, J. Mukherjee, S. M. Petrinec, and I. J. Sillanpaa (2014), The location of magnetic reconnection at Saturn's magnetopause: A comparison with Earth, *Journal of Geophysical Research: Space Physics*, *119*(4), 2563–2578, doi:10.1002/2013JA019684.

Gaidos, E. J., and F. Nimmo (2000), Tectonics and water on Europa, *Nature*, *405*(6787), 637, doi:10.1038/35015170.

Galopeau, P. H. M., and A. Lecacheux (2000), Variations of Saturn's radio rotation period measured at kilometer wavelengths, *Journal of Geophysical Research: Space Physics*, *105*(A6), 13,089–13,101, doi:10.1029/1999JA005089.

Gledhill, J. A. (1967), Magnetosphere of Jupiter [2], *Nature*, *214*(5084), 155–156, doi:10.1038/214155a0.

Goldstein, M. L., R. P. Lepping, and E. C. Sittler (1985), Magnetic field properties of Jupiter's tail at distances from 80 to 7500 Jovian radii, *Journal of Geophysical Research*, *90*(A9), 8223, doi:10.1029/JA090iA09p08223.

Gosling, J. T. (1996), Corotating and Transient Solar Wind Flows in Three Dimensions, *Annual Review of Astronomy and Astrophysics*, *34*(1), 35–73, doi:10.1146/annurev.astro.34.1.35.

Gosling, J. T., and V. J. Pizzo (1999), Formation and Evolution of Corotating Interaction Regions and Their Three Dimensional Structure, *Space Science Reviews*, *7*(89), 21–52, doi:10.1007/978-94-017-1179-1_3.

Grocott, A., S. V. Badman, S. W. Cowley, S. E. Milan, J. D. Nichols, and T. K. Yeoman (2009), Magnetosonic Mach number dependence of the efficiency of reconnection between planetary and interplanetary magnetic fields, *Journal of Geophysical Research: Space Physics*, *114*(7), doi:10.1029/2009JA014330.

Gumett, D. A., A. Lecacheux, W. S. Kurth, A. M. Persoon, J. B. Groene, L. Lamy, P. Zarka, and J. F. Carbary (2009), Discovery of a north-south asymmetry in Saturn's radio rotation period, *Geophysical Research Letters*, *36*(16), L16,102, doi:10.1029/2009GL039621.

Gurnett, D. A. (1975), The Earth as a radio source: The nonthermal continuum, *Journal of Geophysical Research*, *80*(19), 2751–2763, doi:10.1029/JA080i019p02751.

Gurnett, D. A. (2011), An SLS4 Longitude System Based on a Tracking Filter Analysis of the Rotational Modulation of Saturn Kilometric Radiation, in *Planetary Radio Emissions Vii*, pp. 51–64, Austrian Academy of Sciences Press, Vienna, doi:10.1553/PRE7s51.

Gurnett, D. A., W. S. Kurth, and F. L. Scarf (1983), Narrowband electromagnetic emissions from Jupiter's magnetosphere, *Nature*, *302*(5907), 385–388, doi:10.1038/302385a0.

Gurnett, D. A., W. S. Kurth, S. C. Allendorf, and R. L. Poynter (1993), Radio Emission from the Heliopause Triggered by an Interplanetary Shock, *Science*, *262*(5131), 199–203, doi:10.1126/science.262.5131.199.

Gurnett, D. A., W. S. Kurth, D. L. Kirchner, G. B. Hospodarsky, T. F. Averkamp, P. Zarka, A. Lecacheux, R. Manning, A. Roux, P. Canu, N. Cornilleau-Wehrlin, P. Galopeau, A. Meyer, R. Boström, G. Gustafsson, J. E. Wahlund, L. Åhlen, H. O. Rucker, H. P. Ladreiter, W. Macher, L. J. Woolliscroft, H. Alleyne, M. L. Kaiser, M. D. Desch, W. M. Farrell, C. C. Harvey, P. Louarn, P. J. Kellogg, K. Goetz, and A. Pedersen (2004), The Cassini radio and plasma wave investigation, *Space Science Reviews*, *114*(1-4), 395–463, doi:10.1007/s11214-004-1434-0.

Gurnett, D. A., W. S. Kurth, C. B. Hospodarsky, A. M. Persoon, T. F. Averkamp, B. Cecconi, A. Lecacheux, P. Zarka, P. Canu, N. Cornilleau-Wehrlin, P. Galopeau, A. Roux, C. Harvey, P. Louarn, U. Bostrom, G. Gustafsson, J. E. Wahlund, M. D. Desch, W. M. Farrell, M. L. Kaiser, K. Goetz, P. J. Kellogg, G. Fischer, H. P. Ladreiter, H. Rucker, H. Alleyne, and A. Pedersen (2005), Radio and plasma wave obervations at Saturn from Cassini's approach and first orbit, *Science*, *307*(5713), 1255–1259, doi:10.1126/science.1105356.

Gurnett, D. A., A. M. Persoon, W. S. Kurth, J. B. Groene, T. F. Averkamp, M. K. Dougherty, and D. J. Southwood (2007), The variable rotation period of the inner region of Saturn's plasma disk, *Science*, *316*(5823), 442–445, doi:10.1126/science.1138562.

Gurnett, D. A., A. M. Persoon, J. B. Groene, A. J. Kopf, G. B. Hospodarsky, and W. S. Kurth (2009), A north-south difference in the rotation rate of auroral hiss at Saturn: Comparison to Saturn's kilometric radio emission, *Geophysical Research Letters*, *36*(21), L21,108, doi:10.1029/2009GL040774.

Gurnett, D. A., J. B. Groene, A. M. Persoon, J. D. Menietti, S. Y. Ye, W. S. Kurth, R. J. MacDowall, and A. Lecacheux (2010), The reversal of the rotational modulation rates of the north and south components of Saturn kilometric radiation near equinox, *Geophysical Research Letters*, *37*(24), doi:10.1029/2010GL045796.

Hall, C. F. (1975), Pioneer 10 and Pioneer 11, *Science*, *188*(4187), 445–446, doi:10.1126/science.188.4187.445.

Hamilton, D. C., G. Gloeckler, S. M. Krimigis, and L. J. Lanzerotti (1981), Composition of nonthermal ions in the Jovian magnetosphere, *Journal of Geophysical Research: Space Physics*, *86*(A10), 8301–8318, doi:10.1029/JA086iA10p08301.

Hanlon, P. G., M. K. Dougherty, R. J. Forsyth, M. J. Owens, K. C. Hansen, G. Tóth, F. J. Crary, and D. T. Young (2004), On the evolution of the solar wind between 1 and 5 AU at the time of the Cassini Jupiter flyby: Multispacecraft observations of interplanetary coronal mass ejections including the formation of a merged interaction

region, *Journal of Geophysical Research: Space Physics*, *109*(A9), A09S03, doi:10.1029/2003JA010112.

Hansen, C. J., L. Esposito, A. I. Stewart, J. Colwell, A. Hendrix, W. Pryor, D. Shemansky, and R. Wast (2006), Enceladus' water vapor plume, *Science*, *311*(5766), 1422–1425, doi:10.1126/science.1121254.

Hess, S. L., P. A. Delamere, F. Bagenal, N. Schneider, and A. J. Steffl (2011), Longitudinal modulation of hot electrons in the Io plasma torus, *Journal of Geophysical Research: Space Physics*, *116*(11), doi:10.1029/2011JA016918.

Hess, S. L., E. Echer, and P. Zarka (2012), Solar wind pressure effects on Jupiter decametric radio emissions independent of Io, *Planetary and Space Science*, *70*(1), 114–125, doi:10.1016/j.pss.2012.05.011.

Hess, S. L., E. Echer, P. Zarka, L. Lamy, and P. A. Delamere (2014), Multi-instrument study of the Jovian radio emissions triggered by solar wind shocks and inferred magnetospheric subcorotation rates, *Planetary and Space Science*, *99*, 136–148, doi:10.1016/j.pss.2014.05.015.

Hilbe, J. M. (1983), Physics of the Jovian Magnetosphere, in *Physics of the Jovian Magnetosphere*, edited by A. J. Dessler, chap. Magnetosph, pp. 530–531, Cambridge University Press, New York, doi:10.1017/CBO9780511564574.

Hill, T. (1979), Inertial limit on corotation, *Journal of Geophysical Research*, *84*(A11), 6554, doi:10.1029/JA084iA11p06554.

Hill, T. W., A. J. Dessler, and C. K. Goertz (1983), *Magnetospheric models*, 353–394 pp., Cambridge University Press, doi:1983phjm.book..353H.

Hill, T. W., A. M. Rymer, J. L. Burch, F. J. Crary, D. T. Young, M. F. Thomsen, D. Delapp, N. André, A. J. Coates, and G. R. Lewis (2005), Evidence for rotationally driven plasma transport in Saturn's magnetosphere, *Geophysical Research Letters*, *32*(14), 1–4, doi:10.1029/2005GL022620.

Hill, T. W., M. F. Thomsen, M. G. Henderson, R. L. Tokar, A. J. Coates, H. J. McAndrews, G. R. Lewis, D. G. Mitchell, C. M. Jackman, C. T. Russell, M. K. Dougherty, F. J. Crary, and D. T. Young (2008), Plasmoids in Saturn's magnetotail, *Journal of Geophysical Research: Space Physics*, *113*(1), doi:10.1029/2007JA012626.

Hoshino, M., A. Nishida, T. Yamamoto, and S. Kokubun (1994), Turbulent magnetic field in the distant magnetotail: Bottomup process of plasmoid formation?, *Geophysical Research Letters*, *21*(25), 2935–2938, doi:10.1029/94GL02094.

Hunt, G. (2016), Analyses of field-aligned currents in Saturn's nightside magnetosphere, Ph.D. thesis, University of Leicester.

Hunt, G. J., S. W. Cowley, G. Provan, E. J. Bunce, I. I. Alexeev, E. S. Belenkaya, V. V. Kalegaev, M. K. Dougherty, and A. J. Coates (2014), Field-aligned currents in Saturn's southern nightside magnetosphere: Subcorotation and planetary period oscillation components, *Journal of Geophysical Research: Space Physics*, *119*(12), 9847–9899, doi:10.1002/2014JA020506.

Hunt, G. J., S. W. H. Cowley, G. Provan, E. J. Bunce, I. I. Alexeev, E. S. Belenkaya, V. V. Kalegaev, M. K. Dougherty, and A. J. Coates (2015), Field-aligned currents in Saturn's northern nightside magnetosphere: Evidence for interhemispheric current flow associated with planetary period oscillations, *Journal of Geophysical Research A: Space Physics*, *120*(9), 7552–7584, doi:10.1002/2015JA021454.

Iess, L., D. J. Stevenson, M. Parisi, D. Hemingway, R. A. Jacobson, J. I. Lunine, F. Nimmo, J. W. Armstrong, S. W. Asmar, M. Ducci, and P. Tortora (2014), The gravity field and interior structure of Enceladus, *Science*, *344*(6179), 78–80, doi: 10.1126/science.1250551.

Imber, S. M., J. A. Slavin, H. U. Auster, and V. Angelopoulos (2011), A THEMIS survey of flux ropes and traveling compression regions: Location of the near-Earth reconnection site during solar minimum, *Journal of Geophysical Research: Space Physics*, *116*(A2), doi:10.1029/2010JA016026.

Jackman, C. M. (2006), Solar wind-magnetosphere coupling at Saturn, Ph.D. thesis, University of Leicester.

Jackman, C. M., and C. S. Arridge (2011), Solar Cycle Effects on the Dynamics of Jupiter's and Saturn's Magnetospheres, *Solar Physics*, *274*(1-2), 481–502, doi: 10.1007/s11207-011-9748-z.

Jackman, C. M., N. Achilleos, E. J. Bunce, S. W. Cowley, M. K. Dougherty, G. H. Jones, S. E. Milan, and E. J. Smith (2004), Interplanetary magnetic field at 9 AU during the declining phase of the solar cycle and its implications for Saturn's magnetospheric dynamics, *Journal of Geophysical Research: Space Physics*, *109*(A11), doi:10.1029/2004JA010614.

Jackman, C. M., R. J. Forsyth, and M. K. Dougherty (2008), The overall configuration of the interplanetary magnetic field upstream of Saturn as revealed by Cassini observations, *Journal of Geophysical Research: Space Physics*, *113*(8), doi: 10.1029/2008JA013083.

Jackman, C. M., L. Lamy, M. P. Freeman, P. Zarka, B. Cecconi, W. S. Kurth, S. W. H. Cowley, and M. K. Dougherty (2009a), On the character and distribution of lower-frequency radio emissions at Saturn and their relationship to substorm-like events, *Journal of Geophysical Research: Space Physics*, *114*(8), doi:10.1029/2008JA013997.

Jackman, C. M., C. S. Arridge, H. J. McAndrews, M. G. Henderson, and R. J. Wilson (2009b), Northward field excursions in Saturn's magnetotail and their relationship to magnetospheric periodicities, *Geophysical Research Letters*, *36*(16), L16,101, doi:10.1029/2009GL039149.

Jackman, C. M., J. A. Slavin, and S. W. Cowley (2011), Cassini observations of plasmoid structure and dynamics: Implications for the role of magnetic reconnection in magnetospheric circulation at Saturn, doi:10.1029/2011JA016682.

Jackman, C. M., C. S. Arridge, N. André, F. Bagenal, J. Birn, M. P. Freeman, X. Jia, A. Kidder, S. E. Milan, A. Radioti, J. A. Slavin, M. F. Vogt, M. Volwerk, and A. P. Walsh (2014a), Large-scale structure and dynamics of the magnetotails of Mercury, Earth, Jupiter and Saturn, *Space Science Reviews*, *182*(1-4), 85–154, doi:10.1007/s11214-014-0060-8.

Jackman, C. M., J. A. Slavin, M. G. Kivelson, D. J. Southwood, N. Achilleos, M. F. Thomsen, G. A. Dibraccio, J. P. Eastwood, M. P. Freeman, M. K. Dougherty, and M. F. Vogt (2014b), Saturn's dynamic magnetotail: A comprehensive magnetic field and plasma survey of plasmoids and traveling compression regions and their role in global magnetospheric dynamics, *Journal of Geophysical Research: Space Physics*, *119*(7), 5465–5494, doi:10.1002/2013JA019388.

Jackman, C. M., G. Provan, and S. W. Cowley (2016), Reconnection events in Saturn's magnetotail: Dependence of plasmoid occurrence on planetary period oscillation phase, *Journal of Geophysical Research A: Space Physics*, *121*(4), 2922–2934, doi:10.1002/2015JA021985.

Jasinski, J. M., J. A. Slavin, C. S. Arridge, G. Poh, X. Jia, N. Sergis, A. J. Coates, G. H. Jones, and J. H. Waite (2016a), Flux transfer event observation at Saturn's dayside magnetopause by the Cassini spacecraft, *Geophysical Research Letters*, *43*(13), 6713–6723, doi:10.1002/2016GL069260.

Jasinski, J. M., C. S. Arridge, A. J. Coates, G. H. Jones, N. Sergis, M. F. Thomsen, D. B. Reisenfeld, N. Krupp, and J. H. Waite (2016b), Cassini plasma observations of Saturn's magnetospheric cusp, *Journal of Geophysical Research: Space Physics*, *121*(12), 12,047–12,067, doi:10.1002/2016JA023310.

Jia, X., and M. G. Kivelson (2012), Driving Saturn's magnetospheric periodicities from the upper atmosphere/ionosphere: Magnetotail response to dual sources, *Journal of Geophysical Research: Space Physics*, *117*(11), doi:10.1029/2012JA018183.

Jia, X., K. C. Hansen, T. I. Gombosi, M. G. Kivelson, G. Tóth, D. L. Dezeeuw, and A. J. Ridley (2012), Magnetospheric configuration and dynamics of Saturn's magnetosphere: A global MHD simulation, *Journal of Geophysical Research: Space Physics*, *117*(5), doi:10.1029/2012JA017575.

Joy, S. P., M. G. Kivelson, R. J. Walker, K. K. Khurana, C. T. Russell, and T. Ogino (2002), Probabilistic models of the Jovian magnetopause and bow shock locations, *Journal of Geophysical Research: Space Physics*, *107*(A10), SMP 17–1—-SMP 17–17, doi:10.1029/2001JA009146.

Kaiser, M. L., and M. D. Desch (1984), Radio emissions from the planets Earth, Jupiter, and Saturn, doi:10.1029/RG022i004p00373.

Kaiser, M. L., M. D. Desch, J. W. Warwick, and J. B. Pearce (1980), Voyager Detection of Nonthermal Radio Emission from Saturn, *Science*, *209*(4462), 1238–1240, doi:10.1126/science.209.4462.1238.

Kellert, S., E. J. Bunce, A. J. Coates, and S. W. Cowley (2009), Thickness of Saturn's ring current determined from north-south Cassini passes through the current layer, *Journal of Geophysical Research: Space Physics*, *114*(4), doi:10.1029/2008JA013942.

Kennelly, T. J., J. S. Leisner, G. B. Hospodarsky, and D. A. Gurnett (2013), Ordering of injection events within Saturnian SLS longitude and local time, *Journal of Geophysical Research: Space Physics*, *118*(2), 832–838, doi:10.1002/jgra.50152.

Khurana, K. K. (1992), A generalized hinged-magnetodisc model of Jupiter's nightside current sheet, *Journal of Geophysical Research*, *97*(A5), 6269, doi:10.1029/92JA00169.

Khurana, K. K., and M. G. Kivelson (1989), On Jovian plasma sheet structure, *Journal of Geophysical Research*, *94*(A9), 11,791, doi:10.1029/JA094iA09p11791.

Khurana, K. K., D. G. Mitchell, C. S. Arridge, M. K. Dougherty, C. T. Russell, C. Paranicas, N. Krupp, and A. J. Coates (2009), Sources of rotational signals in Saturn's magnetosphere, *Journal of Geophysical Research: Space Physics*, *114*(2), doi:10.1029/2008JA013312.

Kiehas, S. A., V. Angelopoulos, A. Runov, and S. S. Li (2013), On the azimuthal size of flux ropes near lunar orbit, *Journal of Geophysical Research: Space Physics*, *118*(7), 4415–4424, doi:10.1002/jgra.50425.

Kimura, T., L. Lamy, C. Tao, S. V. Badman, S. Kasahara, B. Cecconi, P. Zarka, A. Morioka, Y. Miyoshi, D. Maruno, Y. Kasaba, and M. Fujimoto (2013), Long-term modulations of Saturn's auroral radio emissions by the solar wind and seasonal variations controlled by the solar ultraviolet flux, *Journal of Geophysical Research: Space Physics*, *118*(11), 7019–7035, doi:10.1002/2013JA018833.

Kivelson, M. G., and C. T. Russell (1995), *Introduction to space physics*, 568 pp., Cambridge University Press.

Kivelson, M. G., K. K. Khurana, J. D. Means, C. T. Russell, and R. C. Snare (1992), The Galileo magnetic field investigation, *Space Science Reviews*, *60*(1-4), 357–383, doi:10.1007/BF00216862.

Kivelson, M. G., F. Bagenal, W. S. Kurth, F. M. Neubauer, C. Paranicas, and J. Saur (2003), Magnetospheric interactions with satellites, in *Jupiter. The Planet, Satellites and Magnetosphere*, vol. 1, edited by W. B. M. Fran Bagenal, Timothy E. Dowling, pp. 1–24, Cambridge University Press, Cambridge, UK.

Klimas, A. J., D. Vassiliadis, D. N. Baker, and D. A. Roberts (1996), The organized nonlinear dynamics of the magnetosphere, *Journal of Geophysical Research: Space Physics*, *101*(A6), 13,089–13,113, doi:10.1029/96JA00563.

Klimas, A. J., J. A. Valdivia, D. Vassiliadis, D. N. Baker, M. Hesse, and J. Takalo (2000), Self-organized criticality in the substorm phenomenon and its relation to localized reconnection in the magnetospheric plasma sheet, *Journal of Geophysical Research: Space Physics*, *105*(A8), 18,765–18,780, doi:10.1029/1999JA000319.

Klimas, A. J., V. M. Uritsky, D. Vassiliadis, and D. N. Baker (2004), Reconnection and scale-free avalanching in a driven current-sheet model, *Journal of Geophysical Research: Space Physics*, *109*(A2), doi:10.1029/2003JA010036.

Krimigis, S., and E. Roelof (1983), Low-energy particle population, *Physics of the Jovian Magnetosphere*, pp. 106–156.

Krimigis, S. M., D. G. Mitchell, D. C. Hamilton, N. Krupp, S. Livi, E. C. Roelof, J. Dandouras, T. P. Armstrong, B. H. Mauk, C. Paranicas, P. C. Brandt, S. Bolton, A. F. Cheng, T. Choo, G. Gloeckler, J. Hayes, K. C. Hsieh, W. H. Ip, S. Jaskulek, E. P. Keath, E. Kirsch, M. Kusterer, A. Lagg, L. J. Lanzerotti, D. LaVallee, J. Manweiler, R. W. McEntire, W. Rasmuss, J. Saur, F. S. Turner, D. J. Williams, and J. Woch (2005), Dynamics of Saturn's magnetosphere from MIMI during Cassini's orbital insertion, *Science*, *307*(5713), 1270–1273, doi:10.1126/science.1105978.

Kronberg, E. A., K. H. Glassmeier, J. Woch, N. Krupp, A. Lagg, and M. K. Dougherty (2007), A possible intrinsic mechanism for the quasi-periodic dynamics of the Jovian

magnetosphere, *Journal of Geophysical Research: Space Physics*, *112*(5), doi:10.1029/2006JA011994.

Kronberg, E. A., J. Woch, N. Krupp, and A. Lagg (2008a), Mass release process in the Jovian magnetosphere: Statistics on particle burst parameters, *Journal of Geophysical Research: Space Physics*, *113*(10), doi:10.1029/2008JA013332.

Kronberg, E. A., J. Woch, N. Krupp, A. Lagg, P. W. Daly, and A. Korth (2008b), Comparison of periodic substorms at Jupiter and Earth, *Journal of Geophysical Research: Space Physics*, *113*(4), doi:10.1029/2007JA012880.

Krupp, N., J. Woch, A. Lagg, B. Wilken, S. Livi, and D. J. Williams (1998), Energetic particle bursts in the predawn Jovian magnetotail, *Geophysical Research Letters*, *25*(8), 1249–1252, doi:10.1029/98GL00863.

Krupp, N., V. M. Vasylinunas, J. Woch, A. Lagg, K. K. Khurana, M. G. Kivelson, B. H. Mauk, E. C. Roelof, D. J. Williams, S. M. Krimigis, W. S. Kruth, L. A. Frank, and W. R. Paterson (2004), Dynamics of the Jovian Magnetosphere, in *Jupiter: The Planet, Satellites and Magnetosphere*, edited by F. Bagenal, T. Dowling, and W. McKinnon, Cambridge Planetary Science, chap. 6, Cambridge University Press, New York.

Kunow, H. (2001), *Solar Wind: Corotating Interaction Regions*, Institute of Physics, Bristol, doi:10.1888/0333750888/2311.

Kurth, W. S. (1981), Escaping nonthermal continuum radiation, in *Planetary Radio Emissions III*, edited by H. O. Rucker, S. J. Bauer, and M. L. Kaiser, pp. 329–350, Austrian Acad. of Sci. Press, Vienna, doi:10.1029/JA086iA07p05519.

Kurth, W. S., D. A. Gurnett, J. T. Clarke, P. Zarka, M. D. Desch, M. L. Kalser, B. Cecconi, A. Lecacheax, W. M. Farrell, P. Galopeau, J. O. Gérard, D. Grodent, R. Prangé, M. K. Dougherty, and F. J. Crary (2005), An Earth-like correspondence between Saturn's auroral features and radio emission, *Nature*, *433*(7027), 722–725, doi:10.1038/nature03334.

Kurth, W. S., A. Lecacheux, T. F. Averkamp, J. B. Groene, and D. A. Gurnett (2007), A Saturnian longitude system based on a variable kilometric radiation period, *Geophysical Research Letters*, *34*(2), doi:10.1029/2006GL028336.

Kurth, W. S., T. F. Averkamp, D. A. Gurnett, J. B. Groene, and A. Lecacheux (2008), An update to a Saturnian longitude system based on kilometric radio emissions, *Journal of Geophysical Research: Space Physics*, *113*(5), doi:10.1029/2007JA012861.

Kurth, W. S., G. B. Hospodarsky, D. A. Gurnett, L. Lamy, M. K. Dougherty, J. Nichols, E. J. Bunce, W. Pryor, K. Baines, T. Stallard, H. Melin, and F. J. Crary (2016), Saturn

kilometric radiation intensities during the Saturn auroral campaign of 2013, *Icarus*, *263*, 2–9, doi:10.1016/j.icarus.2015.01.003.

Ladreiter, H. P., P. Zarka, and A. Lecacheux (1994), Direction finding study of Jovian hectometric and broadband kilometric radio emissions: evidence for their auroral origin, *Planetary and Space Science*, *42*(11), 919–931, doi:10.1016/0032-0633(94)90052-3.

Lamy, L. (2011), Variability of southern and northern periodicities of Saturn Kilometric Radiation, in *Planetary Radio Emissions V11*, pp. 15–17, Austrian Academy of Sciences press.

Lamy, L., P. Zarka, B. Cecconi, R. Prangé, W. S. Kurth, and D. A. Gurnett (2008), Saturn kilometric radiation: Average and statistical properties, *Journal of Geophysical Research: Space Physics*, *113*(7), doi:10.1029/2007JA012900.

Lamy, L., B. Cecconi, R. Prangé, P. Zarka, J. D. Nichols, and J. T. Clarke (2009), An auroral oval at the footprint of Saturns kilometric radio sources, colocated with the UV aurorae, *Journal of Geophysical Research: Space Physics*, *114*(10), doi:10.1029/2009JA014401.

Lamy, L., P. Schippers, P. Zarka, B. Cecconi, C. S. Arridge, M. K. Dougherty, P. Louarn, N. Andr, W. S. Kurth, R. L. Mutel, D. A. Gurnett, and A. J. Coates (2010), Properties of Saturn kilometric radiation measured within its source region, *Geophysical Research Letters*, *37*(12), doi:10.1029/2010GL043415.

Lamy, L., B. Cecconi, P. Zarka, P. Canu, P. Schippers, W. S. Kurth, R. L. Mutel, D. A. Gurnett, D. Menietti, and P. Louarn (2011), Emission and propagation of Saturn kilometric radiation: Magnetoionic modes, beaming pattern, and polarization state, *Journal of Geophysical Research: Space Physics*, *116*(4), doi:10.1029/2010JA016195.

Lamy, L., R. Prangé, W. Pryor, J. Gustin, S. V. Badman, H. Melin, T. Stallard, D. G. Mitchell, and P. C. Brandt (2013), Multispectral simultaneous diagnosis of Saturn's aurorae throughout a planetary rotation, *Journal of Geophysical Research: Space Physics*, *118*(8), 4817–4843, doi:10.1002/jgra.50404.

Leisner, J. S., C. T. Russell, K. K. Khurana, M. K. Dougherty, and N. André (2005), Warm flux tubes in the E-ring plasma torus: Initial Cassini magnetometer observations, *Geophysical Research Letters*, *32*(14), 1–4, doi:10.1029/2005GL022652.

Lepping, R. P., M. D. Desch, L. W. Klein, E. C. Sittler, J. D. Sullivan, W. S. Kurth, and K. W. Behannon (1983), Structure and other properties of Jupiter's distant magnetotail, *Journal of Geophysical Research: Space Physics*, *88*(A11), 8801–8815, doi:10.1029/JA088iA11p08801.

Liu, X., T. W. Hill, R. A. Wolf, S. Sazykin, R. W. Spiro, and H. Wu (2010), Numerical simulation of plasma transport in Saturn's inner magnetosphere using the Rice Convection Model, *Journal of Geophysical Research: Space Physics*, *115*(12), doi:10.1029/2010JA015859.

Lockwood, M., and S. W. H. Cowley (1992), Ionospheric convection and the substorm cycle, in *Substorms 1: Proceedings of the First International Conference on Substorms*, vol. 1, pp. 99–109.

Louarn, P., and D. Le Quéau (1996), Generation of the Auroral Kilometric Radiation in plasma cavities - II. The cyclotron maser instability in small size sources, *Planetary and Space Science*, *44*(3), 211–224, doi:10.1016/0032-0633(95)00122-0.

Louarn, P., A. Roux, S. Perraut, W. Kurth, and D. Gurnett (1998), A study of the large-scale dynamics of the jovian magnetosphere using the galileo plasma wave experiment, *Geophysical Research Letters*, *25*(15), 2905–2908, doi:10.1029/98GL01774.

Louarn, P., A. Roux, S. Perraut, W. S. Kurth, and D. A. Gurnett (2000), A study of the Jovian energetic magnetospheric events observed by Galileo: role in the radial plasma transport, *Journal of Geophysical Research: Space Physics*, *105*(A6), 13,073–13,088, doi:10.1029/1999JA900478.

Louarn, P., B. H. Mauk, M. G. Kivelson, W. S. Kurth, A. Roux, C. Zimmer, D. A. Gurnett, and D. J. Williams (2001), A multi-instrument study of a Jovian magnetospheric disturbance, *Journal of Geophysical Research: Space Physics*, *106*(A12), 29,883–29,898, doi:10.1029/2001JA900067.

Louarn, P., W. S. Kurth, D. A. Gurnett, G. B. Hospodarsky, A. M. Persoon, B. Cecconi, A. Lecacheux, P. Zarka, P. Canu, A. Roux, H. O. Rucker, W. M. Farrell, M. L. Kaiser, N. Andre, C. Harvey, and M. Blanc (2007), Observation of similar radio signatures at Saturn and Jupiter: Implications for the magnetospheric dynamics, *Geophysical Research Letters*, *34*(20), L20,113, doi:10.1029/2007GL030368.

Lui, A. T., R. E. Lopez, S. M. Krimigis, R. W. McEntire, L. J. Zanetti, and T. A. Potemra (1988), A case study of magnetotail current sheet disruption and diversion, *Geophysical Research Letters*, *15*(7), 721–724, doi:10.1029/GL015i007p00721.

Lui, A. T., S. C. Chapman, K. Liou, P. T. Newell, C. I. Meng, M. Brittnacher, and G. K. Parks (2000), Is the dynamic magnetosphere an avalanching system?, *Geophysical Research Letters*, *27*(7), 911–914, doi:10.1029/1999GL010752.

Ma, X., A. Otto, and P. A. Delamere (2014), Interaction of magnetic reconnection and Kelvin-Helmholtz modes for large magnetic shear: 2. Reconnection trigger, *Journal of Geophysical Research A: Space Physics*, *119*(2), 808–820, doi:10.1002/2013JA019225.

Masters, A., N. Achilleos, C. Bertucci, M. K. Dougherty, S. J. Kanani, C. S. Arridge, H. J. McAndrews, and A. J. Coates (2009), Surface waves on Saturn's dawn flank magnetopause driven by the Kelvin-Helmholtz instability, *Planetary and Space Science*, *57*(14-15), 1769–1778, doi:10.1016/j.pss.2009.02.010.

Masters, A., J. P. Eastwood, M. Swisdak, M. F. Thomsen, C. T. Russell, N. Sergis, F. J. Crary, M. K. Dougherty, A. J. Coates, and S. M. Krimigis (2012), The importance of plasma β conditions for magnetic reconnection at Saturn's magnetopause, *Geophysical Research Letters*, *39*(8), doi:10.1029/2012GL051372.

Masters, A., M. Fujimoto, H. Hasegawa, C. T. Russell, A. J. Coates, and M. K. Dougherty (2014), Can magnetopause reconnection drive Saturn's magnetosphere?, *Geophysical Research Letters*, *41*(6), 1862–1868, doi:10.1002/2014GL059288.

Mauk, B. H., D. C. Hamilton, T. W. Hill, G. B. Hospodarsky, R. E. Johnson, C. Paranicas, E. Roussos, C. T. Russell, D. E. Shemansky, E. C. Sittler, and R. M. Thorne (2009), Fundamental plasma processes in saturn's magnetosphere, in *Saturn from Cassini-Huygens*, pp. 281–331, Springer Netherlands, Dordrecht, doi: 10.1007/978-1-4020-9217-6_11.

McAndrews, H. J., C. J. Owen, M. F. Thomsen, B. Lavraud, A. J. Coates, M. K. Dougherty, and D. T. Young (2008), Evidence for reconnection at Saturn's magnetopause, *Journal of Geophysical Research: Space Physics*, *113*(4), doi:10.1029/2007JA012581.

McComas, D., and F. Bagenal (2007), Jupiter: A fundamentally different magnetospheric interaction with the solar wind, *Geophys. ˜Res. ˜Lett.*, *34*(August), 1–5, doi: 10.1029/2007GL031078.

McComas, D. J., and F. Bagenal (2008), Reply to comment by S. W. H. Cowley et al. on "Jupiter: A fundamentally different magnetospheric interaction with the solar wind", *Geophysical Research Letters*, *35*(10), 20,106, doi:10.1029/2008GL034351.

McComas, D. J., F. Allegrini, F. Bagenal, F. Crary, R. W. Ebert, H. Elliott, A. Stern, and P. Valek (2007), Diverse plasma populations and structures in Jupiter's magnetotail, *Science*, *318*(5848), 217–220, doi:10.1126/science.1147393.

McComas, D. J., R. W. Ebert, H. A. Elliott, B. E. Goldstein, J. T. Gosling, N. A. Schwadron, and R. M. Skoug (2008), Weaker solar wind from the polar coronal holes and the whole Sun, *Geophysical Research Letters*, *35*(18), L18,103, doi: 10.1029/2008GL034896.

McComas, D. J., F. Bagenal, and R. W. Ebert (2014), Bimodal size of Jupiter's magnetosphere, *Journal of Geophysical Research: Space Physics*, *119*(3), 1523–1529, doi: 10.1002/2013JA019660.

McNutt, R. L., J. W. Belcher, and H. S. Bridge (1981), Positive ion observations in the middle magnetosphere of Jupiter, *Journal of Geophysical Research: Space Physics*, *86*(A10), 8319–8342, doi:10.1029/JA086iA10p08319.

McNutt, R. L., D. K. Haggerty, M. E. Hill, S. M. Krimigis, S. Livi, G. C. Ho, R. S. Gurnee, B. H. Mauk, D. G. Mitchell, E. C. Roelof, D. J. McComas, F. Bagenal, H. A. Elliott, L. E. Brown, M. Kusterer, J. Vandegriff, S. A. Stern, H. A. Weaver, J. R. Spencer, and J. M. Moore (2007), Energetic particles in the Jovian magnetotail, *Science*, *318*(5848), 220–222, doi:10.1126/science.1148025.

Menietti, J. D., O. Santolik, A. M. Rymer, G. B. Hospodarsky, A. M. Persoon, D. A. Gurnett, A. J. Coates, and D. T. Young (2008), Analysis of plasma waves observed within local plasma injections seen in Saturn's magnetosphere, *Journal of Geophysical Research: Space Physics*, *113*(5), doi:10.1029/2007JA012856.

Menietti, J. D., S. Y. Ye, P. H. Yoon, O. Santolik, A. M. Rymer, D. A. Gurnett, and A. J. Coates (2009), Analysis of narrowband emission observed in the Saturn magnetosphere A06206, *Journal of Geophysical Research: Space Physics*, *114*(6), doi: 10.1029/2008JA013982.

Menietti, J. D., R. L. Mutel, P. Schippers, S. Y. Ye, D. A. Gurnett, and L. Lamy (2011), Analysis of Saturn kilometric radiation near a source center, *Journal of Geophysical Research: Space Physics*, *116*(12), doi:10.1029/2011JA017056.

Meredith, C. J., S. W. Cowley, and J. D. Nichols (2014), Survey of Saturn auroral storms observed by the Hubble Space Telescope: Implications for storm time scales, doi:10.1002/2014JA020601.

Meyer-Vernet, N., M. Moncuquet, and S. Hoang (1995), Temperature inversion in the Io plasma torus, *Icarus*, *116*(1), 202–213, doi:10.1006/icar.1995.1121.

Milan, S. E., E. J. Bunce, S. W. Cowley, and C. M. Jackman (2005), Implications of rapid planetary rotation for the Dungey magnetotail of Saturn, *Journal of Geophysical Research: Space Physics*, *110*(A3), doi:10.1029/2004JA010716.

Milan, S. E., G. Provan, and B. Hubert (2007), Magnetic flux transport in the Dungey cycle: A survey of dayside and nightside reconnection rates, *Journal of Geophysical Research: Space Physics*, *112*(1), doi:10.1029/2006JA011642.

Milan, S. E., A. Grocott, C. Forsyth, S. M. Imber, P. D. Boakes, and B. Hubert (2009), A superposed epoch analysis of auroral evolution during substorm growth, onset and recovery: open magnetic flux control of substorm intensity, *Annales Geophysicae*, *27*(2), 659–668, doi:10.5194/angeo-27-659-2009.

Milan, S. E., J. S. Gosling, and B. Hubert (2012), Relationship between interplanetary parameters and the magnetopause reconnection rate quantified from observations of the expanding polar cap, *Journal of Geophysical Research: Space Physics*, *117*(3), doi:10.1029/2011JA017082.

Morioka, A., Y. Miyoshi, F. Tsuchiya, H. Misawa, T. Sakanoi, K. Yumoto, R. R. Anderson, J. D. Menietti, and E. F. Donovan (2007), Dual structure of auroral acceleration regions at substorm onsets as derived from auroral kilometric radiation spectra, *Journal of Geophysical Research: Space Physics*, *112*(6), doi:10.1029/2006JA012186.

Morioka, A., Y. Miyoshi, N. Kitamura, H. Misawa, F. Tsuchiya, J. D. Menietti, and F. Honary (2012), Fundamental characteristics of field-aligned auroral acceleration derived from AKR spectra, *Journal of Geophysical Research: Space Physics*, *117*(2), doi:10.1029/2011JA017137.

Morooka, M. W., R. Modolo, J. E. Wahlund, M. André, A. I. Eriksson, A. M. Persoon, D. A. Gurnett, W. S. Kurth, A. J. Coates, G. R. Lewis, K. K. Khurana, and M. Dougherty (2009), The electron density of Saturn's magnetosphere, *Annales Geophysicae*, *27*(7), 2971–2991, doi:10.5194/angeo-27-2971-2009.

Mutel, R. L., J. D. Menietti, D. A. Gurnett, W. Kurth, P. Schippers, C. Lynch, L. Lamy, C. Arridge, and B. Cecconi (2010), CMI growth rates for Saturnian kilometric radiation, *Geophysical Research Letters*, *37*(19), doi:10.1029/2010GL044940.

Ness, N. F., K. W. Behannon, R. P. Lepping, and K. H. Schatten (1971), Use of two magnetometers for magnetic field measurements on a spacecraft, *Journal of Geophysical Research*, *76*(16), 3564–3573, doi:10.1029/JA076i016p03564.

Ness, N. F., M. H. Acuna, R. P. Lepping, L. F. Burlaga, K. W. Behannon, and F. M. Neubauer (1979a), Magnetic Field Studies at Jupiter by Voyager 1: Preliminary Results, *Science*, *204*(4396), 982–987, doi:10.1126/science.204.4396.982.

Ness, N. F., M. H. Acuna, R. P. Lepping, L. F. Burlaga, K. W. Behannon, and F. M. Neubauer (1979b), Magnetic Field Studies at Jupiter by Voyager 1: Preliminary Results, *Science*, *204*(4396), 982–987, doi:10.1126/science.204.4396.982.

Nichols, J. D., S. W. Cowley, and D. J. McComas (2006), Magnetopause reconnection rate estimates for Jupiter's magnetosphere based on interplanetary measurements at 5AU, *Annales Geophysicae*, *24*(1), 393–406, doi:10.5194/angeo-24-393-2006.

Nichols, J. D., E. J. Bunce, J. T. Clarke, S. W. Cowley, J. C. Gérard, D. Grodent, and W. R. Pryor (2007), Response of Jupiter's UV auroras to interplanetary conditions as observed by the Hubble Space Telescope during the Cassini flyby campaign, *Journal of Geophysical Research: Space Physics*, *112*(2), doi:10.1029/2006JA012005.

Nichols, J. D., B. Cecconi, J. T. Clarke, S. W. Cowley, J. C. Grard, A. Grocott, D. Grodent, L. Lamy, and P. Zarka (2010), Variation of Saturn's UV aurora with SKR phase, *Geophysical Research Letters*, *37*(15), doi:10.1029/2010GL044057.

Nichols, J. D., S. V. Badman, F. Bagenal, S. J. Bolton, B. Bonfond, E. J. Bunce, J. T. Clarke, J. E. Connerney, S. W. Cowley, R. W. Ebert, M. Fujimoto, J. C. Gérard, G. R. Gladstone, D. Grodent, T. Kimura, W. S. Kurth, B. H. Mauk, G. Murakami, D. J. McComas, G. S. Orton, A. Radioti, T. S. Stallard, C. Tao, P. W. Valek, R. J. Wilson, A. Yamazaki, and I. Yoshikawa (2017), Response of Jupiter's auroras to conditions in the interplanetary medium as measured by the Hubble Space Telescope and Juno, *Geophysical Research Letters*, *44*(15), 7643–7652, doi:10.1002/2017GL073029.

Nishida, A., T. Mukai, T. Yamamoto, S. Kokubun, and K. Maezawa (1998), A unified model of the magnetotail convection in geomagnetically quiet and active times, *Journal of Geophysical Research: Space Physics*, *103*(A3), 4409–4418, doi:10.1029/97JA01617.

Øieroset, M., T. D. Phan, M. Fujimoto, R. P. Lin, and R. P. Lepping (2001), In situ detection of collisionless reconnection in the Earth's magnetotail, *Nature*, *412*(6845), 414–417, doi:10.1038/35086520.

Paranicas, C., D. G. Mitchell, E. C. Roelof, P. C. Brandt, D. J. Williams, S. M. Krimigis, and B. H. Mauk (2005), Periodic intensity variations in global ENA images of Saturn, *Geophysical Research Letters*, *32*(21), 1–4, doi:10.1029/2005GL023656.

Parker, E. N. (1958), Dynamics of the Interplanetary Gas and Magnetic Fields., *The Astrophysical Journal*, *128*, 664, doi:10.1086/146579.

Parker, E. N., R. E. Marshak, and G. Johnson (1964), *Internplanetary Dynamical Processes*, vol. 17, 1 ed., 72–72 pp., New York, Interscience Publishers, doi:10.1063/1.3051487.

Persoon, A. M., D. A. Gurnett, W. S. Kurth, G. B. Hospodarsky, J. B. Groene, P. Canu, and M. K. Dougherty (2005), Equatorial electron density measurements in Saturn's inner magnetosphere, *Geophysical Research Letters*, *32*(23), 1–4, doi:10.1029/2005GL024294.

Pilkington, N. M., N. Achilleos, C. S. Arridge, P. Guio, A. Masters, L. C. Ray, N. Sergis, M. F. Thomsen, A. J. Coates, and M. K. Dougherty (2015), Internally driven large-scale changes in the size of Saturn's magnetosphere, *Journal of Geophysical Research A: Space Physics*, *120*(9), 7289–7306, doi:10.1002/2015JA021290.

Pontius, D. H., and T. W. Hill (2009), Plasma mass loading from the extended neutral gas torus of Enceladus as inferred from the observed plasma corotation lag, *Geophysical Research Letters*, *36*(23), L23,103, doi:10.1029/2009GL041030.

Pontius, D. H., R. A. Wolf, T. W. Hill, R. W. Spiro, Y. S. Yang, and W. H. Smyth (1998), Velocity shear impoundment of the Io plasma torus, *Journal of Geophysical Research: Planets*, *103*(E9), 19,935–19,946, doi:10.1029/98JE00538.

Porco, C. C., P. Helfenstein, P. C. Thomas, A. P. Ingersoll, J. Wisdom, R. West, G. Neukum, T. Denk, R. Wagner, T. Roatsch, S. Kieffer, E. Turtle, A. McEwen, T. V. Johnson, J. Rathbun, J. Veverka, D. Wilson, J. Perry, J. Spitale, A. Brahic, J. A. Burns, A. D. DelGenio, L. Dones, C. D. Murray, and S. Squyres (2006), Cassini observes the active south pole of enceladus, *Science*, *311*(5766), 1393–1401, doi:10.1126/science.1123013.

Pritchett, P. L., R. J. Strangeway, R. E. Ergun, and C. W. Carlson (2002), Generation and propagation of cyclotron maser emissions in the finite auroral kilometric radiation source cavity, *Journal of Geophysical Research: Space Physics*, *107*(A12), SMP 13–1–SMP 13–17, doi:10.1029/2002JA009403.

Provan, G., D. J. Andrews, C. S. Arridge, A. J. Coates, S. W. Cowley, S. E. Milan, M. K. Dougherty, and D. M. Wright (2009a), Polarization and phase of planetary-period magnetic field oscillations on high-latitude field lines in Saturn's magnetosphere, *Journal of Geophysical Research: Space Physics*, *114*(2), doi:10.1029/2008JA013782.

Provan, G., S. W. Cowley, and J. D. Nichols (2009b), Phase relation of oscillations near the planetary period of Saturn's auroral oval and the equatorial magnetospheric magnetic field, *Journal of Geophysical Research: Space Physics*, *114*(4), doi:10.1029/2008JA013988.

Provan, G., D. J. Andrews, B. Cecconi, S. W. H. Cowley, M. K. Dougherty, L. Lamy, and P. M. Zarka (2011), Magnetospheric period magnetic field oscillations at Saturn: Equatorial phase "jitter" produced by superposition of southern and northern period oscillations, *Journal of Geophysical Research: Space Physics*, *116*(4), doi:10.1029/2010JA016213.

Provan, G., D. J. Andrews, C. S. Arridge, A. J. Coates, S. W. H. Cowley, G. Cox, M. K. Dougherty, and C. M. Jackman (2012), Dual periodicities in planetary-period

magnetic field oscillations in Saturn's tail, *Journal of Geophysical Research: Space Physics*, *117*(1), doi:10.1029/2011JA017104.

Provan, G., S. W. H. Cowley, J. Sandhu, D. J. Andrews, and M. K. Dougherty (2013), Planetary period magnetic field oscillations in Saturn's magnetosphere: Postequinox abrupt nonmonotonic transitions to northern system dominance, *Journal of Geophysical Research: Space Physics*, *118*(6), 3243–3264, doi:10.1002/jgra.50186.

Pryor, W. R., A. I. F. Stewart, L. W. Esposito, W. E. McClintock, J. E. Colwell, A. J. Jouchoux, A. J. Steffl, D. E. Shemansky, J. M. Ajello, R. A. West, C. J. Hansen, B. T. Tsurutani, W. S. Kurth, G. B. Hospodarsky, D. A. Gurnett, K. C. Hansen, J. H. Waite, F. J. Crary, D. T. Young, N. Krupp, J. T. Clarke, D. Grodent, and M. K. Dougherty (2005), Cassini UVIS observations of Jupiter's auroral variability, *Icarus*, *178*(2), 312–326, doi:10.1016/j.icarus.2005.05.021.

Radioti, A., D. Grodent, J. C. Gérard, B. Bonfond, and J. T. Clarke (2008), Auroral polar dawn spots: Signatures of internally driven reconnection processes at Jupiter's magnetotail, *Geophysical Research Letters*, *35*(3), doi:10.1029/2007GL032460.

Randall, B. A. (1994), Energetic electrons in the magnetosphere of Saturn, *Science*, *99*(4122), 8771–8785.

Reiner, M. J., J. Fainberg, R. G. Stone, M. L. Kaiser, M. D. Desch, R. Manning, P. Zarka, and B.-M. Pedersen (1993), Source characteristics of Jovian narrow-band kilometric radio emissions, *Journal of Geophysical Research*, *98*(E7), 13,163, doi:10.1029/93JE00536.

Reiner, M. J., M. L. Kaiser, and M. D. Desch (2000), Long-term behavior of Jovian bKOM and nKOM radio emissions observed during the Ulysses-Jupiter encounter, *Geophysical Research Letters*, *27*(3), 297–300, doi:10.1029/1999GL003710.

Richardson, I. G., S. W. H. Cowley, E. W. Hones, and S. J. Bame (1987), Plasmoid-associated energetic ion bursts in the deep geomagnetic tail: Properties of plasmoids and the postplasmoid plasma sheet, *Journal of Geophysical Research*, *92*(A9), 9997, doi:10.1029/JA092iA09p09997.

Russell, C. T., K. K. Khurana, D. E. Huddleston, and M. G. Kivelson (1998), Localized reconnection in the near jovian magnetotail, *Science*, *280*(5366), 1061–1064, doi:10.1126/science.280.5366.1061.

Rymer, A. M., B. H. Mauk, T. W. Hill, N. André, D. G. Mitchell, C. Paranicas, D. T. Young, H. T. Smith, A. M. Persoon, J. D. Menietti, G. B. Hospodarsky, A. J. Coates, and M. K. Dougherty (2009), Cassini evidence for rapid interchange transport at

Saturn, *Planetary and Space Science*, *57*(14-15), 1779–1784, doi:10.1016/j.pss.2009.04.010.

Sandel, B. R., D. E. Shemansky, A. A. L. Broadfoot, J. L. Bertaux, J. E. Blamont, S. Belton, J. M. Ajello, J. B. Holberg, S. K. Atreya, T. M. Donahue, H. W. Moos, D. F. Strobel, J. C. McConnell, A. Dalgarno, R. Goody, M. B. Mcelroy, P. Z. Takacs, and M. J. S. Belton (1979), Extreme Ultraviolet Observations from Voyager 2 Encounter with Jupiter, *Science*, *206*(4421), 962–966, doi:10.1126/science.204.4396.979.

Saur, J., D. F. Strobel, F. M. Neubauer, and M. E. Summers (2003), The ion mass loading rate at Io, *Icarus*, *163*(2), 456–468, doi:Doi10.1016/S0019-1035(03)00085-X.

Scarf, F. L., I. M. Green, G. L. Siscoe, D. S. Intriligator, D. D. McKibbin, and J. H. Wolfe (1970), Pioneer 8 electric field measurements in the distant geomagnetic tail, *Journal of Geophysical Research*, *75*(16), 3167–3179, doi:10.1029/JA075i016p03167.

Scarf, F. L., D. A. Gurnett, W. Kurth, and R. L. Poynter (1982), Voyager 2 Plasma Wave Observations at Saturn, *Science*, *215*(4532), 587–594, doi:10.1126/science.215.4532.587.

Schreier, R., A. Eviatar, and V. M. Vasylinas (1998), A two-dimensional model of plasma transport and chemistry in the Jovian magnetosphere, *Journal of Geophysical Research: Planets*, *103*(E9), 19,901–19,913, doi:10.1029/98JE00697.

Scurry, L., and C. T. Russell (1991), Proxy studies of energy transfer to the magnetosphere, *Journal of Geophysical Research*, *96*(A6), 9541, doi:10.1029/91JA00569.

Sergis, N., S. M. Krimigis, D. G. Mitchell, D. C. Hamilton, N. Krupp, B. H. Mauk, E. C. Roelof, and M. K. Dougherty (2009), Energetic particle pressure in Saturn's magnetosphere measured with the magnetospheric Imaging instrument on Cassini, *Journal of Geophysical Research: Space Physics*, *114*(2), doi:10.1029/2008JA013774.

Sittler, E. C., and D. F. Strobel (1987), Io plasma torus electrons: Voyager 1, *Journal of Geophysical Research*, *92*(A6), 5741, doi:10.1029/JA092iA06p05741.

Slavin, J. A., D. N. Baker, J. D. Craven, R. C. Elphic, D. H. Fairfield, L. A. Frank, A. B. Galvin, W. J. Hughes, R. H. Manka, D. G. Mitchell, I. G. Richardson, T. R. Sanderson, D. J. Sibeck, E. J. Smith, and R. D. Zwickl (1989), CDAW 8 observations of plasmoid signatures in the geomagnetic tail: An assessment, *Journal of Geophysical Research*, *94*(A11), 15,153, doi:10.1029/JA094iA11p15153.

Slavin, J. A., M. F. Smith, E. L. Mazur, D. N. Baker, E. W. Hones, T. Iyemori, and E. W. Greenstadt (1993a), ISEE 3 observations of traveling compression regions in the

Earth's magnetotail, *Journal of Geophysical Research*, *98*(A9), 15,425, doi:10.1029/93JA01467.

Slavin, J. A., M. F. Smith, E. L. Mazur, D. N. Baker, E. W. Hones, T. Iyemori, and E. W. Greenstadt (1993b), ISEE 3 observations of traveling compression regions in the Earth's magnetotail, *Journal of Geophysical Research*, *98*(A9), 15,425, doi:10.1029/93JA01467.

Slavin, J. A., C. J. Owen, M. M. Kuznetsova, and M. Hesse (1995), ISEE 3 observations of plasmoids with flux rope magnectic topologies, *Geophysical Research Letters*, *22*(15), 2061–2064, doi:10.1029/95GL01977.

Slavin, J. A., R. P. Lepping, J. Gjerloev, D. H. Fairfield, M. Hesse, C. J. Owen, M. B. Moldwin, T. Nagai, A. Ieda, and T. Mukai (2003), Geotail observations of magnetic flux ropes in the plasma sheet, *Journal of Geophysical Research: Space Physics*, *108*(A1), 1015, doi:10.1029/2002JA009557.

Smith, A. W., C. M. Jackman, and M. F. Thomsen (2016), Magnetic reconnection in Saturn's magnetotail: A comprehensive magnetic field survey, *Journal of Geophysical Research A: Space Physics*, *121*(4), 2984–3005, doi:10.1002/2015JA022005.

Smith, E. J., L. Davis, D. E. Jones, P. J. Coleman, D. S. Colburn, P. Dyal, C. P. Sonett, and A. M. A. Frandsen (1974), The planetary magnetic field and magnetosphere of Jupiter: Pioneer 10, *Journal of Geophysical Research*, *79*(25), 3501–3513, doi:10.1029/JA079i025p03501.

Smith, E. J., L. Davis, D. E. Jones, P. J. Coleman, D. S. Colburn, P. Dyal, and C. P. Sonett (1975), Jupiter's Magnetic Field. Magnetosphere, and Interaction with the Solar Wind: Pioneer 11., *Science (New York, N.Y.)*, *188*(4187), 451–5, doi:10.1126/science.188.4187.451.

Smith, E. J., L. Davis, D. E. Jones, P. J. Coleman, D. S. Colburn, P. Dyal, and C. P. Sonett (1980), Saturn's Magnetic Field and Magnetosphere, *Science*, *207*(4429), 407–410, doi:10.1126/science.207.4429.407.

Smyth, W. H. (1992), Neutral cloud distribution in the Jovian system, *Advances in Space Research*, *12*(8), 337–346, doi:10.1016/0273-1177(92)90408-P.

Smyth, W. H., and M. L. Marconi (2005a), Nature of the iogenic plasma source in Jupiter's magnetosphere. II. Near-Io distribution, *Icarus*, *176*(1), 138–154, doi:10.1016/j.icarus.2005.01.010.

Smyth, W. H., and M. L. Marconi (2005b), Nature of the iogenic plasma source in Jupiter's magnetosphere. II. Near-Io distribution, *Icarus*, *176*(1), 138–154, doi:10.1016/j.icarus.2005.01.010.

Southwood, D. J., and M. G. Kivelson (2009), The source of Saturns periodic radio emission, *Journal of Geophysical Research: Space Physics*, *114*(9), doi:10.1029/2008JA013800.

Spencer, J. R., A. C. Barr, L. W. Esposito, P. Helfenstein, A. P. Ingersoll, R. Jaumann, C. P. McKay, F. Nimmo, and J. H. Waite (2009), Enceladus: An active cryovolcanic satellite, in *Saturn from Cassini-Huygens*, edited by M. K. Dougherty, L. W. Esposito, and S. M. Krimigis, pp. 683–724, Springer Netherlands, Dordrecht, doi:10.1007/978-1-4020-9217-6_21.

Steffl, A. J., and A. I. F. Stewart (2004), Cassini UVIS Observations of the Io Plasma Torus : I . Initial Results, *Icarus*, *172*(1), 78–90, doi:http://dx.doi.org/10.1016/j.icarus.2003.12.027.

Steffl, A. J., F. Bagenal, and A. I. F. Stewart (2004), Cassini UVIS observations of the Io plasma torus. II. Radial variations, *Icarus*, *172*(1 SPEC.ISS.), 91–103, doi:10.1016/j.icarus.2004.04.016.

Stevenson, D. J. (1982), Reducing the Non-Axisymmetry of a Planetary Dynamo and an Application to Saturn, *Geophysical & Astrophysical Fluid Dynamics*, *21*(1-2), 113–127, doi:10.1080/03091928208209008.

Surjalal Sharma, A. (1995), Assessing the magnetosphere's nonlinear behavior: Its dimension is low, its predictability, high, *Reviews of Geophysics*, *33*(1 S), 645–650, doi:10.1029/95RG00495.

Takalo, J., J. Timonen, and H. Koskinen (1993), Correlation dimension and affinity of AE data and bicolored noise, *Geophysical Research Letters*, *20*(15), 1527–1530, doi:10.1029/93GL01596.

Taubenschuss, U., H. O. Rucker, W. S. Kurth, B. Cecconi, P. Zarka, M. K. Dougherty, and J. T. Steinberg (2006), Linear prediction studies for the solar wind and Saturn kilometric radiation, *Annales Geophysicae*, *24*(11), 3139–3150, doi:10.5194/angeo-24-3139-2006.

Terasawa, T., K. Maezawa, and S. Machida (1978), Solar wind effect on Jupiter's non-Io-related radio emission, *Nature*, *273*(5658), 131–132, doi:10.1038/273131a0.

Thomas, N., F. Bagenal, T. W. Hill, and J. K. Wilson (2004), The Io neutral clouds and plasma torus, in *Jupiter. The Planet, Satellites and Magnetosphere*, edited by F. Bagenal, T. E. Dowloing, and W. B. McKinnon, 1 ed., chap. 23, pp. 561–591, Cambridge University Press.

Thomsen, M. F., C. M. Jackman, R. L. Tokar, and R. J. Wilson (2014), Plasma flows in Saturn's nightside magnetosphere, *Journal of Geophysical Research: Space Physics*, *119*(6), 4521–4535, doi:10.1002/2014JA019912.

Thomsen, M. F., A. J. Coates, E. Roussos, R. J. Wilson, K. C. Hansen, and G. R. Lewis (2016), Suprathermal electron penetration into the inner magnetosphere of Saturn, *Journal of Geophysical Research A: Space Physics*, *121*(6), 5436–5448, doi:10.1002/2016JA022692.

Thomsen, M. F., C. M. Jackman, S. W. Cowley, X. Jia, M. G. Kivelson, and G. Provan (2017), Evidence for periodic variations in the thickness of Saturn's nightside plasma sheet, *Journal of Geophysical Research: Space Physics*, *122*(1), 280–292, doi:10.1002/2016JA023368.

Thorne, R. M., T. P. Armstrong, S. Stone, D. J. Williams, R. W. McEntire, S. J. Bolton, D. A. Gurnett, and M. G. Kivelson (1997), Galileo evidence for rapid interchange transport in the Io torus, *Geophysical Research Letters*, *24*(17), 2131–2134, doi:10.1029/97GL01788.

Tóth, G. (1996), A General Code for Modeling MHD Flows on Parallel Computers: Versatile Advection Code, in *Magnetodynamic Phenomena in the Solar Atmosphere*, pp. 471–472, Springer Netherlands, Dordrecht, doi:10.1007/978-94-009-0315-9_101.

Uritsky, V. M., A. J. Klimas, D. Vassiliadis, D. Chua, and G. Parks (2002), Scale-free statistics of spatiotemporal auroral emissions as depicted by POLAR UVI images: Dynamic magnetosphere is an avalanching system, *Journal of Geophysical Research: Space Physics*, *107*(A12), SMP 7–1—-SMP 7–11, doi:10.1029/2001JA000281.

Vasyliünas, V. M. (1983), Plasma distribution and flow, *Physics of the Jovian magnetosphere*, *1*, 395–453, doi:10.1017/CBO9780511564574.013.

Vogt, M. F., M. G. Kivelson, K. K. Khurana, S. P. Joy, and R. J. Walker (2010), Reconnection and flows in the Jovian magnetotail as inferred from magnetometer observations, *Journal of Geophysical Research: Space Physics*, *115*(6), doi:10.1029/2009JA015098.

Vogt, M. F., M. G. Kivelson, K. K. Khurana, R. J. Walker, B. Bonfond, D. Grodent, and A. Radioti (2011), Improved mapping of Jupiter's auroral features to magnetospheric sources, *Journal of Geophysical Research: Space Physics*, *116*(3), doi:10.1029/2010JA016148.

Vogt, M. F., C. M. Jackman, J. A. Slavin, E. J. Bunce, S. W. Cowley, M. G. Kivelson, and K. K. Khurana (2014), Structure and statistical properties of plasmoids in Jupiter's

magnetotail, *Journal of Geophysical Research A: Space Physics*, *119*(2), 821–843, doi: 10.1002/2013JA019393.

Wahlund, J. E., R. Boström, G. Gustafsson, D. A. Gurnett, W. S. Kurth, T. Averkamp, G. B. Hospodarsky, A. M. Persoon, P. Canu, A. Pedersen, M. D. Desch, A. I. Eriksson, R. Gill, M. W. Morooka, and M. André (2005), The inner magnetosphere of Saturn: Cassini RPWS cold plasma results from the first encounter, *Geophysical Research Letters*, *32*(20), 1–4, doi:10.1029/2005GL022699.

Wang, Z., D. A. Gurnett, G. Fischer, S. Y. Ye, W. S. Kurth, D. G. Mitchell, J. S. Leisner, and C. T. Russell (2010), Cassini observations of narrowband radio emissions in Saturn's magnetosphere, *Journal of Geophysical Research: Space Physics*, *115*(6), doi:10.1029/2009JA014847.

Warwick, J. W., J. B. Pearce, A. C. Riddle, J. K. Alexander, M. D. Desch, M. L. Kaiser, J. R. Thieman, T. D. Carr, S. Gulkis, A. Boischot, C. C. Harvey, and B. M. Pedersen (1979), Voyager 1 planetary radio astronomy observations near jupiter, *Science*, *204*(4396), 995–998, doi:204/4396/995[pii]\r10.1126/science.204.4396.995.

Warwick, J. W., D. R. Evans, J. H. Romig, J. K. Alexander, M. D. Desch, M. L. Kaiser, M. Aubier, Y. Leblanc, A. Lecacheaux, and B. M. Pedersen (1982), Planetary Radio Astronomy Observations from Voyager 2 Near Saturn, *Science*, *215*(4532), 582 LP – 587, doi:206/4421/991[pii]\r10.1126/science.206.4421.991.

Wilson, J. K., M. Mendillo, J. Baumgardner, N. M. Schneider, J. T. Trauger, and B. Flynn (2002), The Dual Sources of Io ' s Sodium Clouds, *Icarus*, *489*(2), 476–489, doi:10.1006/icar.2002.6821.

Winglee, R., E. Harnett, A. Kidder, and D. Snowden (2009), Supplying the Io plasma torus: Local versus extended plasma sources, *AGU Fall Meeting Abstracts*, p. C3.

Woch, J., N. Krupp, A. Lagg, B. Wilken, S. Livi, and D. J. Williams (1998), Quasi-periodic modulations of the Jovian magnetotail, *Geophysical Research Letters*, *25*(8), 1253–1256, doi:10.1029/98GL00861.

Wu, C. S., and L. C. Lee (1979), A theory of the terrestrial kilometric radiation, *The Astrophysical Journal*, *230*, 621, doi:10.1086/157120.

Wu, H., T. W. Hill, R. A. Wolf, and R. W. Spiro (2007), Numerical simulation of fine structure in the Io plasma torus produced by the centrifugal interchange instability, in *Journal of Geophysical Research: Space Physics*, vol. 112, Boulder, Colorado, doi: 10.1029/2006JA012032.

Ye, S. Y., D. A. Gurnett, G. Fischer, B. Cecconi, J. D. Menietti, W. S. Kurth, Z. Wang, G. B. Hospodarsky, P. Zarka, and A. Lecacheux (2009), Source locations of narrowband radio emissions detected at saturn, *Journal of Geophysical Research: Space Physics*, *114*(6), doi:10.1029/2008JA013855.

Ye, S. Y., D. A. Gurnett, J. B. Groene, Z. Wang, and W. S. Kurth (2010a), Dual periodicities in the rotational modulation of Saturn narrowband emissions, *Journal of Geophysical Research: Space Physics*, *115*(12), doi:10.1029/2010JA015780.

Ye, S. Y., J. D. Menietti, G. Fischer, Z. Wang, B. Cecconi, D. A. Gurnett, and W. S. Kurth (2010b), Z mode waves as the source of saturn narrowband radio emissions, *Journal of Geophysical Research: Space Physics*, *115*(8), doi:10.1029/2009JA015167.

Yoshikawa, I., F. Suzuki, R. Hikida, K. Yoshioka, G. Murakami, F. Tsuchiya, C. Tao, A. Yamazaki, T. Kimura, H. Kita, H. Nozawa, and M. Fujimoto (2017), Volcanic activity on Io and its influence on the dynamics of the Jovian magnetosphere observed by EXCEED/Hisaki in 2015 7. Planetary science, *Earth, Planets and Space*, *69*(1), 110, doi:10.1186/s40623-017-0700-9.

Yoshioka, K., I. Yoshikawa, F. Tsuchiya, M. Kagitani, G. Murakami, K. Sakai, and T. Homma (2012), Feasibility study of EUV spectroscopic observation of the Io plasma torus from the earth-orbiting satellite EXCEED, *Planetary and Space Science*, *62*(1), 104–110, doi:10.1016/j.pss.2011.12.016.

Zarka, P. (1998), Auroral radio emissions at the outer planets: Observations and theories, *Journal of Geophysical Research: Planets*, *103*(E9), 20,159–20,194, doi:10.1029/98JE01323.

Zarka, P., and F. Genova (1983), Low-frequency Jovian emission and solar wind magnetic sector structure, *Nature*, *306*(5945), 767–768, doi:10.1038/306767a0.

Zarka, P., J. Queinnec, and F. J. Crary (2001), Low-frequency limit of Jovian radio emissions and implications on source locations and Io plasma wake, *Planetary and Space Science*, *49*(10-11), 1137–1149, doi:10.1016/S0032-0633(01)00021-6.

Zarka, P., B. Cecconi, and W. S. Kurth (2004), Jupiter's low-frequency radio spectrum from Cassini/Radio and Plasma Wave Science (RPWS) absolute flux density measurements, *Journal of Geophysical Research: Space Physics*, *109*(A9), A09S15, doi:10.1029/2003JA010260.

Zarka, P., L. Lamy, B. Cecconi, R. Prangé, and H. O. Rucker (2007), Modulation of Saturn's radio clock by solar wind speed, *Nature*, *450*(7167), 265–267, doi:10.1038/nature06237.

Zieger, B., and K. C. Hansen (2008), Statistical validation of a solar wind propagation model from 1 to 10 AU, *Journal of Geophysical Research: Space Physics*, *113*(8), doi:10.1029/2008JA013046.